Université de Lille, Faculté des Sciences et Technologies
Ecole Doctorale Sciences de la Matière, du Rayonnement et de l'Environnement

THÈSE

Présentée pour l'obtention du grade de :

Docteur de l'Université de Lille

Spécialité

Terre, enveloppes fluides

Par

Maria Fernanda SANCHEZ BARRERO

Development of an autonomous integrated mobile system combining lidar and photometer to monitor aerosol properties in near real time

Soutenue le 28 mars 2024

Membres de jury :

P. FORMENTI	Director de recherche	LISA-IPSL, CNRS	Rapportrice (président du jury)
E. LIND	Professeur	AERONET, NASA	Rapportrice
R. CEOLATO	Chercheur	ONERA Toulouse	Examinateur
E. LANDULFO	Professeur	U. Sao Paulo, IPEN	Examinateur
F. NIRO	Ingénieur de recherche	Serco, ESA-ESRIN	Examinateur
A. APITULEY	Chercheur	KNMI Cabauw	Invité

Direction de Thèse :

P. GOLOUB	Professeur	U. Lille, LOA	Directeur
S. VICTORI	Ingénieur de recherche	CIMEL Electronique	Encadrant
I. POPOVICI	Ingénieur de recherche	CIMEL Electronique	Co-encadrant
B. TORRES	Maître de conferences	U. Lille, LOA	Co-encadrant

Laboratoire d'Optique Atmosphérique
Université de Lille - Faculté des Sciences et Technologies
Département Physique
59655 – Villeneuve d'Ascq, France

Université de Lille, Faculté des Sciences et Technologies
Ecole Doctorale Sciences de la Matière, du Rayonnement et de l'Environnement

THÈSE

Présentée pour l'obtention du grade de :

Docteur de l'Université de Lille

Spécialité

Terre, enveloppes fluides

Par

Maria Fernanda SANCHEZ BARRERO

Développement d'un système mobile intégré temps réel combinant sondage lidar et photométrie automatiques pour la mesure des aérosols

Soutenue le 28 mars 2024

Membres de jury :

P. FORMENTI	Director de recherche	LISA-IPSL, CNRS	Rapportrice (président du jury)
E. LIND	Professeur	AERONET, NASA	Rapportrice
R. CEOLATO	Chercheur	ONERA Toulouse	Examinateur
E. LANDULFO	Professeur	U. Sao Paulo, IPEN	Examinateur
F. NIRO	Ingénieur de recherche	Serco, ESA-ESRIN	Examinateur
A. APITULEY	Chercheur	KNMI Cabauw	Invité

Direction de Thèse :

P. GOLOUB	Professeur	U. Lille, LOA	Directeur
S. VICTORI	Ingénieur de recherche	CIMEL Electronique	Encadrant
I. POPOVICI	Ingénieur de recherche	CIMEL Electronique	Co-encadrant
B. TORRES	Maître de conferences	U. Lille, LOA	Co-encadrant

Laboratoire d'Optique Atmosphérique
Université de Lille - Faculté des Sciences et Technologies
Département Physique
59655 – Villeneuve d'Ascq, France

Abstract

Improving our understanding of aerosols spatio-temporal distribution and their impact at local, regional, and global scales, while minimizing uncertainties in their properties, is crucial for accurately assessing their radiative effects. To this end, lidar and photometer are convenient tools for aerosol monitoring, enhanced by the development of networks. However, laboratories in fixed sites are restricted by their local conditions and position with respect to the aerosol sources. Thus, the deployment of mobile laboratories (aboard ship cruises, airplanes or cars) provided a solution to fill these observational gaps within networks. The first experiences using a single-wavelength elastic lidar and sun-photometer have demonstrated the feasibility of in-motion observations and highlighted ongoing technical challenges to be addressed. Therefore, the lightweight CIMEL CE376 lidar, which provides measurements at 532 nm and 808 nm and depolarization at 532 nm, is coupled with the CE318-T sun/moon photometer to enhance mobile aerosol monitoring. Both instrumental and algorithmic assessments were conducted at ATOLL (ATmospheric Observatory of liLLe) platform operated at the Laboratoire d'Optique Atmosphérique (LOA), in Lille, France. In particular, algorithmic developments are proposed to retrieve aerosols properties from the CE376 lidar measurements, envisioning near real time analysis. Data acquired at two sites, ATOLL and IZO (Izaña Observatory, Tenerife, Spain), were therefore analyzed through case studies under presence of different aerosol types (mineral dust, mineral dust-smoke, volcanic ash and sulfates), showcasing, in this way, the capabilities of the lidar system to characterize aerosols. Moreover, a first dataset of CE376 lidar and photometer performing on-road measurements was obtained during the FIREX-AQ (Fire Influence on Regional to Global Environments and Air Quality) field campaign, deployed in summer 2019 over the Northwestern USA. Despite the extreme environmental conditions, the study of smoke aerosols near fire sources was enabled by lidar and photometer mapping in 3D. The future implications of a ship-borne CE376 lidar is also presented, showcase from a single-wavelength lidar aboard the Marion Dufresne research vessel during the AMARYLLIS-TRANSAMA campaign in 2023. This work provides a comprehensive discussion on the capabilities (and limitations) of the CE376 lidar in bridging observational gaps in aerosol monitoring, providing valuable insights for future research in this field.

Résumé

Améliorer notre compréhension de la distribution spatiotemporelle des aérosols et de leur impact aux échelles locale, régionale et mondiale, tout en réduisant les incertitudes sur leurs propriétés, est crucial pour évaluer avec précision leurs effets radiatifs. À cette fin, le lidar et le photomètre sont des outils pratiques pour la surveillance des aérosols, renforcés par le développement de réseaux. Cependant, les laboratoires fixes sont limités par leurs conditions locales et leur position par rapport aux sources d'aérosols. Ainsi, le déploiement de laboratoires mobiles (à bord de croisières, avions ou voitures) fournit une solution pour combler ces insuffisances observationnelles au sein des réseaux. Les premières expériences avec un lidar élastique mono-longueur d'onde et un photomètre solaire automatiques ont démontré la faisabilité des observations en mouvement et ont mis en évidence les verrous techniques à lever. Le lidar léger CIMEL CE376, qui fournit des mesures à 532 nm et 808 nm et polarisation à 532 nm, est couplé au photomètre solaire/lunaire CE318-T pour améliorer la surveillance mobile des aérosols. Des évaluations instrumentales et algorithmiques ont été menées à la plateforme ATOLL (ATmospheric Observatory of liLLe, infrastructure ACTRIS), située au Laboratoire d'Optique Atmosphérique (LOA), Université Lille, France. En particulier, des développements algorithmiques sont proposés pour déduire les propriétés des aérosols à partir des mesures du lidar CE376, envisageant une analyse en temps quasi réel. Les données acquises sur deux sites, ATOLL et IZO (Observatoire d'Izaña, Tenerife, Espagne), ont donc été analysées à travers des études de cas en présence de différents types d'aérosols (poussières désertiques, poussières désertiques-fumée issue de feux de biomasse, cendres et sulfates volcaniques) ; illustrant ainsi les capacités du système lidar pour caractériser les aérosols. De plus, un premier ensemble de données de lidar CE376 et de photomètre effectuant des mesures en déplacement a été obtenu lors de la campagne FIREX-AQ (Fire Influence on Regional to Global Environments and Air Quality), déployée à l'été 2019 dans le nord-ouest des États-Unis. Malgré des conditions environnementales extrêmes, l'étude des aérosols de fumée près des sources d'incendie de forêt a été rendue possible par des observations en 3D du lidar et du photomètre. Les implications futures d'un lidar CE376 à bord d'un navire sont également présentées, grâce à l'intégration test d'un lidar mono-longueur d'onde à bord du navire de recherche Marion Dufresne lors de la campagne AMARYLLIS-TRANSAMA en 2023. Ce travail offre une discussion complète sur les capacités (et les limites) du lidar CE376 pour combler les lacunes observationnelles dans la surveillance des aérosols, fournissant des perspectives précieuses pour la recherche future dans ce domaine.

Acknowledgments

First of all, I would like to express my sincere gratitude to the members of the jury composed of Paola Formenti, Elena Lind, Romain Ceolato, Eduardo Landulfo, Fabrizio Niro and Arnoud Apituley. Your expertise, constructive feedback, and engaging discussions during the defense have greatly enriched my research experience. I extend my gratitude to the LOA and CIMEL who hosted the 3 years of the PhD program in the frame of CIFRE (Conventions Industrielles de Formation par la Recherche) convention. This program permitted me to explore both scientific and industry point of views, giving me the opportunity to develop my skills in a broader field. Special thanks to Didier Crozel, CIMEL CEO, and Prof. Philippe Dubuisson, LOA director, for agreeing to host the convention in both institutions. Also, my gratitude goes to the Doctoral School SMRE (Sciences de la Matière, du Rayonnement et de l'Environnement), which provided me tools to improve my scientific knowledge and communication skills. The constant efforts of the SMRE doctoral school, helping international students to integrate in the French culture, are of great value to overcome the inherent stress associated to the thesis. Thank you, Prof. Frédéric Parol and Cristophe Van Brussel, for all your support and help during these last three years.

I extend my sincere gratitude to my supervisors Philippe Goloub, Stephane Victori, Ioana Popovici and Benjamin Torres, whose thoughtful comments and recommendations guided me and helped me to arrive until this point. I am grateful to you for trusting in me, for helping me to limit the amount of work and overall, for encouraging me to explore new ideas, even if some of them failed at the end. Thanks to your valuable insights and challenging questions, I was able to grow as a researcher, gain confidence in my work and reaffirm my commitment to science. Also, thanks to your patience with my half French, half English and sometimes even half Spanish, now I am capable to speak French in our meetings without jumping immediately to English. I will always treasure the last 3 years of face-to-face meetings or scientific discussions around croissants, pain au chocolat and coffee! The best croissants by the way. Specially, thank you, Philippe, for always looking for my well-being, I am grateful for all your kind words and constant support during this academic journey. As well, I want to thank you Ioana, for taking a lot of your time to teach me with patience about the lidar design, on how to perform the calibrations, alignments and to permitting me to be part of the hard work behind a lidar system.

I acknowledge the continuous efforts of Ioana Popovici, Thierry Podvin, Qiaoyun Hu, Eric Bourrianne, Luc Blarel and Gael Dubois, in maintaining the remote sensing instruments operative at ATOLL (LOA). As well, I highlight the work of Fabrice Ducos and Romain de Fillipi in sustaining the lidar data base and the NRT data processing. Moreover, I acknowledge the constructive collaborations of Yenny Gonzales and Africa Barreto, members of AEMET-Spain, who provided the data and calibrations of the CE376 lidar operating at IZO, Tenerife-Canary Islands. Special thanks to Yenny for all the meetings to debug the codes and to share our results, ¡gracias por todo tu apoyo!

I would like to acknowledge the efforts of the FIREX-AQ DRAGON mobile team, Luc Blarel, Philippe Goloub, Ioana Popovici, Thierry Podvin, Gael Dubois, Aliaksandr Lapionak, Lelia Proniewski, Brent Holben, David Giles and Anthony LaRosa, who participated in the installation and performed the measurements under extreme conditions during the campaign in summer 2019. As well, I would like to recognize the work of the TRANSAMA scientific team, Charlotte Skonieczny, Aloys Bory, Viviane Bout Roumazeilles, Phillipe Goloub and Luc Blarel, that from land and aboard the Marion Dufresne worked hard to accomplish the goals traced at the beginning of the campaign. In particular, thanks to the opportunity of being part of TRANSAMA, now I am certified by king Neptune as a great traveler of both hemispheres.

Further, I would like to thank my colleagues at LOA and the R&D department at CIMEL, that welcomed me and made me part of the teams. J'ai apprécié tous ces moments partagés autour d'un café ou parfois autour d'une bière, grâce à votre gentillesse et votre bon sens de l'humour, ces années ont été pleines de rires et de bons moments. Un grand merci aux 'runners' du LOA, qui nous encouraget à être plus sportifs, grâce à vous j'ai fini une 10 km plus qu'un fois. Un immense merci à Anne et Marie Lyse pour leur aide précieuse dans l'administration, ce qui m'a permis de me sentir soutenu en plein milieu de la bureaucratie.

Thanks to my doctoral fellows for the good times, specially while exploring our cultures with food and drinks, we made a tour! Specially thanks to my office neighbors, Smita, William, Megane, Raphael, Yuyang, Yuliia and Gabriel, for all the laughs and interesting talks. Thanks for being there, not only on the good times but also in the moments of stress or frustration, you made a big difference!

Je remercie mes compagnons de bateau, Luc, Philippe et Viviane, pour tout le temps partagé. Merci de partager avec moi vos connaissances de la vie et de votre profession. Merci pour les conseils pour survivre au mal de mer, pour les cafés après avoir tant mangé à midi, pour les kilomètres parcourus en vélo, pour les moments passés à admirer l'océan. En fin, merci à vous trois d'avoir fait de l'aventure à bord du Marion Dufresne une expérience inoubliable.

Gracias a todos mis colegas del LFA de Bolivia, que aun a la distancia me hacen parte del laboratorio. Gracias especiales a Marcos y Ricardo, por todo lo que me enseñaron y por todos los años de ciencia de altura de los que me permitieron ser parte. Gracias al LFA, descubrí las ciencias atmosféricas y gracias a todos sus esfuerzos por crear colaboraciones, se abrieron las puertas del master y ahora del doctorado. ¡Gracias infinitas! Thank you, Prof. David Whiteman, for all the time that you took to teach me about the lidar, for letting me be part of experiments and for all the interesting discussions, you are for sure an important member of the LFA!

Gracias especiales a mis amigos, Simone, Marita, FC, Javi, Isich, ManuChow, Val, Mari, Di, Costich, Chumita, Sandru y Natta que estuvieron a lado mío, que fueron palabras de aliento, de risas, sin importar distancias, tiempo ni diferencias horarias. Gracias especiales a ti Mili, que estuviste en todas y terminaste convirtiéndote en familia. ¡Siempre agradecida por su apoyo constante queridos amigos!

Gracias a mi familia extendida, Jackicita, Cami, Diego, Glaglita, Anni, que siempre apoyaron nuestros pasos y acompañan de cerca nuestras aventuras. Siempre estoy agradecida por todo el cariño que me dan, por sus palabras de aliento, por los chistes, los buenos momentos y por cuidar a nuestra Ky. ¡Soy muy suertuda por tenerlos en mi vida!

Gracias querida familia por apoyar mi sueño de ser científica. Mamucha, Carlis, Lore, Oscar, Ruben, mi príncipe Fabricio, mis princesas Cael y Myrian Victoria, ustedes forman parte importante de esta aventura, sin su apoyo y comprensión, sería muy difícil llegar hasta aquí. Gracias por todos los años de apoyo en continuar la carrera lejos de la casa. Gracias a mis abuelos, papá Victor, mamá Yola, mamá Margarita, que son mi ejemplo de residencia y fortaleza. Especialmente gracias a ti mamucha por ser ejemplo de mujer, por creer en mis sueños y ayudarme a alcanzarlos, esta tesis va dedicada a ti. ¡Los llevo siempre conmigo!

No tengo palabras suficientes para agradecerte Sergito, mi compañero de vida, de risas y aventuras. Este tiempo atravesaste junto a mí, todas las etapas del doctorado, que fueron a la vez tiempo de introspección. Gracias por todo tu amor, por tu paciencia, por ser mi refugio y mi mayor motivación para alcanzar mis metas. Te dedico estas páginas de mucho trabajo, del que fuiste parte esencial. ¡Te amo esposich! ¡Vamos por más aventuras!

To my mom and my husband

In memory of my dad

Contents

Chapter 1

Introduction

"This is about humanity's future. This is about making sure that the world right now is liveable."
-Elizabeth Wathuti-

1.1 Why is it important to study aerosol properties?

The atmosphere consists of a thin gaseous layer around the Earth, which is constituted mostly of molecular nitrogen (78 %) and oxygen (21 %); the remaining 1 % comprises trace species like water vapor, carbon dioxide (CO_2), ozone (O_3) and methane (CH_4) along with other minor gas constituents, as well as particles. The solid or liquid particles suspended in the atmosphere are defined as aerosols. Although the abundances (by volume) of trace gases and aerosols are small, they are highly variable and play a key role in Earth's radiative budget, which describes the balance of incoming and outgoing energy in the atmosphere. The dramatic increase of aerosol and gas emissions from human activity, compared to the emissions in pre-industrial times, aroused inquietudes within the scientific community. For decades, scientific multidisciplinary efforts have aimed to better understand greenhouse gases (like CO_2 and CH_4) and aerosol effects on climate and human health, as well as to identify their sources. Effects on global climate are accounted through the Earth's radiative balance and effects on human health are mainly accounted for by air quality. It is well-known that the increasing abundance of greenhouse gases, which trap outgoing thermal radiation within the atmosphere, leads to warming effects on the atmosphere, enhancing changes in the global climate. Additionally, these gases, above certain concentration levels, become harmful to the health of living species, including humans (Ahrens, 2000; Salby, 1996; Wallace & Hobbs, 2006).

While gaseous component effects are known with high confidence, aerosol effects are still under question mark due to the high heterogeneity of their properties. Aerosols originate from both natural (e.g., sea salt, dust storms, volcanic eruptions) and anthropogenic (e.g., combustion, agricultural and industrial activities) sources. They can be as well primary or secondary products (gas-to-particle conversion). According to the location and environmental conditions of the emission source, aerosols can vary in size (diameters from 0.001 to 100 μm), morphology, mixing state, chemical composition. Moreover, they can be transformed by physicochemical interactions with other atmospheric components and with radiation. According to the size, photochemical reactivity and transport mechanisms, aerosols can reside in the atmosphere from a few hours to several days, and when they reach higher altitudes in the atmosphere they can stay even longer, up to a few months or a year. (Ahrens, 2000; Salby, 1996; Wallace & Hobbs, 2006)

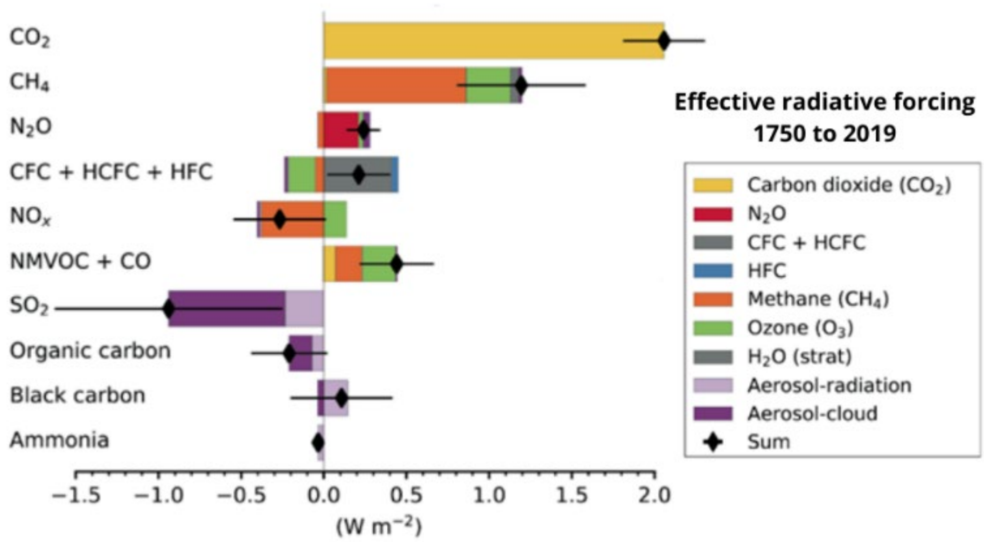

Figure 1.1: Global effective radiative forcings for main atmospheric components (from 1750 to 2019). Source: IPCC AR6, working group 1, chapter 6 (Szopa et al., 2021).

The incident solar radiation and the re-emitted Earth thermal radiation interact with aerosols in the atmosphere (aerosol-radiation interaction); scattering and absorption of radiation have direct effects on the radiative budget. Also aerosols act as cloud condensation and ice nuclei (aerosol-clouds interaction), which influence the cloud properties and therefore the radiative budget (indirect effects). The last Assessment Report (AR) from the IPCC (Inter-Governmental Panel on Climate Change) (AR6 working group 1, Szopa et al., 2021) showed that overall, aerosols have a negative effective radiative forcing impact, related to cooling effects on the atmosphere, contrary to the green-house gases (Fig. 1.1). Nevertheless, large uncertainties are still associated to both direct and indirect impacts, restricting a proper characterization of the climate system. In addition, it has been estimated that up to 3.6 billion people live in situations that are highly vulnerable to the impacts of climate change (IPCC AR6 working group 2, Birkmann et al., 2022).

The aerosol radiative effects depend on several parameters, including aerosol type, lifetime, aging state, mechanism of transport, and altitude at which they reside. For example, the Pinatubo eruption in June 1991 injected enormous amounts of sulfur compounds into the atmosphere, which caused a dropping of the global mean surface temperature for at least 5 years after the eruption (Hansen et al., 1992; Thompson et al., 2009). More recently, in June 2019, the Raikoke volcano eruption injected sulfate aerosols (conversion from sulfur dioxide SO_2) and ash higher into the atmosphere (9 to 18 km altitude) (De Leeuw et al., 2021; Osborne et al., 2022; G. Vaughan et al., 2021). It has been estimated that these aerosols circulated and covered the Northern Hemisphere for more than a year, inducing a negative radiative impact non-negligible at a global scale (Kloss et al., 2021). On the other hand, carbonaceous particles (black carbon) emitted from combustion processes (burnings of biomass and fossil fuel) are likely to absorb light and therefore have a positive radiative forcing (Bond & Bergstrom, 2006), related to a warming effect (Fig. 1.1).

The World Health Organization (WHO) identified air pollution as one of the highest risk factors for noncommunicable diseases, with 99% of the global population exposed to unhealthy levels of Particulate Matter (PM) and nitrogen dioxide. In particular PM2.5, aerosol particles with diameters equal to or smaller than 2.5 µm, are capable of penetrating deep into the lungs and entering the bloodstream, which can cause cardiovascular, cerebrovascular (stroke), and respiratory complications. In 2019, it was estimated that both indoor and outdoor air pollution caused 6.7 million deaths globally. Moreover, as climate is changing due to global warming, more frequent and extreme environmental events are observed. These events, such as storms, heat waves, floods, droughts and wildfires, increase the risk of deaths and spread of infectious diseases. Extreme events can also incite the emission of high aerosol loadings into the atmosphere, such as dense smoke plumes from wildfires or dust transport from enlarged eroded areas. The health-related information presented in this paragraph can be found on the annual statistics reports from WHO (WHO, 2019, 2021, 2023).

Moreover, we are already experiencing the effects of a changing climate. In 2022, several heat waves crossed Western Europe transporting large amounts of dust from the Saharan desert. In particular, in early spring several European cities were impacted by the deposition of dust at ground level, including snowy mountains, possibly impacting the climate locally (e.g., French Alps, Fig. 1.2a) (Skiles et al., 2018). In the summer of the same year, extreme heat waves contributed to the expansion of unprecedented wildfires across Europe, injecting high loads of biomass-burning particles and affecting the air quality of multiple cities (Vasilakopoulou et al., 2023). Likewise, during June 2023, Canadian wildfires emitted huge amounts of smoke that were transported and covered the New York city skies (Fig. 1.2b), impacting aviation and risking human health (McArdle et al., 2023). Both air quality and climate change not only influence human health but also affect the global economy, with the necessity to contain the negative effects on society, infrastructures, and our daily life activities (Saiz-Jimenez, 1993; Stefanis et al., 2009).

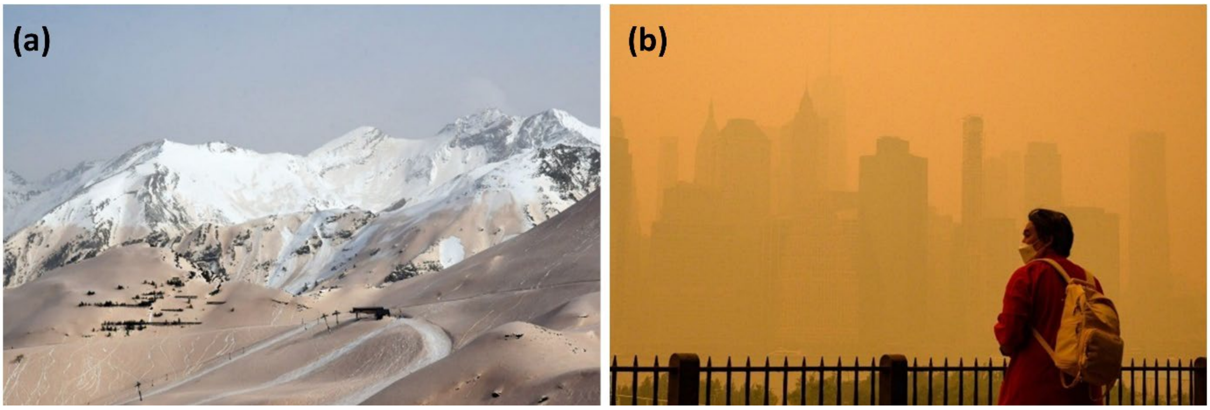

Figure 1.2: Recent extreme events of transported aerosols. (a) Saharan dust covering Piau-Engaly ski resort in southern France (Photography source: Bastien Arberet/Getty Images). (b) Smoke from Canadian wildfires turning New York sky orange (Photography source: Angela Weiss/ Getty Images).

Improving the knowledge of the spatiotemporal variabilities of aerosols and their local, regional and global effects, as well as reducing the uncertainties on aerosols properties is fundamental to quantify their radiative impacts (Boucher et al., 2013). Following the aerosols transport from the main sources and the evaluation of their complex distribution are therefore needed. As negative effects on human health and economy are also accounted to aerosols, the demand for continuous air quality control to develop early warning systems is increasing, as more frequent and extreme environmental events are detected (IPCC AR6 working group 1, Seneviratne et al., 2021).

1.2 How to assess aerosol's properties spatiotemporal variability?

Researchers employ observations and modeling to study aerosol properties variabilities, both of which are highly important and complementary for better understanding the climate system. In-situ observations, meaning that data is collected directly at the location of interest, and remote sensing, denoting to data collected at a distance from the location of interest, are used to characterize aerosol properties. From in-situ measurements, we can obtain precise information on aerosol optical, micro-physical and chemical properties. Nevertheless, the available instruments use a variety of approaches to measure, in particular, aerosol size, resulting in different sizes for the same particle (McMurry, 2000). Measurements are also restricted to a few meters of the lower atmosphere, close to ground level. In exceptional field campaigns in-situ measurements are also possible aboard aircrafts (Anderson et al., 2003; Pratt & Prather, 2010; Q. Zhang et al., 2009), tethered balloons, and more recently, aboard drones reaching aerosols at higher altitudes (Renard et al., 2016). However, due to the high cost of operation, these types of measurements are not frequently used.

Remote sensing techniques are based on radiation scattering and absorption by atmospheric components (aerosols, clouds, gases) comprises two branches; passive (natural radiation-atmosphere interactions) and active (emits its own radiation) remote sensing instruments. Both types of techniques are widely used aboard satellites and at ground-based platforms to monitor atmospheric aerosols. Satellite remote sensing offers unique advantages in assessing the spatial distribution of aerosols, reaching up to global coverage depending on its orbit. Passive remote sensing instruments aboard satellites, such as the two MODIS (Moderate Resolution Imaging Spectrometer; King et al., 1992) aboard AQUA and TERRA satellites, provide long-term aerosol observations with global coverage. As well, the CALIPSO satellite (Cloud-Aerosol Lidar and Infrared Pathfinder Satellite Observations; Winker et al., 2009) with CALIOP (Cloud-Aerosol LIdar with Orthogonal Polarization), a space-borne lidar (active remote sensing instrument), completed a successful mission from 2006 to 2023. CALIOP offered vertically resolved backscattered light signal at two wavelengths, in the visible and infrared (IR), and depolarization ratio observations, which allowed for assessing the atmospheric structure and classifying aerosols and clouds globally. Despite their global coverage, satellite remote sensing instruments are limited by their temporal resolution, meaning they cannot frequently revisit the same location, which is problematic for monitoring rapid changes in aerosol properties. Certain surfaces and atmospheric conditions, such as dense clouds, complex topographies, dense vegetation, or oceans, pose challenges for interpreting satellite data (Wei et al., 2019; J. Zhang et al., 2005). For the case of space-borne lidars, signal profiles are noisier while getting closer to the surface, due to light attenuation by the atmosphere, increasing the observations uncertainties close to ground. Therefore, ground based remote sensing instruments are important for data calibration and validation (CAL/VAL) (Bibi et al., 2015; Chu et al., 2002;

Mamouri et al., 2009; McGill et al., 2007). The development of new satellite missions continues to enhance the capabilities of remote sensing systems, addressing current limitations.

The photometer, a passive sensor providing multispectral information on the aerosols in the atmospheric column, and the lidar, an active remote sensor providing vertically resolved aerosol observations, are widely used for aerosol studies. Both ground-based photometers and lidars have proven to be convenient tools for assessing aerosol properties. To this end, the development of networks plays a key role. For example, the world-wide open-access photometer network AERONET (AErosol Robotic NETwork; Holben et al., 1998) provides insightful tools to monitor aerosols effects on a global scale (e.g., Boichu et al., 2023). In Europe, the research infrastructure ACTRIS-ERIC (Aerosol, Clouds and Trace gases Research InfraStructure, European Research Infrastructure Consortium) with its branch CARS (Center for Aerosol Remote Sensing, https://www.actris.eu/topical-centre/cars), offers support to ACTRIS National Facilities operating aerosol remote sensing instrumentation. The instruments included are deployed in networks for the automatic sun/sky/polarized/lunar photometer (AERONET-Europe), automatic low-power lidars (E-PROFILE, https://e-profile.eu/), and high-power aerosol lidars (EARLINET, European Aerosol Research LIdar Network; Pappalardo, 2010). CARS offers specialized services to users, aiming to enhance the appropriate characterization of aerosols properties and improve the communication of scientific advances. Studies conducted with multiple network sites have allowed for assessing the variability of aerosol properties at a regional level, such as during Saharan dust outbreaks (Ansmann et al., 2003; López-Cayuela et al., 2023; Papayannis et al., 2008) or the long-range transport of biomass burning aerosols (Adam et al., 2020; Nicolae et al., 2013). However, laboratories at fixed sites are restricted by their local conditions and position relative to aerosol sources. Furthermore, some regions with difficult access, such as oceans or mountains, remain unexplored. Additionally, the expansion of aerosol networks for the ground-based sites are mainly covering the land surface of the Northern Hemisphere.

All the mentioned techniques —in-situ, ground-based, and satellite remote sensing—have both advantages and limitations. One common limitation is the access to reliable information in complex topographies and remote areas (such as over oceans), where several natural aerosol sources are identified (volcanoes, forest fires, sea spray). Bridging the observational gaps from the different branches of research will significantly improve our knowledge about aerosols and their climate impacts. In the context of this thesis, the main concern is the observational gaps within the ground based remote sensing sites.

1.3 So, how can we bridge the observational gaps on ground-based aerosol monitoring networks?

The deployment of mobile laboratories (aboard ship cruises, airplanes or cars) provides a solution to fill the observational gaps within ground-based networks (Bohlmann et al., 2018; Müller et al., 2014; Popovici et al., 2018; Smirnov et al., 2009; Tesche et al., 2019). In recent years, the multispectral sun/sky/lunar CIMEL CE318-T photometer (Barreto et al., 2016), widely used around the world and designed by the French company CIMEL Electronique, has been fully adapted for automatic observations during movement onboard ships (Yin et al., 2019). Likewise, the PLASMA (Photomètre Léger Aéroporté pour la Surveillance des Masses d´Air; Karol et al., 2013) photometer was developed exclusively to perform aerosol observations during movement, and has been deployed aboard aircraft and vehicles during field campaigns (Hu et al., 2019; Mascaut et al., 2022; Popovici, 2018; Popovici et al., 2018, 2022). The ship-borne CE318-T and PLASMA photometers have been adapted and developed respectively within AGORA-Lab, a common laboratory between LOA (Laboratoire d'Optique Atmospherique, Lille University) and CIMEL company (https://www.agora-lab.fr/).

Lidar systems are mostly big, complex, require significant space, regular maintenance and controlled operational conditions. Thus, upgrades for mobile observations often involve instrumental modifications and/or creation of adapted laboratory platforms. Studies conducted with lidars aboard mobile vectors showed the possibility to support satellite-based observations (Burton et al., 2013; Warneke et al., 2023), assess air quality in urban-rural transitions and complex topographies (Chazette & Totems, 2023; Dieudonné et al., 2015; Pal et al., 2012; Popovici, 2018; Popovici et al., 2018, 2022; Royer et al., 2011; Shang et al., 2018). For instance, a description of a compact and light mobile system, integrating a compact lidar and a sun photometer was first presented by Popovici et al. (2018). This unique system, deployed by LOA, included the CIMEL CE370 single-wavelength elastic lidar and the PLASMA sun-photometer. During several field campaigns the integrated system performed on-road mobile measurements (Popovici et al., 2018, 2022), demonstrating its versatility for aerosol characterization. Accordingly, the newest model of the CIMEL lightweight lidar, the CE376 dual-wavelength lidar, is proposed to enhance aerosol property studies.

The CE376 lidar measures backscattered light signals at 532 nm and 808 nm and depolarization at 532 nm. Algorithmic and instrumental assessments took place at the ATOLL (ATmospheric Observatory of liLLe) platform operated by LOA in Lille France. METIS, an early version of the CE376 lidar, has been continuously performing observations since 2019. In addition, METIS is co-located with a CE318-T photometer and with a high-power multi-wavelength Raman lidar, LILAS, part of ACTRIS-EARLINET, which are also considered for comparison and validation. By combining observations from the lidar (vertically resolved) and the photometer (column integrated), more reliable assessments of aerosol properties are possible.

The BASIC software developed at LOA, provides Near Real Time (NRT) aerosol properties retrieved from lidar measurements at one wavelength and combines them with photometer data (Mortier, 2013a). Also, the algorithm offers aerosol layer detection and, by identifying the aerosol types, can derive the mass concentration vertical variability, directly related to air quality. Initially, the BASIC algorithm did not support multi-wavelength measurements or observations performed during movement. Nevertheless, multiple studies on simultaneous 2-wavelength lidar observations have presented inversion schemes to improve the derived aerosol properties (Ackermann, 1997, 1999; Kunz, 1999; Lu et al., 2011; Potter, 1987; Vaughan et al., 2004).

This work evaluates the appropiate inversion scheme to retrieve aerosol properties from the CE376 lidar measurements when it is co-located with a photometer, considering observations at fixed location and while in-movement. In accordance with the performance limits of each wavelength detection channel, a modified Klett inversion scheme is proposed for the simultaneous 2 wavelength observations. Furthermore, considering the depolarization observations, insights on the microphysical aerosol properties (size and shape) are available. The aerosols retrievals are evaluated through comparison with the LILAS Raman lidar at ATOLL, establishing the reliability of the results. Case studies are also presented considering the influence of mineral dust, smoke-dust, and volcanic aerosols. Additionally, observations of the CE376 lidar co-located with CE318-T photometer installed at Izaña Observatory (IZO), were also considered for studies on mineral dust and volcanic aerosols. Furthermore, considerations to enhance NRT aerosol properties for air quality assessments or early warning systems, are taken into account. This study not only outlines the findings but discusses the limitations and future implications of the approach.

A first dataset of co-located CE376 lidar and photometer mobile observations was obtained during the FIREX-AQ (Fire Influence on Regional to Global Environments and Air Quality) field campaign, organized over the Northwestern US in the summer 2019 (Warneke et al., 2023). This campaign, led by NASA and NOAA, focused on investigating the chemistry and transport of smoke from wildfires and agricultural burning, in addition to deploying multiple in-situ instruments on fixed platforms around the region and aboard aircraft. Remote sensing instruments were installed in both stationary and mobile DRAGON payloads (Distributed Regional Aerosol Gridded Observations Networks; Holben et al., 2018). Thus, two mobile platforms (2 SUVs) called DMU-1 and DMU-2 (Dragon Mobile Unit) were equipped with lidars and photometers. The dual wavelength CE376 lidar and ship-borne CE318-T photometer were installed aboard DMU-1, and the single-wavelength CE370 lidar and PLASMA photometer onboard DMU-2. Both DMUs performed on-road mobile observations around major fire sources and were able to follow smoke plumes. Height-resolved optical properties of fresh smoke aerosols close to active fire sources were retrieved, despite extreme environmental conditions that limited the performance of the instruments. Consequently, this work presents aerosol property mappings of selected case studies during the Williams Flats fire in Washington State, considering both DMU-1 and DMU-2 for the analysis. Notably, this thesis provides 3D mapping and temporal evolution of aerosol properties, showcasing the relevance of coupling the CE376 lidar and CE318-T photometer even under extreme environmental conditions.

The AMAGAS-AMARYLLIS oceanographic mission, entitled “From Amazon sediments to natural climate variability and slope instability processes,” was deployed between May and July 2023 aboard the Marion Dufresne research vessel. As part of this mission, the Marion Dufresne left La Reunion Island in mid-April 2023, passed around South Africa, crossed the Atlantic Ocean, and reached Barbados by mid-May 2023. During this transit, the campaign TRANSAMA (Transit to AMAGAS-AMARYLLIS, valorization project) was deployed to observe and analyze atmospheric aerosols in a maritime environment using remote sensing measurements. Therefore, the CE370 single-wavelength lidar, a ship-borne CE318-T photometer, and a PLASMA photometer were installed aboard the Marion Dufresne research vessel. This campaign allowed continuous assessments of the instruments' performance while in movement. In particular, the adequate operational conditions for the lidar were evaluated, envisioning the future installation of the CE376 dual-wavelength lidar aboard a ship.

This thesis is developed within the framework of the CIFRE (Conventions Industrielles de Formation par la Recherche) convention, which promotes the collaborative advancement of industry and research in France. Thus, this work aims to further advance both the algorithmic and instrumental developments of the CE376 lidar.

1.4 Objectives

The main objective of this work is to demonstrate the capabilities of a compact dual-wavelength depolarization lidar (CE376 lidar) in assessing the spatio-temporal variabilities of aerosol properties, particularly when it is aboard moving vectors and co-located with a photometer. Both the capabilities and limitations of the CE376 lidar are investigated in detail, illustrating how this study contributes to filling observational gaps within aerosols monitoring networks. To achieve the main objective, the following goals were proposed within the thesis project:

***Consolidation and validation of instrumentation*:** This includes the qualification and validation of the CE376 lidar's two-wavelength and depolarization measurements. For the mobile version, this involve consolidating the instruments from the technical standpoint (resistance to vibrations, operating limits in mobility).

Development of prototype treatment system: This involves the adaptation and development of algorithms to build a prototype software for data processing of simultaneous two-wavelength lidar measurements and for aerosol monitoring in near real time (NRT).

Validation of global performance and aerosol parameter measurements: This entails testing the performance under different conditions of use, environments, and aerosol situations (types, layers, mixtures) to demonstrate scientific interest and operational feasibility. Comparisons with reference instruments (LILAS Raman lidar) will characterize the performance of the solutions. Measurements during exceptional events will be evaluated to define specific applications for aerosol monitoring.

Scientific and Technical valorization: The results will serve as references for promoting new measurement solutions to the scientific community, spatial observation of the Earth and their promotion to air quality field.

1.5 Thesis layout

This thesis is divided into seven chapters:

(1) The first chapter briefly introduces the background of aerosol research, the motivations and objectives of the thesis.

(2) The second chapter provides a short overview of aerosols features, including descriptions of their microphysical and optical properties and their transport in the atmosphere.

(3) The third chapter describes the remote sensing instruments used in this work, focusing on the CE376 lidar data preprocessing (corrections, calibrations) and performance (temperature effects, depolarization measurements).

(4) The fourth chapter presents the algorithmic assessments to integrate the CE376 lidar and photometer for aerosol monitoring in NRT, considering measurements at fixed location and while in-movement. A comprehensive evaluation of aerosol retrieval methods (combining lidar and photometer) available in the literature is presented.

(5) The fifth chapter presents results of selected case studies, from co-located lidar and photometer observations at two sites, ATOLL (Lille, France) and IZO (Tenerife, Spain). Events of dust outbreaks, biomass burning, and volcanic eruption were thoroughly evaluated, showcasing the capabilities and limitations of the lidar system to characterize aerosols. The aerosol properties presented at each study case are outcomes of the prototype software, described in the fourth chapter.

(6) The sixth chapter is dedicated to aerosol observations while lidar and photometer are in movement. Two mobile campaigns, FIREX-AQ (summer 2019) and TRANSAMA (spring 2023), are presented. Results from the first campaign study smoke aerosols near fire sources, displaying the enhanced capabilities of the CE376 lidar for mobile aerosol monitoring even under challenging environmental conditions (high temperatures, difficult roads, thick aerosol layers). Results from the second campaign exhibit the operational challenges to overcome in open sea conditions (salt deposition on windows), with a view toward the ship-borne installation of the CE376 lidar.

(7) Finally, the seventh chapter presents the conclusions and perspectives of this work.

A research article published in an international peer-reviewed journal is presented in Appendix A.

Chapter 2

Atmospheric Aerosols

"The balance of nature is not a status quo; it is fluid, ever shifting, in a constant state of adjustment. Man, too, is part of this balance."

-Rachel Carson, Silent Spring-

Fundamental concepts needed for the development of this work are introduced throughout this chapter. The microphysical properties of aerosols, such as size and morphology, are presented, along with their optical properties derived from their interaction with radiation. Moreover, the spatial spreading of aerosols from their source transported to regional and global scales is described.

2.1 Microphysical properties

The particle size is defined by the equivalent diameter of the aerosol, considering it as a sphere. The particle size covers several orders of magnitude from 0.001 to 100 μm, and they are divided into 3 main groups: coarse (>2.5 μm), fine (<2.5 μm) and ultrafine (0.001- 0.1 μm) modes (Fig. 2.1). Ultrafine particles are also divided into nucleation and Aitken modes and represent the major contributions in number concentrations. In terms of air quality, which considers an aerodynamic equivalent diameter (related to particle behavior in air flows), coarse particles are defined as PM10 (for particles sizes below or equal to 10 μm) and fine particles as PM2.5 (for particles sizes below or equal to 2.5 μm).

Coarse particles are generally emitted from natural processes and they often have a shorter lifetime in the atmosphere, e.g., mineral dust, volcanic ash, sea salt and pollen. These large particles can impact human health by affecting the upper tract of the respiratory system. Fine particles, on the other hand, are generally emitted as primary products by human activities involving combustion processes, e.g., black carbon emitted from fossil fuel combustion in transport and industry. Ultrafine particles can be emitted as secondary products, by the transformation of natural or anthropogenic gas precursors into particles; e.g., sulfate aerosols from sulfur dioxide conversion emitted during volcano eruptions. Moreover, ultrafine particles are harmful to human health, as they can potentially reach the bloodstream, allowing them to be distributed to the rest of the body. During their stay in the atmosphere, aerosol particles undergo aging processes that modify their physical and chemical properties (Wallace & Hobbs, 2006; Seinfeld & Pandis, 2016).

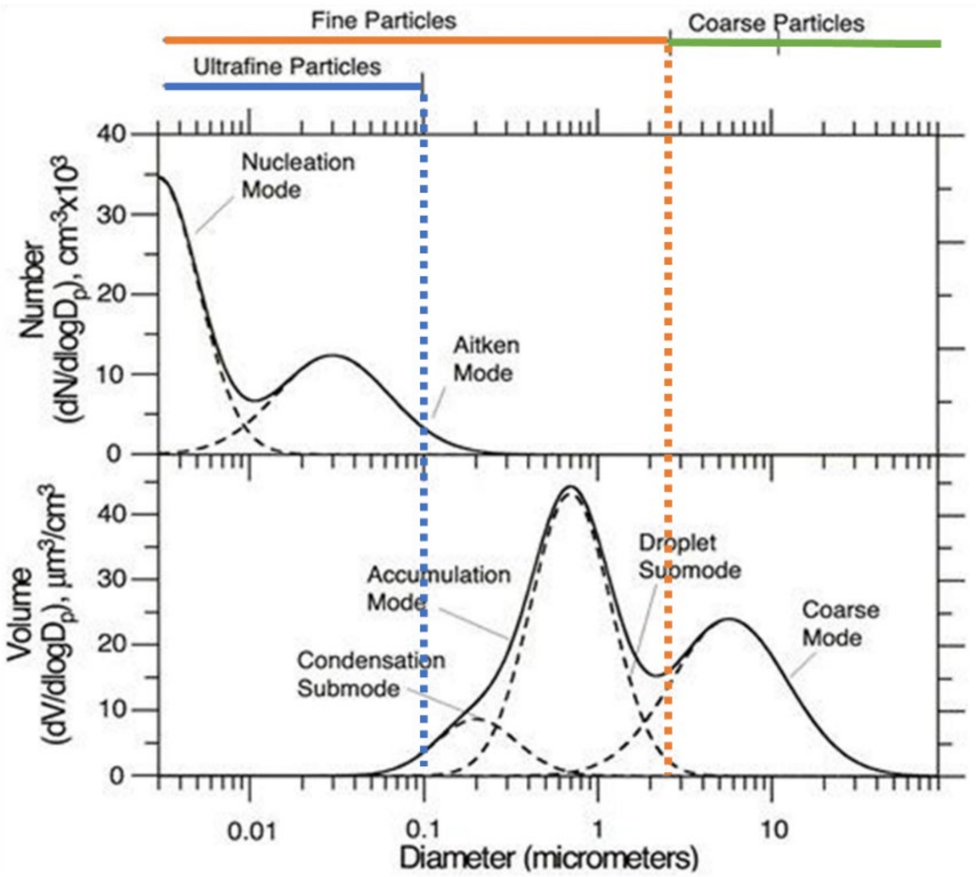

Figure 2.1: Graphical representation of the different particle size modes. The same hypothetical log-normal aerosol distribution plotted, from top to bottom, as number vs. diameter distribution, and as volume vs. diameter distribution. (Source: Seinfeld & Pandis, 2016)

The growth of particles in nucleation mode happens in a matter of minutes up to hours and they are mainly observed as a distinct mode at their source. Then the Aitken particles act as nuclei for the condensation of gases, causing them to grow towards the accumulation mode. The Aitken and accumulation mode particles are usually referred to as fine particles, and they are the most abundant (by volume). For coarse mode particles, while concentrations can be low, the particle mass concentrations are considerable.

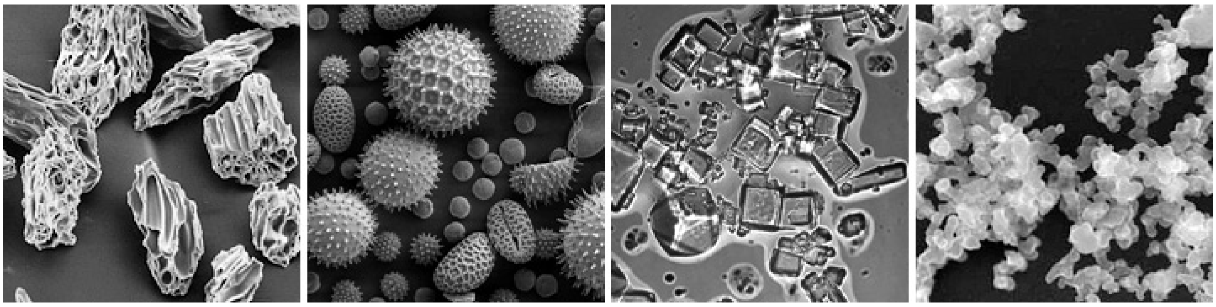

Figure 2.2: Scanning electron microscope images (not at the same scale) show the wide variety of aerosol shapes. From left to right: volcanic ash, pollen, dry sea salt, and soot. [Micrographs courtesy USGS, UMBC (Chere Petty), and Arizona State University (Peter Buseck).

Aerosols are not only variable in size; they also present variability in shape. Figure 2.2 presents images taken with a transmission electron microscope that show examples of different shapes that aerosols can have. Thus, they can be far from the spherical shapes that we assume. According to the processes involved in the aerosol emission and aging, they can also present a gaseous envelope (coating), taking an apparent spherical shape but with a complex mixing state. Aerosols can then mix externally and internally with other aerosols, gases or biological compounds, growing in size and changing shape while they age.

2.2 Optical properties

Considering particles (molecules or aerosols) as targets in a homogeneous medium (atmosphere), an incident monochromatic electromagnetic wave (referred as energy, light or radiation indistinctly) is either scattered and/or transferred to the particle and transformed; the particle absorbs a part of the energy, translates it into thermal radiation, vibration, rotation and also re-emits electromagnetic waves in all directions. The outgoing radiation from the interaction can be at the same wavelength (elastic scattering) or at a different wavelength (re-emitted light, i.e., inelastic scattering) with respect to the incident radiation. The angle between the direction of propagation of the incident radiation and the scattered one is named scattering angle Θ and the scattering phase function defines the intensity of light scattered in all the scattering angles (Petty, 2006).

2.2.1 Scattering

The particle size is in fact the most important defining characteristic in scattering processes. In general, particles that are far smaller than the wavelength will scatter very weakly, though they may still absorb radiation, like green-house gas molecules. This type of scattering can either be negligible or described by Rayleigh theory. A typical example of Rayleigh scattering is given by the blue color of the sky, which is a shorter wavelength (blue) and therefore more efficiently scattered by air molecules. For very large particles with respect to the wavelength of incident radiation, we can approximate the interaction by means of a homogeneous medium using geometric optics (reflection, diffraction, refraction), e.g., cloud droplets. Nevertheless, the majority of aerosols size in the atmosphere are between both considerations, and therefore they need a more complex mathematical interpretation to define their scattering phase functions.

Mie scattering theory was developed for particles with size comparable to the incident wavelength, and assuming that the particle is a homogeneous sphere. To this end it is useful to define a ratio of the particle size to the wavelength of incident monochromatic light, which is also called size parameter (Eq. 2.1).

$$x = \frac{2\pi r}{\lambda} \tag{2.1}$$

By the given value of x, it is possible to determine whether scattering by the particle is likely to be significant and, if so, which scattering regime (Rayleigh, Mie, or geometric optics) is most applicable (Fig. 2.3). Under the context of this study, the CE376 lidar uses light at 532 nm and 808 nm wavelengths, in the visible and NIR (near infrared) respectively. Therefore, air molecules are most likely to scatter the 532 nm light than the 808 nm. Similarly, bigger particles (e.g., radius ~100 μm) are most likely to be in the Mie scattering regime for 808 nm and in the geometric optics regime for 532 nm.

Mie scattering theory is convenient and useful to characterize the intensity of radiation scattered by atmospheric aerosols in a sample of air. Mie theory considers that particles in a volume of air are far enough from each other, so interactions between them are avoided, and therefore the total scattered radiation is approximate to the sum of scattering by each particle. This scenario is observed in the atmosphere even in polluted conditions, with exceptions under clouds presence or at heavy emission sources. To limit the possible contributions of multiple scattering on lidar, narrow field of view are chosen for the detection of radiation. Besides, Mie theory assumes particles to be spherical which is far from reality for several aerosol types. Therefore, more elaborated mathematical expressions are derived to approximate reality (Mishchenko & Travis, 1994; Yang & Liou, 1996; Dubovik et al., 2006), but this still poses a challenge due to the complexity on aerosol shape.

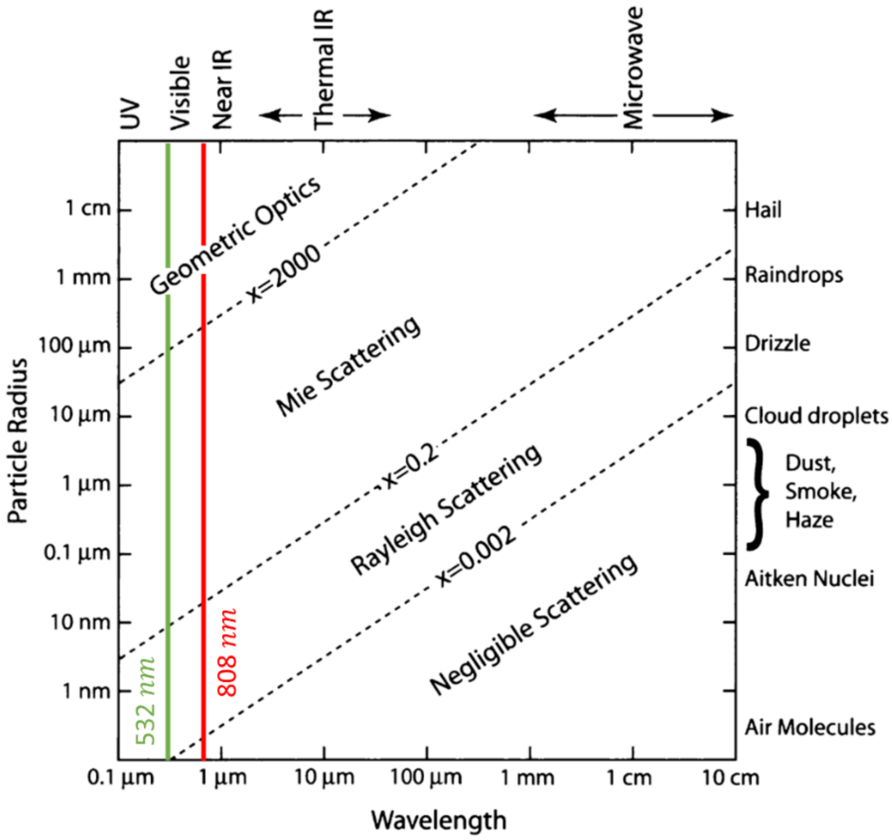

Figure 2.3: Relationship between particle size, radiation wavelength and scattering behavior for atmospheric particles. Diagonal dashed lines represent rough boundaries between scattering regimes. The CE376 lidar wavelengths of detection are indicated with green (532 nm) and red (808 nm) lines. Source: adapted from *(Petty, 2006)*.

Polarization

Polarization of light describes the orientation of the electric field vector within the electromagnetic wave (light), indicating the direction in which the wave vibrates. Aerosol scattering processes can significantly influence the polarization state of light, which varies according to the scattering angle. In Rayleigh scattering regime, the scattered light tends to become polarized perpendicular to the direction of the incident light and presents homogeneous patterns with respect to the incident plane. On the other hand, in the Mie scattering regime the polarization of scattered radiation becomes more complex; the strength and preferred angle of polarization depends on the aerosol size, shape and refractive index. In particular aerosol shape will have an important impact on the polarization. While spherical particles (e.g., small droplets) exhibit polarization effects similar to the Rayleigh regime, non-spherical particles (e.g., dust, pollen) can induce complex polarization changes due to their irregular shape and orientation with respect to the incident light (Kokhanenko et al., 2020; Daskalopoulou et al., 2023).

2.2.2 Absorption

The solar radiation depends on temperature and is defined by the black body theory. While solar irradiance at the Top of Atmosphere (TOA) remains quite constant, the measured irradiance at the surface is controlled by the atmospheric transmission. Trace gas compounds in the atmosphere are most likely to absorb radiation at different spectral bands, and scatter (Rayleigh scattering) radiation at the shorter wavelengths (visible band). In Fig. 2.4, both the solar irradiance electromagnetic spectrum at TOA and at the surface are presented. The spectral bands of absorption and scattering (shadowed areas) by trace gases are indicated for an atmosphere without aerosols and clouds. In the context of this thesis, once again, the detection wavelengths of the CE376 lidar are indicated, with dotted green (532 nm) and red (808 nm) lines. It is important to note that the wavelengths selected to study aerosols are carefully selected outside the gas absorption bands. Moreover, the Rayleigh scattering impact mostly the transmission in the atmosphere at 532 nm than at 808 nm.

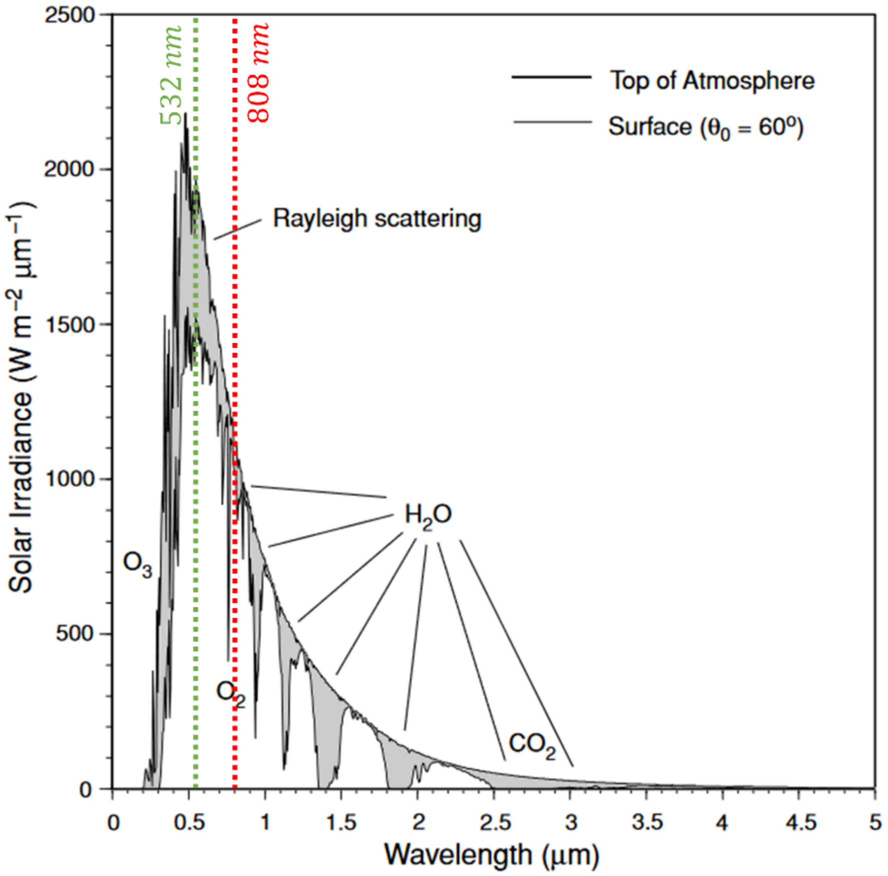

Figure 2.4: Solar irradiance curve for a spectral interval at the top of the atmosphere and at the surface (solar zenith angle of 60◦) in an atmosphere without aerosols or clouds. Absorption and scattering regions are indicated. Source: adapted from (Liou, 2002)

Both scattering and absorption are wavelength dependent, and can be related through the complex refractive index (Eq. 2.2), where the imaginary part (k) is correlated to the aerosol absorption capacity and the real part (n) is related to the phase speed of propagation of a wave within the aerosol medium.

$$m(\lambda) = n(\lambda) - i \cdot k(\lambda) \tag{2.2}$$

2.2.3 Extinction

The scattering cross-section is the effective area that characterizes the probability of scattering. The aerosol efficiency to scatter radiation $Q_{sca}(x, m, \lambda)$, is therefore influenced by its size parameter and refractive index and it is defined as the ratio of the scattering cross-section to the geometrical cross-section of the particle. Then the scattering coefficient of a volume of air is defined as individual aerosol efficiencies integrated over all particle sizes r (Eq. 2.3), where, aerosols efficiency to scatter radiation is $Q_{sca}(x, m, \lambda)$, the aerosol geometrical cross section is πr^2 and the number concentration of aerosols by volume of air is defined by $n(r)$.

$$\alpha_{sca}(\lambda) = \int_0^\infty \pi r^2\, Q_{sca}(x, m, \lambda) n(r) dr \tag{2.3}$$

In the same way, as for scattering, the absorption coefficient is defined by Eq. (2.4). Moreover, both scattering and absorption contributes to the extinction (α) of radiation passing through a volume of air (Eq. 2.5) and following the energy conservation law.

$$\alpha_{abs}(\lambda) = \int_0^\infty \pi r^2\, Q_{abs}(x, m, \lambda) n(r) dr \tag{2.4}$$

$$\alpha_{ext}(\lambda) = \alpha_{sca}(\lambda) + \alpha_{abs}(\lambda) \tag{2.5}$$

The Single Scattering Albedo (SSA) of aerosol, defined in Eq. (2.6), is a parameter that provides information on rather the aerosol is most likely to scatter than absorbing radiation or the other way around.

$$\omega_0(\lambda) = SSA(\lambda) = \frac{\alpha_{sca}(\lambda)}{\alpha_{sca}(\lambda) + \alpha_{abs}(\lambda)} = \frac{\alpha_{sca}(\lambda)}{\alpha_{ext}(\lambda)} \tag{2.6}$$

The absorption efficiency of aerosols depends on their microphysical and chemical properties. Nevertheless, the real effect of aerosols on absorption depends on the amount and interaction with the surrounding gases (Petty, 2006). This causes both primary and secondary aerosols to modify the radiative budget of the atmosphere (e.g., anthropogenic pollution). Moreover, since scattering is generally considered more significant than absorption, this effect is more relevant in estimating the amount of mass loading of aerosols.

The solar radiation passing through the atmosphere is attenuated by both particle scattering and absorption (extinction). The attenuation is then described by the Beer-Lambert law (Eq. 2.7), where I_0 is the radiance at the top of the atmosphere and I at surface, θ_s is the solar zenithal angle and the attenuation is given by the total optical depth $\tau(\lambda)$, which is the integration of all the contributions of extinction at all altitudes (Eq. 2.8). It is important to mention that the term $\frac{1}{cos(\theta_s)}$ in Eq. (2.7) is valid for a plane perpendicular to the solar beam, thus the expression will change for lower solar zenithal angles.

$$I(\lambda) = I_0(\lambda) \exp\left(-\frac{1}{cos(\theta_s)}\tau(\lambda)\right) \tag{2.7}$$

$$\tau(\lambda) = \int_0^{TOA} \alpha_{ext}\, dz \tag{2.8}$$

2.3 Aerosol sources and transport

Before discussing the sources of aerosols and their transport, it is worth mentioning the structure of the atmosphere, which plays an important role in the dispersion of aerosols. The density and pressure of air, following the gas law, decrease exponentially with altitude due to Earth's gravity. This vertical variation in both pressure and density is significant and dominates horizontal or temporal variations. Therefore, defining a Standard Atmosphere, which represents the average atmospheric structure as a function of altitude for a certain latitude, becomes useful. Figure 2.5 shows the pressure and density values for the American Standard Atmosphere (US-Standard Atmosphere), representative of mid-latitudes (Ahrens, 2000).

The variation of air temperature with altitude follows a more complex behavior than pressure and density variation within the atmosphere (Fig. 2.5), because it depends on the photochemical interaction of atmospheric molecular components with solar radiation. Based on the temperature profile, the atmosphere is divided into 4 main layers: troposphere, stratosphere, mesosphere and thermosphere. The boundaries between these layers, marked by an inversion in temperature trends, are called the tropopause, stratopause and mesopause.

The troposphere is the lowest layer of the atmosphere, where the majority of the air mass is concentrated, and where life and climate develop. The temperature in this layer decreases with altitude following the reduction in air pressure, and extends up to 12 km in mid-latitudes and up to 18 km in the tropics. The stratosphere, on the other hand, experiences an increase in temperature within the layer due to the presence of ozone (O_3) which absorbs solar radiation in the ultraviolet (UV) band and releases heat.

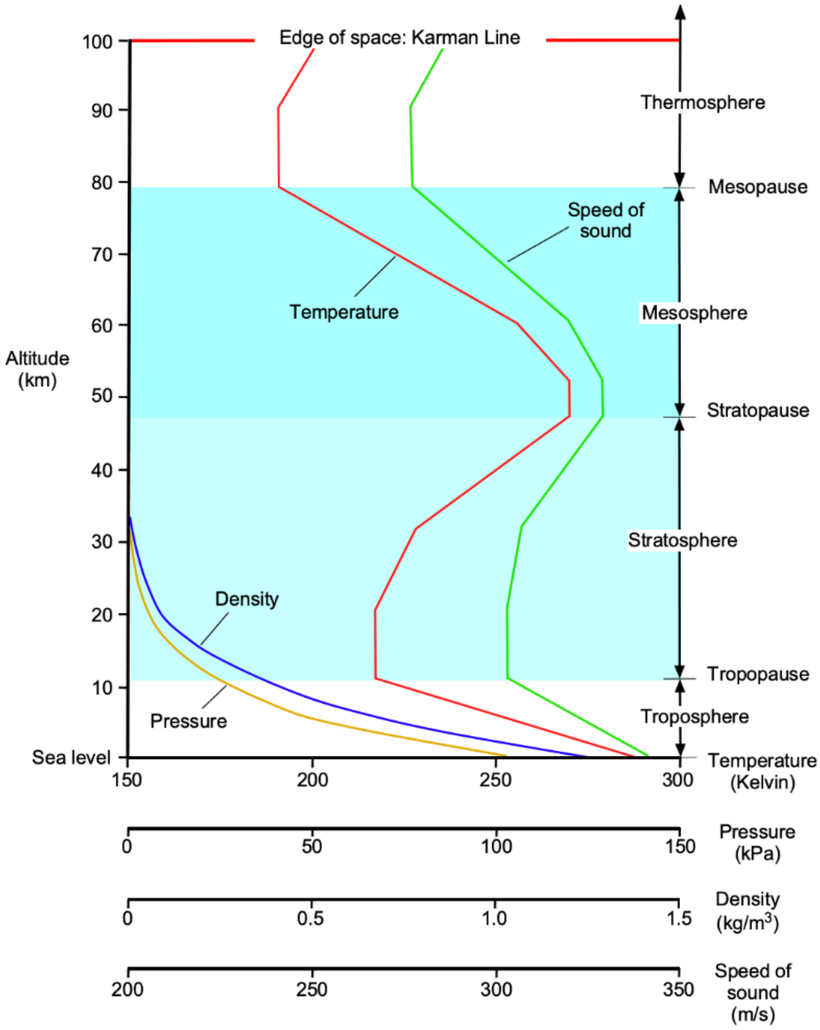

Figure 2.5: Atmospheric vertical structure based on its variations in pressure, temperature, and density. Source: https://eaglepubs.erau.edu/.

At the base of the troposphere, closer to ground, a sublayer known as the Atmospheric Boundary Layer (ABL) develops. The thermal structure in the ABL changes significantly throughout the day due to surface heating and cooling, seasonal changes, and humidity exchanges with the surface. The top of the ABL is also marked by a temperature inversion, which delimits the available volume of air where pollutants are emitted (Stull, 1988). Moreover, the ABL top marks the altitude where clouds are most likely to form. The region of the troposphere above the ABL is known as the free troposphere (FT) due to the usual absence of pollutants.

The ABL is the most important region of the troposphere for studies of air quality and particle transport models. While the air temperature increases during the day by convection of air parcels, the ABL extension increases in altitude, and during nighttime decreases due to the surface cooling. The ABL top altitude is highly variable, ranging from 100 m at night and to up to 2 km on a daily basis. For example, in winter in mid to high-latitudes with low temperatures during the entire day, the ABL remains shallow and stratified, reducing the volume of air available for pollutants, and thus endorsing bad air quality peaks due to heating systems (Fig. 2.6a). In hot and arid regions like deserts, the ABL top can reach even higher than 4 km, enhancing the vertical extension of dust storms (Fig. 2.6.b).

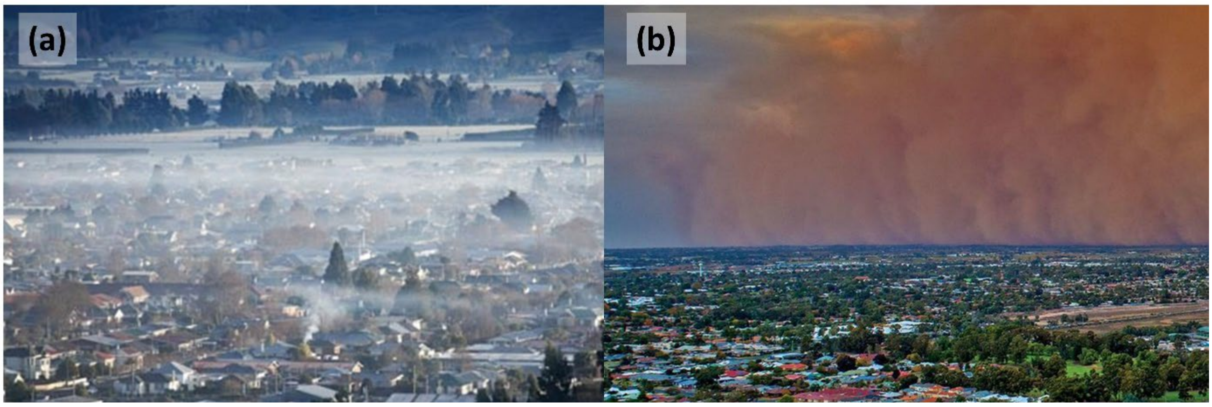

Figure 2.6: ABL influence on aerosol transport. (a) winter air pollution on New Zeland (©davidwallphoto.com). (b)Dust storm in Victoria, Australia (© ESCAP/APDIM/Robert Klarich)

Moreover, the ABL dynamics depend not only on local conditions, but can also be influenced by synoptic circulations. Therefore, the ABL is important for the transport of aerosols towards higher altitudes, whereas winds are responsible for their long-range transport. For physical processes involving convective air parcels, those with enough energy can break through the ABL top, reaching the FT or higher, where winds will transport the aerosols to regional or even global scales.

For example, volcanic eruptions can inject high amounts of sulfur compounds into the upper troposphere and lower stratosphere (Boichu et al., 2023; Kloss et al., 2021). The formation of pyro-cumulus clouds during intense wildfires can transport (updraft) smoke aerosols to the upper troposphere and lower stratosphere (Ansmann, Ohneiser, Mamouri, et al., 2021; Khaykin et al., 2020). Moreover, the permanence of aerosols in the atmosphere depends on their size and lifetime, which are defined by their photo-chemical reactivity and removal mechanisms.

Around the world, major aerosol sources, both anthropogenic and natural, are identified. Figure 2.7 illustrates these sources and the aerosol transport from local to regional and up to global scales.

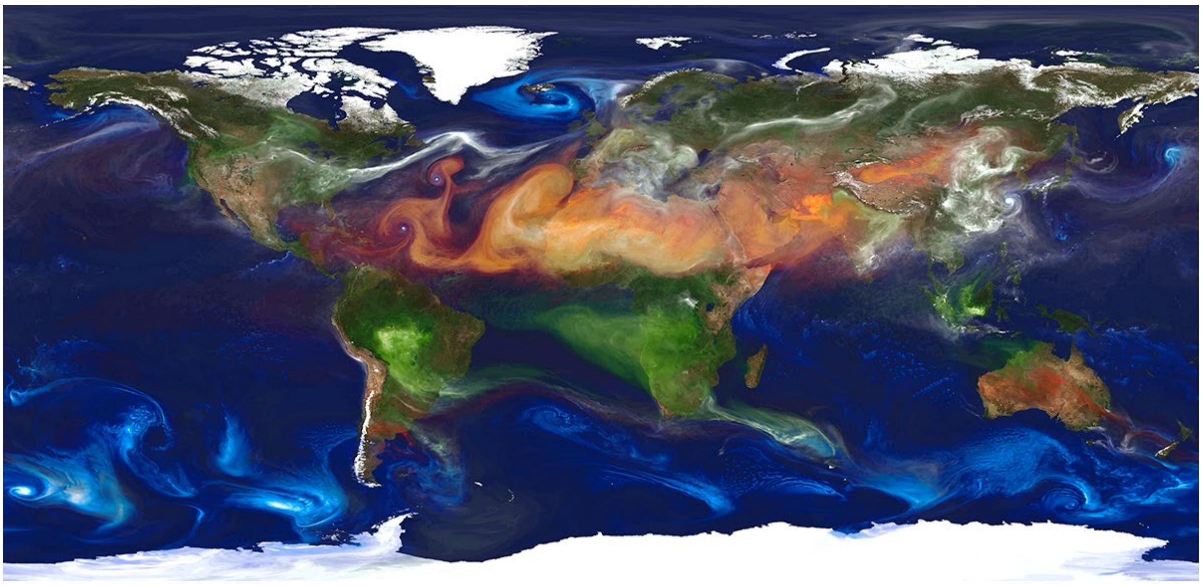

Figure 2.7: Modeling perspective on global aerosol content represented by different colors. Red indicates dust, blue indicates sea salt, smoke aerosols are in green and sulfate aerosols in white. Credits: William Putman and Arlindo da Silva, NASA/Goddard.

A brief description on the aerosols shown in Fig. 2.7 is presented below:

- Mineral dust (red color on Fig. 2.7) accounts for two-thirds of the global aerosol mass (Adebiyi et al., 2023). The desert belt, including the Sahara in North Africa and the Arabian deserts (tropical latitudes, hot deserts), and Gobi Desert covering Northwestern China (mid-latitude desert), emit high amounts of mineral dust that can be transported at regional levels (Mona et al., 2006; Papayannis et al., 2008; Tesche et al., 2009). Notably, dust from the Sahara travels even further, crossing the Atlantic Ocean and reaching the Amazonian rainforest (Ansmann et al., 2009) and North America (Middleton & Goudie, 2001). Mineral dust affects several aspects of climate through their interactions with radiation, cloud formation, and hydrology. Dust is extremely aspherical and either scatters or absorbs radiation, showing spectral dependency (Adebiyi et al., 2023). Dust can be found in the fine mode but is mostly reported as coarse aerosol (up to super-coarse and giant modes), even far from source.
- Sea salt aerosols (blue color on Fig. 2.7) are among the most abundant aerosol species over the oceans. They are mainly generated by air bubbles bursting at the ocean surface due to wind stress. Sea salt is mobilized by winds over the ocean surface, limited by a shallow ABL. Sea salt (or marine) aerosols are typically large, spherical particles with low light

absorption efficiency, and they act as cloud condensation nuclei (Bohlmann et al., 2018; Burton et al., 2013; Jaeglé et al., 2011; Pierce & Adams, 2006).

- Smoke aerosols (green color on Fig. 2.7) are emitted in high amounts from seasonal agricultural fires and wildfires, and are primarily carbon-based. Forest and savanna fires (e.g., Amazon, African Savanna) are major sources of black carbon, known for its high light absorption efficiency. Fresh smoke aerosols are usually fine and spherical (due to coating) and impact local to regional levels. Smoke can be transported long distances when reaching the upper troposphere or lower stratosphere (e.g., by pyro-cumulus cloud formation) (Ansmann, Ohneiser, Mamouri, et al., 2021; Q. Hu et al., 2019; Khaykin et al., 2020; Kumar et al., 2022; Warneke et al., 2023).
- Sulfate aerosols (white on Fig. 2.7) are mostly secondary products from both anthropogenic (fossil fuel combustion, i.e., urban/industrial emissions) and natural sources (marine and volcanic). Sulfate aerosols are fine and spherical with high light scattering efficiency. However, they enhance absorption when deposited as a coating on black carbon (Boucher et al., 2013). At lower altitudes, they affect air quality locally and regionally. Furthermore, sulfate aerosols reaching the upper troposphere and lower stratosphere due to strong volcanic eruptions can significantly affect the global climate (Boichu et al., 2023; Córdoba-Jabonero et al., 2023; De Leeuw et al., 2021; Hansen et al., 1992; Kloss et al., 2021; Navas-Guzmán et al., 2013).

Readers can explore more detailed information on the concepts developed in this chapter through dedicated books (Stull, 1988; Ahrens, 2000; Liou, 2002; Petty, 2006; Wallace & Hobbs, 2006; Lenoble, Remer & Tanre, 2013; Seinfeld & Pandis, 2016).

The following chapter will introduce the remote sensing instrumentation used in this work, focusing on the dual wavelength and polarization lidar (CE376).

Chapter 3

Remote sensing instrumentation and methodology

"Science and everyday life cannot and should not be separated"
-Rosalind Franklin-

Remote sensing techniques allow for the acquisition of information from a distance. Atmospheric remote sensing facilitates the characterization of atmospheric components (molecules, clouds, aerosols) through the observation of their interaction with radiation. The techniques are classified as passive and active, depending on the energy emission source. Passive technique instruments measure radiation emitted from natural sources (such as the Sun) or reflected by the moon and the underlaying Earth's surface, which is transmitted, absorbed and scattered in the atmosphere. Spectrometers, radiometers and photometers are some examples of passive sensors. For active techniques, the instruments (lidar using light emission and radar, radio frequency emission) emit radiation into the atmosphere and recover the backscattered energy resulting from the radiation-atmosphere interaction. Both types of techniques have proven to be fruitful and are broadly used to monitor gases and aerosols properties from space (satellites), aboard aircraft and at ground level. This chapter is therefore dedicated only to the description of the ground-based remote sensing instruments used for measuring atmospheric aerosols properties. Photometers and lidars, passive and active techniques, respectively, will be introduced with their respective instrumental descriptions. In particular, this thesis is dedicated to the development and study of the compact CE376 lidar, designed by CIMEL company for aerosols monitoring. Therefore, this chapter describes extensively the CE376 lidar characteristics, data processing and performance. The features of the CE376 lidar are certainly improvements from a previous model CE370 lidar, which will be also described in this chapter. An early version of the CE376 lidar and the CE318-T photometer operating at ATOLL platform, part of LOA at Lille University, are considered for the instrumental and methodology assessments. Moreover, all the instruments presented here are able to perform measurements aboard moving platforms. By the end of this chapter, the readers will have a complete view of the instruments proposed for enhancing mobile aerosol monitoring and to assess their spatio-temporal variability.

3.1 Photometer

Photometers, passive remote sensing instruments, are widely use around the world to monitor aerosol contain in the atmospheric column. The AERONET network, deployed in the 90s by NASA in collaboration with PHOTONS (PHOtométrie pour le Traitement Opérationnel de Normalisation Satellitaire, LOA-University of Lille), now accounts for more than 500 active photometer stations (see Fig. 3.1), including both permanent and temporary sites. AERONET stations mostly cover the northern hemisphere’s land surface with more than 400 sites, in contrast to less than 100 sites on the South hemisphere land surface and oceans.

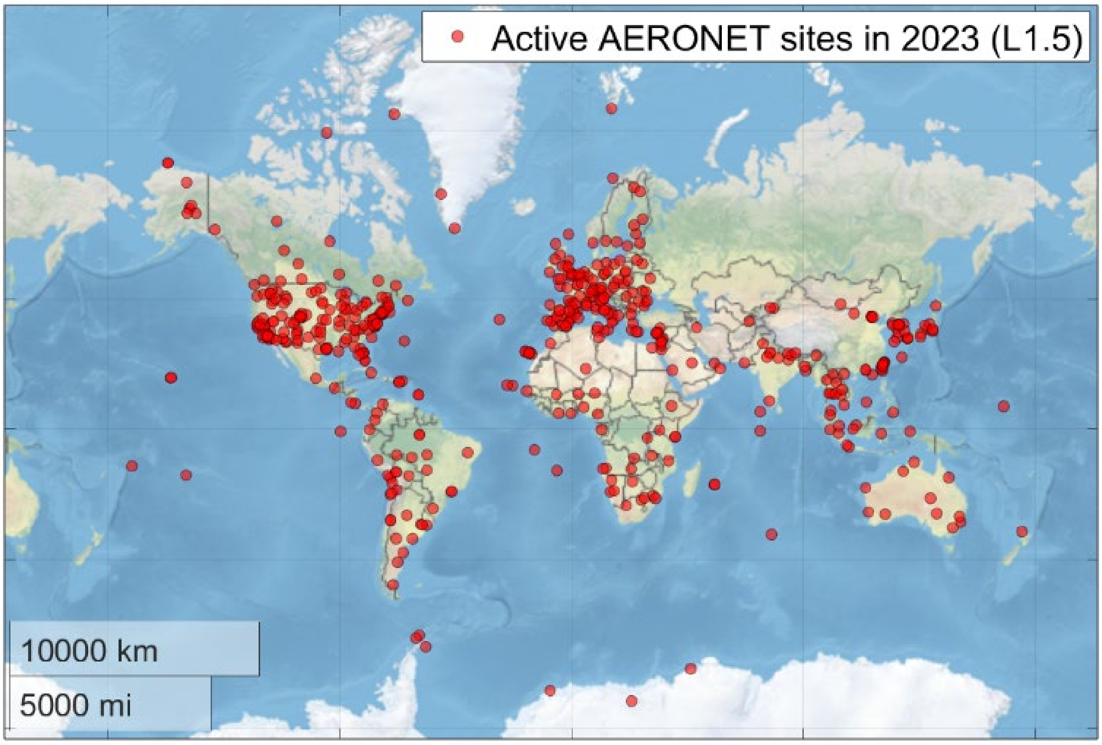

Figure 3.1: Global distribution of active AERONET sites in 2023, with available data at Level 1.5. Stations coordinates are available on AERONET website.

AERONET sites are equipped with different versions of the automatic CE318 photometer developed by CIMEL Electronique. The CE318 versions vary mainly according to their capabilities to measure the direct incident sunlight arriving to the Earth's surface (sun), the diffused light in the atmosphere (sky), and the incident light reflected by the moon (lunar or moon). Most sites are equipped with CE318-N sun/sky photometer, and an increasing number of stations incorporate the latest version, the CE318-T sun/sky/lunar photometer, also called "triple" photometer. It is important to mention that the measurements acquired at each AERONET station are uploaded automatically to 3 dedicated database servers in France, Spain and USA, where they pass through the same data processing line and inversion schemes. The aerosol properties derived from the measurements are visualized in near real time and are accessible at AERONET website (https://aeronet.gsfc.nasa.gov). Data processing is labeled as data level 1.0 without cloud screening and data level 1.5 with cloud screening (Smirnov et al., 2000). Level 2 is achieved for data that are manually inspected (quality assured), and can also be reprocessed to implement new parameters (e.g., calibration). In particular, CARS, the remote sensing branch of ACTRIS, facilitates the maintenance and monitoring of AERONET sites in Europe.

To bridge the observational gaps over oceans, photometer mobile observations were deployed by the Maritime Aerosol Network (MAN; Smirnov et al., 2009), part of AERONET, which collects direct sun measurements manually with Microtops II handheld sun photometers onboard ship cruises. Manual measurements provide insights into aerosols in a marine environment, though they are limited to the availability of observers and the precision of the measurements. Thus, in recent years the automatic CE318-T photometer has been adapted to perform measurements aboard ship cruises. The developments in mobile photometers aim not only to fill the gaps over oceans, but also over land in regions with complex topographies or close to aerosol sources. The PLASMA sun photometer, developed exclusively for mobile observations, has been tested onboard vehicles and aircraft during several campaigns. The PLASMA sun photometer also follows and meets the AERONET standards and is included in the data processing. The CIMEL CE318-T sun/sky/lunar photometer and PLASMA sun photometer were used in this thesis and are presented with its features in Sect. 3.1.1 and Sect. 3.1.2 respectively.

3.1.1 CE318-T photometer

The **sun/sky/lunar CIMEL CE318-T photometer** is a fully automated and robust instrument. The photometer consists of a sensor head mounted on a robot with two axes of movement (azimuthal and zenithal) that provides the capability to track the sun/moon (Fig. 3.2a). The photometer performs two types of observations; direct sun/moon and sky radiance measurements, following different protocols of measurements:

a) *Direct measurements* (sun, moon) detect the direct light that reaches the photometer after being attenuated in the atmosphere, i.e., from the top of the atmosphere to the photometer position. For example, in the case of direct sun measurements, the sensor is pointing in direction of the sun (i.e., at the solar zenith angle θ_s). Direct measurements should be done under clear conditions, to avoid high attenuation by clouds. The attenuation of the monochromatic light that reaches the detector can be expressed by the Beer-Lambert law, where I_0 is the radiance at the top of the atmosphere and I is the one detected at the sensor. M is the air mass, defining the atmospheric path traversed by light, which depends on the solar zenith angle θ_s, approximated by $1/\cos(\theta_s)$ for θ_s<75° (Eq. 2.7). The attenuation is given by the total optical depth $\tau(\lambda)$, which contains contributions of aerosols $\tau_a(\lambda)$ or AOD (Aerosol Optical Depth), molecules $\tau_m(\lambda)$ and absorbing gases $\tau_g(\lambda)$. The exact formulation can be found in Kasten & Young (1989) and Young (1994).

$$I(\lambda) = I_0(\lambda)\exp\big(-M\tau(\lambda)\big)$$
$$\tau(\lambda) = \tau_a(\lambda) + \tau_m(\lambda) + \tau_g(\lambda) \tag{3.1}$$

Direct sun/lunar measurements are collected automatically through nine channels (340, 380, 440, 500, 670, 870, 936, 1020, and 1640 nm) every 15 min by default. The wavelengths of the detection channels are selected at the bands where the atmospheric gases absorption is negligible, except for the 936 nm channel which is used to derive the total water vapor content. Direct measurements derive in spectral AOD, with an accuracy of 0.01. As well, Extinction Angstrom Exponent EAE (Eq. 3.2) can be calculated for pairs of wavelengths, giving insights on the aerosols size. Values of EAE close to 0, indicate predominance of coarse aerosols and EAE greater than 1 indicate predominant presence of fine aerosols.

$$EAE(\lambda_1/\lambda_2) = -\ln\left(\frac{\tau_a(\lambda_1)}{\tau_a(\lambda_2)}\right)\left[\ln\left(\frac{\lambda_1}{\lambda_2}\right)\right]^{-1} \tag{3.2}$$

b) *Almucantar sky radiance measurements* are performed only during daytime when the intensity of diffuse light is strong enough to be detected by the sensor. This protocol of measurements (Fig. 3.2b) consists on keeping a constant viewing angle equal to θ_s and varying azimuthal angle φ_a. The observations are performed at two symmetrical branches, on the right and left sides with respect to the sun position. This symmetry permits to filter data contaminated by clouds.

c) *Principal plane sky radiance measurements* consist on keeping a constant azimuthal angle (φ_a=180° or 0°) and varying the viewing angle θ_v (Fig. 3.2c). The principal plane provide access to measurements at higher scattering angles than the almucantar plane for low θ_s, however no symmetry is met (Torres et al., 2014).

d) Hybrid sky measurements combine both almucantar and principal planes measurements (Fig. 3.2d). This measurement protocol has been incorporated with the CE318-T photometer to enhance the sky measurements, particularly when the scattering angles are limited in the almucantar (with low θ_s).

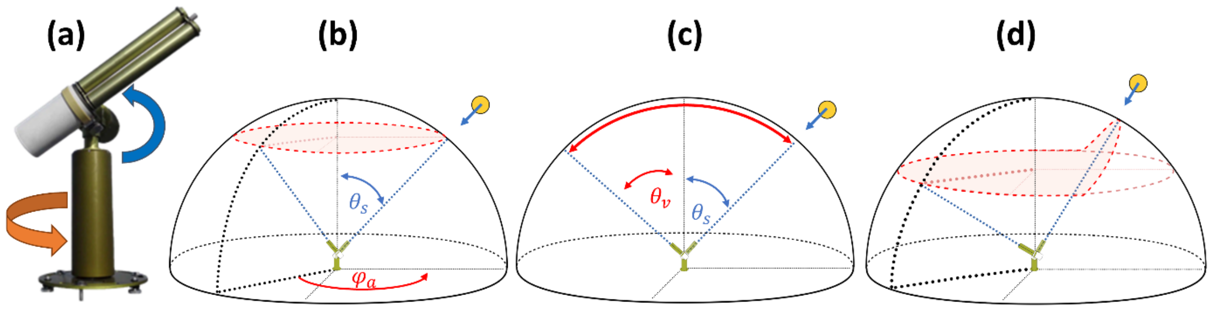

Figure 3.2: (a) CE318 photometer and the measurement protocols for sky observations, (b) almucantar, (c) principal plane and (d) hybrid measurements. Adapted schemes from (Torres, 2012; Almansa Rodríguez, 2021).

The sky observations (almucantar, principal and hybrid) permit to measure at different scattering angles giving more information on the phase function of aerosols contained in the atmosphere. Within the AERONET network, inversion procedures are applied to the measurements of sky radiance and direct sun, deriving in optical and microphysical aerosol properties (Dubovik & King, 2000). Explicitly, the volume size distribution (VSD) and, when AOD values are higher than 0.4 at 440 nm (to be upgraded to data level 2), the complex refractive index (decomposed in imaginary and real parts), and therefore by calculations the single-scattering albedo (SSA or ϖ_0). In particular, inversions with the hybrid measurements are incorporated in the AERONET version 3 algorithms (Sinyuk et al., 2020).

In principle, the CE318-T photometer is designed for ground-based fixed locations with all the features mentioned before and it is extensively described by Barreto et al. (2016). Nonetheless, to fill the spatial gaps in measurements within the network and to expand over ocean, the photometer needs to be adapted for mobile platforms. The ship-borne CE318-T developed at LOA and described by Yin et al. (2019) enables AOD measurements during movement. The system is coupled with a compass and GPS modules to obtain additional information (date, time, geolocation, heading, pitch and roll) to target the sun/moon continuously. With the help of an accelerated tracking feedback loop, the photometer can switch into its regular tracking mode to improve measurements quality. Sky radiances are also measured with additional information for each angle from GPS and compass to have accurate knowledge of the observation geometry. The ship-borne CE318-T is operational and continuously measuring since January 2021 on board Marion Dufresne research vessel, covering mainly the southern hemisphere/Indian Ocean.

3.1.2 PLASMA

The **sun-tracking-photometer PLASMA** (Photomètre Léger Aéroporté pour la Surveillance des Masses d´Air), developed by LOA and SNO/PHOTONS, has the capability of performing direct solar radiation measurements during movement. The instrument is easy to set up and transport due to its light and compact design (~5 kg and 23 cm height). PLASMA has 9 spectral channels: 339, 379, 440, 500, 674, 870, 1019 and 1643 nm and 937 nm for water vapor measurements. Spectral AOD, with an accuracy of 0.01, and EAE are derived from the direct solar radiation measurements (Karol et al., 2013), providing qualitative information on the size distribution of aerosols. Furthermore, the inversion scheme proposed by Torres et al.(2017), using spectral AOD and providing VSD, has being tested on PLASMA data.

Figure 3.3: PLASMA sun photometer developed by LOA.

PLASMA follows and meets the AERONET standards and is included in the network. A more detailed description of the instrument and its application to airborne measurements weas presented by Karol et al. (2013). PLASMA onboard an aircraft during AEROMARINE field campaign at Reunion Island (Mascaut et al., 2022) demonstrated the alternative use of the instrument to obtain AOD and EAE vertical profiles during ascendant/descendant trajectories. The integration of PLASMA and CE370 lidar onboard a car performing on-road ground measurements (Hu et al., 2019; Popovici et al., 2018, 2022) has been carried out during several campaigns.

3.2 Lidar

Lidar, an acronym for light detection and ranging, is a powerful active remote sensing technique to monitor the atmospheric structure and the vertical distribution of aerosol properties. The technique essentially involves transmitting laser pulses into the atmosphere, where some energy returns to the surface due to scattering. The backscattered light is then collected by a telescope and detected as a function of the time delay relative to the emitted pulse. The time delay is directly proportional to the range (or distance) from the lidar. A lidar for aerosol studies can be multi-wavelength and, with the same receiver, can deploy various detection channels. Thus, lidar systems adopt different instrumental designs given by their applications and are mainly classified according to the type of light-aerosol interaction considered for each detection channel. Elastic channels filter backscattered light to the same wavelength as the emission source, while Raman channels measure light at a different wavelength, where Raman signals (molecular interaction) are expected. Depolarization channels account for changes in the polarization state due to aerosol scattering, primarily linked to the aerosol shape. Fluorescence channels exploit the emission of fluorescence light, once interacted with UV radiation, in the presence of specific aerosol types, indicative of chemical composition. Raman and fluorescence signals, in particular, require high-power laser sources to be detectable at night. Moreover, High Spectral Resolution Lidars (HSRL) use very narrow bandwidth filters to distinguish light scattered by aerosols and molecules.

Contrary to the achieved standardization of photometer instruments within AERONET network, lidar systems can vary from one instrument to the other. This instrumental heterogeneity can lead to multiple interpretations of atmospheric observations. Therefore, the network EARLINET, now part of CARS, attempt to regulate the data processing, inversion schemes and calibrations of the multi-wavelength Raman depolarization lidars at European sites. Similarly, the network LALINET (Latin America Lidar NETwork, Landulfo et al., 2020) follows the protocols of calibration and quality assurance proposed by ACTRIS-CARS.

Most of the lidars included in these networks are complex and costly, requiring high maintenance and surveillance, so they are usually managed by experienced staff. However, the capabilities of lidar systems to assess air quality monitoring and contribute to early warning systems are demanded by a broader public. The increasing interest on lidar systems is mainly related to the insightful information on aerosol vertical distribution, which is important for properly evaluating climatological predictions and pollution dispersion models. Thus, micro-pulse lidars (low laser energy <20 μJ) and ceilometers (designed for cloud detection, in the NIR), which are low maintenance and typically automatic, are mostly used in airports and by meteorological institutions. Despite their lower Signal to Noise Ratio (SNR), these systems are able to retrieve aerosol properties effectively, especially in synergy with photometer observations. Hence, the network MPLNet (Micro-Pulse Lidar Network; Welton et al., 2001) was created for micro-pulse lidars and accounts 25 active sites in 2023, most of them located in the USA (https://mplnet.gsfc.nasa.gov/) and co-located with AERONET sites. Likewise, ACTRIS-CARS has recently included the network E-PROFILE with more than 100 European sites, whose efforts are on coordinating the measurements of vertical profiles of wind, aerosols and clouds from radars and low power lidars (https://e-profile.eu/).

Though both high and low-power lidar networks are expanding, they mainly cover the northern hemisphere's land surface, with broader observational gaps in the southern hemisphere and over oceans compared to the photometer distribution. Achieving mobile observations with lidar systems not only helps to fill these gaps within networks but also provides access to information of the atmospheric dynamics in complex topographies and close to aerosol sources. Moreover, mobile lidar systems can be easily placed on satellites ground tracks to enhance their data validation. However, the adaptation of existing lidars for mobile applications requires achieving: i) operational autonomy and ii) robustness (i.e. stability of opto-mechanics). These two challenges are not easy to overcome by high power lidar systems, whose adaptation is linked to instrumental modification and/or large laboratory platforms. Therefore, the CIMEL company proposes compact lightweight automatic lidar systems as a solution for air quality and mobile aerosol monitoring. The first model, the CE370 lidar (no longer commercially available), is a mono-wavelength elastic micro-pulse lidar system and the latest model, the CE376 lidar is a micro-pulse lidar with up to two wavelengths and depolarization channels.

Both systems were used in this thesis and are described in Sect. 3.2.1. In particular, the performance and capabilities of the CE376 lidar are evaluated in detail throughout the thesis.

3.2.1 Compact micro-pulse lidar systems

The CE370 lidar is an eye-safe micro-pulse elastic lidar (Pelon et al., 2008; Mortier et al., 2013; Popovici et al., 2018) operating at 532 nm with 20 µJ pulse energy at 4.7 kHz repetition rate (Table 3.1). It is designed with a shared transmitter-receiver telescope connected through a 10 m optical fiber to the control and acquisition system. The backscattered signal is detected by photon counting with an avalanche photodiode (APD). The CE370 lidar was designed by CIMEL Electronique to monitor aerosols and clouds properties up to 15-20 km with a vertical resolution of 15 m. For several field campaigns, the CE370 lidar, embarked on mobile platforms, has demonstrated the viability to characterize vertical aerosols properties during the platform's movement (Popovici et al., 2018, 2022). Therefore, the latest model of lidar, CE376, operating at up to two wavelengths, is proposed to replace the CE370 lidar and continue the developments towards mobile aerosols monitoring (https://www.cimel.fr/solutions/ce376/). Both lidar systems are showed in Fig. 3.4 and their features are presented in Table 3.1.

Table 3.1 Micro-pulse lidars technical specifications. * CIMEL CE370 is no longer commercially available. ** Some systems used in this work had higher pulse energy.

	CIMEL CE370*	CIMEL CE376 GPN	
Wavelength	532 nm	532 nm	808 nm
Laser source	Frequency doubled Nd:YAG	Frequency doubled Nd:YAG	Pulsed laser diode
Pulse energy	20 Mj	5-10 uJ (15-20 µJ) **	3-5 uJ
Repetition rate	4.7 kHz	4.7 kHz	4.7 kHz
Emission/Reception (E/R)	Coaxial	Biaxial	Biaxial
Telescope (E/R)	Galilean	Galilean	Galilean
Diameter (E/R)	200 mm	100 mm / 100 mm	100 mm / 100 mm
Half Field of View (E/R)	55 µrad	100 µrad / 120 µrad	240 µrad / 330 µrad
Depolarization	No	Yes	No

The CE376 elastic lidar is designed for up to 2 wavelengths and depolarization channels within different model configurations (G, GP, GPN, N). In this thesis we use mainly the CE376 GPN (Green Polarized Near-infrared) model, described in the following section.

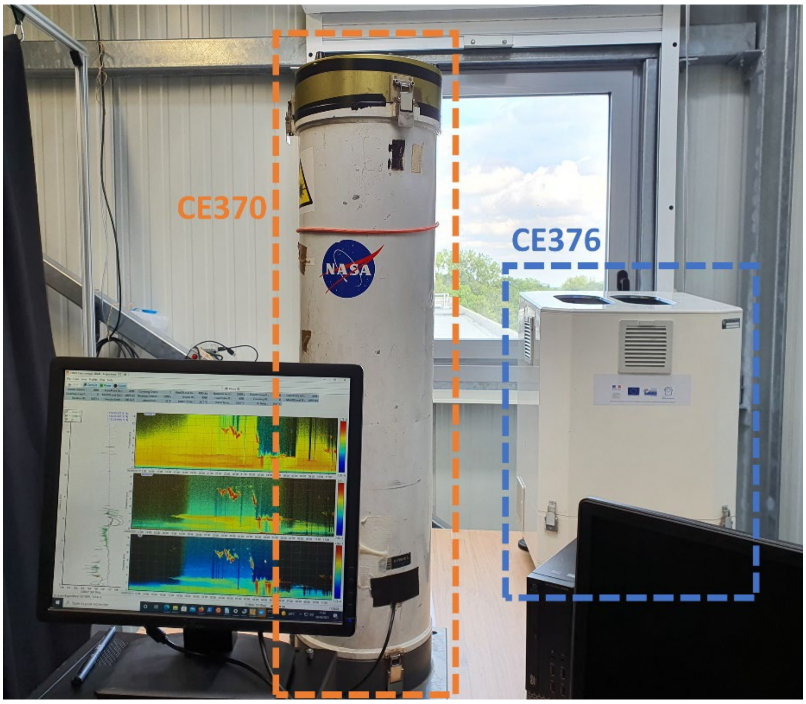

Figure 3.4: CE370 lidar and CE376 lidar installed at ATOLL (LOA, Lille University).

3.2.1.1 CE376 GPN lidar

The CE376 GPN is an autonomous, lightweight, and compact micro-pulse lidar. It operates at two wavelengths, 532 nm and 808 nm, with pulse energy of 5-10 μJ and 3-5 μJ, respectively, at a repetition rate of 4.7 kHz (Table 3.1). Measurements of elastic backscattered light at both wavelengths and depolarization at 532 nm are acquired. In two systems used in this work, the laser source at 532 nm was replaced with one of higher pulse energy (not eye-safe) to increase the SNR. The Emission-Reception design consists of two Galilean telescopes in biaxial configuration. The simplified 2D layout of the lidar system is presented in Fig. 3.5. Light pulses at 532 nm from a frequency doubled Nd: YAG laser source are transmitted through an arrangement of dichroic mirrors and collimation lenses on the green emission system. Similarly, a simplified optical system, including a pulsed narrow bandpass laser diode source, optical fiber and collimation lenses emits light pulses in the near infrared (NIR) at 808 nm. The elastic backscattered light is collected, collimated and filtered in the reception at each emitted wavelength (elastic channels) and detected with APDs in photon counting mode. Electronic cards developed by CIMEL communicate with the control and acquisition software.

Linear depolarization measurements at 532 nm are also acquired by separating the parallel (co-polarized) and perpendicular (cross-polarized) components of the backscattered light using a polarizing beamsplitter cube (PBS) in the reception. The PBS is a Thorlabs CCM1-PBS25-532 with reflectivities Rp and Rs and transmittances Tp and Ts as given by the manufacturer. A manual half-wave plate (HWP) in front of the PBS controls the polarization angle of the incident light with a precision of 2°. Measured signals behind the PBS on the reflected and transmitted branches are named parallel or perpendicular according to the reception configuration. More details about the depolarization measurements are presented in Sect. 3.3.2 and about the depolarization calibration in Sect. 3.4.3.

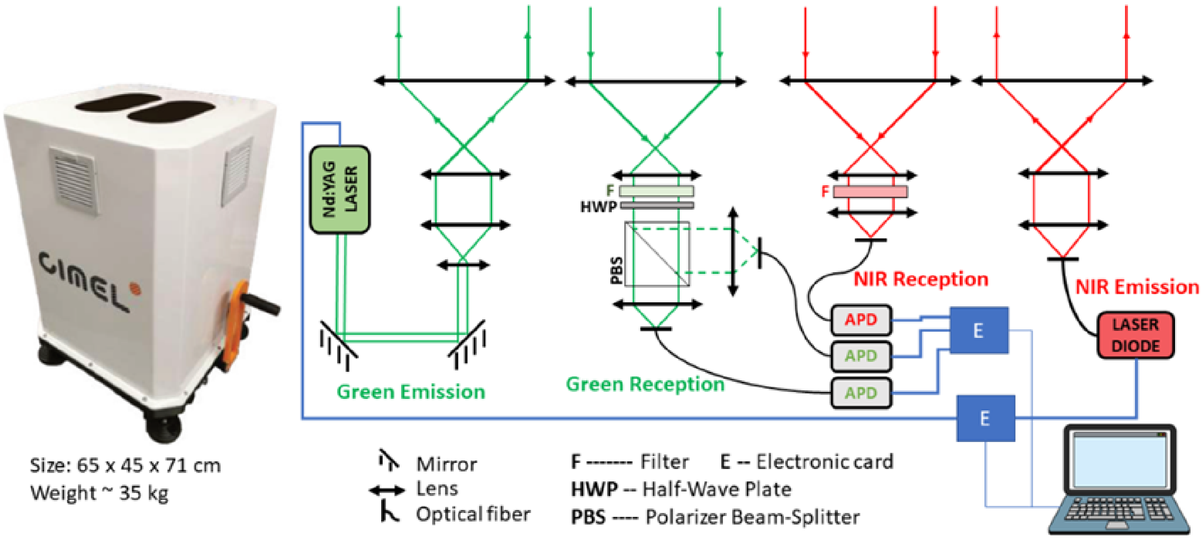

Figure 3.5: CE376 GPN lidar and its 2D design. The optical design of the biaxial systems at 532 nm (Green Emission/Reception) and 808 nm (NIR Emission/Reception), and layout of the control/acquisition system through electronic cards are shown in a simplified plan.

3.3 Lidar data processing

In this section, the methodology to process data, particularly from the CE376 GPN lidar, is described extensively. Detailed description of methods and corrections applied to the mono-wavelength CE370 lidar can be found in previous works (Pelon et al., 2008; Mortier et al., 2013; Popovici et al., 2018). This section describes the methods used to obtain atmospheric properties directly derived from the measurements, such as the total attenuated backscatter, volume depolarization ratio and attenuated color ratio. To simplify the reading of the thesis, the CE376 GPN lidar is hereafter referred to simply as CE376.

The light backscattered by molecules and aerosols is collected by a telescope and detected with an APD in photon counting mode by each detection channel. The measured counting rates P_{raw}

in counts per second [$\#counts\ s^{-1}$] are corrected by dead time t_d, dark current D_c and detection efficiency Q_e. For this purpose, the correction factor (Eq. 3.3) and the equation, provided by the APD manufacturer, to obtain the real signal P are applied (Eq. 3.4).

$$\mathrm{C}_{\mathrm{APD}} = 1/(1 - P_{raw}\ t_d) \tag{3.3}$$

$$P = (P_{raw} \cdot C_{APD} - D_c)/Q_e \tag{3.4}$$

Considering the elastic lidar equation (Kovalev & Eichinger, 2004; Weitkamp, 2005), the detected backscattered signal as a function of distance P(r) can be described as Eq. (3.5) for each detection channel.

$$P(\lambda, r) = P_0 A \xi(\lambda) \frac{O(\lambda,r)}{r^2}\ [\beta_{\mathrm{m}}(\lambda, \mathrm{r}) + \beta_{\mathrm{P}}(\lambda, \mathrm{r})]\ \mathrm{T}_{\mathrm{m}}^2(\lambda, \mathrm{r})\ \mathrm{T}_{\mathrm{a}}^2(\lambda, \mathrm{r}) + B(\lambda) \tag{3.5}$$

$$\mathrm{T}_{\mathrm{m}}^2(\lambda, \mathrm{r})\mathrm{T}_{\mathrm{a}}^2(\lambda, \mathrm{r}) = \exp\left(-2\int_0^r \alpha_m(\lambda, r')dr'\right) \exp\left(-2\int_0^r \alpha_a(\lambda, r')dr'\right) \tag{3.6}$$

Where $P(\lambda, r)$ is the signal received from a distance r in photons per second [Ph s^{-1}]. The factor $P_0 A \xi(\lambda) = C_L$ is known as the lidar calibration constant C_L, which depends on the system; P_0 is the power of the emitted laser pulse, A is the area of the receiver telescope and $\xi(\lambda)$ is the spectral transmission factor of the emission/reception modules. $O(\lambda, r)/r^2$ is the geometric factor, where $O(\lambda, r)$ is the overlap function and $1/r^2$ derives from the inverse square law. $B(\lambda)$ is the background noise. $\beta_m(\lambda, r)$ and $\beta_a(\lambda, r)$ are the backscatter coefficients in [$m^{-1}sr^{-1}$]. $\mathrm{T}_{\mathrm{m}}^2(\lambda, \mathrm{r})$ and $\mathrm{T}_{\mathrm{a}}^2(\lambda, \mathrm{r})$ are the non-dimensional two-way atmospheric transmittances derived from the Beer-Lambert law and defined in Eq. (3.6), where α is the extinction coefficient in [m^{-1}]. Subscripts *m* and *a* represent contributions of molecules and aerosols, respectively.

Moreover, the backscatter coefficient is defined as Eq. (3.7), where $p(\pi)$ is the phase function at a 180° scattering angle.

$$\beta(\lambda, r) = \alpha_{sca}(\lambda, r)\frac{p(\pi)}{4\pi} \tag{3.7}$$

Then the extinction to backscatter ratio, well known as Lidar Ratio *LR*, is defined as Eq. (3.8), where ω_0 is the SSA defined in Chapter 2, Sect. 2.2.3. This parameter depends on the wavelength and the aerosol type, which is influenced by the aerosol size distribution, shape and refractive index. Therefore, the LR is an important parameter for aerosol classification and will be further used in Chapter 4.

$$LR(\lambda, r) = \frac{\alpha(\lambda,r)}{\beta(\lambda,r)} = \frac{4\pi}{\omega_0(\lambda,r)p(\pi)} \tag{3.8}$$

The backscattered signal $P(\lambda, r)$ is affected primarily by the background signal B, adding a bias to the signal, and the geometrical factor, which influences the intensity of the detected light (Fig. 3.6). To reduce these influences on the signal, standard corrections are applied:

a) *Background signal (B) correction:* This is done by extracting the averaged signal $P(\lambda, r)$ in the last 5 km of a profile, i.e., above 25 km for a profile of 2048 bins at a 15 m range resolution. The solar irradiance increases during the day, adding noise to the background. Therefore, the background signal and corresponding noise during daytime reduce the SNR considerably in all the detection channels of the CE376, with a greater impact on the 808 nm and 532 nm cross-polarized channels.

b) *Range correction:* The inverse square law states that the intensity of light is inversely proportional to the square of the distance from the emission source. To account for this dependency, we simply multiply the signal by r^2.

c) *Overlap correction*: The $O(\lambda, r)$ function describes the overlap between the outgoing emitted laser beam (emission) and the telescope field of view (reception), therefore $O(\lambda, r)$ takes values from 0 to 1. The incomplete overlap ($O(\lambda, r) < 1$) for the CE376 channels is theoretically calculated to be extended up to 1.5 km for 532 nm and 0.7 km for the 808 nm. The $O(\lambda, r)$ function can be determined by modelling and experimentally in order to correct the signal impacted by the incomplete overlap. More details on the methods to determine the overlap function for the CE376 lidar are presented in Sect. 3.4.4.

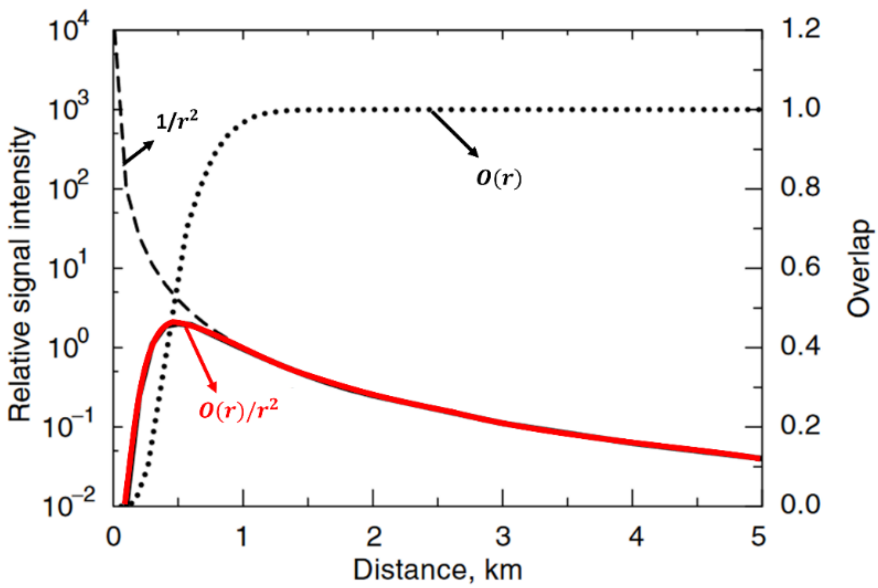

Figure 3.6: Influence of geometric factors on the detected signal. Source: Weitkamp, 2005.

After the initial corrections applied to $P(\lambda, r)$, we obtain $RCS(\lambda, r)$, defined in Eq. (3.9), which is well known as the Range Corrected Signal (RCS) in [Ph s^{-1} m^2]. RCS profiles are obtained for each detection channel of the CE376.

$$RCS(\lambda, r) = [P(\lambda, r) - B(\lambda)]\, r^2 / O(\lambda, r) \tag{3.9}$$

Then Eq. (3.5) can be rewritten as Eq. (3.10).

$$RCS(\lambda, r) = \mathrm{C_L}(\lambda)\, [\beta_m(\lambda, r) + \beta_a(\lambda, r)]\, T_m^2(\lambda, r)\, T_a^2(\lambda, r) \tag{3.10}$$

$$\beta_{att}(\lambda, r) = \frac{RCS(\lambda, r)}{\mathrm{C_{L(\lambda)}}} \tag{3.11}$$

The right side of Eq. (3.10) is described only in terms of atmospheric optical properties correlated to the measured signal RCS through a calibration constant C_L in [Ph s^{-1} m^3 sr], which can vary according to the detection channel. Then, correcting the RCS by the calibration lidar constant, we remain with the total attenuated backscatter $\beta_{att}(\lambda, r)$ (Eq. 3.11) in $[m^{-1} sr^{-1}]$. The method used to obtain the calibration constant is described in Sect. 3.4.2.

The molecular properties, $\beta_m(\lambda, r)$ and $T_m^2(\lambda, r)$, can be determined from available radiosonde data of temperature and pressure or from standard atmosphere models. Therefore, the aerosol properties, $\beta_a(\lambda, r)$ and $T_a^2(\lambda, r)$, remain unknown. Various inversion procedures were proposed in the literature to retrieve the aerosols properties from the elastic lidar measurements. In this work, some inversion methods were evaluated to get the most of information from the CE376 observations at two wavelengths. The description and discussion around the inversion methods are presented in Chapter 4.

3.3.1 Mobile measurements

For mobile observations, a GPS module is coupled with the lidar. The geolocation is measured with high temporal resolution (1 second). For each RCS profile, we determine its latitude, longitude and altitude above sea level (asl) by comparing recorded times for both GPS and lidar. The velocity of the mobile platform is derived from the geolocation and time in order to flag the stationary and mobile measurements for further analysis.

3.3.2 Depolarization measurements

The schematic of the receiver part that separates the light into its polarization components using a PBS cube, with reflectivities Rp and Rs and transmittances Tp and Ts, is presented in Fig.

3.7. $P_{\parallel}$ (or $\mathrm{RCS}_{\parallel}$) and $P_{\perp}$ (or $\mathrm{RCS}_{\perp}$) are the parallel and perpendicular backscattered signals with respect to the emitted laser plane of polarization, P_p and P_s are the signal components with respect to the incident plane of the PBS, i.e., linearly polarized light parallel (p) and perpendicular (s). φ is the angle between the plane of polarization of the laser and the incident plane of the PBS. The signals measured by the detectors behind the PBS are P_R (or RCS_R) on the reflected branch and P_T (or RCS_T) on the transmitted branch. V_R and V_T are the corresponding amplification factors which include the optical transmittances. In this section, the range and wavelength dependencies are omitted to simplify the reading.

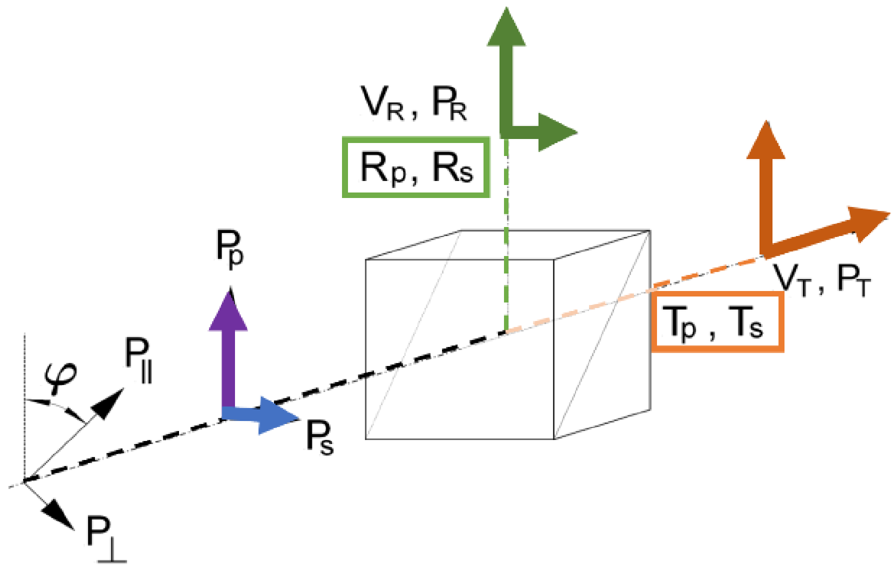

Figure 3.7: Separation of linearly polarized backscattered light using a PBS cube on the lidar receiver. Adapted from Freudenthaler et al., 2009.

The different components presented in Fig. 3.7 are defined as follow:

a) *Backscattered light components* (Eq. 3.12 and Eq. 3.13) are defined similarly to Eq. (3.10), but only the backscatter terms $\beta_m(\lambda, r)$ and $\beta_a(\lambda, r)$ are changed according to the polarization direction. The transmission terms are considered independent of the polarization component, although the light transmission through certain anisotropic particles, e.g., uniformly oriented ice particles, might be correlated with the polarization state (Hu, 2018).

$$\mathrm{RCS}_{\parallel} = C_L\ [\beta_m(\lambda_{\parallel})+\beta_a(\lambda_{\parallel})]\ T_m^2(\lambda)\ T_a^2(\lambda) \tag{3.12}$$

$$\mathrm{RCS}_{\perp} = C_L\ [\beta_m(\lambda_{\perp})+\beta_a(\lambda_{\perp})]\ T_m^2(\lambda)\ T_a^2(\lambda) \tag{3.13}$$

b) *Light components with respect to the incident plane of the PBS*

$$P_s\ (\varphi) = RCS_{\parallel} \sin^2(\varphi) + RCS_{\perp}\ cos^2(\varphi) \tag{3.14}$$

$$P_p\ (\varphi) = RCS_{\parallel} \cos^2(\varphi) + RCS_{\perp}\ sin^2(\varphi) \tag{3.15}$$

c) *Measured signals behind the PBS branches*

$$RCS_{\mathrm{R}}(\varphi) = [P_{\mathrm{P}}(\varphi)\, R_p + P_{\mathrm{s}}(\varphi)\, R_s]V_R \tag{3.16}$$

$$RCS_{\mathrm{T}}(\varphi) = [P_{\mathrm{P}}(\varphi)\, T_p + P_{\mathrm{s}}(\varphi)\, T_s]V_T \tag{3.17}$$

Typical values on commercial PBS cubes correspond to $\mathrm{R_s} > \mathrm{R_p}$ with $\mathrm{R_s}{\sim}1$, $\mathrm{T_p} > \mathrm{T_s}$ and considering $\mathrm{R_p} = 1 - \mathrm{T_p}$ and $\mathrm{R_s} = 1 - \mathrm{T_s}$, i.e., higher reflectivity for the P_s, and higher transmittance for P_p. Then two configurations are defined; when $\varphi = 0°$ ($P_{\mathrm{p}} = RCS_{\parallel}$ *and* $P_s = RCS_{\perp}$) and $\varphi = 90°$ ($P_{\mathrm{p}} = RCS_{\perp}$ *and* $P_s = RCS_{\parallel}$). The total backscattered signal $\mathrm{RCS} = \mathrm{RCS}_{\parallel} + \mathrm{RCS}_{\perp}$ is therefore derived into Eq. (3.18). The relative amplification factor V* is derived from calibration which is described later on Sect. 3.4.3.

$$RCS = RCS_{R} + V^{*}RCS_{T} \tag{3.18}$$

The Volume Linear Depolarization Ratio (VLDR) $\delta^{v} = RCS_{\perp}/RCS_{\parallel}$ is derive in accordance with the configuration as Eq. (3.20) and Eq. (3.21), where δ^{*} is the ratio of the measured components (Eq. 3.19). VLDR values contain depolarization ratios of both molecules and aerosols.

$$\delta^{*} = \frac{RCS_{\mathrm{R}}}{RCS_{\mathrm{T}}} \tag{3.19}$$

$$\delta^{v} = \frac{R_p - (\delta^{*}/V^{*})\, T_p}{(\delta^{*}/V^{*})\, T_s - R_s} \qquad \text{for} \quad \varphi = 0° \tag{3.20}$$

$$\delta^{v} = \frac{(\delta^{*}/V^{*})\, T_p - R_p}{R_s - (\delta^{*}/V^{*})\, T_s} \qquad \text{for} \quad \varphi = 90° \tag{3.21}$$

The definition of VLDR and the total signal RCS presented in this section are derived using the methods described by Freudenthaler et al. (2009). These methods are widely used within the lidar community.

For the case of the CE376 lidar, the detection channels are named according to the configuration, with $\varphi = 0°$ *or* $90°$. The configuration is changed using the HWP in front the PBS that controls the polarization plane of the incident light with a precision of 2 degrees. The system configuration with $\varphi = 0°$ is achieved maximizing the parallel (or co-polarized) signal in the transmitted branch of the PBS, therefore the detection channels are named parallel at the transmitted branch and perpendicular at the reflected branch, $\mathrm{RCS_T} \approx \mathrm{RCS}_{\parallel}$ and $\mathrm{RCS_R} \approx RCS_{\perp}$. Moreover, it is convenient to use the configuration $\varphi = 90°$ to reduce noise and errors from cross-talk effects. The configuration $\varphi = 90°$ is achieved maximizing the parallel signal in the reflected branch of the PBS, with $\mathrm{RCS_T} \approx \mathrm{RCS}_{\perp}$ and $\mathrm{RCS_R} \approx RCS_{\parallel}$.

3.3.3 Attenuated Color Ratio

The Color Ratio (CR), defined as the ratio of aerosol backscatter at two different wavelengths, has been widely used to discriminate clouds from aerosol layers and for aerosol typing (Burton et al., 2013; Omar et al., 2009; Qi et al., 2021; Wang et al., 2020). However, this requires the selection of an appropriate aerosol extinction-to-backscatter ratio (LR). Therefore, approximations of the aerosol backscatter were proposed without going through complex inversion schemes. Baars et al. (2017) proposed a simplified forward inversion method, using a constant LR and the total attenuated backscatter to derive a first estimation of aerosol properties, named "quasi-aerosol". The quasi-aerosol properties, CR_{quasi} and $PLDR_{quasi}$ (Particle Linear Depolarization Ratio), are retrieved with a LR of 50 sr and are used for aerosol typing (Baars et al., 2017; Wang et al., 2020). On the other hand, CALIPSO algorithms use the layer mean total attenuated backscatter as a first approximation of the aerosol backscatter $\bar{\beta}_{att} = [1/(r_{top} - r_{base})] \int_{base}^{top} \beta_{att}(r')dr'$ and defines the layer-integrated attenuated color ratio as $\chi' = \bar{\beta}_{att}(1064)/\bar{\beta}_{att}(532)$. Both layer-integrated features are used for classification of stratospheric aerosols (Kim et al., 2018; Omar et al., 2009; Vaughan et al., 2004). The LR of 50 sr for the quasi-aerosol properties was defined as a good compromise for continental European sites, still it is imposing an important restriction for further aerosol classification. Thus, in this work the considerations of CALIPSO are rather followed. Further discussion on the methods mentioned here is available in Chapter 4 Sect. 4.1.

The attenuated total backscatter corrected by the two-way molecular transmittance term is considered as a first approximation of the aerosol backscatter. Therefore, the Attenuated Color Ratio (ACR) for all the ranges is defined by Eq. (3.22). The terms λ_S and λ_L refer to the shorter and longer wavelength, respectively, which are 532 nm and 808 nm for the CE376 lidar. The two-way molecular transmittances are modeled using available pressure and temperature profiles.

$$ACR(\lambda_L/\lambda_S, r) = \frac{\beta_{att}(\lambda_L, r)\, T_m^{-2}(\lambda_L, r)}{\beta_{att}(\lambda_S, r)\, T_m^{-2}(\lambda_S, r)} \tag{3.22}$$

$$ACR(\lambda_L/\lambda_S, r) = \frac{[\beta_m(\lambda_L, r) + \beta_a(\lambda_L, r)]}{[\beta_m(\lambda_S, r) + \beta_a(\lambda_S, r)]} \exp\left(-2\int_0^r [\alpha_a(\lambda_L, r') - \alpha_a(\lambda_S, r')]dr'\right)$$

The ACR contains information about the atmospheric molecules and aerosols, particularly it providing insights on the aerosol size. For a purely molecular atmosphere, the ACR is reduced to the ratio of molecular backscatter coefficients ACR(808/532)~0.19. Clouds are generally composed of large particles compare to the lidar wavelengths, so the backscatter and extinction coefficients are not expected to show spectral variation. Therefore, ACR values for clouds are likely to be close to 1. Assuming that only one type of aerosols is present in the atmospheric column, the exponential term remains constant and the ACR is controlled by the ratio $\beta_a(\lambda_L, r)/\beta_a(\lambda_S, r)$. Under this assumption, ACR values for aerosols roughly between 0 and 1, with low values for fine aerosols and close to 1 for coarse aerosols.

3.4 Lidar data quality control and calibrations

This section is dedicated to the description of the standard methods used for data quality control (QC), lidar constant, and depolarization calibrations. The methods to determine the overlap function for the detection channels of a CE376 lidar are also described.

3.4.1 Rayleigh fit

For QC of lidar data, the standard Rayleigh fit procedure (Freudenthaler et al., 2018) proposed within the EARLINET network is followed. This means normalizing the $RCS(\lambda, r)$ to the molecular profile $\beta_m(\lambda, r)T_m^2(\lambda, r)$ at a reference distance (r_{ref}), where we assume an aerosol free zone, i.e. $\beta_a(\lambda, r_{ref}) = 0$. The molecular backscatter coefficients $\beta_m(\lambda, r)$ and the two-way molecular transmittance $T_m^2(\lambda, r)$ are modeled using pressure and temperature profiles from standard atmosphere models or from available radiosonde data. The lidar data is considered of good quality when the RCS profile overlays the molecular profile in the aerosol free regions. When optical parts are misaligned, the lidar profile does not overlay and deviates from the molecular profile.

Figure 3.8 presents an example of the Rayleigh fit applied to the three channels of the CE376 lidar operating at ATOLL. Data obtained during night-time is selected and averaged over 30 minutes at the same reference altitude (4065-4560 m asl) for all channels, and a moving average of 300 m window is used to smooth the profile. For this case, the majority of aerosols are contained in the first 2 km and aerosol layers are observed between 5 km and 11 km asl. The clean air regions of the RCS profile overlay over the molecular profile within 10 % relative deviations (up to 16 km asl) for the 532 nm parallel channel (ch532par). The other two channels (ch532per and ch808tot) are noisier beyond 5 km but still fit the molecular profile with 20 to 40 % deviation (up to 12 km asl).

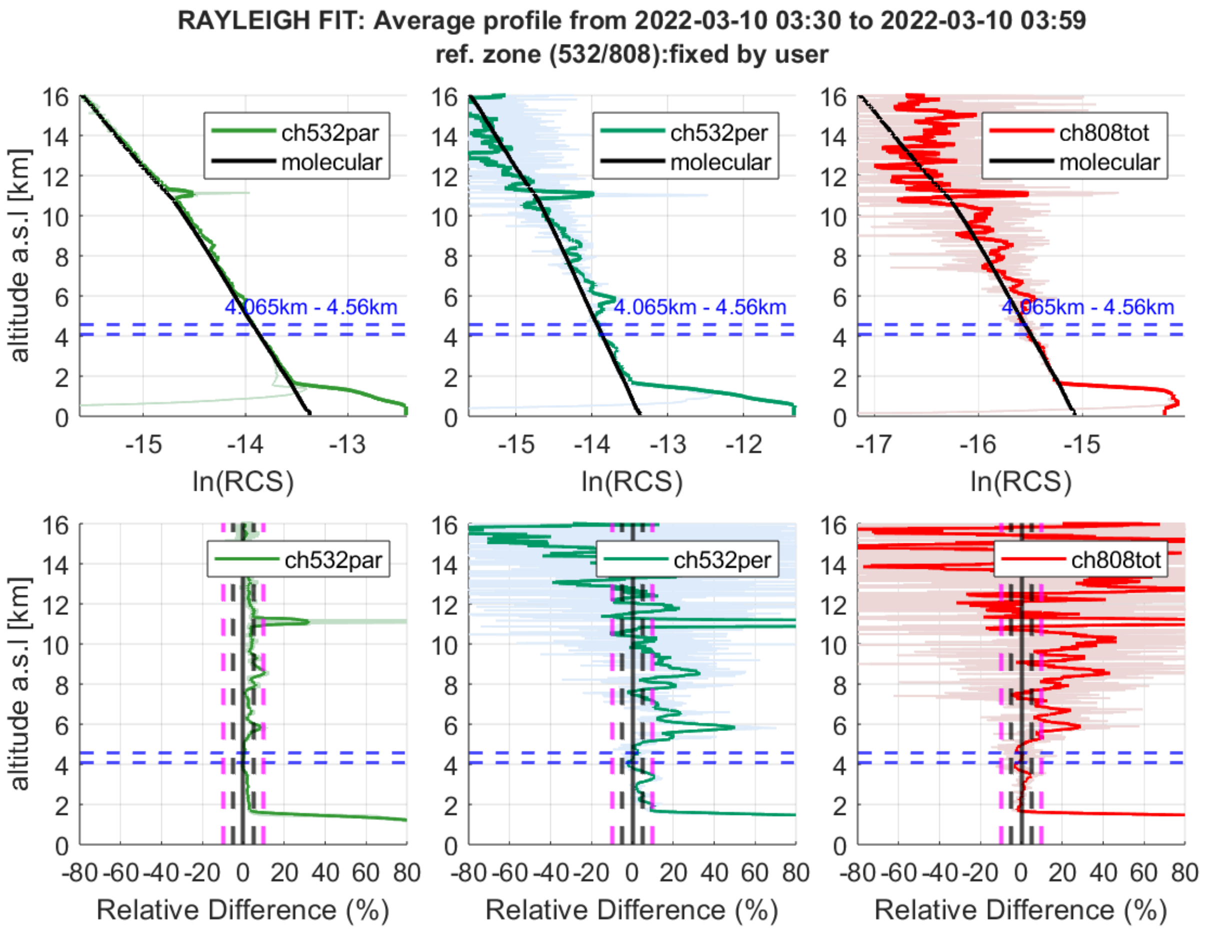

Figure 3.8: Example of Rayleigh fit for the CE376 detection channels, 532 nm parallel (ch532par), 532 nm perpendicular (ch532per) and 808 nm (ch808tot). Top panel presents the Rayleigh fit and the bottom panel shows the relative difference of the RCS with respect to the molecular profile. In the bottom panel, the black dashed lines represent the relative differences of 5 % from Rayleigh and the magenta dashed line represents the 10 % deviations.

3.4.2 Lidar constant calibration

Various calibration methods are described in the literature to derive the lidar constant using either clouds or clean air as reference. The main ideas behind these methods are described here:

a) *Cloud attenuation method:* This type of calibration uses liquid stratocumulus or cirrus clouds as a reference (Platt, 1973; O'Connor et al., 2004; Jin et al., 2018; Li et al., 2021). The method consists of retrieving the cloud LR (LR_c) by integrating the total attenuated backscatter $\beta_{att}(\lambda, r_b - r_t)$ from the cloud base r_b to the cloud top r_t, when clean air conditions below and above the thick cloud are met, so that $\mathrm{T}_{\mathrm{a}}^2(\lambda, r_b)$ can be approximated to 1. Assuming a multiple scattering factor, η, of 1 for the cloud, the lidar constant can be approximated as Eq. (3.23).

$$C_L(\lambda) = 2\eta LR_c(\lambda) \int_0^{r_t} RCS(\lambda, r) dr \tag{3.23}$$

b) *Rayleigh calibration:* The same considerations as for the Rayleigh fit are taken into account to determine the calibration constant $C_L(\lambda)$. Hence, Eq. (3.24) can be derived from Eq. (3.10).

$$C_L(\lambda)=\frac{RCS(\lambda,r_{ref})}{\beta_m(\lambda, r_{ref})T_m^2(\lambda,r_{ref})T_a^2(\lambda, r_{ref})} \quad (3.24)$$

Considering cases with low aerosol loading, the aerosol transmittance term $T_a^2(\lambda, r_{ref})$ is approximated to 1 (Wang et al., 2020; Li et al., 2021).

Both methods (cloud and Rayleigh calibrations) take into account rough considerations for the multiple scattering and/or the aerosol transmittance. Therefore, selecting the data to be used requires special attention. In addition, the thick clouds selected for the cloud method, due to the low pulse energy of CE376, can easily saturate the signal, adding errors to the calibration.

However, considering observations of a collocated photometer, we can improve the Rayleigh calibration. The aerosol transmittance term $T_a^2(\lambda, r_{ref})$ in Eq. (3.24) can be calculated if the AOD from the photometer (AOD_{ph}) is available. Under the hypothesis that clean air is present above r_{ref}, the integral $\int_0^{r_{ref}} \alpha_a(\lambda, r')dr'$ (in Eq. 3.6) is equivalent to the $AOD_{ph}(\lambda)$.

$$T_a^2(\lambda, r_{ref}) = \exp\left[-2\, AOD_{ph}(\lambda)\right] \quad (3.25)$$

And the lidar constant can be calculated using Eq. (3.24), where all terms are known.

Taking into account the limitations of both methods, the Rayleigh calibration is selected to determine the lidar constant for the total signal of the CE376 lidar wavelengths, $RCS(532, r)$ and $RCS(808, r)$. An example of the Rayleigh calibration during a day with low aerosol loading is presented in Fig. 3.9. Profiles are averaged over 5 minutes and the reference zone (6-7 km asl) used for calibration is highlighted by red lines on top of the temporal variations of $RCS(532, r)$ (Fig. 3.9a) and $RCS(808, r)$ (Fig. 3.9b). The lidar constant determined using the Rayleigh method, $C_{L,est}$, as well as the one calculated using the input of photometer measurements, C_L, are shown in Fig. 3.9c.

For this case, the differences between $C_{L,est}(532)$ and $C_L(532)$, for values of $AOD_{ph}(532) < 0.07$, are up to 15%, while the differences for 808 nm rise up to 10 % for values $AOD_{ph}(808) < 0.05$. During daytime (15:30-17:30) the noise increases, especially at 808 nm, influencing the calculation of the lidar constant; therefore, the calibration is applied in preference during nighttime when lunar measurements are available.

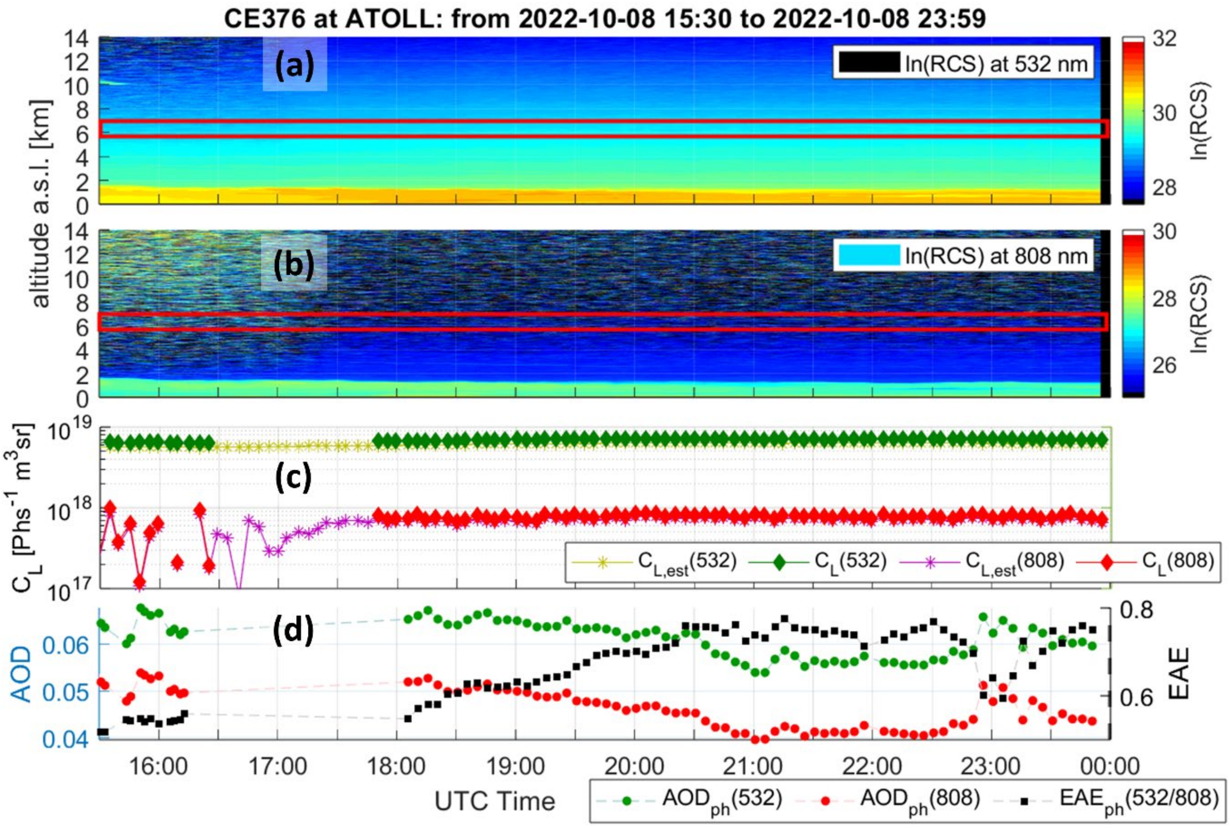

Figure 3.9 : Example of Lidar Constant calibration. From top to bottom: spatial-temporal variability of ln(RCS) at (a) 532 nm and (b) 808 nm, (c) lidar constant at both wavelengths and (d) photometer information. The reference altitude for the Rayleigh calibration is highlighted with red lines.

Furthermore, if there are no changes on the lidar system configuration, the $C_L(\lambda)$ stability over time is mainly controlled by the laser energy and the opto-mechanical stability.

3.4.3 Depolarization calibration

Under clear sky and stable atmospheric conditions, we calculate the V^* parameter (Eq. 3.26) from the standard $\pm 45°$ calibration. This method described by Freudenthaler et al. (2009), aims to simplify the equations (presented in Sect. 3.3.2) by adjusting the system configuration angle ($\varphi = 0°$ *or* $90°$)) to $\varphi \pm 45°$ and derive the relative amplification factor $V^*$of the PBS cube.

$$V^* = \frac{V_R}{V_T} = \frac{T_p + T_s}{R_p + R_s}\sqrt{\delta^*(+45^o)\;\delta^*(-45^o)} \tag{3.26}$$

The error induced on V^* by the angle error ($\varphi \pm \gamma$) depends on the system precision and has been estimated by Freudenthaler et al., (2009). The error represents less than 5 %, when considering measurements at both angles +45° and −45° instead of just at one of them (Fig. 3.10).

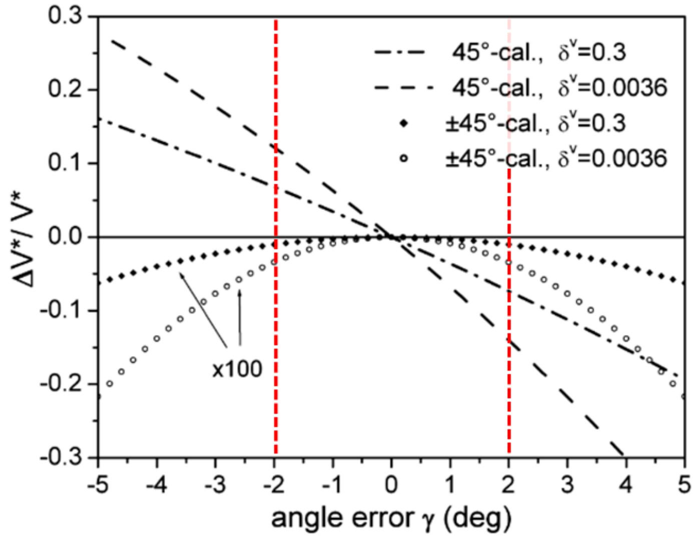

Figure 3.10: Relative errors of V∗ over the calibration angle error γ calculated, with Tp =0.95, Rp = 0.05, Rs = 0.99 and Ts = 0.01 for δv = 0.0036 (clean air) and δv = 0.30 (desert dust). The ±45◦ calibration errors are multiplied by a factor of 100. Red dashed lines indicate the angle uncertainty for CE376 lidar. Source : *(Freudenthaler et al., 2009)*.

For the case of CE376 lidar, the HWP rotates the angle of the incident polarization plane φ by means of 2θ. Thus, for the calibration we should rotate θ=±22.5◦ with respect to the initial configuration (φ=0° or 90°) to obtain equal polarized signals $RCS_{\parallel} = RCS_{\perp}$. Since the precision of θ is 2◦, we consider for the calibration either θ=±22 (φ±44°) or θ=±23 (φ±46°).

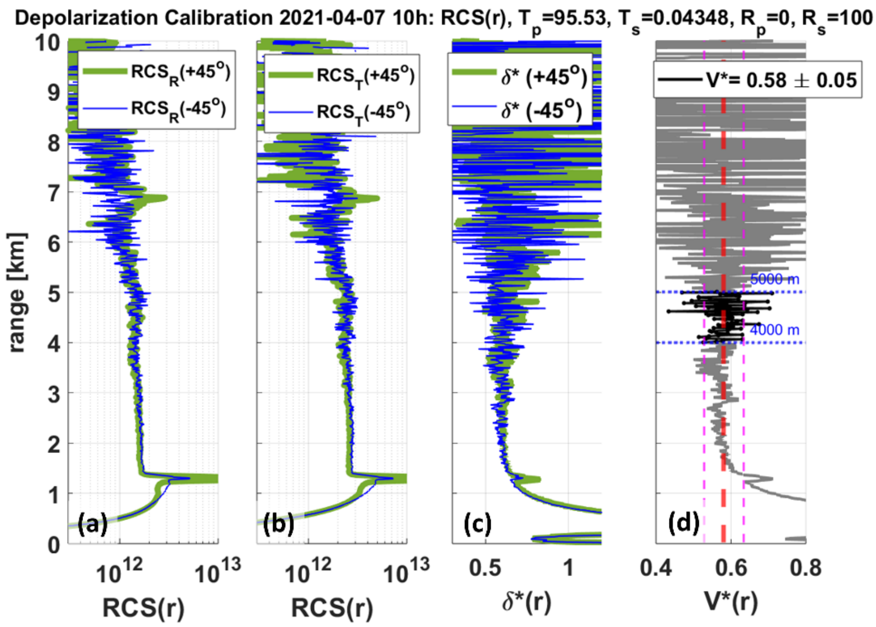

Figure 3.11: Example of ±45° polarization calibration of the depolarization channels for the CE376 lidar at ATOLL. Detected signals at the (a) reflected and (b) transmitted branches of the PBS are shown for $\varphi + \sim 45°$, and $\varphi - \sim 45°$. The (c) measured polarization ratios δ^* at ±45° and the (d) profile of V^*.

An example of depolarization calibration for the CE376 lidar is presented in Fig. 3.11. The configuration uses φ=90º, i.e., $P_p = RCS_{\perp}$ and $P_s = RCS_{\parallel}$, and the PBS factors are $T_p = 95.53\ \%$, $T_s = 0.04\ \%$, $R_p = 4.47\%$ and $R_s = 99.96\%$. Particularly for this case, a polarizer sheet was placed behind the PBS reflected branch to reduce the cross talk, so that $R_p{\sim}0\%$ and $R_s{\sim}100\%$. A profile of calibration factor V^* is derived (Fig. 3.11d) and the final value is averaged within a region where V^* is linear, between 4 to 5 km. The error induced, on the calibration factor V^* by the precision of the HWP (red dashed lines in Fig. 3.10) is negligible in comparison to the 9% statistical error in the averaged V^*. However, additional errors during the calibration and in regular measurements can come from polarizing optical components that need detailed characterization (Freudenthaler, 2016), which are not considered in this work.

3.4.4 Determination of the Overlap function

The overlap function O(r), taking values from 0 to 1, can be estimated by modeling of the system's optical paths and through experimental methods. The model methods use ray tracing software or analytical approaches to the geometrical optics (Ancellet et al., 1986; Kokkalis, 2017; Sassen & Dodd, 1982; Velotta et al., 1998). These methods require a precise description of the optical arrangement in the emission and reception modules and are recurrently used to define the optical design of a lidar. Nevertheless, they are limited to theoretical values and can be far from the real overlap function. Likewise, the optical system's geometry might vary with time, due to modifications in the system during calibrations and by strong temperature gradients or abrupt movements.

In contrast, experimental methods are applied on atmospheric observations. Most of these techniques use observations under atmospheric stable conditions searching for homogeneously distributed aerosols. The atmospheric conditions in the incomplete overlap are extrapolated using polynomial regression on the RCS profile where there is high confidence that O(r)=1 (Sasano et al., 1979; Kunz & De Leeuw, 1993; Dho et al., 1997a, 1997b). Similarly, considering a purely molecular atmosphere, the overlap function can be approximated comparing the RCS to the molecular profile and using the same considerations as the Rayleigh fit (Hu et al., 2005). Calibration-type methods are based on comparisons between lidar systems, and are used mainly when Raman lidar or lidars with a confident low overlap are available (Wandinger & Ansmann, 2002; Guerrero-Rascado et al., 2010; Sicard et al., 2020).

For the case of the CE376 lidar, two experimental methods are used to determine the overlap function. One of the methods considers a well-mixed boundary layer to extrapolate the RCS in the incomplete overlap by linear regression. The second method considers solely molecular contributions in the profile (cases of very low aerosol loading) and uses the Rayleigh fit to determine the overlap function. As example, Fig. 3.12 presents the determination of the overlap function using the molecular approximation (Fig. 3.12a) for the 532 nm parallel channel (ch532par) and using the linear regression for the 808 nm (ch808tot) channel (Fig. 3.12b).

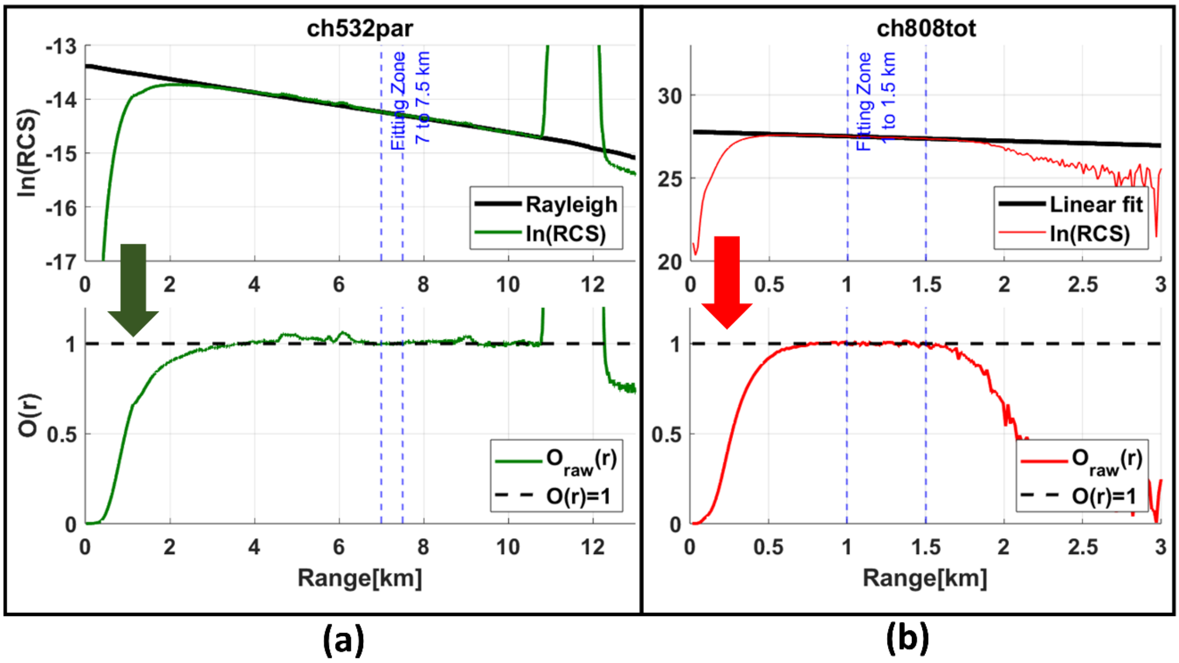

Figure 3.12: Overlap function determination by two experimental methods, using a (a) molecular approximation and a (b) linear regression.

The examples presented correspond to different days in order to match the considerations of each method. The Rayleigh fit zone for ch532par is considered between 7 to 7.5 km and the linear regression for ch808tot is applied in the range from 1 to 1.5 km. In particular, the 808 nm channel reaches the complete overlap at a lower range (~0.8 km) than 532 nm channels (~3 km). This difference is primarily influenced by the emission and reception optical designs, higher FOV, and fiber core (105 μm) for the 808 nm channel than for the 532 nm one (50 μm fiber).

3.5 CE376 lidar performance

In this section, the performance of the CE376 lidar installed at ATOLL (LOA, University of Lille) is presented. The CE376 lidar, named METIS, accomplished continuous observations without any changes to its configuration for almost a year, from March 2022 to January 2023. Hence, it was possible to evaluate METIS's detection limits and mechanical stability in a long period. During this time, improvements in the depolarization measurements were achieved and are also presented in this section. Moreover, METIS is co-located with CE318-T sun/sky/lunar photometer and with LILAS (LIlle Lidar AtmosphereS) Raman lidar, both considered for the evaluation of CE376 lidar performance.

3.5.1 Detection limits

Applying a simple SNR threshold, we can determine where the signal is too noisy to extract information from the lidar observations. Following the guidelines proposed by Morille et al. (2007), the noise level of the measured signal, influenced mainly by the background noise $B(\lambda)$, can be described as Eq. (3.27), where $\sigma(\lambda, r)$ is the noise level, $\sigma_B(\lambda)$ is the standard deviation of the background noise $B(\lambda)$ and $P(\lambda, r)$ is the measured signal before corrections.

$$\sigma(\lambda, r) = \frac{\sigma_B(\lambda)}{\sqrt{B(\lambda)}}\sqrt{P(\lambda, r)} \tag{3.27}$$

Then the SNR for each lidar profile can be defined by Eq. (3.28),

$$SNR(\lambda, r) = \frac{P(\lambda,r) - B(\lambda)}{\sigma(\lambda,r)} \tag{3.28}$$

The range at which a single profile gets too noisy to extract information is defined as the detection limit for that profile (r_{lim}). For the CE376 lidar, the detection limits r_{lim} for all the channels are considered where the $SNR = 1.5$, taking into account that the background noise is higher due to the low power emission sources. High power lidars usually consider r_{lim} at SNR=4 or even higher.

Figure 3.13 presents the temporal variation from March 2022 to January 2023 of detection limits for all the channels of METIS. The detection limits, (Fig. 3.13a) $r_{lim}(532par)$, (Fig. 3.13b) $r_{lim}(532per)$ and (Fig. 3.13c) $r_{lim}(808tot)$, are calculated for averaged profiles of 30 min. Points in darker colors represent daily minimum and daily maximum values of r_{lim} for each channel. Also, the variations of the instrument's internal temperature (Fig. 3.13a), relative humidity (Fig. 3.13b), and AOD (Fig. 3.13f for 532 nm and Fig. 3.13g for 808 nm) from co-located photometer are presented. Darker lines correspond to moving average of one day. The detection limits of the 532 nm channels are on average, $r_{lim}(532par) = 14.3 \pm 7.8\ km$ and $r_{lim}(532per) = 6.9 \pm 3.8\ km$ for average $AOD_{ph}(532) = 0.12 \pm 0.9$. The detection limit of the 808 nm channel is on average $r_{lim}(808) = 4.8 \pm 3.4\ km$ for $AOD_{ph}(808) = 0.08 \pm 0.06$.

It is important to note that these detection limits correspond to an CE376 that is not eye-safe, such as the METIS lidar at ATOLL, which is equipped with a more powerful laser. The detection limit for eye-safe models of CE376 would be lower, but are not presented here.

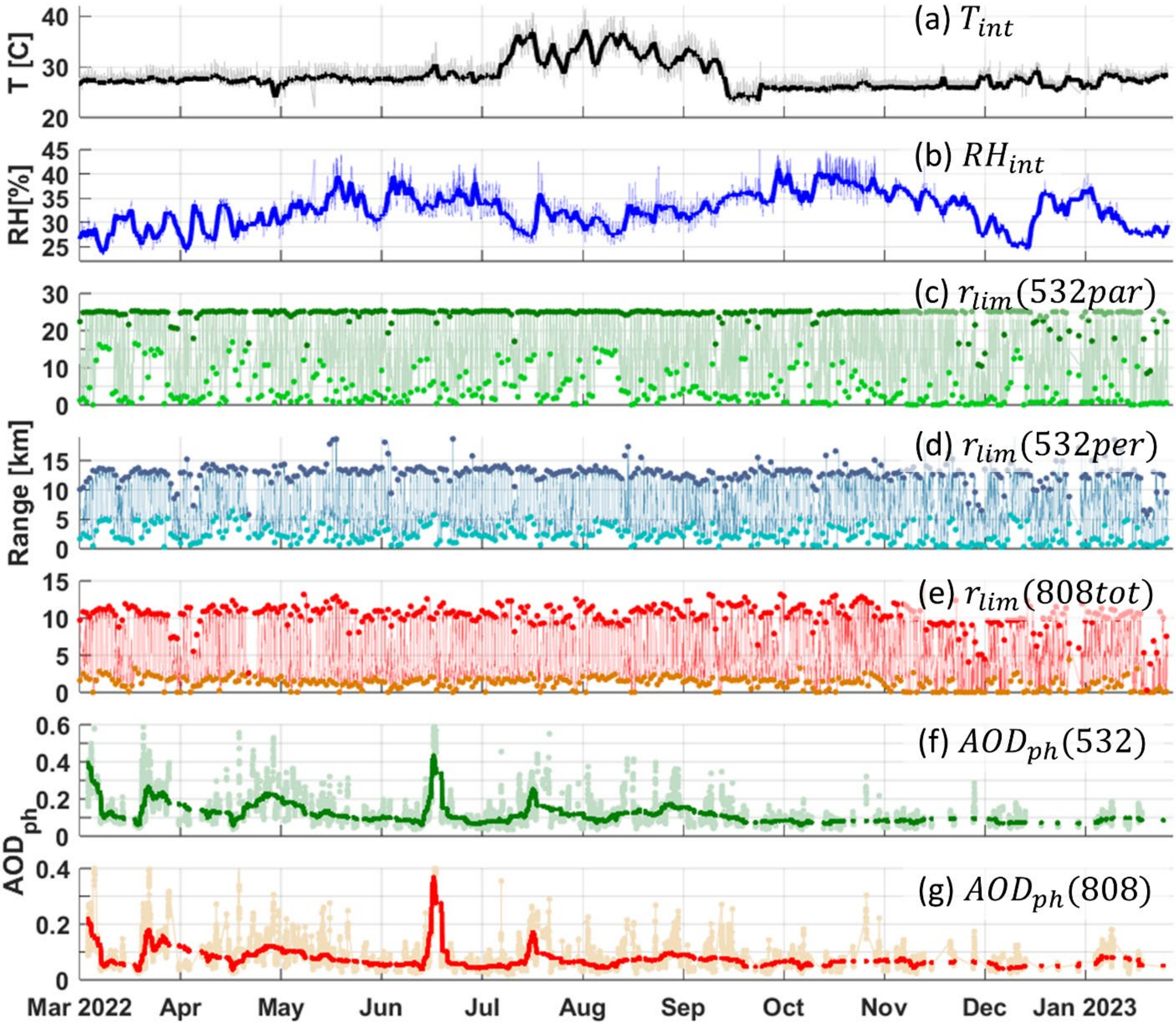

Figure 3.13: Monitoring of CE376 lidar performance from March 2022 to January 2023. The instrument's internal (a) temperature and (b) relative humidity, the detection limits with their daily maximum and minimum values for the (c) 532 nm parallel, (d) 532 nm perpendicular and (e) 808 nm total channels are presented. AOD values derived from the photometer with daily average at (f) 532 nm and (g) 808 nm are also presented.

The detection limits vary during the day according to the increase in background noise (solar irradiance) and can be impacted by high aerosol loadings, clouds and haze presence. Clouds are observed all around the year at ATOLL (Lille, Nord France), with higher frequency during winter, which is also commonly influenced by early morning haze. Thus, the daily maximum detection limits for the 532 nm channels are on average $r_{lim}(532par) = 24.2 \pm 2.4\ km$ and $r_{lim}(532per) = 13 \pm 2\ km$, in contrast to the daily minimum which are on average $r_{lim}(532par) = 4.3 \pm 4.3\ km$ and $r_{lim}(532per) = 2.3 \pm 1.4\ km$. The daily maximum and minimum detection limits for 808 nm are on average $10.4 \pm 2\ km$ and $1.2 \pm 0.8\ km$

respectively. On the other hand, the temperature and relative humidity variations apparently do not have influence on the detection limits of the CE376 lidar.

The daily variation of the detection limit plays an important role on the selection of the inversion methods to be used in order to retrieve aerosol properties at the two wavelengths of the CE376 lidar. These inversion methods are discussed later in Chapter 4.

3.5.2 Temperature effects on CE376 lidar

Strong gradients of temperature can cause misalignments in the optical paths of any lidar system, mainly due to dilations in the opto-mechanical components. These misalignments can be small and temporary, causing changes the overlap function while the temperature varies (Hervo et al., 2016). Otherwise, these variations can completely change the configuration of the system, i.e., changing the detection limits, lidar constant and/or overlap function shape. As we saw in Sect. 3.5.1, there is no indication that the temperature variation influenced the detection limits. However, during the summer of 2022, significant heat waves impacted Lille. The air conditioning system installed at ATOLL was not strong enough to maintain the recommended operating temperature (22 °C). The CE376 lidar, METIS, measured internal temperatures up to 40 °C during July, August and September 2022.

To evaluate the effect of the extreme temperatures during the summer of 2022 on the METIS lidar, the RCS needs to be corrected by the overlap function. The overlap functions were determined using the experimental methods described in Sect. 3.4.4. Both methods, molecular approximation and linear regression, are applied to data sets taken on at least 3 different days for each detection channel and if possible, at different temperatures (Fig. 3.14). Particularly, Lille is constantly influenced by transported aerosols and local pollution, so finding the adequate conditions to estimate the overlap function is not an easy task. Therefore, for the final overlap function at each channel (Fig. 3.14 panels (a) 532par, (b) 532per and (c) 808tot), is convenient to take the median of the overlap estimations rather than the average. If an aerosol layer (a peak on the signal) is observed, it is filtered by a low pass filter to not add artifacts to the final overlap function. On the same note, previous works suggested to fit the overlap function with a Gompertz function to obtain a mathematical expression (Guerrero-Rascado et al., 2010). Nonetheless, applying such fitting to the final overlap function can introduce greater errors, like it is presented on Fig. 3.14, with the residuals from the Gompertz fit for the three channels. Therefore, the final overlap function for each channel corresponds to the median of experimental overlap functions.

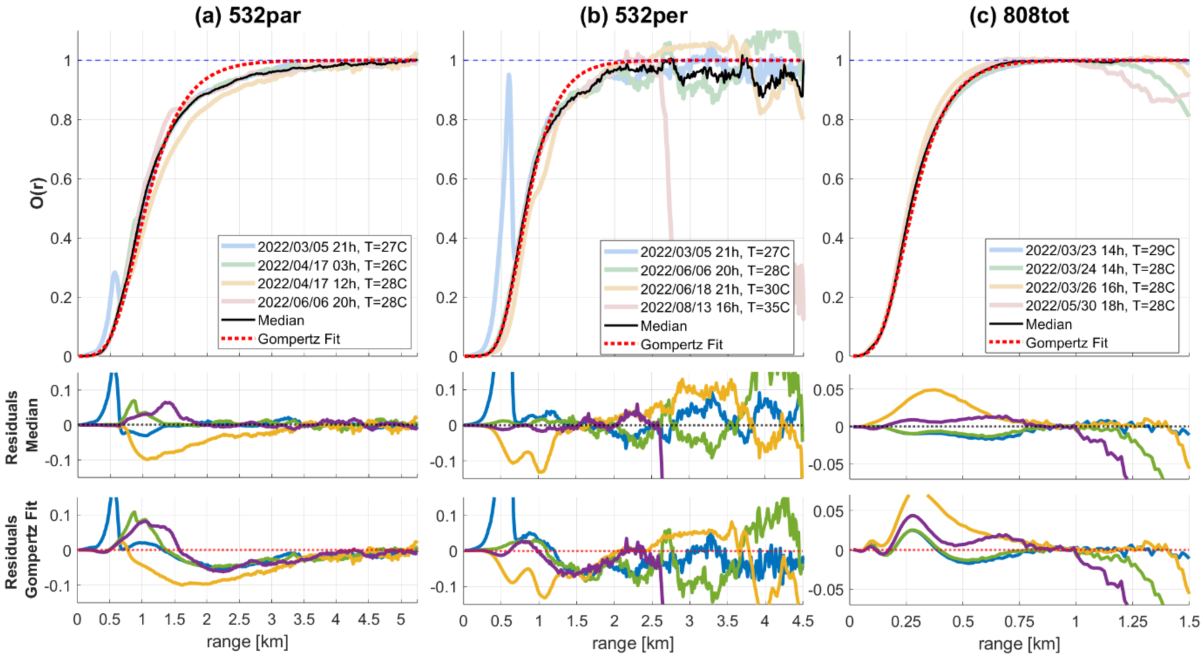

Figure 3.14: Overlap functions estimation for the CE376 lidar METIS installed at ATOLL. Overlaps for (a) 532 nm parallel, (b) 532 nm perpendicular and (c) 808 nm channels. The residuals of each estimation with respect to the median and to the Gompertz fit are also presented for all the channels.

The O(r) at 532 nm parallel channel arrives to 0.98 at $r = 3.8\ km$ with less than 1% of standard deviation, as well errors below 7% are observed for $r > 0.6\ km\ (with\ O(r) > 0.1)$ and higher than 50% for $r < 0.3\ km\ (with\ O(r) < 0.02)$. The O(r) at the 532 nm perpendicular channel arrives to 0.98 at $r = 2.8\ km$ with 2 % of error, and errors below 18% for $r > 0.6\ km$ (with $O(r) > 0.2$) and higher than 30% for $r < 0.48\ km\ (with\ O(r) < 0.05)$ are observed. The O(r) at 808 nm channel arrives to 0.98 at $r = 0.8\ km$ with less than 1 % of error, and errors below 13% for $r > 0.2\ km$ (with $O(r) > 0.2$) and higher than 20% for $r < 0.1\ km\ (with\ O(r) < 0.05)$ are observed. Defining the instrument blind zone below r_o according to $O(r_o) = 0.1$, we have that r_o at each detection channel of the CE376 METIS lidar is: $r_o(532par) = 0.6\ km$, $r_o(532per) = 0.5\ km$ and $r_o(808tot) = 0.15\ km$. For further analysis, measurements in the defined blind zone are not considered.

Temperature vs. Overlap function

The RCS profiles from METIS corrected by the obtained overlap functions were evaluated, particularly from June to September 2022, in order to detect possible temperature effects on the system. When the shape of the overlap function is affected by temperature, artifacts appear on the RCS profiles, leading to erroneous interpretations of the atmospheric conditions. Thus, the gradient of the RCS is used to reveal discontinuities in the region of O(r)<1.

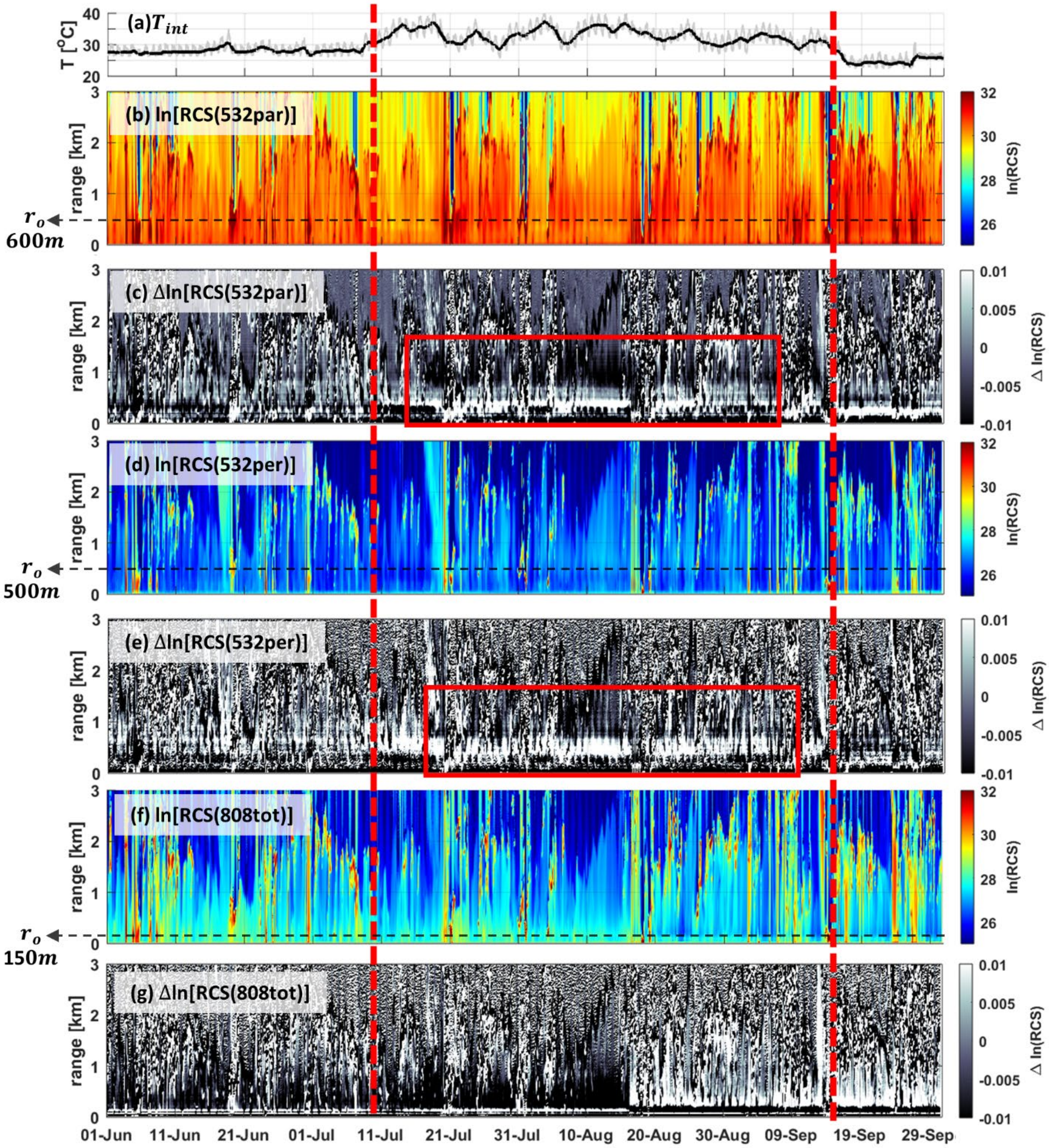

Figure 3.15: Monitoring of temperature effects on METIS RCS profiles during summer 2022. From top to bottom: (a) internal temperature in °C, (b) ln(RCS) profiles from channel 532par, (c) gradient of the profiles in (b), (d) ln(RCS) profiles from channel 532per, (e) gradient of the profiles in (d), (f) ln(RCS) profiles from the channel 808tot and (g) gradient of the profiles in (f).

Figure 3.15 presents the temporal variabilities of ln(RCS) profiles (for the channels 532par in Fig. 3.15b, 532per in Fig. 3.15d and 808tot in Fig. 3.15f) and their gradient $\Delta\ln(RCS)$ at all detection channels (532par in Fig. 3.15c, 532per in Fig. 3.15e and 808tot in Fig. 3.15g) for

CE376 METIS lidar. The blind zone delimited by r_o is indicated by the black dashed arrow on the ln(RCS). The temporal variability of the internal temperature is presented as well (Fig. 3.15a). The period highlighted by the red dashed lines corresponds to the time when the temperatures overpassed 30 °C, reaching 35 °C on daily averages. During this period of time with persisting high temperatures, the overlap functions for the 532 nm channels no longer correct properly the lower ranges, generating artifacts (horizontal stripes on the gradient profiles). The region most affected is in the first 1 km, close to the blind zone and where $O(r) < 0.5$ for both channels at 532 nm. These artifacts will mostly impact the detection of the atmospheric boundary layer which is frequently associated to maximum values on the RCS gradient. Therefore, for this time period, it is more appropriate to use a higher r_o. The modified r_o and the error introduced to the profile can be estimated by determining a new overlap function.

In contrast, the overlap function for the 808 nm channel proved to be stable even during the high temperature period. Nevertheless, a change on the ln(RCS) profiles is observed after more than one month of high temperatures, which is not explicitly impacting the overlap function. As mentioned before (in Sect. 3.4.4), the main difference between the channels for the 2 wavelengths lies in the optical design. For 532 nm, two additional opto-mechanical elements (dichroic mirrors) are placed on the optical emission path, in contrast to the optical fiber for the 808 nm. These differences not only influence the range where the complete overlap is achieved but also the stability of the optical alignment, as seen in this section.

Temperature vs. Lidar Constant

Another parameter that can be evaluated to detect possible impacts of the temperature on the lidar system is the Lidar Constant obtained from calibration (described in Sect. 3.4.2). For METIS, the lidar constant calibration was applied on various days of 2022 for total signals at both CE376 wavelengths (Fig. 3.16). In particular, the calibration for 808 nm is constrained to nighttime data, when lunar photometer measurements are available, to avoid introducing noise.

The temporal variation of C_L at both wavelengths show a change on the trends during summer. The changes at 808 nm are observed since June, which can also be related to other factors, such as reduced availability of nighttime hours and the presence of multiple aerosol layers (affecting the selection of a reference zone) during events with $AOD_{ph}(808)$ higher than usual (Fig. 3.13 in Sect. 3.5.1). Nevertheless, the standard deviations (grey horizontal lines in Fig. 3.16) attached to the average of all the calibrations (dashed horizontal lines in Fig. 3.16) represent less than 20 % of error. Thus, the lidar constant is on average $C_L(532) = (7.201 \pm 1.128) * E^{+18}\ Phs^{-1}m^3sr$ (16 % of error) and $C_L(808) = (6.740 \pm 1.207) * E^{+17}Phs^{-1}m^3sr$ (18 % of error).

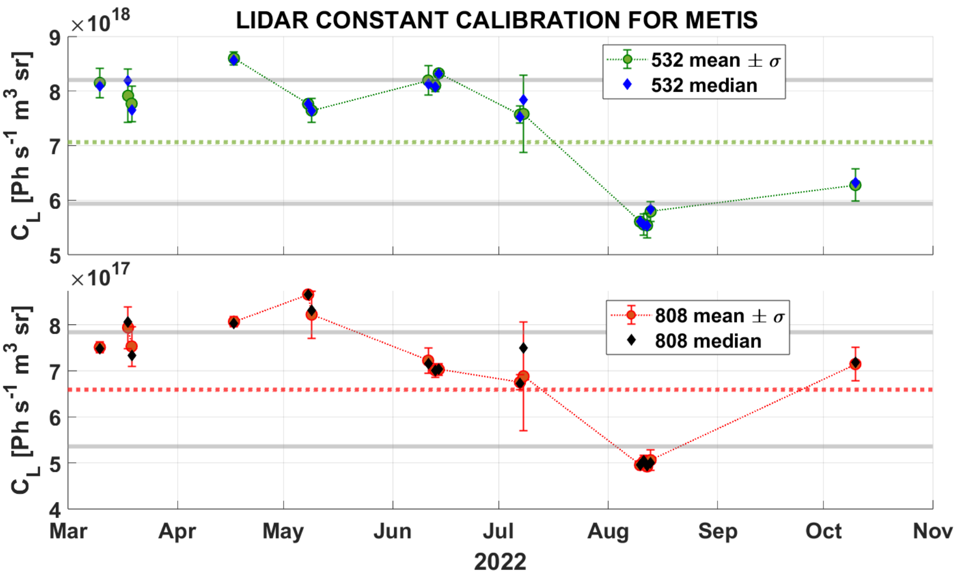

Figure 3.16: Lidar constant calibration during 2022 for the CE376 lidar, METIS, at ATOLL.

3.5.3 Depolarization measurements improvements

The CE376 lidar METIS has been performing continuous observations since 2019 at the ATOLL platform. The continuity of measurements is ensured by setting the lidar in a temperature-controlled room and using a high transmission glass on the roof for zenithal laser shooting. Since the installation of METIS at ATOLL, several studies and instrumental assessments have taken place to improve the depolarization measurements. Comparisons of METIS and LILAS Raman lidar, the reference lidar at ATOLL, showed an important bias (greater than 20 %) in the VLDR values between the instruments. Therefore, several tests were performed to improve METIS observations and identify the sources of the depolarization bias. The first set of tests, conducted within the AGORA lab framework by the LOA-CIMEL team, checked for misalignments, internal light reflections and damage to METIS optical parts. Additionally, tests with METIS under different measurement conditions (with and without the window) were carried out. Comparisons of METIS and LILAS under the same operating conditions, with air conditioning and no windows, showed better agreement on the VLDR with a relative bias of 10%, revealing that the main source of the depolarization bias was the high transmission window glass on the roof used for METIS continuous observations. The roof glass window was tempered, had an anti-reflective coating and suffered deformations due to its size and weight, creating significant biases in the depolarization measurements.

Currently, a frame designed to contain four windows is used, avoiding deformations due to the glass weight. The glass material was changed to extra-clear glass, and the windows are set up on the frame using silicone to avoid adding stress to the glass. Now, the depolarization bias between LILAS and METIS has been reduced to 12% under METIS's normal operating conditions. This bias might result from differences on the instrument designs, such as the FWHM (Full Width at Half Maximum) bandwidth of interference filters and the optical path configuration, as well as the influence on depolarization of every optics, whose depolarization must be characterized separately. Also, to rotate the depolarization plane of the incident light to PBS, METIS uses a manual rotating mount for the HWP with 2 degree precision, while LILAS uses a motorized polarizer for the calibration, with an obvious higher precision. More details and discussion on the comparisons between LILAS and METIS are presented in Chapter 5 Sect. 5.3.2 and Sect. 5.4.2.

Moreover, in pursuit of system improvements, wire-grid polarizers have been included behind the CE376 lidar PBS branches since February 2022 to reduce tcross-talk between the parallel and perpendicular channels. For current versions of the CE376 lidar being manufactured, an improved optical fiber design, motorized HWP mount, and more precise polarization measurements are integrated.

3.6 Chapter Summary

This chapter provides an overview of ground-based remote sensing techniques, such as lidar and photometer, widely used for aerosol observations. The dedicated networks for both measurement techniques were described, highlighting the challenges in bridging observational gaps within the networks. Thus, the CE376 dual wavelength lidar and CE318-T sun/sky/lunar photometer, both proposed for mobile aerosol monitoring, were presented in detail. The instruments used in previous mobile campaigns, the CE370 single wavelength lidar and PLASMA sun photometer, were also presented.

This chapter, focuses on the CE376 lidar data processing and performance. Therefore, the data quality control and calibration methods used for the CE376 lidar system are described, addressing procedures for Rayleigh fit, lidar constant calibration, depolarization calibration, and the determination of the overlap function. Along with the description of methods used on CE376 lidar data, examples of the procedures were also included. In particular, it has been highlighted that the altitude at which the overlap function equals 1 (i.e., signal is completely in the detection FOV) for the 532 nm channels is higher than expected, leading to extended blind zones.

Moreover, by using continuous observations from March 2022 to January 2023 the detection limits and temperature effects on the CE376 were revealed. The signals on the reception channels, 808 nm and perpendicular component at 532 nm, were the most affected by daylight (i.e., inducing noise in the background signal). Thus, an important reduction in the detection limit altitude (where SNR>1.5) is observed during daytime, going from 13 km (night time) to below 3 km (daytime) on the channel 532per and from 10 km (night time) to below 2 km (daytime) on the 808 nm channel. The detection limits do not appear to be directly influenced by changes in temperature and relative humidity.

However, temperature changes directly influence the opto-mechanical stability of the system. High temperatures can induce changes on the incomplete overlap region, especially below 1 km for the 532 nm channels, and affect the lidar constant at both wavelengths. Therefore, especial attention is needed for further aerosol studies. Moreover, this chapter presents the improvements in the operational conditions for continuous aerosol monitoring at ATOLL, specifically to enhance the depolarization measurements.

It is worth mentioning that all the instruments evaluated in this thesis are the first manufactured CE376 lidar systems. Each system later used for data analysis in Chapter 5 and Chapter 6 presents differences in the overlap functions, and thus the uncertainties associated with the overlap functions might vary between systems. Moreover, the assessments presented here were addressed by the R&D and technical departments of CIMEL company. The new versions of the instrument take into account the technical barriers observed in this thesis, such as extended overlap functions, temperature effects and depolarization improvements. Thus, enhanced capabilities of the CE376 lidar can be expected in future studies.

The next chapter is dedicated to the algorithmic developments for estimations on aerosol properties.

Chapter 4

Lidar-photometer integrated system

"Like what you do, and then you will do your best."
-Katherine Johnson-

Elastic backscatter lidars, such as the CE376 lidar, are valuable and commonly used tools for atmospheric aerosol observations. However, one crucial limitation in retrieving optical properties from these lidar systems is related to the underdetermination of the elastic lidar equation. The underdetermination results from the dependence of the backscattered light on both backscatter and extinction coefficients. Thus, to solve the equation and retrieve the aerosol optical properties, it is necessary to define the LR, i.e., extinction to backscatter ratio (Fernald, 1984; Klett, 1981, 1985). The absence of prior knowledge of the LR values, in practice, leads to the use of a vertically constant value, named effective LR. Moreover, the uncertainty linked to the selection of an adequate effective LR can be reduced by constraining the solution using direct sun/moon photometer measurements (Mortier, 2013) and in-situ observations (Popovici, 2018).

Other types of lidars, such as elastic-Raman or HSRL lidars, are capable of providing independent backscatter and extinction coefficients. Nevertheless, they can also be limited. For example, during the day-time, Raman signals are masked by the solar background noise. In consequence, even high-power, complex lidars (Raman lidars) rely on retrieval methods used for purely elastic scattering lidar measurements, such as the Klett method.

In this chapter, the lidar-photometer integrated system is described as the algorithmic integration of lidar-photometer synergistic measurements to retrieve vertically resolved optical properties rather than from an instrumental point of view. In the context of this work, which envisions near real time (NRT) retrievals, both the selection of an adequate inversion scheme and its automatization are considered. Moreover, this chapter also presents the requirements to retrieve optical properties while system is in motion.

4.1 Aerosol lidar retrieval methods

In order to retrieve backscatter and extinction coefficients from the lidar equation, different approaches have been proposed over the years. For single elastic backscatter signals, the most common and reliable method is the Klett solution, which will be described in this section. Lidar inversion schemes using forward iterative processes have been proposed in recent years and are also described. Moreover, multiple studies performed on simultaneous two-wavelength lidar measurements have shown the added capabilities to retrieve aerosol properties with at least two wavelengths.

4.1.1 Klett solution

The fundamental analytical solution of the lidar equation was proposed and evolved during the period of 1970-1990 (Fernald, 1984; Fernald et al., 1972; Klett, 1981, 1985; Sasano et al., 1985). The lidar inversion scheme was named the Klett-Fernald-Sasano solution, after their publications. However, due to the originality proposed by Klett (1981, 1985), the inversion method is most commonly named Klett's solution. Nowadays, the Klett's inversion scheme is still used due to its demonstrated mathematical stability. Nevertheless, a sign error in Klett's publications, later rectified, is still present in current publications (Speidel & Vogelmann, 2023). Therefore, it is worth to mention, that this work takes into account the corrected Klett solution (Kovalev & Eichinger, 2004; Weitkamp, 2005).

To further advance towards the lidar equation solution, the definition of both molecular and aerosol LR is needed. In contrast to the variable aerosol LR, the LR for molecules, following the Rayleigh theory, is assumed constant for all wavelengths and is given as $8\pi/3$ sr. Therefore, hereafter the term of LR only refers to the aerosol extinction-to-backscatter ratio. By solving the Bernoulli differential equation (lidar equation, Eq. (3.10)) and assuming a vertically constant LR, we retrieve $\beta_a(\lambda, r)$ as in Eq. (4.1).

$$\beta_a(\lambda,r) = \frac{RCS(\lambda,r)\exp\left[-2\left(LR(\lambda)-\frac{8\pi}{3}\right)\int_{r_b}^{r}\beta_m(\lambda,r')dr'\right]}{\frac{RCS(\lambda,r_b)}{\beta_a(\lambda,r_b)+\beta_m(\lambda,r_b)}-2\,LR(\lambda)\int_{r_b}^{r}RCS(\lambda,r')\exp\left[-2\left(LR(\lambda)-\frac{8\pi}{3}\right)\int_{r_b}^{r'}\beta_m(\lambda,r'')dr''\right]dr'} - \beta_m(\lambda,r) \tag{4.1}$$

The molecular coefficients $\beta_m(\lambda,r)$ and $\alpha_m(\lambda,r)$ are modeled from temperature and pressure profiles, either from radiosonde data available or standard atmosphere. For mobile measurements, the surface altitude (asl) for each RCS profile is considered to model the molecular profiles correctly. The boundary conditions $RCS(\lambda,r_b)$ and total backscatter $\beta_a(\lambda,r_b)+\beta_m(\lambda,r_b)$, are given by the position of r_b, and therefore two forms of the Klett solution are specified. Both forms of the solution are considered in this work and described below.

Klett Backward Integration

The solution placing the position r_b at a far-end ($r_b = r_{ref}$ and $r_b > r$) considers a backward integration, and it is well known as the backward (BW) solution. The same considerations of Rayleigh fit (Chapter 3 Sect. 3.4.1) are considered, i.e., a region free of aerosols so $\beta_a(\lambda,r_{ref}) = 0$. The BW is the most used form of the Klett solution because it doesn't need calibrated values (β_{att}). Nevertheless, it has an obvious difficulty when defining r_{ref}.

The BASIC algorithm, developed by Mortier (2013), is a NRT software developed in Scilab, used for automatic lidar and photometer data processing of LOA lidar database and at ICARE AERIS Data Center for several lidars in ACTRIS-France. BASIC uses the Klett BW solution for single wavelength measurements and limits the solution with the AOD from photometer. By iterating the solution, i.e., by varying the LR, the AOD derived from the extinction profile ($AOD = \int_0^{r_{ref}}\alpha_a(\lambda,r')dr'$) is compared to the AOD_{ph} (measured by photometer) until they match. Therefore, the inputs of the algorithm are the RCS and AOD from photometer. Moreover, BASIC applies signal smoothing, filtering and provides the altitude of clouds, aerosol layers and ABL. In particular, the detection of the ABL top altitude is useful for both air quality and aerosol studies. The algorithm has shown to be a useful tool and demonstrated the importance of monitoring aerosol properties in NRT.

The CE376 lidar, which accounts two wavelengths, is also included in the data processing line of BASIC. Nevertheless, the retrievals are limited for the 808 nm measurements, especially during the daytime when the detection limit is low and therefore affects the search for a reference zone (r_{ref}). Hence, other solutions were explored in this work to obtain the most information from the 808 nm measurements. The FW form of the Klett solution, iterative forward methods and two-wavelength approach were considered.

Klett Forward Integration

The near-end solution with forward integration or forward (FW) solution is given by $r_b = r_o$ ($r_b < r$), where r_o is close to the ground. Thus, the boundary condition of total backscatter is defined as Eq. 4.2, assuming that aerosol transmittance close to the ground is roughly 1.

$$\beta_a(\lambda, r_o) + \beta_m(\lambda, r_o) = \frac{\beta_{att}(\lambda, r_o)}{T_m^2(\lambda, r_o) T_a^2(\lambda, r_o)} \quad with \; T_a^2(\lambda, r_o) = 1 \tag{4.2}$$

Due to the incomplete overlap and the lidar's instability (i.e., lidar constant instability), especially for high power and complex systems, the FW solution is usually not considered. However, it can be applied on measurements from ceilometer-type systems like the 808 nm channel of CE376, which has available measurements closer to the ground and stable configuration. Similarly, to the BW Klett's solution, an iterative process can be applied to constrain the solution by the AOD measured by the photometer.

In-situ instruments (such as nephelometer and aethalometer) providing aerosol optical properties such as scattering and absorption coefficients, coupled to particle sizers, can also be considered to define the boundary conditions for the FW Klett's solution. In particular, the limitations and advantages of using in-situ measurements were extensively discussed and presented by Popovici (2018). The methods were tested and are included in BASIC algorithm. In this work, with the focus on CE376 lidar measurements, the consideration of in-situ observations is not included.

4.1.2 Forward methods

In recent years, algorithms using forward methods were suggested to simplify the retrieval of aerosol optical coefficients, especially for aerosol typing (Baars et al., 2017; Wang et al., 2020) as mentioned in Chapter 3 Sect. 3.3.3. The method proposed by Baars et al. (2017), presenting quasi-aerosol properties, aims only to achieve aerosol typing. Moreover, for ceilometer measurements, a forward iterative method was proposed by Li et al. (2021) showing promising results when the ceilometer is coupled to the photometer. Both approaches are briefly described below:

(a) *Quasi-aerosol approach (Baars et al., 2017; Wang et al., 2020):* This approach consists in two iterations, considering a first approximation of the aerosol backscatter as Eq. 4.3, where the total attenuated backscatter β_{att} is corrected by the molecular transmittance and the aerosol transmittance equals to 1. Then, by applying a LR vertically constant, the quasi-extinction coefficients are retrieved (Eq. 4.4). The second iteration of aerosol backscatter, named as quasi-backscatter (Eq. 4.5), considers the β_{att} corrected by both molecular and quasi-extinction transmittances.

$$\beta_a^{quasi*}(\lambda,r) = \beta_{att}(\lambda,r)\, e^{2\int_0^r \alpha_m(\lambda,r)dr} - \beta_m(\lambda,r) \tag{4.3}$$

$$\alpha_a^{quasi}(\lambda,r) = \beta_a^{quasi*}(\lambda,r)\cdot LR(\lambda) \tag{4.4}$$

$$\beta_a^{quasi}(\lambda,r) = \beta_{att}(\lambda,r)\, e^{2\int_0^r [\alpha_m(\lambda,r)+\alpha_a^{quasi}(\lambda,r)]dr} - \beta_m(\lambda,r) \;\approx \beta_a(\lambda,r) \tag{4.5}$$

(b) Forward iterative (Li et al., 2021): This approach consists in two levels of iterations. The first level, considering a vertically constant LR, initializes the iteration similarly than the quasi-aerosol approach with Eq. 4.3, but only considering it for the first point (at r_o), three parameters are then re-calculated, the first point of extinction as in Eq. (4.4), of backscatter as in Eq. (4.5) and the AOD_{lid} like Eq. (4.6) to retrieve the aerosol transmittance. Later for every point r_i, k iterations are initiated with $\alpha_a^{k=0}(\lambda,r_i)$=0 by using Eq. (4.7) and recalculating the extinction and backscatter. The iteration is terminated when $[\alpha_a^k(\lambda,r_i) - \alpha_a^{k-1}(\lambda,r_i)]/\alpha_a^k(\lambda,r_i) < 0.01$ or when $k \geq 30$.

$$AOD_{lid}(\lambda,r_o) = \alpha_a^{quasi}(\lambda,r_o)\cdot dr \tag{4.6}$$

$$AOD_{lid}^k(\lambda,r_i) = AOD_{lid}(\lambda,r_{i-1}) + \alpha_a^{k-1}(\lambda,r_i)\cdot dr \tag{4.7}$$

The second level of iterations consists in varying the LR to constrain the solution by the AOD from photometer.

Both methods consider calibrated lidar measurements (β_{att}) and their validity depends on the aerosol transmittance term modeled. The quasi-aerosol approach is particularly used to derive a profile of quasi-EAE (Extinction Angstrom Exponent) and CR (Color Ratio) from measurements of a pair of wavelengths and quasi-PLDR (Particle Linear Depolarization Ratio). In this way, it facilitates the distinction between fine and coarse aerosols contributions, and between spherical and non-spherical aerosols. On the other hand, the forward iterative method is used to retrieve aerosol optical properties, showcasing the capabilities of a low power lidar (ceilometer type). These two forward approaches were explored in order to find the adequate retrieval method to derive information from the 808 nm measurements especially during day-time.

4.1.3 Two-wavelength approach

Multiple studies on simultaneous two-wavelength lidar measurements have proposed inversion schemes to retrieve backscatter and extinction profiles. Methods proposed by Potter (1987), Sasano and Browell (1989), Ackermann (1997, 1998, 1999) were based on the analytical development of two elastic lidar equations, one for each wavelength. These methods involve four unknown variables and two equations, showing that the underdetermination does not disappear and therefore some assumptions are made (Kunz, 1999; Gimmestad, 2001; Kovalev & Eichinger, 2004). These approaches established linear relationship between extinction coefficients from the two wavelengths requiring that the LR at both wavelengths are known a priori (Ackermann, 1997, 1998, 1999; Potter, 1987). Sasano & Browell (1989), on the other hand, imposed the boundary conditions to be at the far end so that only molecular contributions were found at both wavelengths, enabling the retrieval of the lidar ratios. In the context of this work, the lidar ratios are unknown, and for daytime 808 nm measurements to assume a molecular region will be not possible. Therefore, these methods proposed are complicated to apply to the CE376 lidar. Nevertheless, it is worth noting that these approaches are more reliable for lidar systems with Raman-elastic channels at one wavelength, i.e., independent aerosol coefficients, and only an elastic channel at a second wavelength.

On the other hand, the approach presented by Vaughan (2004) introduced the term of CR for CALIOP (Cloud-Aerosol Lidar with Orthogonal Polarization, part of CALIPSO satellite mission) elastic lidar measurements at 532 and 1064 nm, considering a two-component atmosphere (molecules and aerosols). The proposed scheme attempted to obtain spectral information on the aerosols contained within a layer by defining the Total Attenuated Color Ratio (χ') for layer-integrated attenuated backscatter coefficients (Chapter 3 Sect. 3.3.3). The goal of CALIPSO algorithms was to base aerosol typing on the available lidar observations, depolarization and two-wavelength backscatter, minimizing the use of a priori assumptions. The challenges faced by this approach were presented in several publications while CALIPSO algorithms evolved (Kim et al., 2018; Omar et al., 2009; Tackett et al., 2023; M. Vaughan, 2004; D. Winker et al., 2006; D. M. Winker et al., 2009).

The biggest challenge in using χ' is its dependence on the aerosol transmittance term at each wavelength. Because it involves the integration of the extinction, the attenuation due to layers above and the layer concerned (nadir observations) limits the correct aerosol identification. Thus, to extract the aerosol backscatter of either wavelength, it is necessary to correct the data for the attenuation of molecules and aerosols. This, in turn, requires the selection of an adequate LR. To solve this dilemma, the aerosol typing decision tree includes the layer-integrated attenuated backscatter, the altitude of the aerosol layer, estimated depolarization, and geographical location. After the aerosol type is identified, the layer LR is imposed from look up tables, except for elevated layers with clean air below, where the transmittance method can be used (Young, 1995). Moreover, in the stratosphere and upper troposphere within molecular conditions, χ', coupled with depolarization, has shown the ability to distinguish aerosol types (Fig. 4.1), such as ash (coarse and depolarizing aerosol), sulfates (fine and no depolarizing aerosol) and smoke (fine and low depolarizing aerosol). Therefore, it is employed in the subtyping processing of stratospheric aerosols (Omar et al., 2009; Kim et al., 2018).

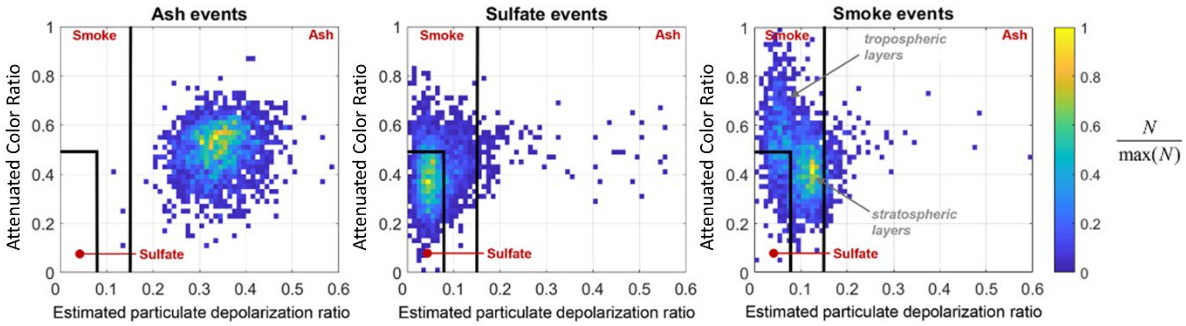

Figure 4.1: Joint distributions used in CALIPSO V4.2 development, estimated particulate depolarization ratio and feature-integrated attenuated backscatter color ratio (χ ′) for manually classified layers during events dominated by the aerosol type indicated in the title. Histograms of layer numbers (N) are min–max normalized. Black lines indicate discrimination thresholds in V4.2, and red text indicates the algorithm classification. Source: *Fig. 4 of Tackett et al., 2023*.

Throughout the years of the CALIPSO mission, its products related to aerosol typing and characterization have provided valuable information to the scientific community. Likewise, by evaluating its retrievals through comparisons with airborne and ground-based lidars, the algorithms evolved, improving the approximations involved in aerosol classification (Ansmann et al., 2021; Burton et al., 2013; Tackett et al., 2023). In this work, the ideas and the evolution of the CALIPSO algorithms are taken into account. Therefore, the ACR defined in Chapter 3 Sect. 3.3.3 is considered an atmospheric property directly derived from measurements. For the moment, any approximation of the attenuation by layer is considered. Nevertheless, the ACR is calculated and evaluated during different case studies (Chapter 5, Chapter 6). This, in perspective, will permit the exploration of the property behavior for future applications like aerosol typing.

4.1.4 Inversion Methods evaluation

The two-wavelength approach has proven to be complex for use in elastic two-wavelength lidar observations. Thus, users of lidar systems like CALIOP had to develop new ideas to gain aerosol spectral information from their elastic dual-wavelength measurements. In this context, the advantage of coupling the CE376 lidar with photometer measurements lies in the fact that it can *constrain the inversion at each wavelength individually*. Therefore, the retrieval methods described before (Sect. 4.1.1 and Sect. 4.1.2) were evaluated to improve the aerosol optical properties, in particular for 808 nm daytime observations. Moreover, at this point, it is worth recalling that the effective LR is retrieved (i.e., vertically constant).

To apply the FW Klett's solution and forward methods, the key is the correct determination of the lidar constant (Chapter 3 Sect. 3.4.2), contrary to the BW Klett's solution which does not need it. As an example of the methods evaluation done within this work, Figures 4.2 and 4.3 show the use of the different procedures at both wavelengths in two scenarios (night and day) during 23 March 2022. The profiles at both wavelengths were averaged to one hour to reduce noise effects, between 02:00 to 03:00 UT (at night, Fig. 4.2) and between 07:00 to 08:00 UT (during the day, Fig. 4.3), while the atmospheric conditions were quite stable. Values below 600 m were assumed constant due to the higher uncertainty in the overlap. Direct moon and sun photometer measurements were used to constrain the BW Klett solution, which is considered here as reference for the other methods. Therefore, the effective lidar ratios retrieved from the BW Klett are used to run the other methods and compare them. By daytime, when the 808 nm is impacted by noise, the same lidar ratio retrieved at nighttime time is considered as an approximation. Moreover, a change of ±15% in the lidar constant is applied to see the effects on the retrievals. The EAE derived from extinction profiles is also presented. In particular for the EAE, the extinction at 532 nm is the one derived from BW Klett's solution and the extinction at 808 nm is retrieved from the different methods.

Comparing the methods, one can recognize that the FW Klett's solution (in yellow) and the Iterative forward method (in red) give the same results, even though they consist in two very different approaches. In contrast, the quasi-aerosol approach always underestimates the aerosol content, leading to overestimation of the EAE, which can be expected due to the rough approximations involved.

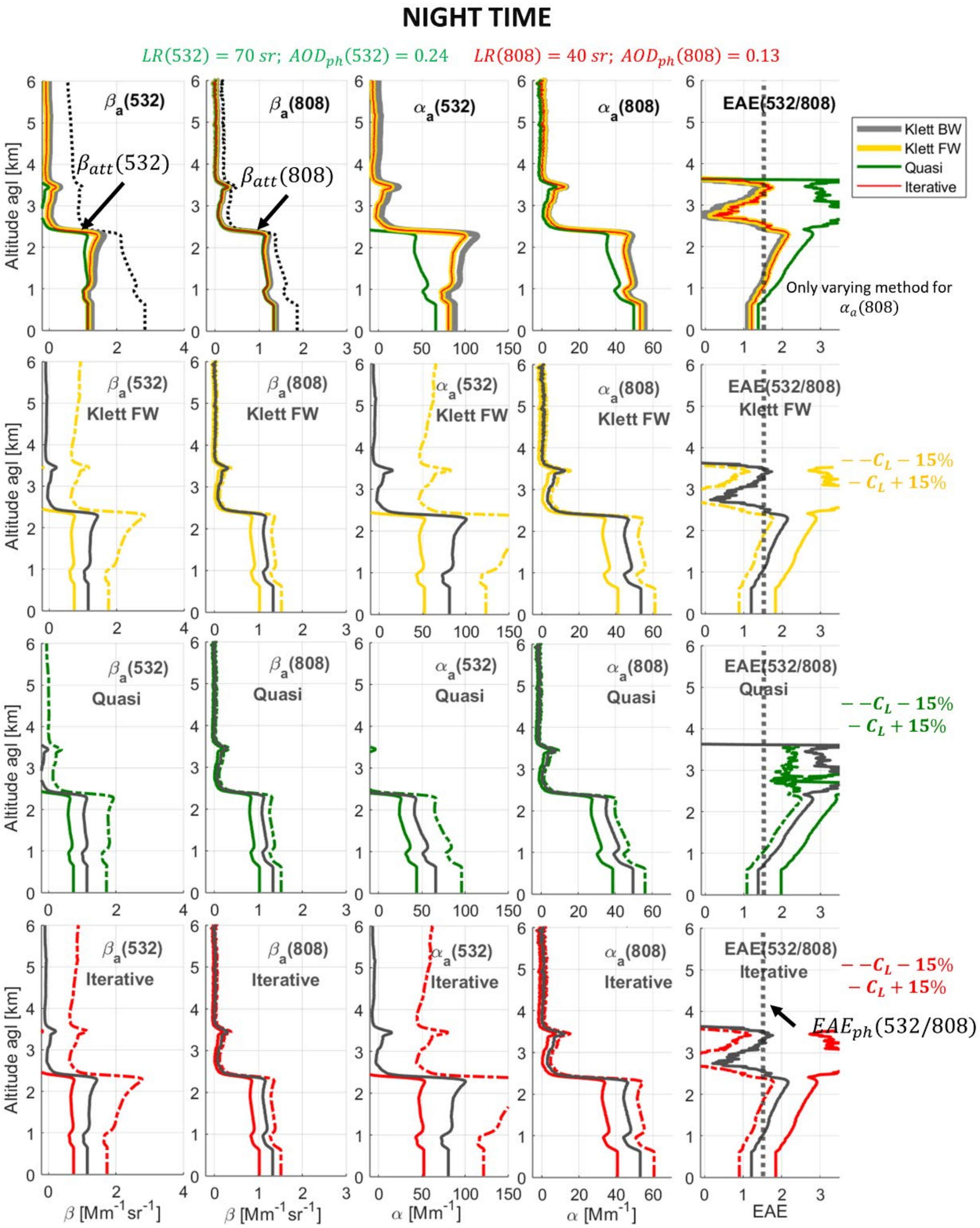

Figure 4.2: Aerosol retrieval methods evaluation for night time measurements between 02:00 to 03:00 UT on 23 March 2022 at ATOLL. Top panel shows the aerosol optical properties retrieved with the right lidar constant using different methods (including BW Klett), and the following three panels present the retrieved properties considering the lidar constant with a 15 % variation. The methods considered are FW (in yellow, second panel) Klett's solution, Quasi-aerosol approach (in green, third panel) and Iterative Forward method (in red, fourth panel). From left to right the properties are: aerosol backscatter at 532 nm and 808 nm, aerosol extinction at 532 nm and 808 nm and the extinction Angstrom exponent. In particular for the derived EAE, the extinction at 532 nm is obtained with the BW Klett's solution and extinction at 808 nm retrieved from the different methods.

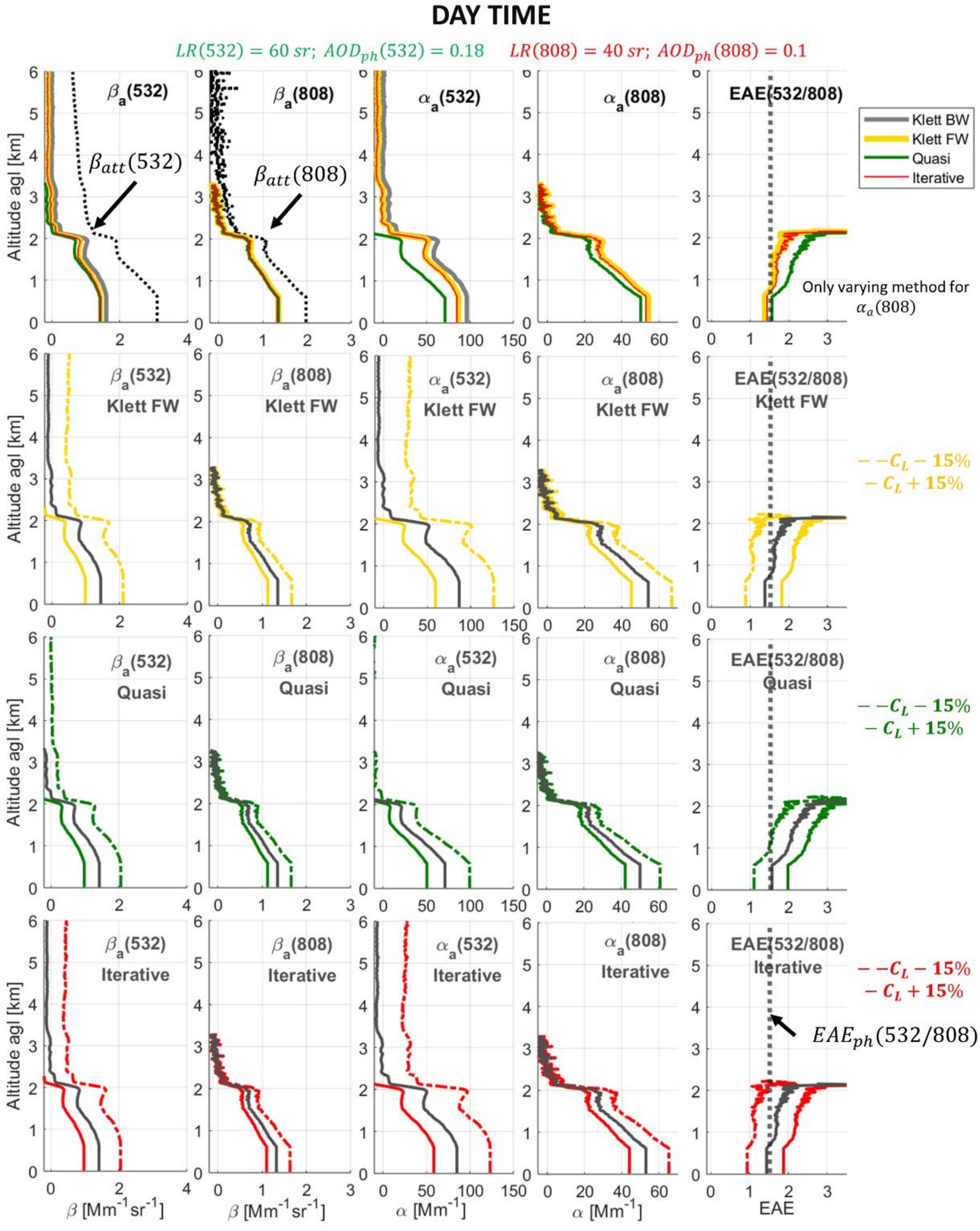

Figure 4.3: Aerosol retrieval methods evaluation for day time measurements between 07:00 to 08:00 UT on 23 March 2022 at ATOLL. Same as Fig. 4.2. Top panel shows the aerosol optical properties retrieved with the right lidar constant using different methods (including BW Klett), and the following three panels present the retrieved properties considering the lidar constant with a 15 % variation for the different methods (FW Klett's solution, Quasi-aerosol approach and Iterative method).

During nighttime (Fig. 4.2), the retrievals from FW Klett and Iterative methods, using the correct lidar constant (first panel on top), are similar to the properties retrieved by BW Klett. Nevertheless, by varying 15 % around the correct lidar constant, the retrievals at 532 nm (second to fourth panels) are highly impacted (up to 200 % difference in comparison to the BW

Klett), which is related to the scattering efficiency. The detection at 532 nm is more sensitive to molecular contributions than at 808 nm (see the β_{att}, first panel Fig. 4.2 and 4.3). Therefore, the β_{att} calibrated with an incorrect lidar constant might induce a significant bias on the boundary conditions for measurements at 532 nm, affecting the retrievals. In contrast, at 808 nm, the impact on the retrievals, considering a 15 % variation in the lidar constant, deviates from the BW Klett by differences below 30 % during nighttime.

During daytime (Fig. 4.3), it is not possible to compare the methods against the BW Klett for 808 measurements. However, the comparisons of EAE retrieved from the lidar and the one retrieved from the photometer (EAE_{ph}), show that the retrievals are coherent with the column integrated observations.

Though the Iterative method has shown to be efficient in retrieving the aerosol properties, it will not be included for case studies analysis in this work, which targets a future NRT application. This decision is based on the computational time that the method uses for the iterative process at each altitude, considering that two sets of iterations are needed to constrain the solution. Nevertheless, the iterative approach can be explored for future applications, like aerosol characterization using integrated layers, including estimations of LR at each layer.

The evaluation of the different methods permitted the development of an algorithm during this thesis work to retrieve the aerosol properties of simultaneous 2-wavelength elastic lidar measurements. This algorithm takes into account the detection limits at both wavelengths and is described in the following section.

4.2 Prototype algorithm for mobile measurements

During night-time measurements, the detection limits (using SNR=1.5 on 30 minutes averaged profiles) for all CE376 channels can exceed 10 km, making it possible to usually find an aerosol-free zone (r_{ref}) for both 532 nm and 808 nm wavelengths (Chapter 3 Sect. 3.5.1). Therefore, the BW Klett's solution can be applied for both wavelengths. Nevertheless, during daytime, strong solar background light limits the detection to ~10 km and below 4 km for 532 nm and 808 nm, respectively. Thus, the BW Klett's solution can still be applied for 532 nm but not for 808 nm. Therefore, as discussed in the previous section, the FW Klett's solution is considered suitable for RCS profiles at 808 nm during daytime. Considering all these factors, a modified two-wavelength inversion scheme is proposed below.

4.2.1 Modified two-wavelength Klett inversion

The steps of the inversion scheme proposed in this work and the calculation of derived properties are described as follow:

a) **BW Klett solution**: Applied to RCS total signals and constrained by AOD_{ph} at both wavelengths 532 nm and 808 nm. Then LR(λ), $\beta_a(\lambda, r)$ and $\alpha_a(\lambda, r)$ at both wavelengths are retrieved.

b) **FW Klett solution (when $\mathbf{r_{ref}(532) > r_{lim}(808)}$):** Applied to RCS at 808 nm if the r_{ref} determined for 532 nm is higher than the detection limit (r_{lim}) for 808 nm. The solution is constrained by an estimated AOD at 808 nm (AOD_{est}). AOD_{est}, defined in Eq. (4.8), is derived from the lidar retrievals at 532 nm and the interpolated EAE_{ph} for the pair of wavelengths 532 nm and 808 nm.

$$\mathrm{AOD_{est}}(808) = \left[\int_{r_o}^{r_{lim}(808)} \alpha_a(532, r)dr\right] \left(\frac{808}{532}\right)^{-\mathrm{EAE_{ph}}} \tag{4.8}$$

c) **Extinction Angstrom Exponent profile ($\boldsymbol{EAE_{lid}}$):** Derived from $\alpha_a(\lambda, r)$ at 532 nm and 808 nm and defined in Eq. (4.9) for the CE376 measurements. This parameter provides insights into the vertical distribution of aerosols size, where EAE values close to 0 indicate dominant presence of coarse mode aerosols and values higher than 1 are related to higher presence of fine mode aerosols.

$$\mathrm{EAE_{lid}}(r) = -\ln\left(\frac{\alpha_a(532,r)}{\alpha_a(808,r)}\right) / \ln\left(\frac{532}{808}\right) \tag{4.9}$$

d) **Color Ratio (CR):** Defined as the ratio between the aerosol backscatter at 808 nm and 532 nm (Eq. 4.10) and is described in Chapter 3 Sect. 3.3.3 along with the ACR.

$$\mathrm{CR}(r) = \frac{\beta_a(808,r)}{\beta_a(532,r)} \tag{4.10}$$

e) **Particle Linear Depolarization Ratio (PLDR):** Defined by Eq. (4.12), where the molecular depolarization ratio δ^m is the theoretical value according to the filter's bandwidth in front of the half-waveplate in a CE376 system (δ^m~0.004 at 532 nm). R is known as the backscatter ratio (Eq. 4.11) and $\delta^v(r)$ is the VLDR profile derived directly from depolarization measurements (Chapter 3 Sect. 3.3.2). PLDR provides insights into the vertical distribution of aerosol shapes, with low values (close to 0) indicating the predominance presence of spherical aerosols. Values above 0.20 correspond to predominant presence of non-spherical aerosols like dust or ice crystals in cirrus clouds (Freudenthaler et al., 2009; Burton et al., 2015; Floutsi et al., 2023).

$$\mathrm{R} = \frac{\beta_a(\lambda,r)+\beta_m(\lambda,r)}{\beta_m(\lambda,r)} \tag{4.11}$$

$$\delta^{p}(r) = \frac{[1+\delta^{m}]\,\delta^{v}(r)R(\lambda,r) - [1+\delta^{v}(r)]\,\delta^{m}}{[1+\delta^{m}]R(\lambda,r) - [1+\delta^{v}(r)]} \tag{4.12}$$

The data processing and inversion scheme presented in this section are initial steps towards NRT observations integrating CE376 lidar and CE318-T photometer. The implications of NRT mobile aerosol monitoring are discussed in the following section.

4.2.2 What are the considerations for NRT (mobile) aerosol monitoring?

When we think of NRT, we immediately think of automation. One goal of this work is to provide tools that can be easily translated into a NRT processing chain. Therefore, most of the developed algorithms consider the possibility to be automatized. The adaptations and developments accomplished in this work, from pre-processing to aerosol retrievals, are described below.

The lidar acquisition software provided by CIMEL is called LidarII and it provides a graphical interface of the height-resolved signal acquired every 1 minute for all channels. The software displays automatically the observations in real time and saves the raw data in a binary file and in a txt files every 10 min. For the moment, the software is independent and does not produce atmospheric nor aerosol properties. To do so, the software iAAMS (Integrated Automatic Aerosol Monitoring Solution), developed at CIMEL, is accessible to every user of their instruments (lidar and/or photometer). The first version of iAAMS was developed in Matlab environment, and had the purpose to derive the aerosol properties from either of the CIMEL instruments. For the case of the CE376 lidar and CE370 lidar (a previous model), integration with photometer was considered. This thesis, in particular, is under the frame of CIFRE convention (between industry and research), thus part of the algorithms developed in this work were tested, adapted and incorporated in iAAMS software. Moreover, the proposed inversion scheme is also considered in the evolution of iAAMS.

To begin the development of algorithms, both BASIC (developed in Scilab by LOA) and iAAMS (developed in Matlab by CIMEL) were considered and also algorithms developed by Popovici (2018). Functionalities from both softwares were evaluated and unified in a single code, developed in Matlab environment. At this moment the unified code is capable to evaluate a single txt file to 30 days of data from the CE376 and CE370 lidars (single file in less than 30 seconds and 30 days of data in 4-5 hours). Moreover, the code considers the different configurations possible for the CE376 lidar, such as one wavelength with or without polarization, two wavelengths with one or two polarization wavelengths. The organization of the code is modular (i.e., by independent blocks of functions), separated as start parameters, pre-processing, alternative pre-processing, data-processing, aerosol retrievals and two-wavelength inversion retrievals. The features of each module are briefly described below.

a) **Start parameters module** is based on pop-up dialogs, including the selection of the lidar system to be used, then the automatic reading of a txt file with information proper to the system, such as APD coefficients, site location including altitude, identifier of the nearby radiosonde station (up to two stations) from either Météo France or Wyoming data bases. Likewise, the selection and automatic reading of a configuration file is included. The selection of dates, average time can be included on the configuration file or defined afterwards.
b) **Pre-processing module**, corresponds to the reading of lidar data, APD correction, dead time correction, time average, background correction, overlap correction, range correction and calculation of VLDR and total signal at 532 nm (or 808 nm) in the case of CE376 lidar. The path of the files corresponding to the overlap functions are defined in the configuration file. The background noise imposes the detection limits (SNR=1.5) at each channel, thus SNR for all data points is calculated.
c) **Alternative pre-processing module** can go into two modes, for fixed location and mobile measurements, which is specified by the user in the configuration file. In case of mobile configuration, the reading of a GPS file is included. The automatic search of coincident times between lidar and GPS points is performed. Likewise, a classification of mobile and stationary measurements within the GPS track is derived by applying velocity thresholds. This in particular simplifies further analysis of mobile lidar observations. Other alternative features are data smoothing and signal normalization.
d) **Data processing module,** includes the modeling of molecular coefficients, search of reference zone for each profile, application of the Rayleigh fit, calculation of the attenuated backscatter and ACR. Thus, the automatic download and reading of the radiosonde data available, for $\pm 12\ hours$ of the time threshold under study, is part of the routine. If two radiosonde sites are available, the closest to the lidar site is selected. To model the molecular coefficients, the radiosonde data closest in time is considered for each set of profiles. The $\mathrm{r_{ref}}$ (free of aerosol region) for each channel is searched automatically by a moving window within a threshold a-priori defined in the configuration file (e. g., window of 500 m within 6 km to 10 km), and determined by minimizing the root mean square error

with respect to the molecular signal. This procedure takes into account the altitudes asl, which can change for each acquisition time during mobile observations.

e) **Aerosol retrieval module,** accounts for the reading and processing of the photometer observations (interpolation of data to the lidar wavelengths) and the routines for lidar inversion of data. The retrievals methods are specified in the configuration file, it can be either BW Klett's solution with AOD constraint or LR fixed, and the same for the FW Klett's solution. In particular for mobile observations, the possibility to reduce noise effects by averaging in time is limited by the spatial configuration, therefore usually noisier profiles of 1 min are used. Moreover, it is well known, that the noise in the reference zone for BW Klett solution might induce biases on the retrievals when a single point r_{ref} is selected. Here is where the inversion schemes differ, between BASIC algorithm and this work:

- In this work, instead of considering a single point as boundary condition, like in BASIC, the average of RCS in the reference zone is considered, i.e. assuming homogeneity in the region selected therefore a constant value (Fig. 4.4a).

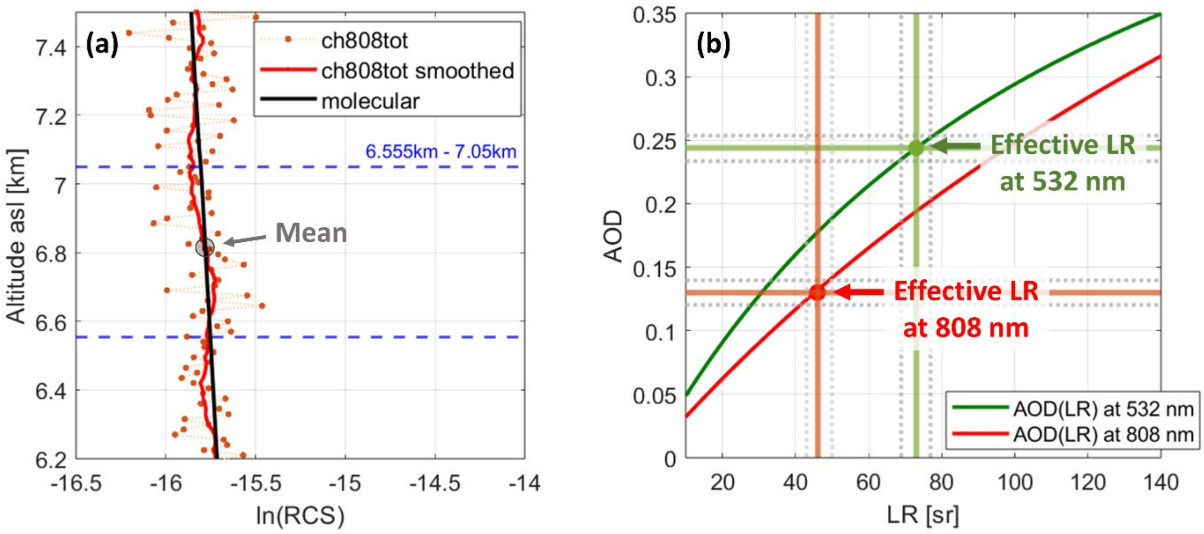

Figure 4.4 : Examples of determination of (a) reference zone and (d)effective lidar ratios.

- To constrain the solution, the iterative process of LR also differs from the one in BASIC algorithm. BASIC proposed a stochastic approach, beginning the iteration with a LR fixed at 50 sr, calculating AOD_{lid} from lidar, and then depending on the differences against the AOD_{ph} (photometer observations) the iteration either take steps (0.5 sr) towards lower LR values, or higher LR. The iteration is terminated when the difference between AODs is less than 10% or when it arrives to the limits (10 sr or 140 sr). In contrast, in this work the iteration is done in two parts, first the AOD_{lid} is calculated for LR steps of 10 sr (from 10 sr to 140 sr), and latter LR steps are reduced to 1 sr between the lidar ratios where the AOD_{lid} is within $AOD_{ph} \pm 0.1$ (the value of 0.1 is only a reference, can be changed). The effective LR is then defined at the minimum difference between AODs (Fig. 4.4b), thus the convergence and uncertainty of the effective LR is defined by the uncertainty of the photometer observations ($AOD_{ph} \pm 0.01$). In this way we get the closest as possible to the AOD_{ph} and get information on the uncertainty of the method. Moreover, the iterations in this way might consume less computational time when the effective LR is close to the limits. For example, in presence of marine aerosols with expected LR around 20 sr or in presence of biomass burning aerosols with LR reported up to 100 sr.

f) **Two-wavelength inversion retrievals module** is dedicated to the inversion scheme proposed in this work (Sect. 4.2.1). Additionally, to maintain the continuity of the measurements, the algorithm fills the gaps in the effective LR temporal variation, when photometer is not available. To do so, the user can define in the configuration file the type of "fill" to use, such as assuming constant the nearest LR or using a linear approximation between two LR.

g) Moreover, the **development of a module dedicated to automatized plots** and individual profiles analysis were undergoing. Even though they are not yet part of the modules, the functions are already used in the main code. The automatized plots functions are as well considering two scenarios, for fixed location or mobile measurements. The individual profile analysis is dedicated to the Rayleigh fit and aerosol retrievals analysis with the possibility to change the parameters and observe changes on the results.

The unified code gave the option to put under test different methods and to evaluate the CE376 lidar measurements from its raw signal to the derived aerosol properties. To this day, the code is shared and used in the Research and Development Department of CIMEL and permitted all the studies presented in this work. In perspective, the adaptation of parts of the code and its further extension into a robust NRT software will be evaluated in the frame of AGORA-Lab. The future versions of iAAMS and BASIC will be the hosts of the tools developed in this work. Moreover, as part of the code, a first estimation of uncertainties is associated to each derived property. Thus, the algorithm products and their associated uncertainty are presented in the next sub-section.

4.2.3 Uncertainties

A first evaluation of uncertainties at each step in the data processing and retrievals are approached using first order derivatives. Thus, error propagation guidelines and studies presented in the literature were followed (Kovalev, 1995, 2004; Morille et al., 2007; Rocadenbosch et al., 2012; Russell et al., 1979; Sasano et al., 1985; Sicard et al., 2020; Welton & Campbell, 2002). The main error sources are related to the overlap function estimation, background noise, lidar constant and depolarization calibrations. Therefore, standard deviations from the overlap function and calibrations are considered, and propagated from the RCS and VLDR to the aerosol retrievals. The uncertainty on the LR is estimated by the convergence within the AOD uncertainties (0.01) in the iterative Klett solution (Sect. 4.2.2). Errors on the molecular optical properties are considered negligible. All the parameters derived from the CE376 lidar are listed in Table 4.1 and Table 4.2, and for each of them the uncertainty equation is provided. Table 4.1 contains the atmospheric properties derived directly from measurements and the Table 4.2 the properties retrieved from inversion. For simplification, the wavelength and altitude dependencies are overlooked.

The uncertainties associated to the calibrations, polarization ΔV^* and lidar constant ΔC_L, are derived from the standard deviations.

Table 4.1 : Uncertainties associated to the atmospheric properties directly derived from the lidar measurements.

Product	Uncertainties
RCS	$\Delta RCS = RCS\sqrt{\left(\frac{\Delta P_{raw}}{P_{raw}-B}\right)^2+\left(\frac{\Delta O}{O}\right)^2+\left(\frac{\Delta B}{P_{raw}-B}\right)^2}$
RCS for total signal	$\Delta RCS_{tot} = \sqrt{(RCS_R)^2+(V^*\,\Delta RCS_T)^2+(RCS_T\Delta V^*)^2}$
VLDR	$\Delta\delta^V = \delta^V\sqrt{\left(\frac{\Delta\delta^*}{\delta^*}\right)^2+\left(\frac{\Delta V^*}{V^*}\right)^2}$ where $\Delta\delta^* = \delta^*\sqrt{\left(\frac{\Delta RCS_R}{RCS_R}\right)^2+\left(\frac{\Delta RCS_T}{RCS_T}\right)^2}$
β_{att}	$\Delta\beta_{att} = \beta_{att}\sqrt{\left(\frac{\Delta RCS_{tot}}{RCS_{tot}}\right)^2+\left(\frac{\Delta C_L}{C_L}\right)^2}$
ACR	$\Delta ACR = ACR\sqrt{\left(\frac{\Delta\beta_{att,S}}{\beta_{att,S}}\right)^2+\left(\frac{\Delta\beta_{att,L}}{\beta_{att,L}}\right)^2}$ where S and L correspond to shorter and longer wavelength

For the aerosol retrievals by using the Klett's solution, it is necessary to redefine Eq. 4.1, in the way that it depends on the main sources of errors. Rocadenbosch et al. (2012) presented the error propagation equations by redefining Eq. 4.1 in terms of RCS, LR and the boundary condition (Eq. 4.12). Aerosol and molecular backscatter coefficients are assimilated into the total backscatter coefficient, $\beta = \beta_a + \beta_m$, hence the derivatives are $d\beta = d\beta_a$ (molecular is neglected). Note that in Eq. 4.12, the integral bounds are inverted, therefore the sign is changed in front the integrals (G and H) in comparison to Eq. 4.1. *These considerations are for the BW Klett solution*. The errors for the FW Klett's solution follow the same steps but with the signs changed. Moreover, the uncertainties derived here are considering a vertical resolved LR, which is not our case. Nevertheless, in perspective, for a probable definition of a LR profile, we let the uncertainties equations like presented in literature (Rocadenbosch et al., 2012). For simplicity, only BW Klett errors are presented, for more details on the FW Klett, the reader can be referred to Rocadenbosch et al. (2012).

$$\beta(\beta(r_b), RCS, LR) = \frac{\beta(r_b)\, RCS\, F(LR)}{RCS(r_b) + 2\beta(r_b) H(RCS, LR)} \tag{4.12}$$

where,

$$F = exp(2G),$$

$$G = \int_{r}^{r_b} (LR(\mathrm{r}') - LR_m)\beta_m(\mathrm{r}')dr'$$

and

$$H = \int_{r}^{r_b} (LR(\mathrm{r}') - LR_m)RCS(r')\, F(LR)dr'$$

Then the uncertainties of the aerosol retrievals and derived properties are in Table 4.2. Note that the 3 components of the calculation for $\Delta\beta_a$ are showed independently in the Table. Moreover, the error associated to the boundary conditions, $\Delta\beta(r_b)$, is strongly dependent on the SNR and Overlap uncertainty (ΔO) for the BW and FW Klett's solutions respectively.

All the properties and their associated errors are products of the prototype algorithm presented in this chapter. Moreover, they are part of case studies analysis that will be presented in the following chapters.

Table 4.2: Uncertainties associated to the aerosol properties retrieved from lidar measurements.

Product	Uncertainties
β_a	$\Delta\beta_a = \sqrt{\left(\frac{\partial\beta}{\partial RCS}\,\Delta\mathrm{RCS}\right)^2 + \left(\frac{\partial\beta}{\partial LR}\,\Delta\mathrm{LR}\right)^2 + \left(\frac{\partial\beta}{\partial\beta(r_b)}\,\Delta\beta(\mathrm{r}_b)\right)^2}$
$\frac{\partial\beta}{\partial RCS}\,\Delta RCS$	$\frac{\partial\,\beta}{\partial RCS}\,\Delta\mathrm{RCS} = -\frac{\beta}{RCS}\,\Delta\mathrm{RCS} - \frac{\beta}{RCS\,\exp(2G)}\int_r^{r_b}(LR(\mathrm{r}') - LR_m)\exp(2G)\,\Delta\mathrm{RCS}\,dr'$
$\frac{\partial\beta}{\partial LR}\,\Delta LR$	$\frac{\partial\,\beta}{\partial LR}\,\Delta\mathrm{LR} = 2\,\beta\int_r^{r_b}\beta_m\,dr\,\Delta\mathrm{LR} - \frac{2\,\beta^2}{\mathrm{RCS}\exp(2G)}\int_r^{r_b}\mathrm{RCS}(r)\exp(2G)\,dr\,\Delta\mathrm{LR}$ $- \frac{4\,\beta^2}{\mathrm{RCS}\exp(2G)}\int_r^{r_b}\mathrm{RCS}\exp(2G)\,dr\int_r^{r_b}\beta_m\,dr\;\;\Delta LR^2$
$\frac{\partial\beta}{\partial\beta(r_b)}\,\Delta\beta(r_b)$	$\frac{\partial\,\beta}{\partial\beta(r_b)}\,\Delta\beta(\mathrm{r}_b) = \left(\frac{\beta}{\beta(r_b)}\right)^2\frac{\mathrm{RCS}(r_b)}{\mathrm{RCS}\;\exp(2G)}\Delta\beta(\mathrm{r}_b)$
α_a	$\Delta\alpha_a = \alpha_a\sqrt{\left(\frac{\Delta\beta_a}{\beta_a}\right)^2 + \left(\frac{\Delta\mathrm{LR}}{LR}\right)^2}$
BAE	$\Delta\mathrm{BAE} = \frac{1}{ln\left[\frac{\lambda_1}{\lambda_2}\right]}\sqrt{\left(\frac{\Delta\beta_{a,\lambda_1}}{\beta_{a,\lambda_1}}\right)^2 + \left(\frac{\Delta\beta_{a,\lambda_2}}{\beta_{a,\lambda_2}}\right)^2}$
EAE	$\Delta\mathrm{EAE} = \frac{1}{ln\left[\frac{\lambda_1}{\lambda_2}\right]}\sqrt{\left(\frac{\Delta\alpha_{a,\lambda_1}}{\alpha_{a,\lambda_1}}\right)^2 + \left(\frac{\Delta\alpha_{a,\lambda_2}}{\alpha_{a,\lambda_2}}\right)^2}$
CR	$\Delta\mathrm{CR} = \mathrm{CR}\sqrt{\left(\frac{\Delta\beta_{\mathrm{a,S}}}{\beta_{\mathrm{a,S}}}\right)^2 + \left(\frac{\Delta\beta_{\mathrm{a,L}}}{\beta_{\mathrm{a,L}}}\right)^2}$
$PLDR$	$\Delta\delta^{\mathrm{p}} = \delta^{\mathrm{p}}\sqrt{\left(\frac{\mathrm{B}[\,\delta^{\mathrm{v}}+1][\,\delta^{\mathrm{m}}-\delta^{\mathrm{v}}]}{\mathrm{K}[\,\delta^{\mathrm{v}}+1-\mathrm{K}]}\;\frac{\Delta\mathrm{B}}{\mathrm{B}}\right)^2 + \left(\frac{\delta^{\mathrm{v}}[\mathrm{B}+1]}{\mathrm{K}[\,\delta^{\mathrm{v}}+1-\mathrm{K}]}\;\frac{\Delta\delta^{\mathrm{v}}}{\delta^{\mathrm{v}}}\right)^2}$ Where B= R-1 and $\mathrm{K} = \mathrm{B}[\,\delta^{m} - \delta^{v}] + 1$ $\;and\;\Delta R = \mathrm{R}\sqrt{\left(\frac{\Delta\beta_a}{\beta_a}\right)^2}$

4.3 Chapter Summary

This chapter focused on the algorithmic integration of elastic dual-wavelength lidar and photometer observations, such as CE376 lidar and CE318-T photometer. The challenges for retrieving aerosol optical properties were discussed, in particular when low detection limits at 808 nm measurements are met by daytime. Therefore, different methods for single and dual wavelength elastic lidar signals were introduced and discussed, showing the restrictions to apply, in particular, the two-wavelength methods. Nevertheless, the original ideas proposed along the years of CALIPSO mission were considered important to be explored. Therefore, in this work the ACR is adopted and further used in the case studies included in next chapters.

The BW Klett's solution, a widely used method, is presented along with the FW Klett's solution, Quasi-aerosol approach and Iterative forward method. These methods were described and evaluated through comparisons of their aerosol retrievals. Two scenarios were presented, day and night, showing advantages and limitations of each method. In conclusion, the FW Klett's solution and the Iterative method showed to be suitable for measurements at 808 nm by day. Nevertheless, the Iterative method was not taken into account for further developments, due to potentially higher computational time involved in this method. In perspective, the Iterative method can be used for aerosol characterization of integrated layers.

The chapter introduces an algorithm developed during this thesis to enhance the capabilities in retrieving aerosol properties from simultaneous two-wavelength elastic lidar measurements, considering detection limits at both wavelengths. The advantage of the approach resides in the availability of photometer observations, which constrains the solutions and reduces uncertainties in the effective LR. The retrieved parameters are effective LR, backscatter and extinction coefficients at both wavelengths. Moreover, other properties can be derived to qualitatively evaluate microphysical aerosol characteristics. Vertical resolved BAE and EAE are related to the aerosol size, values close to 0 indicating presence of coarse aerosols and values close to 1 or higher indicate presence of fine aerosols. The CR, also derived from the backscatter coefficients, can be related to aerosol size but following contrary sense compared to BAE, i.e., values close to 1 indicate presence of coarse aerosols and values closer to 0 indicate presence of fine aerosols. Moreover, by combining the VLDR and backscatter coefficients, the PLDR can be derived, which contains information on the aerosol shape, values close to 0 related to spherical particles and higher to 0.2 being related to non-spherical particles.

Considerations for NRT aerosol monitoring at fixed location and for mobile measurements are taken into account. Therefore, in this chapter, a comprehensive overview of the proposed prototype algorithm is presented. As well, its future integration in NRT monitoring, and a detailed analysis of associated uncertainties are presented. The schematic description of the algorithm described is presented in Fig. 4.5.

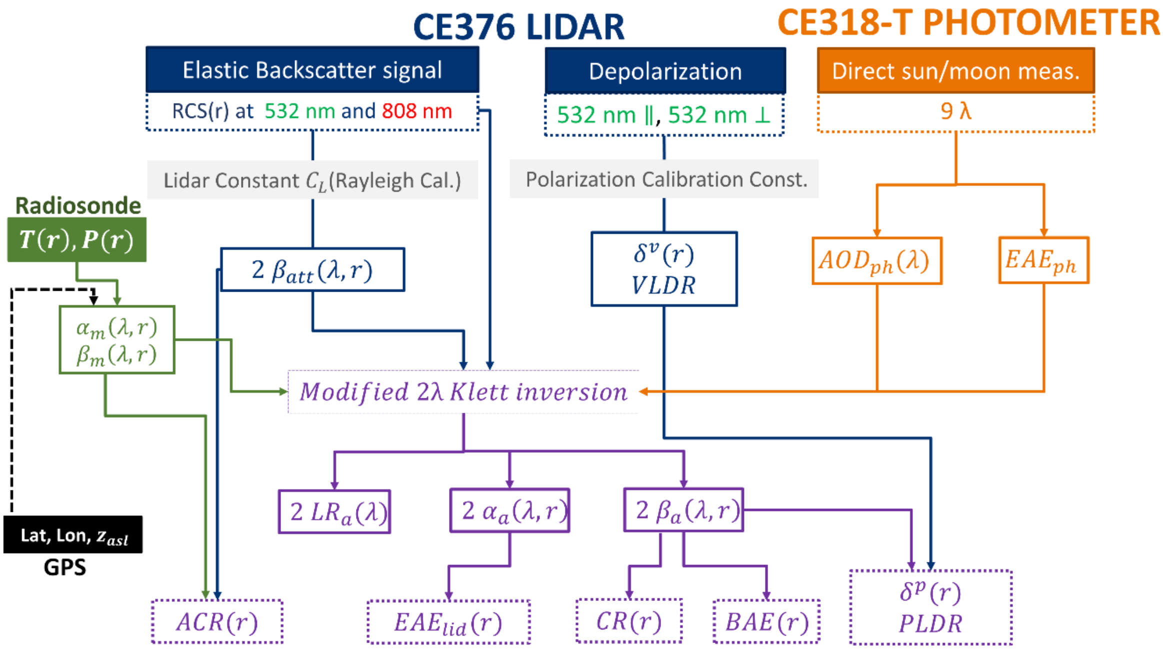

Figure 4.5 : Schematic description of the prototype algorithm presented in this work.

The developed tools presented in this chapter, in combination with the evaluation of CE376 lidar performance (Chapter 3), showed the advantages and limitations of the instrument. Moreover, both instrumental and algorithmic developments have important roles for further developments on the CE376 lidar and for its future applications, such as aboard mobile vectors and for NRT aerosol monitoring. To showcase the capabilities of the CE376 lidar for aerosol characterization, the next two chapters are dedicated to comprehensive analysis of case studies, considering fixed location (Chapter 5) and while in movement (Chapter 6).

Chapter 5

Aerosol observations using CE376 lidar and CE318 photometer

" Je suis de ceux qui pensent que la science est d'une grande beauté. Un scientifique dans son laboratoire est non seulement un technicien : il est aussi un enfant placé devant des phénomènes naturels qui l'impressionnent comme des contes de fées."

-Marie Curie-

This chapter presents case studies of aerosol observations using the CIMEL CE376 lidar and CE318 photometer at fixed location laboratories. The platforms considered are ATOLL at Lille University (Lille, France) and the Izaña observatory (IZO), operated by the Izaña Atmospheric Research Center (Meteorological State Agency of Spain, IARC-AEMET), in Tenerife, Spain. Both sites host early versions of the CE376 lidar and co-located with CE318-T sun/sky/lunar photometers. Case studies are selected from continuous observations with the CE376 lidar to demonstrate its capabilities for monitoring different aerosol types. Additionally, comparisons with co-located Raman high-power lidar data at the ATOLL site further validate the CE376 lidar's performance. This chapter is part of joint collaborations between CIMEL and LOA (AGORA-Lab, Lille, France) and between CIMEL and IARC (Tenerife, Spain). Note that throughout this chapter, the index ¨a¨ and ¨aer¨ are used indistinguishable to mention aerosol properties.

5.1 Sites description

In the following sections, the observatories ATOLL (Lille, France) and IZO (Tenerife, Spain) are described, along with the remote sensing instrumentation that are considered in this study. A general overview of the aerosols observed at each site is also provided.

5.1.1 ATOLL observatory (Lille, France)

The ATOLL platform, operated by LOA at Lille University (50.61° N, 3.14° E, 60 m asl) (Fig. 5.1), is a calibration center for AERONET-Europe within PHOTONS, and part of ACTRIS. The platform is equipped with online in-situ and remote sensing instruments providing valuable information on aerosol properties and cloud-aerosol interactions.

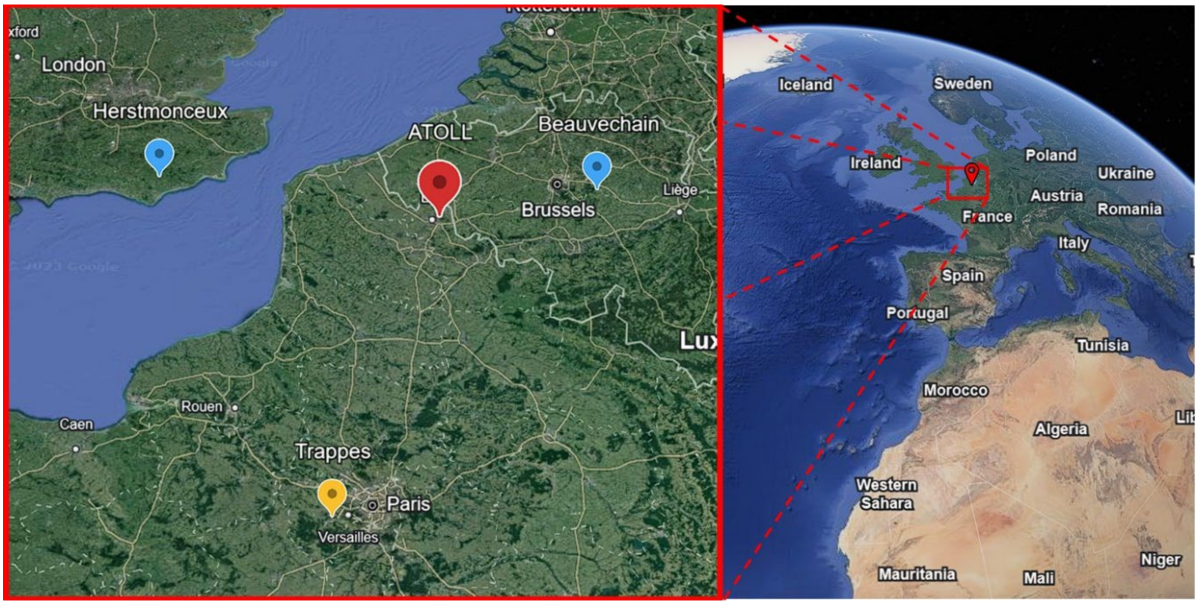

Figure 5.1: ATOLL platform location along with the 3 closest radiosonde sites, Beauvechain (Belgium) and Herstmonceux (England) from Wyoming University database (in light blue), and Trappes (France) from Météo-France database (in yellow). © Google Earth.

METIS, an early version of the CE376 GPN lidar with two-wavelengths at 532 nm and 808 nm and depolarization at 532 nm, is operational at ATOLL platform since 2019 in the frame of AGORA-Lab. The system laser source at 532 nm has been replaced with one of higher pulse energy (15-20 μJ, not eye safe) to increase the SNR. The lidar setup follows a depolarization configuration with φ=90°, measuring the parallel polarization component on the PBS reflected branch, using wire-grid polarizers to reduce the cross-talk (Tp~1, Ts~0 and Rp~0, Rs~1). Continuous measurements are ensured by a temperature-controlled room and using a high transmittance glass on the roof. The depolarization configuration is described in detail in Chapter 3 section 3.3.2, and section 3.5.3 describes the improvements to enhance depolarization measurements. Moreover, METIS is co-located with a master CE318-T photometer and with LILAS (LIlle Lidar AtmosphereS) ACTRIS lidar, both considered in this study. Figure 5.2 illustrates the ATOLL platform remote sensing considered in this work; METIS and LILAS lidars are presented side by side (Fig. 5.2a) and the installation of the photometer calibration center on the LOA rooftop (Fig. 5.2b).

LILAS is a high-power Mie-Raman-Depolarization-Fluorescence multi-wavelength lidar developed and upgraded by LOA since 2013. From its simultaneous multiple wavelength measurements, independent height-resolved optical properties are derived: 3 backscatter (355 nm, 532 nm, 1064 nm), 2 extinction (355 nm, 532 nm), 3 particle depolarization ratio (355 nm, 532 nm, 1064 nm) and 1 fluorescence backscatter (at 466 nm) profiles. A detailed description of LILAS system, retrievals and uncertainties can be found in previous works (Bovchaliuk et al., 2016; Q. Hu et al., 2019, 2022; Veselovskii et al., 2022). The aerosol optical properties retrieved with METIS at 532 nm are validated by comparisons with LILAS.

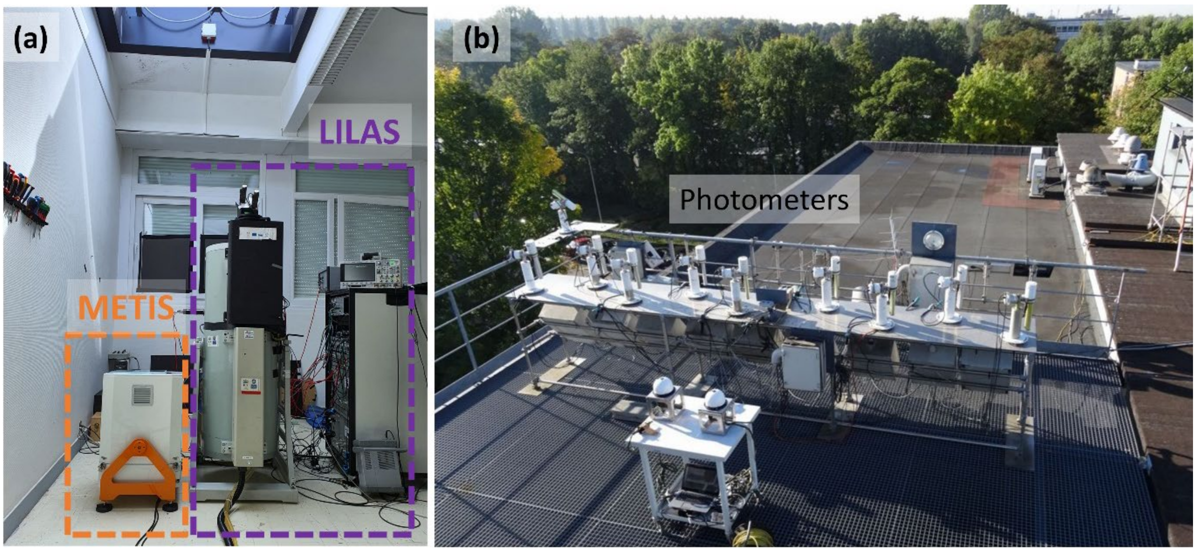

Figure 5.2: ATOLL platform instrumentation considered in this thesis. (a) METIS, early version of CE376 lidar, and LILAS, high power EARLINET-ACTRIS lidar, are presented. (b) LOA rooftop installation for photometer AERONET/PHOTONS calibration center.

To derive aerosol properties from the lidar measurements, vertical profiles of temperature and pressure are essential to account the molecular contributions. Molecular coefficients are modeled using radiosonde measurements from three nearby stations. Beauvechain (50.78° N, 4.76° E, Belgium) and Herstmonceux (50.90° N, 0.32° E, England) from Wyoming University database (https://weather.uwyo.edu/upperair/sounding.html), and Trappes (48.77° N, 1.99° E, France) from Météo-France database (https://donneespubliques.meteofrance.fr). Beauvechain is the closest site, about 120 km away from Lille, Herstmonceux is 200 km and Trappes is 240 km far from Lille (Fig. 5.1).

5.1.1.1 Aerosol characterization at ATOLL: a general overview

The ATOLL location is mainly influenced by urban-industrial emissions, ship traffic, and marine aerosols (~80 km from the nearest coast). The Lille metropolitan area accounts nearly, with nearly 1.2 million inhabitants, ranks as the third French city with poorest air quality, following Paris and Marseille. Additionally, the site is in close proximity to three major capitals—Brussels, London, and Paris—each densely populated with significant industrial activity. Brussels is located 90 km away to the E with more than 1 million inhabitants. London is located 250 km away to the W with a population of around 8.8 million inhabitants. Paris is located 200 km away to the S with an estimated population of 12 million residents, which are accounted for the metropolitan area of Île-de-France. Lille and its continental neighbor cities, Paris and Brussels, are placed in a quite flat terrain, whereas London is separated by the English Channel. Moreover, the English Channel is well known to be one of the world's busiest maritime ship-paths.

A recent climatological study by Velazquez Garcia (2023) conducted a comprehensive source analysis focused on black carbon emissions by using back-trajectories and in-situ observations. Two distinct periods of aerosol sources influencing the ABL at ATOLL were detected (cold=fall-winter and warm=spring-summer). During winter, higher values of extinction and absorption coefficients were observed, and during summer those values reduced by 26% and 45% respectively. Aerosol content within the ABL during fall (September-November) and winter (December-February) is mostly influenced by winds from S to SW, impacted by urban/industrial emissions from Paris (and Southern France), maritime aerosols and ship traffic. During spring (March-May) and summer (June-August), winds from SW to W are predominant, influenced by urban emissions from London, agricultural sector emission (rural area), marine aerosols and ship traffic. Winds from the N to NE are as well influencing the site throughout the year in less proportion (5-10 %), transporting aerosols from urban emissions in Germany, Belgium and marine aerosols from the North Sea. Moreover, new particle formation were evidenced during summer when air masses from North Sea reach the site (Crumeyrolle et al., 2023). Pollen outbreaks, corresponding to spring-summer seasons, are also observed by LILAS (Veselovskii et al., 2021). Likewise, events of long-range transport impact the region with aerosols from Saharan mineral dust storms (Veselovskii et al., 2022), North American wildfires (Q. Hu et al., 2019, 2022) and volcanic eruptions (Mortier et al., 2013).

A previous climatological work focused on column-integrated and vertical-resolved aerosol optical properties, using photometer and lidar (CE370 single-wavelength lidar), was presented by Mortier (2013). Both Mortier (2013) and Velazquez Garcia (2023), presented long term temporal variability of sun photometer observations using data from 1999 to 2013 and from 2008 to 2021, respectively. Complementary to these studies, Figure 5.3 presents long-term temporal variability of aerosol properties by means of sun/sky/lunar photometer observations at ATOLL, since 2000 until December 15th 2023. The optical properties are obtained through v3 AERONET algorithms at data level 2.0 until August 2022, and level 1.5 since September 2022. Continuous direct moon measurements are data level 1.5 and are available since 2017. This work takes into account moon direct measurements, increasing the number of observations, especially during winter long nights. VSD monthly distributions, retrieved from measurements under sky almucantar scenario, and SSA (at 440 nm and 870 nm) when available, are also presented. Thus, the key features observed on Fig. 5.3 are described as follows:

(a) The $\mathrm{AOD_{ph}}(440)$ (Fig. 5.3a) temporal series shows mean values of 0.21 ± 0.16 (over all data points ~24 years). A seasonal variation on aerosol content highlighted by previous works is as well observed. AOD maximum values are detected during spring (March-May) followed by summer (June-August) and minimum values were evidenced during winter (December-February). Moreover, a yearly reduction of 0.005 ($-1.4 * 10^{-5}$ day^{-1}) on $\mathrm{AOD_{ph}}(440)$ is reported. Even though a strong seasonality of AOD is marked, this doesn't coincide with the observations at ground level (Velazquez Garcia, 2023). In particular, Mortier (2013) observed a low altitude ABL top throughout winter days (below 700 m) and moderate to high altitudes ABL top during spring and summer (up to 1.1 km during spring and ~2 km during summer), which can be connected to the different seasonality compared to the ground observations.

(b) The $\mathrm{EAE_{ph}}(440/870)$ (Fig. 5.3b) temporal series yields mean values of 1.2 ± 0.4 (over all data points), showing a strong presence of fine mode particles (related to anthropogenic emissions). Similarly to AOD trends, a yearly reduction of 0.01 ($-2.7 * 10^{-5}$day^{-1}) on $\mathrm{EAE_{ph}}(440/870)$ is observed, in agreement with previous works. Seasonality on $\mathrm{EAE_{ph}}(440/870)$ is also observed showing a major influence of coarse mode particles during winter (i.e., lower values of EAE).

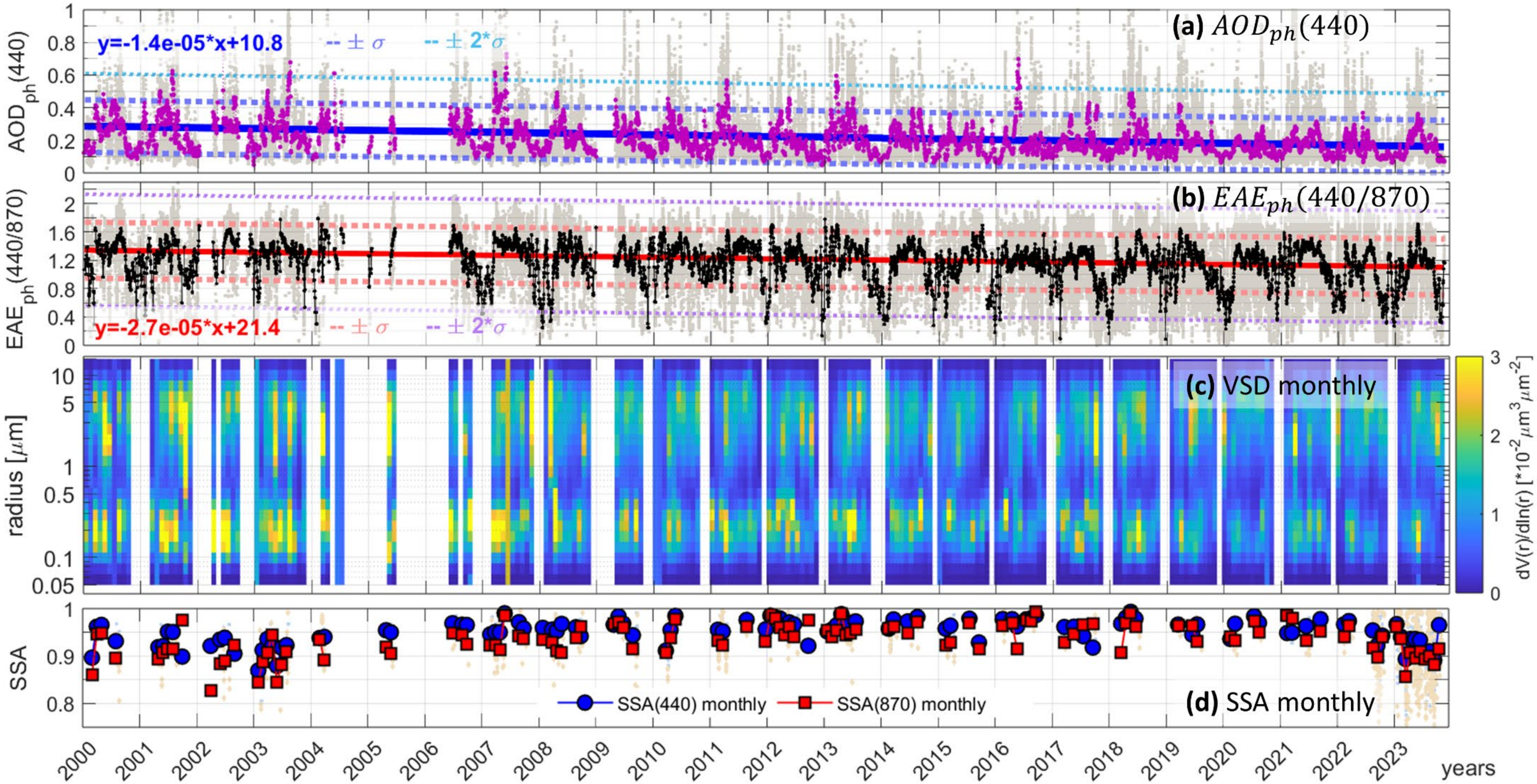

Figure 5.3: Climatology of column integrated optical properties from sun/sky/moon photometer measurements since 2000 until 2023 (December 15th 2023) at ATOLL. From top to bottom: (a) AOD_{ph} temporal series (all data points in grey, 15 day moving average in purple) with its corresponding linear fit in blue (fit to daily averages), $\pm\sigma$ and $\pm 2\sigma$; (b) EAE_{ph} temporal series (all data points in grey, 15 day moving average in black) with its corresponding linear fit in red (fit to daily averages), $\pm\sigma$ and $\pm 2\sigma$; (c) temporal variation of VSD (monthly averages) where y axis represent the radius (in logarithmic scale); finally (d) temporal series of monthly averages for SSA(440) and SSA(870). The optical properties are obtained through v3 AERONET algorithms using data level 2.0 until August 2022, and level 1.5 since September 2022. Continuous direct moon measurements are available since 2017.

(c) The temporal variation of monthly averaged VSD (Fig. 5.3c), throughout the 24 years (288 months) of photometer observations (5607 VSD in total), show a quasi-permanent bimodal behavior, i.e., with both fine (radius ≤1 μm) and coarse (radius >1 μm) mode aerosol contributions. It is worth to mention that each derived VSD accounts 22 bins (radius from 0.05 to 15 μm). For 215 months with available VSD, the mean radius at both fine and coarse modes are $(0.21 \pm 0.17)\ \mu m$ and $(3.58 \pm 1.13)\ \mu m$, respectively. Major concentrations are accounted on the fine mode for 133 months, mostly during spring and summer (65 %); 82 months on the coarse mode are reported mainly during summer and fall (38%). These results however do not present a clear connection with the seasonality well defined by the AOD and EAE, which might be related to the differences in the measurements scenarios (Chapter 3, section 3.1.1). While direct sun/moon measurements are retrieved every 5 min (nowadays), the sky measurements are taken every hour and they take ~15 min to complete all the scenarios. Moreover, during winter, the cloud coverage is higher than 60% on a daily basis (Chesnoiu, 2023) and even within clear sky thresholds the passage of small clouds is inevitable, contaminating the observations, which results in the absence of VSD in December. Nevertheless, it is important to highlight that an increasing number of months with strong presence of coarse mode aerosols (by volume) with respect to the fine mode is detected, which can be related to the negative trend on EAE.

(d) The temporal variation of monthly SSA at 440 and 870 nm (Fig. 5.3d) throughout the 24 years (288 months) of photometer observations (5526 data points in total) is presented. In general, a decrease on the aerosol absorption from 2003 to 2007 (SSA from ~0.85 towards ~0.95) is evidenced, also since 2007 until 2022 the SSA values have maintained on average at 0.95 at both wavelengths. In the last year (2023), an increase on aerosol absorption is observed that might be related to the extended influence of biomass burning aerosols from Canadian wildfires. It needs to be recalled that SSA (at level 2.0) is available only for AOD values (>0.4), so it can be related to specific events rather than the general aerosol conditions. Thus, from SSA long term series, we cannot conclude further without going into details about the individual event conditions which will not be considered in this work.

In agreement with previous studies, surface and remote sensing measurements do not present a direct connection between them, which might be related to instrumental limitations (clouds impact on the photometer) or aerosol layers above the ABL (not detected by in-situ). Therefore, more elaborated studies by using in-situ and remote sensing in order to characterize the aerosol contributions within and above the ABL are still needed. In perspective, the CE376 lidar, METIS, with its continuous observations and capacity to distinguish different aerosol types in the atmosphere can be used to establish the connection missing between in-situ and passive remote sensing at ATOLL.

This chapter present case studies of aerosols transported above the ATOLL ABL, focusing on dust (Sect. 5.3), dust-smoke (Sect. 5.4) and volcanic aerosols (Sect. 5.5.2) events.

5.1.2 IZO observatory (Tenerife-Canary Islands, Spain)

The IZO observatory, part of IARC and operated by AEMET at Tenerife Island (28.31° N, 16.50° W, 2373 m asl) (see Fig. 5.3). IZO is one of the calibration centers of AERONET-Europe, part of ACTRIS, and is a global station of GAW-WMO (Global Atmospheric Watch-World Meteorological Organization).

Figure 5.4: IZO platform location along with the closest radiosonde site, Guimar (Tenerife) from Wyoming University database (in light blue). Both Teide and Cumbre Vieja volcano locations are presented by green marks. © Google Earth.

The CE376 GPNP lidar, elastic backscatter and depolarization measurements at 532 nm and 808 nm, is operational at IZO platform since July 2019. The CE376 GPNP lidar at IZO is characterized by the usual features of a CE376 GPN lidar system (Chapter 3, Section 3.2.1), i.e., emission source at 532 nm (5-10 μJ, eye safe). However, the lidar system provides additional depolarization measurements at 808 nm, which is not commercially available due to low SNR at this wavelength and will not be considered in this work. The depolarization measurements setup at both wavelengths currently follows a configuration with φ=90°, measuring the parallel component of the polarization on the PBS reflected branch. Wire-grid polarizers behind PBS branches were installed in November 2022 to reduce the cross-talk in the signals (Tp~1, Ts~0 and Rp~0, Rs~1). Controlled temperature room and a window roof with extra-clear glass are considered to support continuous observations. Following the recommendations to enhance depolarization measurements (Chapter 3, Section 3.5.3), the glass weight and its placement on the window frame are carefully considered and have been improved over the years. Moreover, the lidar system is co-located with a master CE318-T photometer, which is used in this work.

Molecular coefficients are modeled using temperature and pressure profiles data from the Guimar radiosonde site (28.32° N, 16.38° W, 115 m asl). The radiosonde station is located 11.5 km away from IZO (Fig. 5.4) and the data is available at Wyoming University database (https://weather.uwyo.edu/upperair/sounding.html).

5.1.2.1 Aerosol characterization at IZO: a general overview

Due to IZO location and the existence of the trade wind inversion (Hadley cell), a meteorological feature on the island, the observatory is usually isolated from Tenerife urban emissions (~1 million inhabitants). Therefore, clean air and clear sky conditions are normally meet along the year, offering ideal conditions for in-situ trace gases and aerosols studies under FT (free troposphere) conditions (Bergamaschi et al., 2000; Schneider et al., 2010). Moreover, the platform's geographical location (300 km W of the nearest African coast) permits studies on mineral dust transport from the Sahara Desert towards North-Atlantic Ocean (Rodríguez et al., 2015). IZO observatory is also 15 km NE of the Teide volcano (28.27° N, 16.64° W, 3718 m asl), and 140 km E of Cumbre Vieja volcano (28.57° N, 17.84° W, 1100 m asl) (Fig. 5.4). In particular, the observatory monitored continuously the evolution of the recent volcanic eruption of Cumbre Vieja, located in La Palma Island, which emitted important amounts of sulfur compounds that were transported across the Atlantic and Europe for 3 months since 19 September 2021 (Bedoya-Velásquez et al., 2022; García et al., 2022; Milford et al., 2023; Sicard et al., 2022).

A comprehensive aerosol characterization using long-term photometer observations on Tenerife island has been presented by Barreto et al. (2022b). The analysis considered long term photometric observations (2005-2020) of four AERONET stations located from sea level to 3555 m asl on the island of Tenerife. Two of these stations are located within the marine ABL, and the other two (including IZO) are higher in altitude mostly under FT conditions. From consistent measurements within the four stations, two main scenarios were identified as background conditions and dust-laden conditions. Background conditions prevail along the year while dust-laden conditions are predominant during summer in all the stations. Furthermore, a long term analysis of lidar and radiosonde measurements (2007-2008) has shown two distinct dust vertical structure at Tenerife according to the season (Barreto et al., 2022a). During winter outbreaks, dust is transported in a compressed layer (~2 km asl) within a drier, colder (with respect to no-dust scenario during winter) and well mixed marine ABL. During summer outbreaks, dust is transported at a lofted well stratified layer (extended from ~2 km asl to ~6 km asl), within more humid and warmer (with respect to FT during summer) air masses. Regarding IZO station, background FT conditions dominate most of the year, except in July and August, when the number of days under dust-laden conditions is higher, which is in direct connection to the presence of the extended lofted dust layer during summer.

This chapter presents two particular cases observed at IZO, one showing dust laden conditions during summer (Sect. 5.2) and the other one during the Cumbre Vieja eruption (Sect. 5.5.1). The case studies at both sites, ATOLL and IZO, presented in the following sections are selected to demonstrate the capabilities of the CE376 lidar for aerosol characterization.

5.2 Saharan dust near-source (IZO, 15 August 2021)

Dust measurements near the source are largely classified as pure dust, although it is a mixture of various components such as clays, quartz, and iron oxides. The proportions of the different components can vary depending on the source and environmental conditions, which can result in changes in the optical properties accordingly (Veselovskii et al., 2020). IZO station is mostly impacted by dust outbreaks from Western Sahara during July and August (as mentioned in Sect. 5.1.2.1). An example of the dust-laden conditions encountered at IZO is presented in this section with a case study during summer 2021. Figure 5.5 shows images of total column Dust Optical Depth (DOD) at 550 nm showing the predictions of dust transport from North-Western Africa towards the Atlantic passing by the Canary Islands. The images correspond to 14 August 2021 at 12:00 (Fig. 5.5a), 15 August 2021 at 12:00 (Fig. 5.5b), and 16 August 2021 at 12:00 (Fig. 5.5c), with DOD(550) values up to 0.8. The multi-model forecast, mean values over 11 models, is considered for the DOD images (Basart et al., 2019), which are provided by the WMO Barcelona Dust Regional Center and the partners of the Sand and Dust Storm Warning Advisory and Assessment System (SDS-WAS) for Northern Africa, the Middle East and Europe (https://dust.aemet.es/products/daily-dust-products). Furthermore, the SDS-WAS center uses remote-sensing retrievals from sun-photometer (AERONET) and satellite (MODIS) measurements for model comparisons and evaluation.

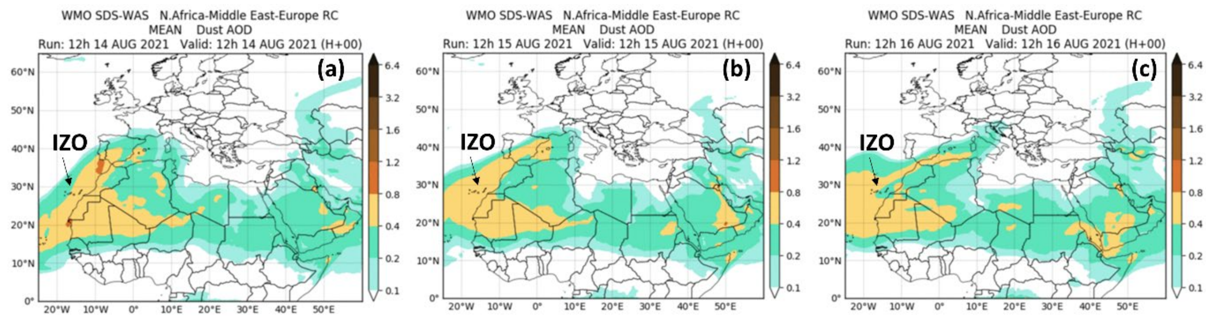

Figure 5.5: Forecast images of total column dust optical depth at 550 nm over Northern Africa, Middle East and Europe. (a) 14 August 2021 at 12:00, (b) 15 August 2021 at 12:00 and (c) 16 August 2021 at 12:00. Images are generated with multi-model forecast and are provided by WMO Barcelona Dust Regional Center and the partners of SDS-WAS (*https://dust.aemet.es/products/daily-dust-products*).

To study this case of dust outbreak, we focus our attention on the 15 August 2021 (Fig. 5.5b), which is characterized by estimated DOD(550) values from 0.4 to 0.8 over the entire territory of the Canary Islands. Thus, a comprehensive study of the CE376 lidar and photometer observations is presented for the 15 August 2021 in the following subsection.

5.2.1 CE376 lidar and photometer analysis

The CE376 GPNP lidar blind zone is defined from the overlap function estimations (i.e., r_o where O(r) <0.1). During this period for each channel, they were: $r_o(532par) = 0.6\ km$, $r_o(532per) = 0.5\ km$ and $r_o(808tot) = 0.15\ km$. Thus, the first 2 km of the total signal RCS at 532 nm are influenced by relative errors of 5 % at 2 km going towards 15 % at 600 m due to the overlap estimations. In the case of RCS at 808 nm, the influence of overlap error ranges from 4 % at 1 km to 10 % at 150 m.

An overview of the lidar and photometer observations during 15 August 2021 is presented in Fig. 5.6. The height-temporal variations of β_{att} at 808 nm (see Fig. 5.6a), VLDR at 532 nm (see Fig. 5.6b) and extinction α_a at 532 nm (see Fig. 5.6c) show a fairly homogeneous depolarizing aerosol layer extending up to 6 km asl (~3.6 km above IZO station). VLDR at 532 nm presents values above 0.1 up to 0.2 indicating the predominant presence of non-spherical particles, which is expected for dust. This impressive column of dust persisted throughout the day with $AOD_{ph}(532)$ (i.e., AOD derived from the photometer) values of ~0.3 in the morning towards ~0.45 in the afternoon (Fig. 5.6d), in accordance with the DOD(550) forecast (Fig. 5.5b). The $AOD_{ph}(532)$ increases during the day while $EAE_{ph}(532/808)$ slightly decreases from ~0.2 to ~0.15. The low values of EAE indicate the dominant presence of coarse aerosols.

Additionally, VSD retrievals from photometer observations on 15 August 2021 (Fig. 5.7a) show the strong predominance of aerosols in the coarse mode with an effective radius of $\sim 2.2\ \mu m$. Moreover, spectral SSA derived from the photometer retrievals (Fig. 5.7b) show higher absorption efficiency at shorter wavelengths (SSA~ 0.94) than at longer wavelengths (SSA~ 0.98-0.99), similar to the results presented in previous works for dust near source (Dubovik et al., 2002; Veselovskii et al., 2020). It is worth noting that SSA (at level 2.0) is available only for $AOD_{ph}(440) > 0.4$, which is the case for this event.

Using the two-wavelength modified Klett inversion, effective LR at both wavelengths was derived while sun photometer measurements were available. Although moon direct observations are not available, constant LR at both wavelengths is used to maintain continuity on the retrievals (Fig. 5.6c). The LR values are 50 sr and 74 sr at 532 nm and 808 nm respectively before 07:00 UT, and 58 sr and 79 sr at 532 nm and 808 nm respectively after 19:00 UT. As a result, AOD_{lid} (i.e., from lidar retrievals) at both wavelengths and $EAE_{lid}(532/808)$ are derived (see Fig. 5.6d). In the first threshold of time from 00:00 to 07:00

UT, AOD_{lid} and EAE_{lid} values indicate a decrease of aerosol loading while coarse aerosols predominance increases. $AOD_{lid}(532)$ goes from 0.4 (at 01:00) to ~0.3 (at 07:00) which is in accordance with the last photometer measurement taken the day before ($AOD_{ph}(532)$ =0.4 at 19:00 2021-08-14). Similarly, $EAE_{lid}(532/808)$ decreases from 0.5 (at 01:00) to ~0.2 (at 07:00), which is two times the last EAE value from the day before (EAE_{ph}(532/808)=0.25 at 19:00 2021-08-14), nevertheless corresponding to the increasing trend on EAE values towards sunset the day before.

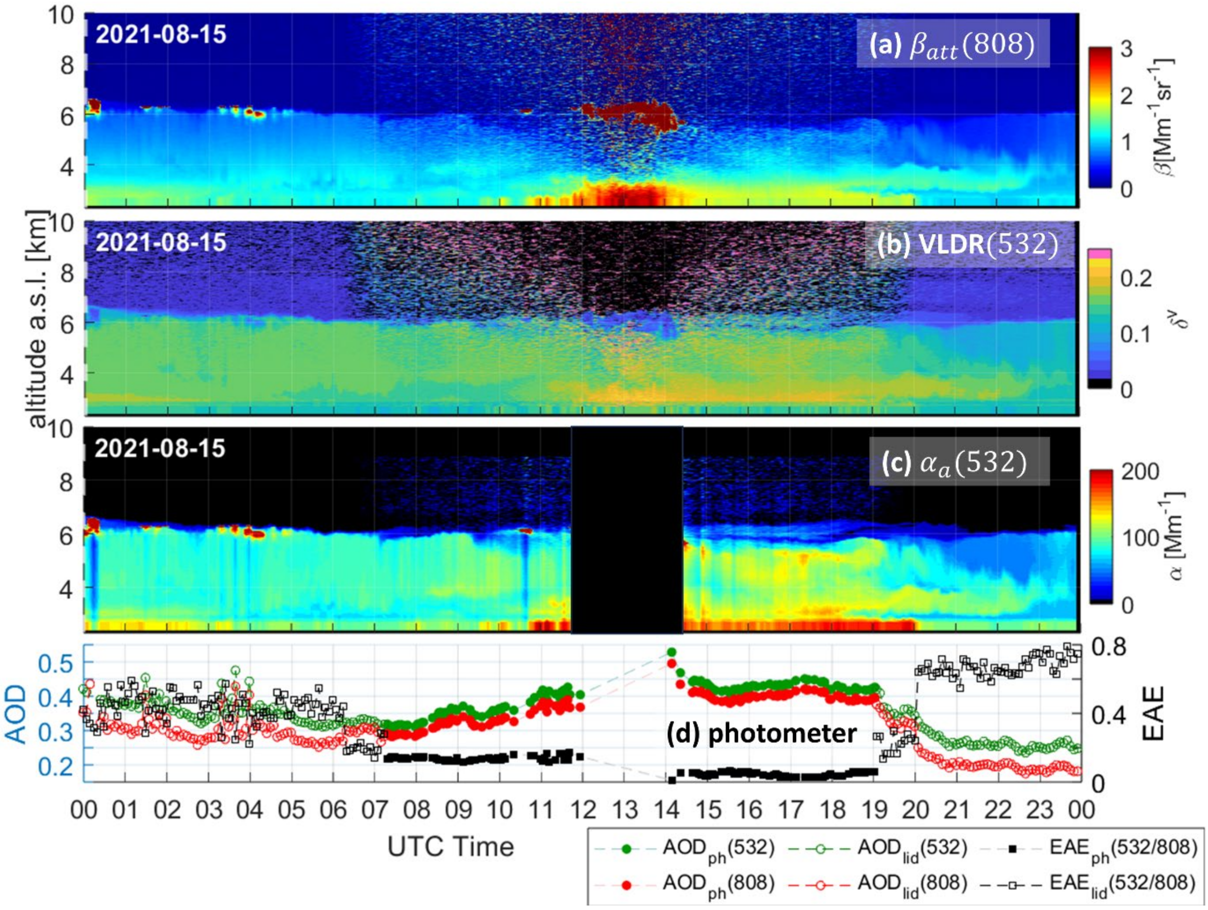

Figure 5.6: Overview of synergetic measurements of CE376 lidar and photometer during an event of Saharan dust outbreak at IZO station (Tenerife, Canary Islands) on 2021-08-15. Height-temporal variation of (a) β_{att} at 808 nm, (b) VLDR at 532 nm, (c) extinction at 532 nm, and (d) time series of AOD at 532 nm and 808 nm and EAE(532/808) derived from photometer are presented. The altitude axis on (a), (b) and (c) starts at 2.3 km asl, IZO being located at 2.37 km asl.

In the second threshold from 19:00 to 24:00 on 15 August 2021, AOD_{lid} and EAE_{lid} values indicate a decrease in aerosol loading and on coarse aerosols predominance. $AOD_{lid}(532)$ decreases from 0.4 (at 19:00) to ~0.25 (at 24:00), which is lower than the first photometer measurement taken the day after ($AOD_{ph}(532)$ =0.3 at 08:00 2021-08-16). Similarly, $EAE_{lid}(532/808)$ increases from 0.15 (at 19:00) to ~ 0.8 (at 24:00), which is double the first observation the next day (EAE_{ph}(532/808) =0.4 at 08:00 2021-08-16), still following the increasing trend in EAE observed the next day.

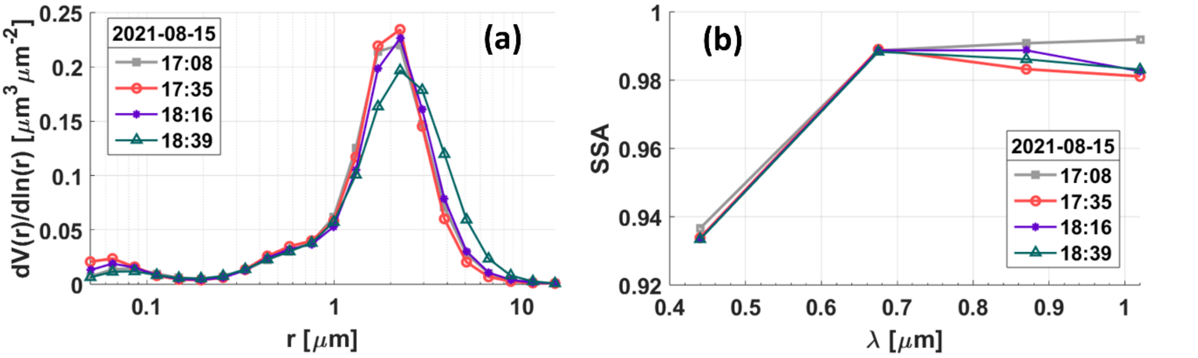

Figure 5.7 : (a)VSD and (b) SSA(λ) derived from photometer sky almucantar and AOD measurements during 2021-08-15 at IZO. Data is level 2 from AERONET version 3 algorithms.

The differences encountered on the AOD and EAE, derived from lidar with respect to the photometer, are clearly related to the constant LR imposed at both wavelengths. In the second threshold of time, specifically, the layer evolves into a different structure towards midnight, i.e., higher backscatter and higher VLDR values below ~4 km asl (Fig. 5.6). Moreover, the increase of the EAE_{ph}(532/808) the next day indicates as well a change in the aerosol content in the atmosphere. Consequently, a change on the effective LR is expected rather than the constant value imposed. Still AOD and EAE temporal series derived from the lidar are in agreement with the trends of the photometer measurements a day before and a day after. In this context, the effectiveness of the CE376 lidar, in synergy with photometer, for continuous aerosol monitoring is emphasized.

For further study, total (molecules + aerosol) optical properties derived from the lidar and photometer are evaluated. Relative probabilities of derived properties from the lidar measurements within the homogeneous dust layer (3-6 km asl) from 07:00 to 19:00 UT on 15 August 2021 are presented in Fig. 5.8. The first 600 m of the profiles are not considered due to the higher uncertainty (>15 %) on RCS profiles induced by the overlap corrections at 532 nm channels. For this purpose, averaged profiles on 5 minutes with 15 m height resolution (200 points within the layer per profile) are considered. To avoid artifacts induced by noise and errors, filtering is applied. Values with relative errors higher than 1, and data corresponding to backscatter coefficients too small ($\beta < 0.2\ Mm^{-1}sr^{-1}$) are not taken into account. Similarly, data under presence of clouds is not included (from 12:00 to 14:30 15 August 2021). Atmospheric properties, i.e., β_{att} at both wavelengths, $VLDR$ at 532 nm and $ACR(808/532)$, are compared against the aerosol retrievals, i.e., β_{aer} and α_{aer} at both wavelengths, PLDR at

532 nm, $CR(808/532)$, $EAE(532/808)$, $BAE(532/808)$. Likewise, Table 5.1 summarize the results presented in Fig. 5.8. The mean, median, Standard Deviation (SD) of the mean and Standard Error (SE) are presented. Note that in this work the standard deviation and the standard error can give different values. While the SD gives us information on the dispersion of the points taken into account for the average, the SE shows the variance in the errors associated to those data points. Therefore, in the case of derived properties after the inversion, such as PLDR, CR, EAE or BAE, the standard error can be significantly larger than the standard deviation.

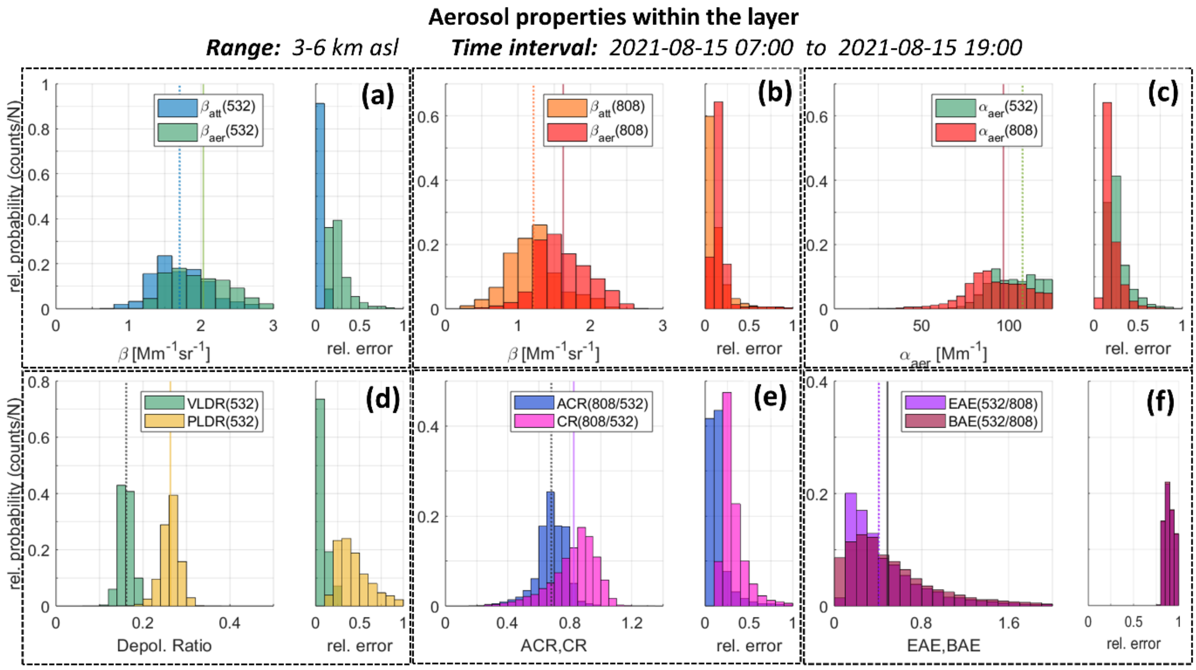

Figure 5.8: Relative probability histograms for all the variables with their corresponding relatives errors derived from CE376 lidar profiles in the range 3 – 6 km asl from 2021-08-15 07:00 UT to 2021-08-15 19:00 UT. Total attenuated and aerosol backscatter (β_{att} and β_{aer}) at 532 nm (a) and 808 nm (b) are presented. Aerosol extinction α_{aer} at 532 and 808 nm (c), VLDR and PLDR at 532 nm (d), ACR(808/532) and CR(808/532) (e), and EAE(532/808) and BAE(532/808) (f) are also presented. Mean values are indicated by lines.

In general, the retrieved intensive aerosol properties, such as $PLDR(532)$ (Fig. 5.8d), CR(808/532) (Fig. 5.8e), EAE(532/808) and BAE (Fig. 5.8f) yield the presence of coarse non-spherical particles in the extended layer up to 6 km asl. Nevertheless, the SD of 101 % shows non consistency of EAE(532/808) over time which can be related to its associated high error and the decrease in EAE observed with the photometer (see Fig. 5.6d). It is important to note that β_{att} values at both wavelengths are comparable to the retrieved β_{aer} values with relative differences up to 25 %. In contrast VLDR(532) (with respect to PLDR(532)) is significantly influenced by the molecular contributions. Still VLDR and ACR, give clues about the shape ($VLDR(532) = 0.16$, non-spherical) and size (ACR(808/532)=0.68, big particles) of the monitored aerosols. Regarding the error associated to each property, one can notice the increasing error while propagating in the retrievals.

Table 5.1: Summary of atmospheric properties within the extended dust layer up to 6 km asl from 07:00 to 19:00 UT on 15 August 2021 at IZO station. The profiles are averaged on 5 minutes and filtered to reduce impact of noise. Mean, median, SD and SE are presented for each property. The relative values in percentage are also presented for SD and SE.

Property	$\lambda\ [nm]$	MEAN	MEDIAN	SD		SE	
				abs.	rel. (%)	abs.	rel. (%)
LR [sr]	532	55	56	8	15	2	4
$\beta_{att}\ [Mm^{-1}sr^{-1}]$		1.71	1.67	0.37	22	0.11	6
$\beta_{aer}\ [Mm^{-1}sr^{-1}]$		2.03	1.94	0.51	25	0.72	36
$\alpha_{aer}\ [Mm^{-1}]$		108	108	17	15	32	30
LR [sr]	808	60	61	3	5	15	25
$\beta_{att}\ [Mm^{-1}sr^{-1}]$		1.21	1.2	0.36	30	0.15	12
$\beta_{aer}\ [Mm^{-1}sr^{-1}]$		1.62	1.57	0.36	22	0.32	20
$\alpha_{aer}\ [Mm^{-1}]$		97	95	21	21	18	19
$VLDR$	532	0.16	0.16	0.01	9	0.02	10
$PLDR$		0.26	0.26	0.02	8	0.12	47
ACR	808/532	0.68	0.68	0.10	15	0.10	15
CR		0.83	0.85	0.15	18	0.27	32
EAE	532/808	0.41	0.32	0.42	101	0.37	90
BAE		0.49	0.37	0.45	94	0.46	95

Moreover, the retrieved aerosol properties are comparable to previous works on dust characterization near the North-Western Saharan desert (Table 5.2). As 808 nm is not a common wavelength used in the lidar community, the 1064 nm is considered instead. CALIOP satellite-based lidar algorithms (CALIPSO V4, Kim et al., 2018) impose effective LR by layer to both of its elastic backscatter signals according to the aerosol type identified. The campaigns SAMUM 1 and 2 (Saharan Mineral dUst ExperiMent) were dedicated to characterize mineral dust near Saharan source. SAMUM-1 was developed on the southern Morocco in May-June 2006 (Heintzenberg, 2009) and SAMUM-2 on Cape Verde in January-February and May-June 2008 (covering winter and summer conditions). Ground based Raman lidar systems and HSRL lidar aboard aircraft were part of both campaigns and their results are showed in Table 5.2 in particular for summer conditions (Floutsi et al., 2023; Freudenthaler et al., 2009; Groß et al., 2013; Müller et al., 2013; Tesche et al., 2009b). A more recent campaign SHADOW (study of SaHAran Dust Over West Africa) included LILAS, Raman high power lidar developed at ATOLL, and was organized in Mbour, Senegal during March-April 2015. Results from SHADOW are also included in Table 5.2 (Hu, 2018; Veselovskii et al., 2016).

Table 5.2: Aerosol properties obtained in previous studies for dust near source. In parenthesis the standard deviations are presented. *CALIPSO algorithms consider and estimated PLDR.

	Location	LR(532) [sr]	LR(1064) [sr]	PLDR (532)	CR (1064/532)	BAE (532/1064)
CALIPSO V4	-	44 (9)	44 (13)	>0.2*	-	-
SAMUM-1 and 2	Morrocco, Cape Verde	55 (7)	55 (13)	0.30 (0.03)	0.77 (0.09)	0.28 (0.16)
SHADOW	Mbour	53 (8)	-	0.30 (0.04)	-	-

5.2.2 Conclusions

A Saharan dust outbreak observed at IZO station (Tenerife, Canary Islands) has been presented. The event developed during summer 2021 is taken as an example of the dust-laden conditions seasonally impacting IZO with major frequency during July and August. During 15 August 2021, both CE376 lidar and CE318-T photometer measurements are used to characterize the dust aerosol properties. Thus, atmospheric properties derived directly from lidar measurements (β_{att}, $VLDR$ and ACR) and aerosol properties (β_{aer}, α_{aer}, $PLDR$, CR, EAE and BAE) retrieved through the inversion scheme (lidar + photometer) were evaluated. Alongside, the estimated errors for each property were presented. Temporal series of AOD, EAE from direct sun photometer measurements, VSD and SSA derived from AOD and almucantar photometer measurements were also presented.

During this event, a layer of dust extending up to 6 km asl (3.6 km above IZO station altitude) was identified and persisted throughout the day. Notably, changes in the internal structure and possibly the aerosol composition (indicated by higher EAE next day) were observed towards midnight. Within the dust layer, as anticipated, coarse non-spherical aerosols predominated, resulting in low values of EAE, BAE (conversely, high values on ACR, CR) and high values of PLDR (similarly, high values on $VLDR$). Moreover, the results are comparable with previous works on Saharan dust characterization using high power lidar systems.

The next section will present as well Saharan dust aerosols but this time transported across Western Europe.

5.3 Saharan dust transport (ATOLL, 31 March- 2 April 2021)

Saharan dust layers transported over ATOLL are frequently observed and monitored. One of these events took place from 31 March to 02 April 2021 (early spring). Figure 5.9 presents images of total column Dust Optical Depth (DOD) at 550 nm showing the predictions of dust transport from North-Western Africa towards Western Europe. The images correspond to the period when the dust event was observed at ATOLL: 31 March 2021 at 12:00 (Fig. 5.9a), 01 April 2021 at 00:00 (Fig. 5.9b), 01 April 2021 at 12:00 (Fig. 5.9c) and 02 April 2021 at 12:00 (Fig. 5.9d). The forecast shows the dust air masses passing over Portugal-Spain towards the Northern Atlantic and reaching UK and Northern France with DOD(550) values up to 0.8. According to the event development, ATOLL is impacted by the highest DOD values on 1 April 2021.

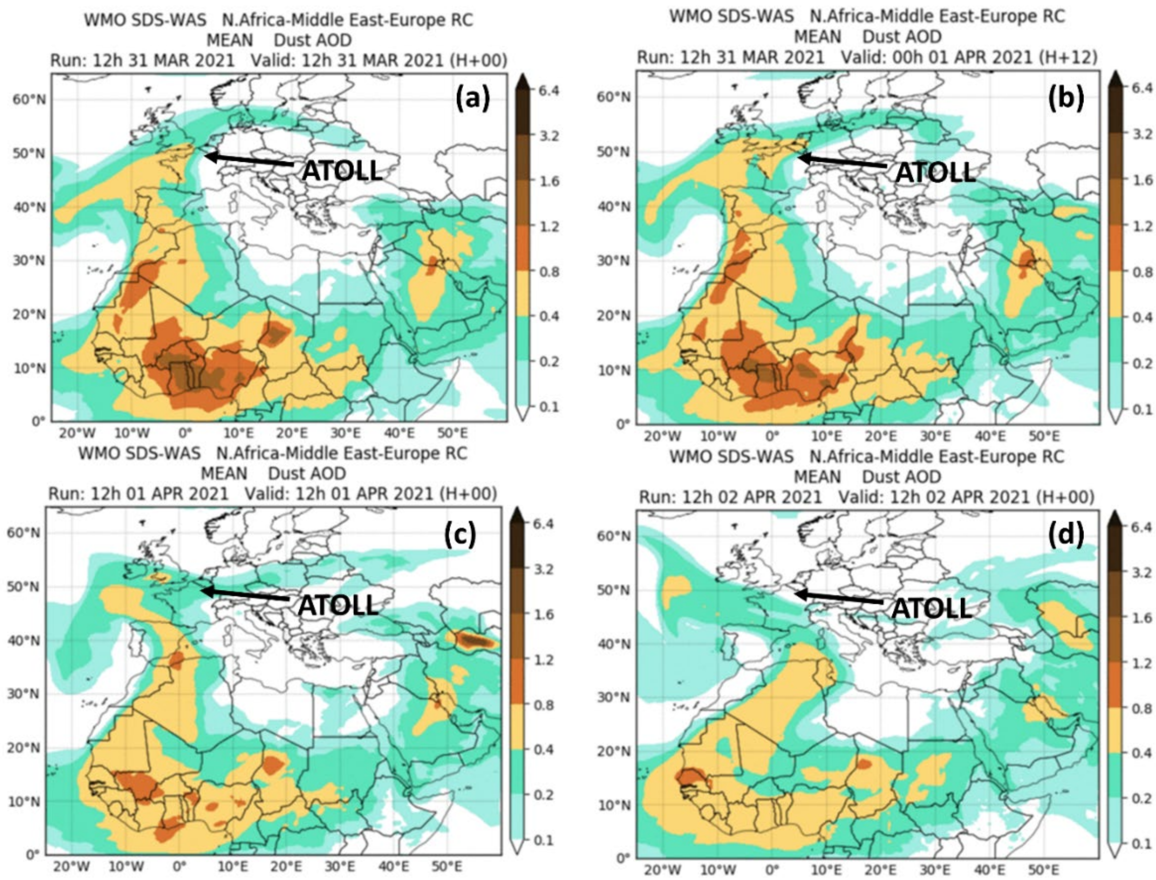

Figure 5.9: Forecast images of total column dust optical depth at 550 nm over Northern Africa, Middle East and Europe. (a) 31 March 2021 at 12:00, (b) 01 April 2021 at 00:00, (c) 01 April 2021 at 12:00 and (d) 02 April 2021 at 12:00. Images are generated with multi-model forecast and are provided by WMO Barcelona Dust Regional Center and the partners of SDS-WAS (*https://dust.aemet.es/products/daily-dust-products*).

To study this event of dust transported over ATOLL, CE376 lidar and CE318-T photometer synergetic measurements are evaluated in the following subsection (Sect. 5.3.1). Moreover, a comparison against a Raman high power lidar system is presented (Sect. 5.3.2) to evaluate the aerosol retrievals obtained with the CE376 lidar.

5.3.1 CE376 Lidar-photometer analysis

During this event, the Saharan dust layer transported over Lille was monitored with both METIS (CE376 lidar) and sun/sky/lunar photometer. An overview of both instruments measurements is presented in Fig. 5.10. On this day, METIS continuous measurements were still performed using the roof window that impacted the depolarization measurements. Nevertheless, the roof window of METIS was open on 1 April at 07:00 UT, represented by the black dashed line in Fig. 5.10 panels (a), (b) and (c). The influence of the window on the measurements can be observed on 532 nm depolarized channels. VLDR values are the most impacted, being higher by 0.02 when METIS is with the roof window (see Fig. 5.10c). More information on the depolarization measurements at different operational conditions were presented in Chapter 3 Sect. 3.5.3. For this case study, only measurements under "without window" conditions are considered for analysis. Furthermore, the blind zone, defined from the overlap function estimation (i.e., r_o where O(r) <0.1), during this period for each channel were: $r_o(532par) = 0.42\ km$, $r_o(532per) = 0.6\ km$ with and $r_o(808tot) = 0.15\ km$. Note that the first 2 km of the total signal RCS at 532 nm are influenced by relative errors of 5 % at 2 km going towards 20 % at 500 m due to the overlap estimations. In the case of RCS at 808 nm, the influence of overlap error goes from 5 % at 1 km towards 10 % at 150 m.

The dust event at ATOLL had a period of strong aerosol loading during the night of 31 March 2021 to the afternoon of 1 April 2021, as seen by METIS and photometer observations (Fig. 5.10) and estimated by the DOD multi-model forecast (Fig. 5.9). Intrusions of aerosol layers between 1.5 km to 6 km asl were observed, with high VLDR values, up to 0.25, indicating the presence of non-spherical aerosols. While multiple layers are observed on the β_{att} height-temporal variations at both wavelengths (Fig. 5.10 (a) and (b)), VLDR(532) suggests the presence of one likely homogeneous layer instead (Fig. 5.10c). AOD_{ph} values at 532 nm and 808 nm increase up to 1 and 0.9 respectively. EAE_{ph} (532/808) decreases from 1.4 to 0.2 associated to the increase of coarse mode particles concentration.

Additionally, VSD retrievals from photometer observations during 1 April 2021 (Fig. 5.11a) show the strong predominance of aerosols in the coarse mode with an effective radius at 1.7 µm. Thus, with the identified non-spherical coarse particles, the presence of dust is confirmed.

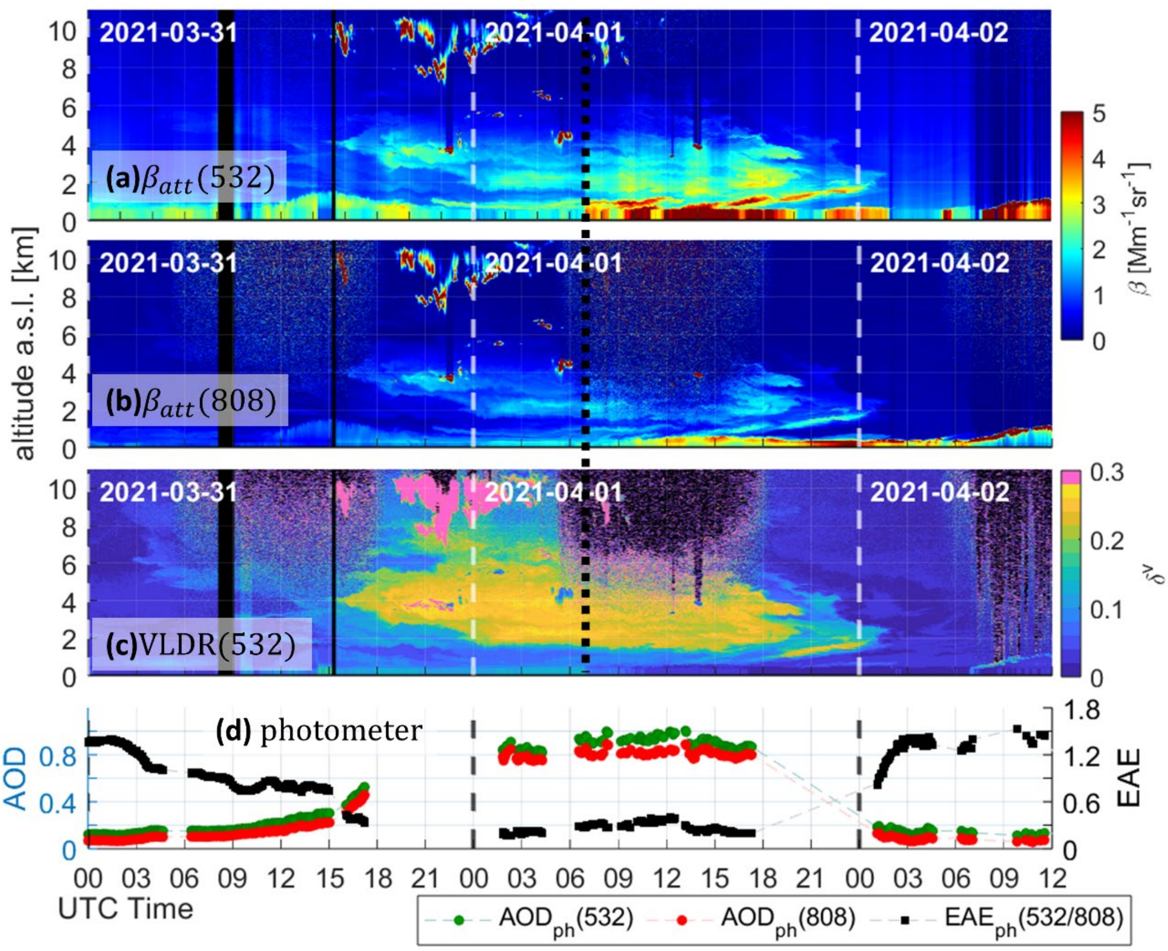

Figure 5.10: Overview of synergetic measurements of METIS lidar and photometer during an event of Saharan dust transport from 2021-03-31 to 2021-04-02. Heigh-temporal variation of (a) $\boldsymbol{\beta_{att}}$ at 532 nm, (b) $\boldsymbol{\beta_{att}}$ at 808 nm, (c) VLDR at 532 nm, and (d) time series of AOD_{ph} at 532 nm and 808 nm with $EAE_{ph}(532/808)$ derived from photometer. Black dashed line in (a), (b) and (c) indicates the change of measurements conditions for METIS lidar.

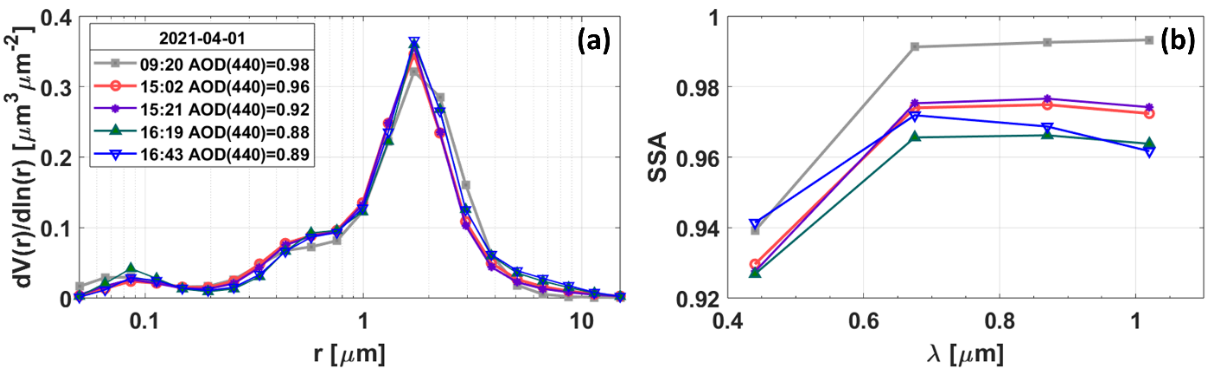

Figure 5.11: (a)VSD and (b) SSA(λ) derived from photometer sky almucantar and AOD measurements during 2021-04-01 at ATOLL. Data is level 2 from AERONET version 3 algorithms.

Moreover, spectral SSA derived from the photometer retrievals (Fig. 5.11b) indicate higher absorption efficiency at shorter wavelengths (SSA~ 0.93-0.94) than at longer wavelengths (SSA~ 0.96-0.99), similar to the results presented for dust near source at IZO (Sect. 5.2.1). Towards the night of 1-2 April 2021, the dust layers slowly vanish. A shallow boundary layer (<1000 m) with a strong inversion on the top, constrains the mixing of dust within the boundary layer. During the day of 2 April 2021 the $EAE_{ph}(532/808)$ increases up to 1.5 and the VLDR decreases below 0.1 showing the end of the dust event.

Back-trajectories analysis

The NOAA HYSPLIT back trajectory analysis (Stein et al., 2015) is used to identify the possible sources of the transported aerosols. In this case, the GFSQ (Global Forecast System 0.25 degrees) dataset is considered as the meteorological input for the model and the vertical velocity of air mass is modeled using vertical motion velocity calculation; the model is run for 5 days of transport. Figure 5.12 presents back-trajectories ending at 3 altitudes above ATOLL platform (500 m, 2 km and 4 km) on 1 April 2021 at 00:00 UT (Fig. 5.12a), 12:00 UT (Fig. 5.12b) and 21:00 UT (Fig. 5.12c). These back-trajectories confirm that the air masses between 1.5-6 km asl follow the paths of transported dust as forecasted by the DOD images (Fig. 5.9). Contrary, at lower altitudes within the ABL, back-trajectories suggest different sources along the day probably influenced by urban/industrial emissions (Fig. 5.12a and Fig. 5.12b) as reported for ATOLL by previous studies (Velazquez Garcia, 2023; Velazquez-Garcia et al., 2023). In this context, the lidar observations showing two distinct aerosol contributions, below and above the ABL, is supported.

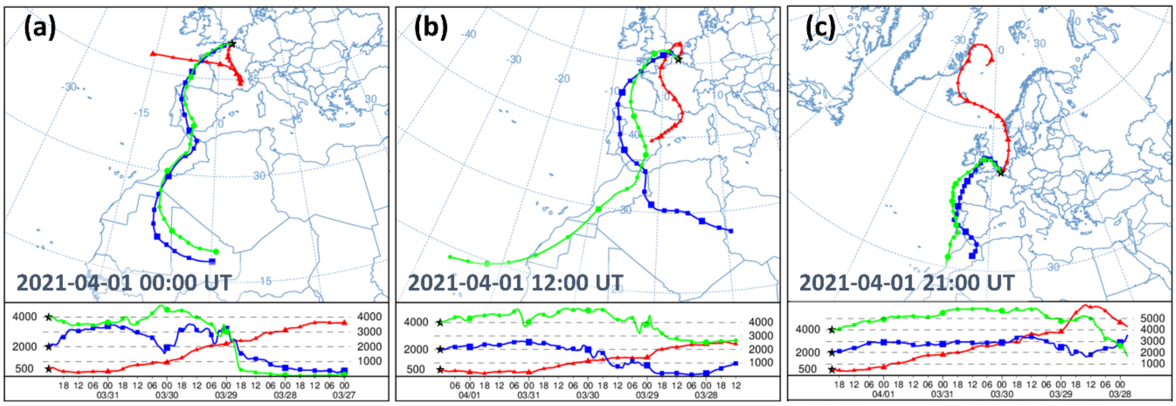

Figure 5.12: NOAA HYSPLIT back-trajectories ending at 500 m, 2 km and 4 km above ATOLL (Lille, France). Different ending hours during 1 April 2021 are considered: (a) 00:00, (b) 12:00 and (c) 21:00 UT. GFSQ meteorological data is used to run the model for 5 days of transport. The web interface was used to obtain these results (https://www.ready.noaa.gov/HYSPLIT_traj.php).

Lidar observations analysis during daytime

During daytime of 1 April 2021, lidar signals are rapidly attenuated due to the high aerosol loading ($AOD_{ph}(532)$~1) under the presence of the lofted 5 km dust air mass, as well as due to the increasing background noise. Thus, low SNR is encountered above the layers at both wavelengths, making difficult to find a reference zone (free of aerosol region) for the inversion procedure. In consequence, aerosol retrievals were impacted by high uncertainties or were not even possible, meaning that convergence to an effective LR in the inversion was not achieved. Therefore, only atmospheric (molecules + aerosol) properties directly derived from measurements are used for further analysis of the dust-laden conditions.

Figure 5.13 presents profiles averaged every 2 hours for the properties derived from 2021-04-01 07:00 UT to 2021-04-02 01:00 UT. Averaging to 2 hours during day time enabled SNR>1.5 up to 8 km asl and 4 km asl for signal at 532 nm and 808 nm respectively. Thus two time periods are determined, one from 07:00 to 17:00 UT 2021-04-01 characterized by the homogeneous VLDR(532) values from 1.5 km asl up to to~6 km asl (Top panel Fig. 5.13); the second period from 2021-04-01 17:00 UT to 2021-04-02 01:00 UT is characterized by the dust layers fading away (Bottom panel Fig. 5.13). Moreover, the associated errors to each property are presented in Fig. 5.14.

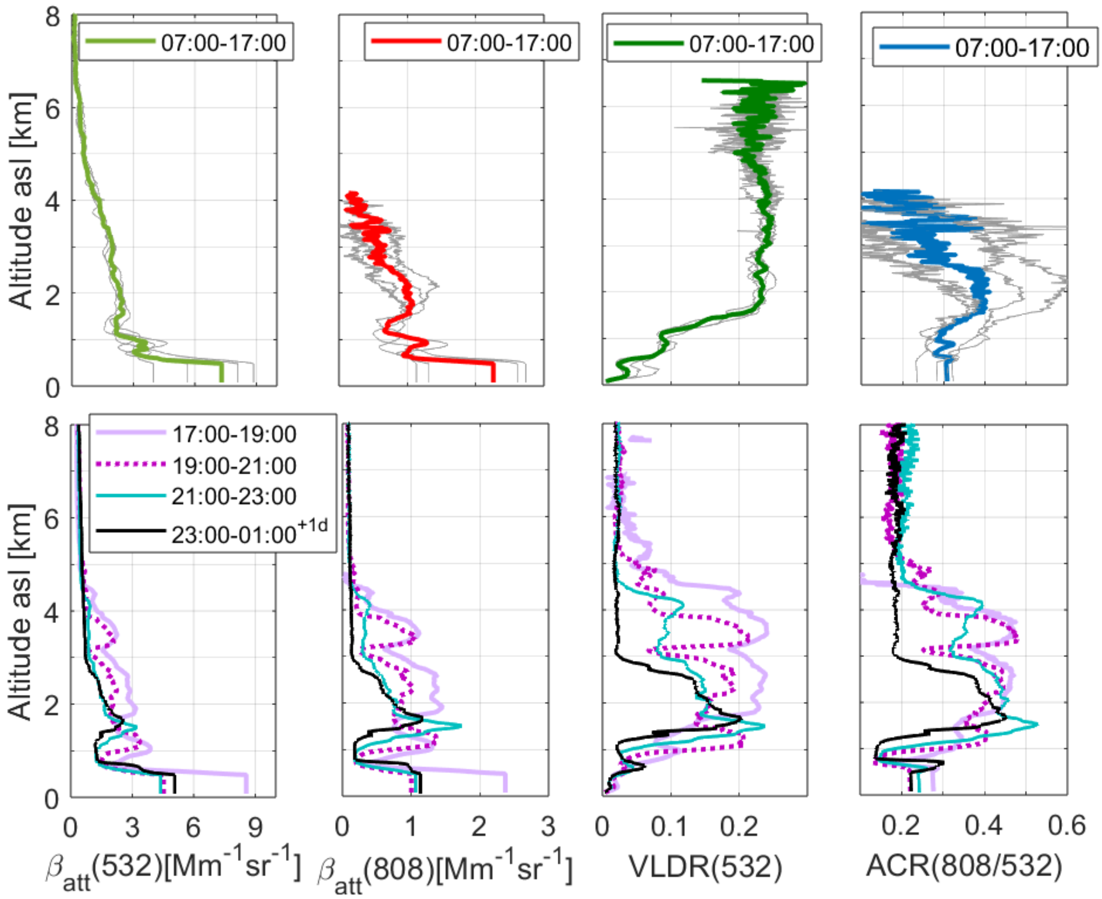

Figure 5.13: Atmospheric optical properties derived from lidar measurements during an event of dust transported over ATOLL (Lille, France) on 1 April 2021. Profiles averaged to 2 hours from 07:00 UT 2021-04-01 to 01:00 UT 2021-04-02 are considered and presented in two panels. Top panel includes averaged profiles from 07:00 to 17:00 UT 2021-04-01, and bottom panel includes averaged profiles from 17:00 UT 2021-04-01 to 01:00 UT 2021-04-02. From left to right, the properties presented are β_{att} at 532 nm (a, e), β_{att} at 808 nm (b, f), $VLDR$ at 532 nm (c, g) and ACR(808/532) (d, h).

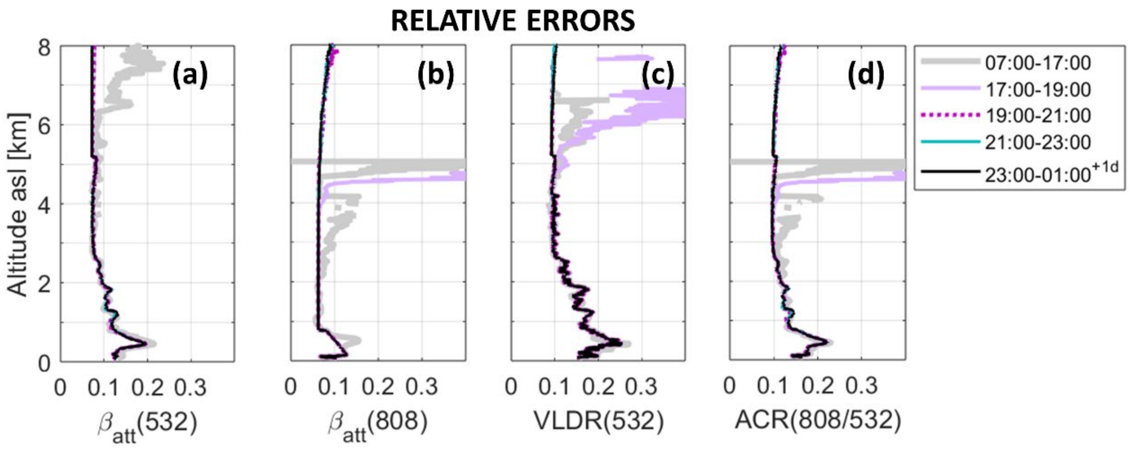

Figure 5.14: Relative errors for the properties presented in Fig. 5.13.

The VLDR values within the lofted dust air masses (1.5-6 km asl) during the first period are likely constant (0.23 ± 0.02). Due to noise (inducing larger errors) at higher altitudes, ACR is largely impacted above 3 km asl during day-time, as can be observed in Fig. 13d contrasting with its errors in Fig. 14d (in gray line). Nevertheless, ACR provides information on the stratification within the dust air mass contrary to the VLDR values. On the other hand, the second time period after 17:00 UT 2021-04-01 (bottom panel Fig. 13) is characterized by the decrease of the dust layer width accompanied by the reduction of $VLDR$ values (~0.15). The stratification within the dust air mass is more evident in all the parameters towards the end of the event. Moreover, lower ACR values (with respect to the dust case at IZO) are detected, influenced by the ABL attenuation (Burton et al., 2013; Omar et al., 2009). Moreover, the results over all the observations presented are summarized in Table 5.3.

Table 5.3: Summary of properties derived directly from the lidar measurements on 2021-04-01 and presented in Fig. 5.13 and Fig.514. The absolute and relative values are also presented for SD and SE.

Property	λ [nm]	MEAN	MEDIAN	SD		SE	
				abs.	rel. (%)	abs.	rel. (%)
$\boldsymbol{\beta_{att}}$ [$\boldsymbol{Mm^{-1}sr^{-1}}$]	532	1.8	1.9	1	50	0.2	11
$\boldsymbol{\beta_{att}}$ [$\boldsymbol{Mm^{-1}sr^{-1}}$]	808	0.7	0.8	0.3	42	0.1	14
$\boldsymbol{VLDR}$	532	0.19	0.22	0.06	32	0.02	10
$\boldsymbol{ACR}$	808/532	0.39	0.41	0.12	31	0.05	13

LILAS Mie-Raman high power lidar monitored as well this particular event of Saharan dust transport. Taking advantage of its capacity to provide independent backscatter and extinction coefficients, comparisons between METIS CE376 lidar and LILAS are performed for evaluation. The results of the comparisons are presented in the next subsection.

5.3.2 METIS and LILAS retrievals comparisons

For comparisons of METIS and LILAS, averaged profiles on 1 April between 20:00 to 22:00 UT were used, when Raman measurements from LILAS were available. Aerosols optical properties were retrieved with the modified two-wavelength method for METIS and Raman inversion is used for LILAS. Molecular coefficients were calculated using the radiosonde data taken at 00:00 UT on 2 April 2021 from the station Herstmonceux. Lunar measurements were not acquired until later that night, so, the two closest pair of AOD_{ph} were considered to constrain the inversion for METIS at 1 April 2021 17:50 and 2 April 2021 00:45 UT. Hence, backscatter and extinction profiles at 532 nm and 808 nm for METIS and at 532 nm for LILAS were retrieved and are presented in Fig. 5.15 panels (a) and (b). VLDR and PLDR at 532 nm for both lidars are also compared (Fig. 5.15c), as well as LR (Fig. 5.15f). The ACR and CR of 808-532 nm from METIS are presented (Fig. 5.15e) as well as EAE (532/808) from METIS and the photometer (Fig. 5.15d). To avoid artifacts on the retrievals induced by the blind zone of 532 nm, RCS values below 500 m are considered constant for both wavelengths. Likewise, PLDR, EAE and CR values are not shown when the aerosol backscatter at 532 nm is less than 0.3 Mm^{-1} sr^{-1}.

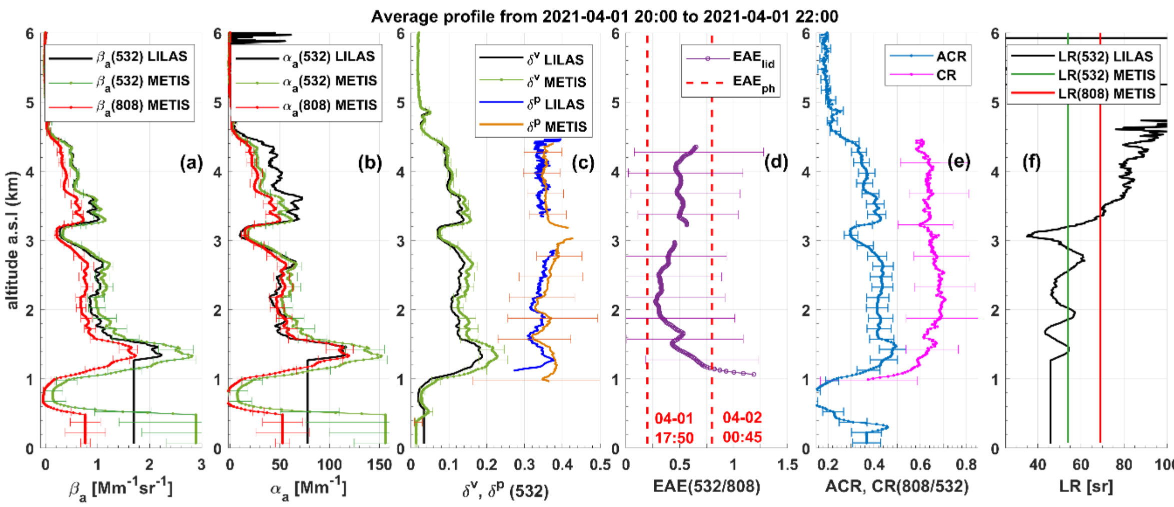

Figure 5.15: Aerosol optical properties retrieved from METIS and comparison with LILAS retrievals for the averaged measurements between 20:00 to 22:00 UTC on 2021-04-01. Vertical profiles of (a) Backscatter, (b) Extinction and (f) LR at 532 and 808 nm for METIS and 532 nm for LILAS, (c) VLDR and PLDR at 532 nm for METIS and LILAS, (d) EAE (532/808) from METIS and the 2 closest values from the photometer, and (e) ACR, CR (808/532).

Backscatter and extinction profiles comparisons showed good agreement between both lidars. The differences in extinction observed are related to the constant LR of 54 ± 3 sr for METIS retrievals at 532 nm. From the profile of LR at 532 nm for LILAS (Fig. 5.15f), we can see that the first layer between 1.5-3 km asl is 48 sr on average, in contrast with 72 sr of the second layer between 3.3-4.7 km asl. Thus, a better agreement in the lower layer than within the second layer especially for extinction coefficients is observed. From METIS retrievals, the first layer extinction values are on average 61 ± 14 Mm^{-1} and 52 ± 10 Mm^{-1} at 532 nm and 808 nm, respectively. Extinction values in the second layer are in contrast lower, with 43 ± 3 Mm^{-1} and 35 ± 6 Mm^{-1} at 532 nm and 808 nm, respectively. Moreover, the LR retrieved for 808 nm is 69 ± 4 sr.

Absolute differences up to 0.02 for METIS VLDR profile with respect to LILAS are observed. METIS shows VLDR and PLDR values within the two layers of 0.14 ± 0.02 and 0.36 ±0.05, respectively. Lower EAE values for the first layer (0.4 ± 0.1) were observed compared to 0.5 ± 0.1 for the second layer. The ACR (808/532) and CR (808/532) profiles show values of 0.42 ± 0.05 and 0.69 ± 0.14, respectively, for the lower layer and 0.38 ± 0.04 and 0.65 ± 0.12 for the second layer. These results suggest the presence of two different dust layers, with larger dust aerosols in the lower layer, which it is also shown in the LR profile from LILAS lidar.

Moreover, the results presented in this section are comparable to values reported in previous works for Saharan dust transported towards Northern Europe (Table 5.4).

Table 5.4: Aerosol properties obtained in previous studies for transported dust. In parenthesis the standard deviations are presented. *CALIPSO algorithms consider and estimated PLDR. **This multi-site EARLINET study considered VLDR values rather than PLDR.

	Location	**LR(532) [sr]**	**LR(1064) [sr]**	**PLDR (532)**	**EAE (532/1064)**	**BAE (532/1064)**
This work	France	54 (3)	LR(808) 69 (4)	0.36 (0.05)	EAE(532/808) 0.4-0.5	
CALIPSO V4 (Kim et al., 2018)	-	55 (22)	48 (24)	> 0.2*	-	-
(Ansmann et al., 2003)	Poland, UK, Germany	40-80	40-80	0.15-0.25**	-	0-0.5
(Haarig et al., 2022)	Germany	50 (5)	69 (14)	0.29 (0.02)	-0.08 (0.2)	0.35 (0.26)

5.3.3 Conclusions

In this section, an event of Saharan dust transported above ATOLL platform (Lille, France) was studied using METIS CE376 lidar and CE318-T photometer (31 March 2021 to 2 April 2021). Due to the high attenuation of signal within the dust layers, only volume properties derived directly from lidar measurements (β_{att}, $VLDR$ and ACR) were evaluated for the entire day. Towards the end of the event, at night time, lower aerosol loads were encountered. Therefore, aerosol properties (β_{aer}, α_{aer}, $PLDR$, CR, EAE) retrieved through the inversion scheme (lidar + photometer) were investigated and compared against co-located LILAS Mie-Raman lidar. Alongside, the estimated errors for each property derived from the CE376 were presented. Temporal series of AOD, EAE from direct sun photometer measurements, VSD and SSA derived from AOD and almucantar photometer measurements were also presented.

The findings suggest that the elevated dust air masses, originated from North Western Sahara and traversing above ATOLL, maintained their characteristics as pure dust without significant interaction with other atmospheric components. While VLDR values indicated a quite homogeneous dust layer, signs of stratification within the extensive volume of air were observed in β_{att} and ACR instead. Moreover, METIS showed VLDR values 10 % higher than LILAS under the same operational conditions (without window, controlled temperature). This reduced bias likely comes from differences on the optical design proper to the instruments and showcase the capabilities of CE376 lidar to retrieve depolarization properties comparable to complex high power lidars.

5.4 Dust and Smoke mixture (ATOLL, July 2022)

Several heatwaves crossed Europe during spring-summer 2022, meaning that air masses from the equatorial region (North Africa) moved northwards, given by the synoptical weather conditions, pushing temperatures up in several areas, especially in the Western Europe. The unusual long periods of heat since spring intensified the dry conditions during summer.

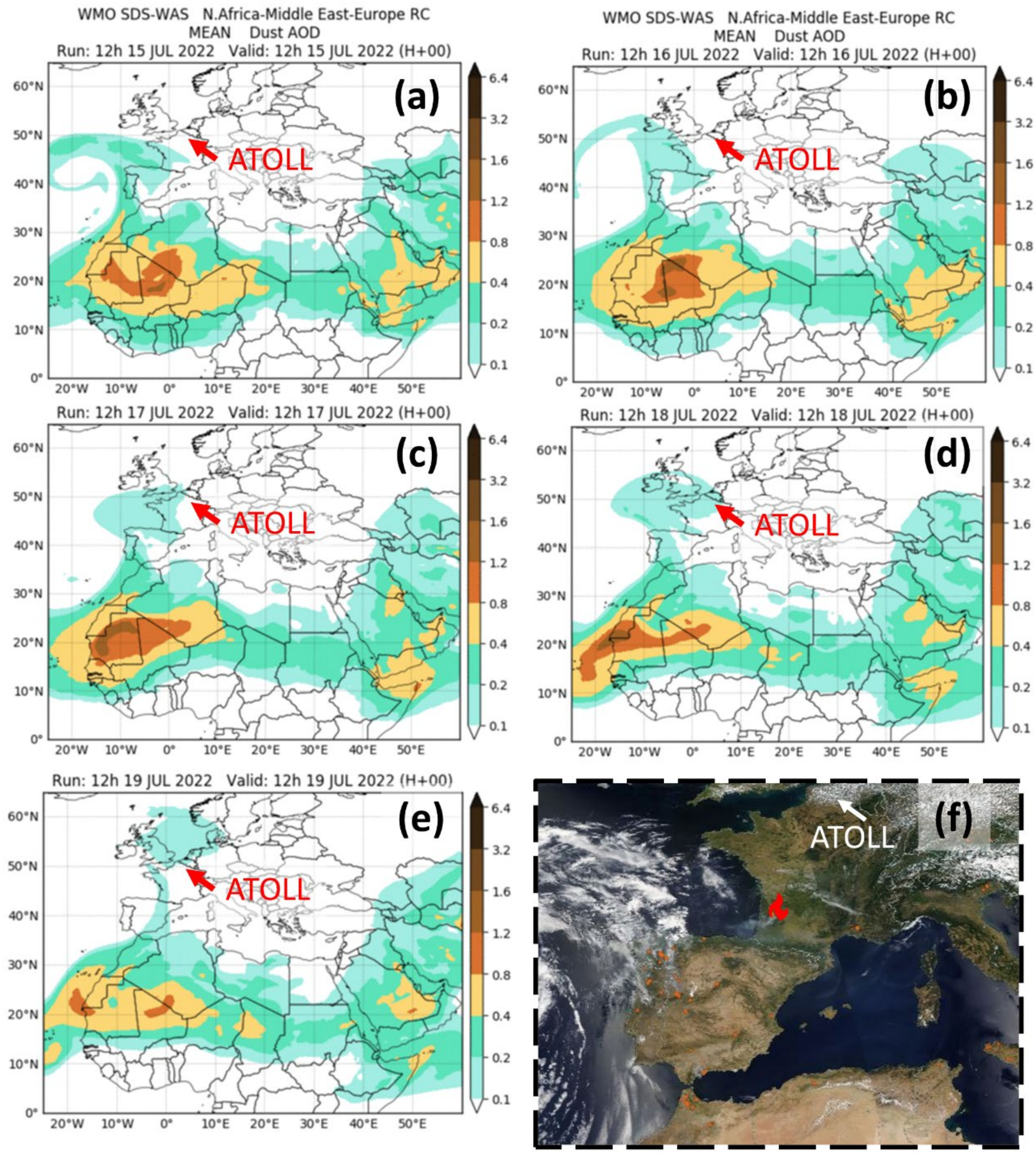

Figure 5.16: Forecast images of total column dust optical depth at 550 nm over Northern Africa, Middle East and Europe, and satellite image showing active fires over Western Europe. Forecast images correspond to (a) 15 July 2022 at 12:00, (b) 16 July 2022 at 12:00, (c) 17 July 2022 at 12:00, (d) 18 July 2022 at 12:00 and (e) 19 July 2022 at 12:00. (f) MODIS-AQUA True Color Image for 15 July 2022 over Western Europe is also presented, where the thermal anomalies (active fires) are indicated by orange dots and a red flame for Gironde Fires. Forecast images are generated with multi-model forecast and are provided by WMO Barcelona Dust Regional Center and the partners of SDS-WAS (*https://dust.aemet.es/products/daily-dust-products*). MODIS products are available through NASA Worldview Snapshots (https://wvs.earthdata.nasa.gov).

Moreover, due to the vegetation dryness and the extreme high temperatures, multiple fires were detected in Southwestern Europe in July-August 2022. Unprecedented wildfires have broken out on 12 July 2022 in the Gironde department, Southwestern France, intensified by a heatwave passing, over ~270 km^2 of burned surface were accounted in the region with the highest forest losses in France. During this event, biomass burning aerosols injected to the atmosphere by the wildfires in Western Europe got mixed with the mineral dust transported within the hot air masses.

DOD(550) images from 15 July 2022 to 19 July 2022 (Fig 5.16a to Fig 5.16e) show the evolution of the dust transport path from the North Western Sahara passing through Portugal-Spain passing above the Atlantic towards France. The images correspond to the model run at 12:00 for each day. The active fires are also indicated on top MODIS image for the 15 July 2022 (Fig. 5.16f), and are located on the predicted path of dust for that day. Moreover, according to the dust transport path, ATOLL site was most likely to be influenced by DOD(550) values between 0.1 and 0.2 during 17 and 18 July 2022. Therefore, at the time that the heatwave traversed Lille, both dust and smoke were detected in the atmospheric column.

In the following subsections, the description of the event seen by the remote sensing instrumentation, METIS CE376 lidar and CE318-T photometer, installed at ATOLL is presented. Moreover, comparisons of retrievals against LILAS are also evaluated (Sect. 5.4.2).

5.4.1 CE376 lidar-photometer analysis

For this case, METIS was performing measurements under the current operational conditions, i.e. adapted roof window and air conditioning. Also, METIS overlap corrections induce errors in the first 2 km of the RCS at 532 nm, from 3 % at 2 km going towards 20 % at 600 m. For RCS at 808 nm the influence of overlap error goes from 5 % at 600 m towards 20 % at 100 m. For retrievals using both RCS, values are therefore considered constant below 600 m. To assess the continuity of the aerosol optical properties, the closest data points are used to constrain the inversion when measurements from photometer are not available.

An overview of the retrieved aerosol properties from METIS and photometer is presented in Fig. 5.17 for the period of 17 July to 20 July 2022 when the dust and smoke particles were detected at ATOLL. From height-temporal variations in Fig. 5.17 panels (a) to (d), two periods can be distinguished during the event. On 17 July 2022, a predominant depolarizing layer of ~1.5 km width and quite homogeneously distributed is observed, in contrast to the three compacted layers (with different depolarization ratios) detected from 18 July until 19 July 2022 12:00 UT. Contrariwise to the complexity observed with the lidar, the temporal series from the photometer are fairly stable (Fig. 5.17e).

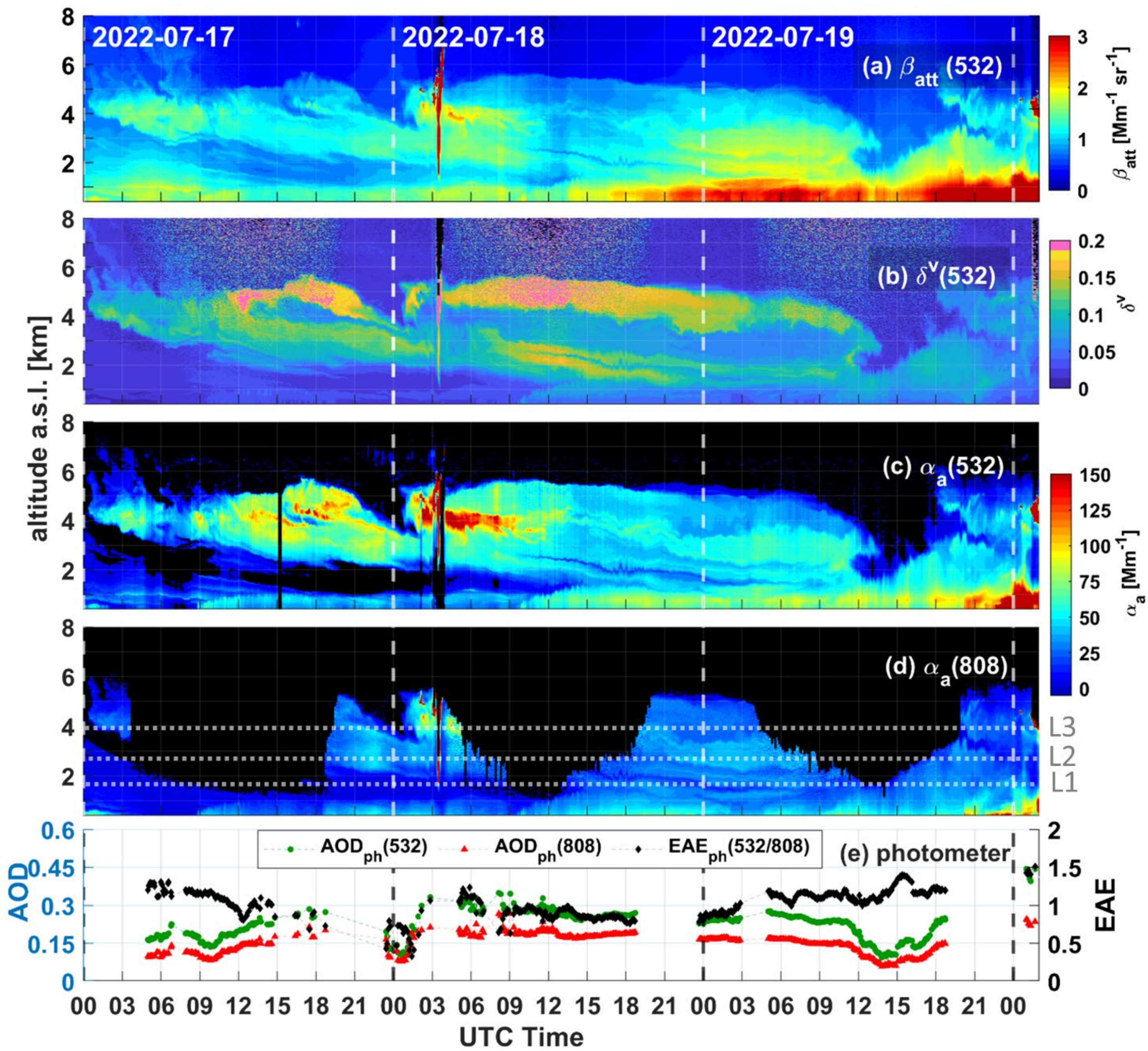

Figure 5.17: Overview of atmospheric optical properties from synergetic measurements of METIS lidar and sun/lunar photometer at ATOLL platform from 17 to 20 July 2022. Height-temporal variation of (a) β_{att} and (b) VLDR at 532 nm, aerosols extinction at (c) 532 nm and (d) 808 nm, and (e) time series of AOD$_{ph}$ at 532 nm and 808 nm with EAE$_{ph}$ 532/808 derived from the photometer. The layer center altitudes for layer 1 (L1), layer 2 (L2) and layer 3 (L3), identified during 18 and 19 July 2022, are indicated by dashed white lines in panel d.

The VSD distributions during the event (Fig. 5.17) showed the predominance of three aerosol size ranges, one in the fine mode centered at 0.11 µm of radius, and two in the coarse mode centered at 1.7 µm and 5 µm. On 18 July 2022 (Fig. 5.18b) 5 VSD were retrieved, all having higher contributions than the day before (Fig. 5.18a), only one VSD in the morning is offset to higher values (0.15 µm) for the fine mode peak. On 19 July 2022 (Fig. 5.18c), 7 VSD were retrieved, 4 of them in the morning showing the same shape as the ones from 18 July. The rest of the VSD show higher contribution at 5 µm size, representing the conditions after 15:00 on 19 July which correspond to a drop on the AOD values and the vanishing of the layers.

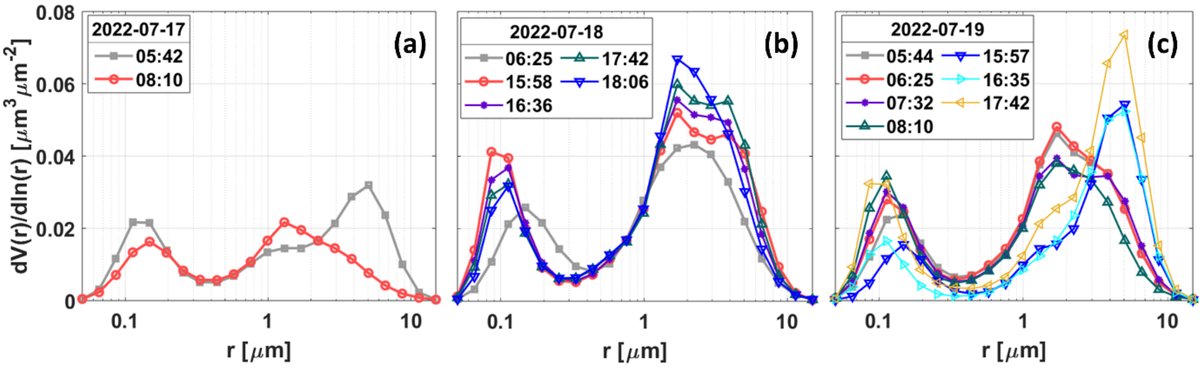

Figure 5.18: VSD derived from photometer sky almucantar and AOD measurements during (a) 2022-07-17, (b) 2022-07-18 and (c) 2022-07-19 at ATOLL. Data is level 2 from AERONET version 3 algorithms.

Therefore, the presence of both smoke (fine mode) and dust (coarse mode) aerosols is confirmed during the entire event by the VSD (Fig. 5.18), with mainly two different stages in the aerosol vertical distributions (Fig 5.17). Furthermore, towards 12:00 UT on 19 July 2022, the 3 layers disappear while the boundary layer height increases and probably mixes with the layer closer to the ground.

Back-trajectories analysis

During 17 July 2022, a layer extended between ~3 km to 5 km asl is lofted on top of apparently clean air, as indicated by the low values on VLDR and extinction height-temporal variations (Fig. 5.17 panels b, c and d). Likewise, HYSPLIT back-trajectories ending at 1.5 km and 4 km above ATOLL corroborate that different air masses are impacting the site (Fig. 5.19). The transport path of the aerosol layer detected at ~4 km asl (Fig. 5.19b) coincide with the dust transport track forecasted on the DOD(550) images, i.e., crossing the Portugal-Spain fires (Fig. 5.16). Moreover, the cleaner air intrusion (~1.5 km asl) is influenced by air masses transported from higher altitudes above the North Atlantic Ocean (Fig. 5.19a). The back-trajectories are modeled for 3 days of transport with GFSQ meteorological database.

During the second period on 18-19 July 2022, the layer from the day before now reduced to ~0.5 km width is descending from 3 km towards 1.5 km asl accompanied by 2 separated layers above it. In particular, we focus our attention on the afternoon of 18 July 2022 to early morning of 19 July 2022, where quite stable AOD_{ph} and EAE_{ph} are observed. Back-trajectories ending at 3 altitudes, 1.7 km (L1 in red), 2.7 km (L2 in blue) and 4 km (L3 in green) above ATOLL, and at different arrival hours (model run for 5.5 days) are presented in Fig. 5.20. The altitudes considered representing the layers observed are also indicated as L1, L2, L3 in Fig. 5.17d.

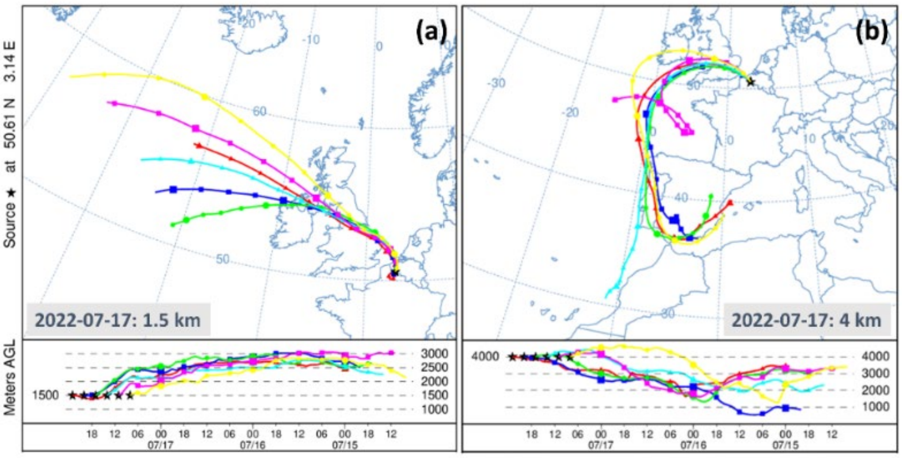

Figure 5.19: NOAA HYSPLIT back-trajectories ending at 1.5 km (a) and 4 km (b) above ATOLL (Lille, France). Each trajectory corresponds to a different ending hour during 17 July 2022, every 3 h since 09:00 UT. GFSQ meteorological data is used to run the model for 5 days of transport. The web interface was used to obtain these resutls (https://www.ready.noaa.gov/HYSPLIT_traj.php).

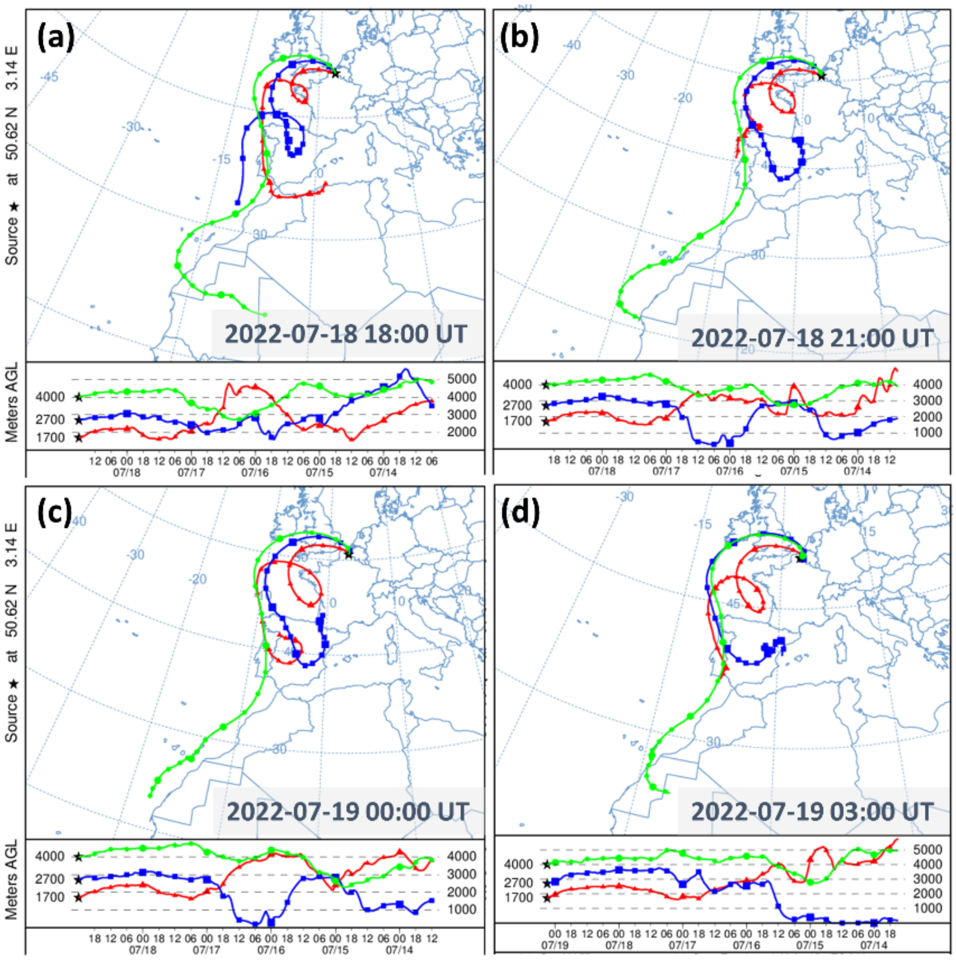

Figure 5.20: NOAA HYSPLIT back-trajectories ending at 1.8 km, 2.7 km and 4 km above ATOLL (Lille, France). Different arrival times are considered, 18:00 UT (a) and 21:00 UT (b) on 18 July 2022, 00:00 UT (c) and 03:00 UT (d) on 19 July 2022. GFSQ meteorological data is used to run the model for 5 days of transport. The web interface was used to obtain these resutls (https://www.ready.noaa.gov/HYSPLIT_traj.php).

From the back-trajectories, it can be seen that similarly to the day before (17 July 2022) the layer between 3.2 to 4.5 km asl (L3 in green) follows the path of *dust crossing Portugal fires* as predicted by DOD images. In contrast, back-trajectories for the layer between 2.4 km and 3.2 km asl (L2 in blue), with lower VLDR values and higher extinction (Fig. 5.17), show that air masses follow a quite different path than the transported dust. This time the source is identified at South West France and North East Spain, closer to the Gironde region where active fires were detected. On the other hand, L1 in red show that air masses are transported over or near the dust transport path and pass over active fires. Therefore, the layer L2 appears to be under higher influence of smoke aerosols rather than dust like L1 and L3.

Table 5.5 summarize the results obtained during the second period of this event, where three layers are identified. Profiles averaged to 1 hour between 2022-07-18 18:00 UT to 2022-07-19 09:00 UT are used and layers are defined as L1 (1.5-2.2 km asl), L2 (2.4-3.2 km asl) and L3 (3.2-4.5 km asl). The mean, median, Standard Deviation (SD) of the mean and Standard Error (SE) are presented for each layer and property obtained.

From the results obtained in this work, L2 is well differentiated from the other 2 layers due to its PLDR values (0.1 ± 0.01) which are in accordance with reported values in previous works for transported smoke (Table 5.6). Likewise, back-trajectories confirm the higher interaction of the L2 air masses with active fires than L1 and L3. In contrast PLDR values for L1 (0.19 ± 0.04) and L3 (0.25 ± 0.06) are in accordance with previous observations of dust and smoke mixtures (Table 5.7). It is worth to mention that the considered dust-smoke mixture studies correspond mostly to observations during SAMUM campaigns, i.e., close to Saharan desert and fires in the Sahel region. Previous studies showed that for mixtures of dust-smoke, lower values of PLDR correspond to higher predominance of smoke over dust and the other way around (Ansmann et al., 2009; Tesche et al., 2009b).

Table 5.5: Summary of atmospheric properties within 3 layers from 2022-07-18 18:00 UT to 2022-07-19 09:00 UT at ATOLL station. The layers are defined as L1 (1.5-2.2 km asl), L2 (2.4-3.2 km asl) and L3 (3.2-4.5 km asl). The profiles are averaged (1 hour) and filtered. Mean, median, SD, SE are presented for each property.

Property	$\lambda\ [nm]$	MEAN			MEDIAN			SD			SE		
		L1	L2	L3	L1	L2	L3	L1	L2	L3	L1	L2	L3
LR [sr]	532	39			40			3			2		
$\beta_{att}\ [Mm^{-1}sr^{-1}]$	532	1.7	1.6	1	1.8	1.7	1.1	0.2	0.2	0.2	0.1	0.1	0.1
$\beta_{aer}\ [Mm^{-1}sr^{-1}]$	532	1.1	1.4	0.9	1.2	1.4	1	0.2	0.2	0.2	0.1	0.1	0.1
$\alpha_{aer}\ [Mm^{-1}]$	532	43	53	36	45	54	37	8	6	10	3	3	2
LR [sr]	808	38			38			2			2		
$\beta_{att}\ [Mm^{-1}sr^{-1}]$	808	0.9	0.9	0.6	0.9	1	0.7	0.1	0.1	0.2	0.1	0.1	0.1
$\beta_{aer}\ [Mm^{-1}sr^{-1}]$	808	0.8	1	0.7	0.8	1	0.7	0.1	0.1	0.2	0.1	0.2	0.1
$\alpha_{aer}\ [Mm^{-1}]$	808	30	36	26	31	37	27	4	5	7	7	9	7
$\boldsymbol{VLDR}$	532	0.09	0.06	0.11	0.09	0.06	0.12	0.02	0.01	0.03	0.01	0.01	0.01
$\boldsymbol{PLDR}$	532	0.19	0.10	0.25	0.19	0.1	0.27	0.04	0.01	0.06	0.02	0.01	0.03
$\boldsymbol{ACR}$	808/532	0.5	0.55	0.52	0.49	0.57	0.54	0.05	0.06	0.12	0.03	0.04	0.08
$\boldsymbol{CR}$	808/532	0.73	0.71	0.71	0.72	0.74	0.74	0.12	0.11	0.13	0.15	0.16	0.21
$\boldsymbol{EAE}$	532/808	0.87	0.91	0.96	0.90	0.83	0.83	0.31	0.32	0.39	0.50	0.50	0.60
$\boldsymbol{BAE}$	532/808	0.78	0.83	0.82	0.80	0.72	0.7	0.38	0.4	0.45	0.48	0.50	0.60

Table 5.6: Properties obtained in previous studies for transported smoke in the troposphere. In parenthesis the standard deviations are presented if they are provided. *CALIPSO algorithms consider and estimated PLDR.

	Location	LR(532) [sr]	LR(1064) [sr]	PLDR(532)	CR(1064/532)	BAE(532/1064)
This work	France	39 (3)	LR(808)= 38 (2)	0.1 (0.01)	CR(808/532)= 0.71 (0.16)	BAE(532/808)= 0.83 (0.5)
CALIPSO V4 (Kim et al., 2018)	-	70 (16)	30 (18)	<0.08*	-	-
HSRL-1 aerosol classification (Burton et al., 2013)	-	55-73	55-73	0.04-0.09	0.53-0.52	-
(Alados-Arboledas et al., 2011)	Spain	60-65	-	-	-	-
(Veselovskii et al., 2022)	France	80 (12)		0.03 (0.01)	-	1.2 (0.2)

Moreover, in previous studies using Raman-Mie lidars, the LR at 1064 nm are not usually provided since observations at this wavelength were obtained through elastic channels for the majority of the lidar systems, nevertheless BAE is usually calculated by using Klett inversion at 1064 nm channel. For comparisons of the results obtained in this work against previous studies, the properties are presented with its larger deviation (SD or SE) to better characterize the observations, especially when the standard error is significantly larger than the standard deviation.

Table 5.7: Dust-smoke properties obtained in previous studies. In parenthesis the standard deviations are presented if they are provided. In particular, DeLiAn is a database that compile lidar observations for different aerosol types (Floutsi et al., 2023).

	Location	**LR(532) [sr]**	**LR(808) [sr]**	**PLDR (532)**	**BAE (532/1064)**	**Smoke proportion**
This work	France	39 (3)	38 (2)	L1: 0.19 (0.04) L3: 0.25 (0.06)	L1: 0.78 (0.5) L3: 0.82 (0.6)	
(Tesche et al., 2011)	Morocco, Cape Verde	67 (12)	-	0.16 (3)	0.67 (0.27)	60- 40 %
(Ansmann et al., 2009)		53 (8)	-	0.15-0.30	-	60 -10 %
(Groß et al., 2013)		63 (7)	-	0.14 (0.02)	-	-
DeLiAn (Floutsi et al., 2023)	-	56 (7)	-	0.19 (0.01)	1 (0.05)	-

Further discussion on the complexity of this case is presented in the next sub-section, where comparisons against LILAS aerosol retrievals are presented.

5.4.2 METIS and LILAS retrievals comparisons

For comparisons of METIS and LILAS, averaged profiles between 01:00 to 03:00 UT on 19 July 2022 are used (when Raman measurements from LILAS are available). Direct moon photometer measurements available are averaged during the same time period to constrain the inversion for METIS. During this event, LILAS lidar got affected by the extreme environmental conditions, so a wider incomplete overlap is acknowledged and we will not consider retrievals comparisons below 1.7 km. Once again, PLDR, EAE and CR values are not shown when the aerosols backscatter at 532 nm is less than 0.3 Mm^{-1} sr^{-1} and at altitudes below 600 m.

Backscatter coefficients (Fig. 5.21a) and depolarization ratios (Fig. 5.21c) comparisons show good agreement between both lidars above 2 km asl (12 % bias on depolarization) with an obvious influence of the vertically-constant LR assumption on METIS. The extinction coefficients (Fig. 5.21b) and consequently the EAE (Fig. 5.21d) are the most impacted (LR values of 38 ± 2 sr for 532 nm and 40 ± 2 sr for 808 nm), showing the limitation of the inversion method under complex scenarios. However, VLDR and PLDR values retrieved from METIS are highly sensitive to the change of dust-smoke composition within the layers.

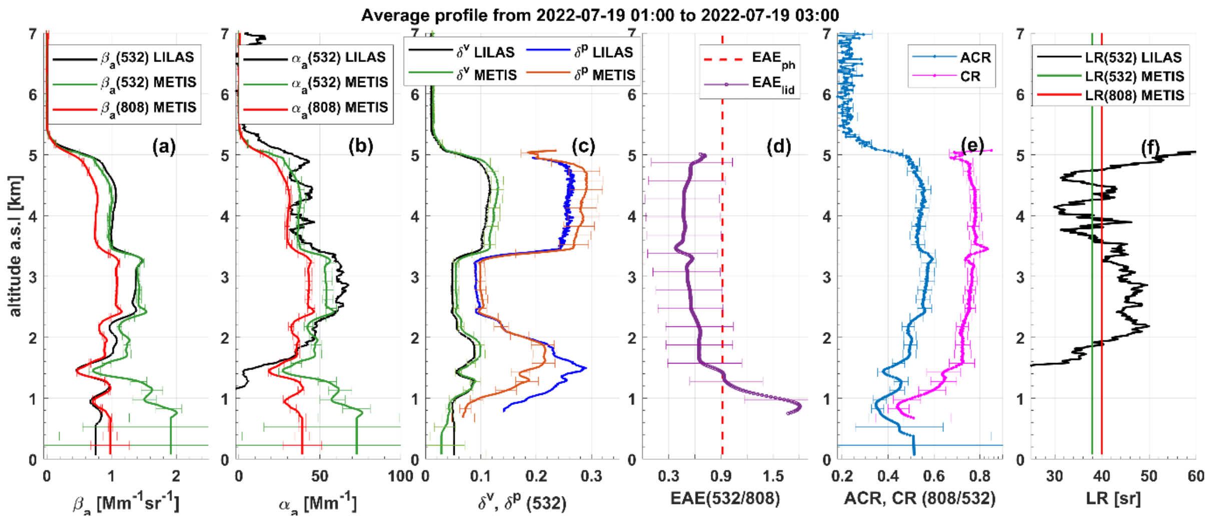

Figure 5.21: Aerosols optical properties retrieved from METIS and comparison with LILAS retrievals for the averaged measurements between 01:00 to 03:00 UT on 2022-07-19. Vertical profiles of (a) Backscatter, (b) Extinction and (f) LR at 532 and 808 nm for METIS and 532 nm for LILAS, (c) VLDR and PLDR at 532 nm for METIS and LILAS, (d) EAE (532/808) from METIS and the photometer, and (e) ACR, CR (808/532).

The first layer, between 1.6-2 km, asl and the third layer between 3.5-5 km asl showed PLDR (VLDR) values in average 0.20 ± 0.02 (0.09 ± 0.01) and 0.27 ± 0.03 (0.12 ± 0.01), respectively. Both layers with insights of dust predominant presence, higher dust concentration can be expected at L3 than at L1. In contrast, the second layer (2.4 - 3.2 km asl) yields the unique presence of smoke aerosols with PLDR (VLDR) of 0.09 ± 0.01 (0.05 ± 0.01). Therefore, EAE values (Fig. 5.21d) are expected to be higher than 1 for the second layer, which is not the case due to the use of vertically-constant LR. In this context, in a complex scenario like this one, CR, EAE and BAE derived with Klett method (Fig. 5.21 and Table 5.5), do not show significant changes within the layers to distinguish between fine and large particles. Nevertheless, ACR values directly derived from METIS measurements are influenced by the aerosol attenuation but are still sensitive to the different layers.

5.4.3 Conclusions

In this section, an event of Saharan dust mixed within smoke aerosols transported above ATOLL platform (Lille, France) during a heat-wave was studied using METIS CE376 lidar and CE318-T photometer (17 to 19 July 2022). Atmospheric properties derived directly from lidar measurements (β_{att}, $VLDR$ and ACR) and aerosol properties ($\beta_{\rm aer}$, $\alpha_{\rm aer}$, $PLDR$, CR, EAE) were retrieved through the inversion scheme. Temporal series of AOD, EAE from direct sun photometer measurements and VSD derived from almucantar and AOD photometer measurements were also presented. Moreover, VSD distributions showed the presence of dust (coarse mode) and smoke (fine mode) during the entire event. Likewise, back-trajectories were presented to track the sources.

Based on the observed vertical aerosol variations using the CE376 lidar, we can distinguish two distinct periods during the event. On 17 July 2022, a dominant layer, approximately 1.5 km thick (centered at 4 km asl), containing homogeneously distributed dust and smoke is observed. In contrast, from 18 to 19 July 2022, until 12:00 UT, three compacted layers (L1, L2, L3) exhibit significantly different depolarization ratios, indicating varying proportions of dust-smoke content.

The layers L1 (1.5-2.2 km asl) and L3 (3.2-4.5 km asl) present predominance content of dust with PLDR values (0.19 ± 0.04 and 0.25 ± 0.06 respectively) comparable to those presented in previous works on dust-smoke mixtures. In contrast, PLDR values (0.10 ± 0.01) within L2 (2.4-3.2 km asl) and back-trajectories suggest the unique presence of smoke rather than dust. Contrariwise to the complexity observed with the lidar, the temporal series from the photometer are fairly stable.

This unusual event of stratified dust and smoke transported over ATOLL, emphasizes both the limitations and capabilities of the CE376 lidar for aerosol characterization. The assumption of a constant LR in the atmospheric column limits the aerosol typing within layers, particularly affecting EAE, BAE and CR. Nevertheless, depolarization measurements prove to be reliable for aerosol classification even in complex scenarios. Furthermore, operational improvements, such as the roof window of METIS CE376 lidar, result in relative VLDR bias of 12 % compared to LILAS Raman lidar.

5.5 La Palma Eruption (IZO and ATOLL, Sept.-Oct. 2021)

The Cumbre Vieja volcano, located on the Canary Island of La Palma, erupted on 19 September 2021 (Fig. 5.22). The eruption process persisted during 85 days (until 13 December 2021) being the longest volcanic eruption in La Palma in the last 5 centuries. The eruption was catalogued as Strombolian type (Bedoya-Velásquez et al., 2022; Córdoba-Jabonero et al., 2023), meaning that it involved moderate gases bursts that ejected lava clots in cyclical or nearly continuous eruptions. The lava rivers from the eruption led to the evacuation of thousands of residents and caused significant damage to infrastructures. Moreover, the regional air quality was affected by the high concentrations of SO_2, fine aerosols (non-ash, probably sulfates aerosols) and ash emitted by the volcano. In addition, in particular during September-October, events of dust transported from the Sahara (up to 6 km asl) were also impacting the region (Milford et al., 2023; Sicard et al., 2022).

Figure 5.22: (a) Cumbre Vieja, La Palma, eruption view from spatial station on 4 October 2021 and the (b) lava flows observed during 29 November 2021. Astronaut photograph ISS065-E-439221 is provided by the ISS Crew Earth Observations Facility and the Earth Science and Remote Sensing Unit, Johnson Space Center. Lava flow photography source: Emilio Morenatti/AP (Le Monde).

Scientific, private and governmental organizations joint collaborative efforts, in the frame of ACTRIS-Spain (https://actris.es.webstsc.webs.upc.edu/en/node/11), permitted the deployment of in-situ and remote sensing instrumentation in La Palma as part of an emergency response. Moreover, the volcano activity was monitored by the PEVOLCA (Plan Especial de Protección Civil y Atención de Emergencias por Riesgo Volcánico en la Comunidad Autónoma de Canarias; https://info.igme.es/eventos/Erupcion-volcanica-la-palma/pevolca). Thus, the continuous monitoring of the eruption was possible. High concentrations of SO_2, PM_{10} and $PM_{2.5}$ were observed at ground level in La Palma and also sporadically at IZO Observatory (Milford et al., 2023). Moreover, the characteristic atmospheric trade wind inversion played an important role on the stratification and transport of the volcanic emissions. Thus, considerably low plume injection height was observed between 3 and 3.5 km asl (Bedoya-Velásquez et al., 2022) and occasionally up to 6 km asl. In particular, Sicard et al. (2022) and Córdoba-Jabonero et al. (2023) studied the vertical variation of fresh aerosol produced near the eruption episode (less than 20 km away). These studies applied the POLIPHON (POlarisation LIdar PHOtometer Networking, Ansmann et al., 2011) algorithm to separate the volcanic particulate matter into two aerosol components by means of the depolarization properties: ash particles (assumed as coarse-dominating aerosol with high depolarization), and non-ash particles (fine-mode of the volcanic aerosols, mainly sulphates, with low depolarization). These studies showed PLDR(532) values of 0.2-0.3 for the ash particles and closer to 0.01 for non-ash. Moreover, ash particles were not detected at aerosol layers above 4 km asl.

To study the aerosols generated by the volcanic eruption, both IZO (near source) and ATOLL (long-range) are considered. Thus, a case study of intermittent presence of non-ash aerosols at IZO is studied during the first days of eruption (Sect. 5.5.1). On the other hand, a case study of aerosols accompanying an impressive atmospheric river of SO_2 arriving to ATOLL is presented (Sect. 5.5.2). The following subsections are dedicated to the analysis of the observations of the CE376 lidar and photometer at both sites.

5.5.1 Near Source (IZO, 22-24 September 2021)

IZO station (Tenerife, Canary Islands) was separated from Cumbre Vieja volcano eruption by the ridge of Teide and by a distance of ~140 km (Fig. 5.23d). Thus, due to its proximity to the eruption episode, the monitoring of ash and non-ash aerosols was possible. In particular, we focus our attention to some days within the first week of the eruption (2021-09-21 to 2021-09-24). These days were characterized by high emissions of SO_2 reaching up to 20 DU in density (DU= Dobson Unit equivalent to 2.69 × 1016 molecules/cm²) as seen by the TROPOMI (TROPOspheric Monitoring Instrument) spectrometer on board Sentinel-5 satellite. Figure 5.23 presents the TROPOMI images of SO_2density at the region of La Palma during the days considered for analysis. It is shown that Tenerife Island is always within the SO2 plume with higher densities towards the 24 September 2021. The TROPOMI images presented were obtain by using the VolcPlum interactive portal, developed in the frame of AERIS data center and LOA (https://volcplume.aeris-data.fr/, Boichu & Mathurin (2022)). VolcPlum is a versatile tool that permit the monitoring of volcanic events around the world by means of satellite instrumentation and AERONET photometer sites.

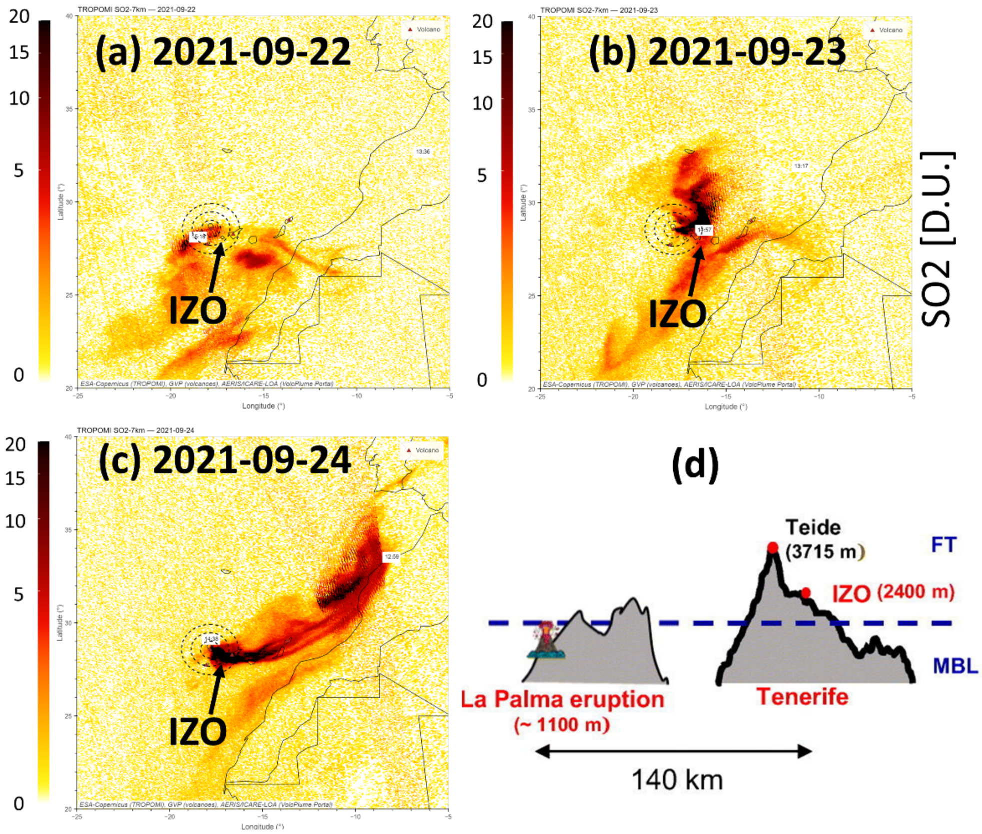

Figure 5.23: TROPOMI SO_2total vertical column density (in DU) images are presented for (a) 2021-09-22, (b) 2021-09-23 and (c) 2021-09-24 during Cumbre Vieja eruption. The (d) position of IZO site with respect to the eruption is also presented. The TROPOMI images are available at VolcPlume portal https://volcplume.aeris-data.fr/, source: Boichu, M. & Mathurin, T. (2022). Schematic diagram of IZO and the eruption site is adapted from Milford et al. (2023).

In the following lines, a comprehensive analysis of the observations, using CE376 lidar and photometer, during 22 to 24 September 2021 is presented.

CE376 lidar-photometer analysis

The CE376 lidar (CE376 GPNP at IZO) blind zone is defined from the overlap function estimations (i.e., r_o where O(r) <0.1). During this period, same as the dust case, for each channel were: $r_o(532par) = 0.6\ km$, $r_o(532per) = 0.5\ km$ with and $r_o(808tot) = 0.15\ km$. The first 2 km agl of the total signal RCS at 532 nm are influenced by relative errors of 5 % at 2 km going towards 15 % at 600 m. In the case of RCS at 808 nm, the influence of overlap error goes from 4 % at 1 km towards 10 % at 150 m.

An overview of the atmospheric properties from CE376 lidar and photometer is presented in Fig. 5.24 for the period of 22 to 24 September 2021. During this time, no evidence of dust presence is observed. Thus, IZO station, located in the FT, was influenced mainly by the volcanic aerosols from Cumbre Vieja. From height-temporal variations of β_{att} at 808 nm (Fig. 5.24a), which is less influenced by molecular contributions, and VLDR at 532 nm (Fig. 5.24b), one can observe the intrusion of thin aerosol plumes mostly below 4.5 km asl with varying values of depolarization below 0.06. In particular, on 24 September 2021 a lofted layer above 4.5 km asl and descending towards 3 km asl is detected. Within this layer, higher values of $\beta_{att}(808)$, indicating higher aerosol concentration, and nearly non depolarization is observed. Likewise, the presence of the layer is accompanied by an increase of AOD and EAE (Fig. 5.24d). Moreover, height-temporal variations of ACR(808/532) (Fig. 5.24c) show clearly the different layers presence.

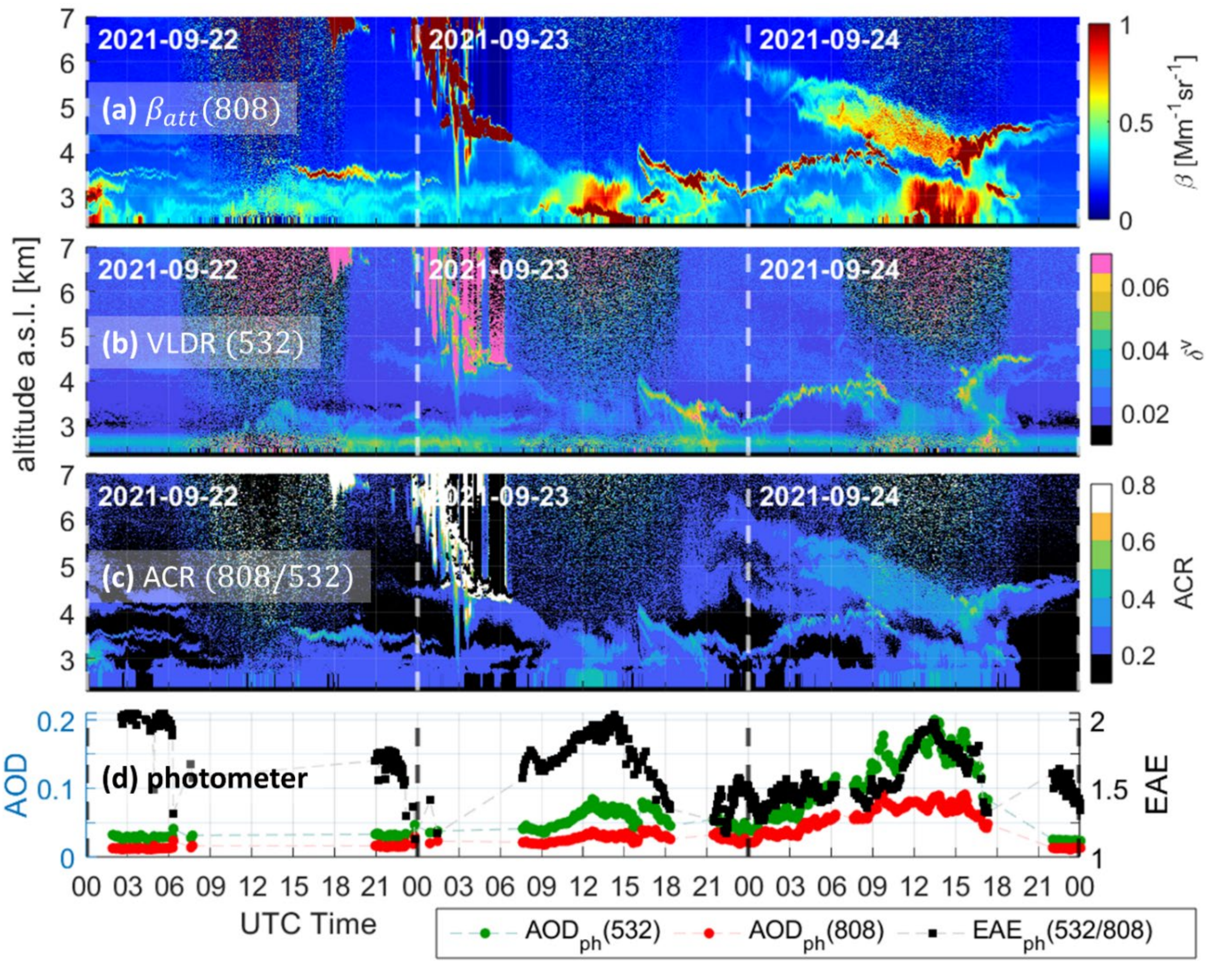

Figure 5.24: Overview of atmospheric optical properties from synergetic measurements of CE376 lidar and sun/moon photometer at IZO observatory from 2021-09-22 to 2021-09-24. Heigh-temporal variation of (a) $\boldsymbol{\beta_{att}}$ at 808 nm, (b) VLDR at 532 nm, (c) ACR at 808-532 nm and (d) time series of AOD$_{ph}$ at 532 nm and 808 nm with EAE$_{ph}$ 532/808 derived from the photometer.

Thus, indications of varying aerosol sizes (ACR<0.4), mostly within the fine mode ($EAE_{ph} >$ 1.2, Fig. 5.24d), and presence of nearly spherical particles (VLDR<0.06) are stated. Similarly, VSD distributions obtained during 23 September 2021 (Fig. 5.25) show the higher concentration of aerosols in the fine mode (radius of 0.15 μm) over the coarse mode. In this context, a large predominance of non-ash aerosols can be established. It is important to point out the high sensitivity of ACR to discriminate the aerosols layers from the molecular influences, in contrast with VLDR(532) and $\beta_{att}(808)$.

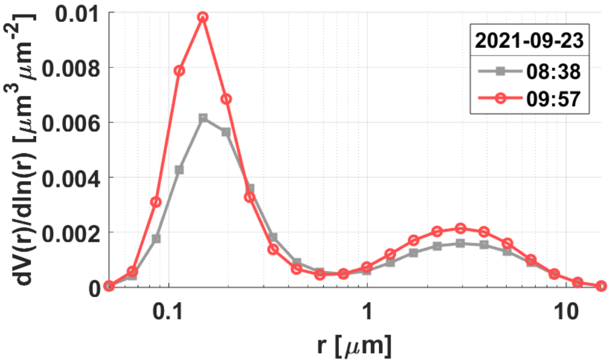

Figure 5.25: VSD derived from photometer sky almucantar and AOD measurements during 2021-09-23 at IZO. Data is level 2 from AERONET version 3 algorithms.

Aerosol retrievals profiles

For further analysis of the aerosols observed at IZO, selected time thresholds under presence of aerosol plumes are studied. Averaging to one to two hours, the SNR improves, resulting in more reliable information. Due to several layers observed below 500 m agl (i.e, in O(r)<0.1 at 532 nm), the altitude defining the blind zone is reduced to 300 m, taking into account that the uncertainties can be higher than 20 %, in particular for 532 nm channels. Four time-thresholds (T1, T2, T3, T4) are selected, averaged, individually analyzed and presented in Fig. 5.26. Aerosol properties in the Fig. 5.26 presented (from left to right) are aerosol backscatter β_a and aerosol extinction α_a at both wavelengths, VLDR and PLDR at 532 nm, EAE and BAE for 532-808 nm and ACR and CR for 808-532nm. Additionally, black dashed line boxes highlight the aerosol layers of interest. The analysis of the results is presented below:

(a) ***T1 (2021-09-23 16:00 to 2021-09-23 18:00 UT, Fig. 5.26a):*** the effective LR retrieved at both wavelengths are quite similar, $49 \pm 10\ sr$ at 532 nm and $48 \pm 17\ sr$ at 808 nm, and both are affected by large errors, related to the low aerosol loading. However, two layers well defined are detected of ~0.4 km width, one centered at 3 km asl and the other at ~3.8 km asl. The lower layer presents higher extinction ($\sim 60\ Mm^{-1}$ at 532 nm and $\sim 30\ Mm^{-1}$ at 808 nm) and lower PLDR (0.05) than the layer at higher altitude, with extinction $\sim 30\ Mm^{-1}$ at 532 nm and $\sim 20\ Mm^{-1}$ at 808 nm and PLDR values of 0.08. The derived EAE and BAE are identical, with values slightly varying around the EAE from the photometer ($EAE_{ph}(532/808) = 1.67$), and implying the predominance of fine aerosols. Similarly, ACR values are lower than 0.35, as well associated to fine aerosols. Nevertheless, CR values are higher than 0.5 with large uncertainty (~30 %), in relation to the LR error propagation. In this context BAE and EAE are also largely affected. Though errors are larger, both layers show a predominance of fine spherical aerosols with rather higher contribution in the lower layer than on the higher layer.

(b) ***T2 (2021-09-24 08:00 to 2021-09-24 09:00 UT, Fig. 5.26b):*** the effective LR retrieved at both wavelengths are $39 \pm 5\ sr$ at 532 nm and $61 \pm 10\ sr$ at 808 nm. This set of profiles reveal 3 thin aerosol layers (~100 m width) between 3.6 and 4.2 km asl, all three with similar extinction coefficients, around ~65 Mm^{-1} at 532 nm and ~40 Mm^{-1} at 808 nm, and similar PLDR values around 0.06. Immediately above, a wider layer between 4.3 and 5.3 km asl is detected, with extinction coefficients around ~40 Mm^{-1} at 532 nm and ~30 Mm^{-1} at 808 nm and PLDR considerably lower (0.03). In contrast EAE, BAE, ACR and CR are likely constant within the 4 layers, all showing values related to the presence of fine aerosols. In particular, the wider layer, yields the unique presence of non-ash particles, most likely sulfate aerosols.

(c) ***T3 (2021-09-24 12:00 to 2021-09-24 13:00 UT, Fig. 5.26c):*** the effective LR retrieved at both wavelengths are $38 \pm 2\ sr$ at 532 nm and $59 \pm 8\ sr$ at 808 nm. Due to the increasing background noise caused by solar radiation at this time, the LR at 808 nm is retrieved by means of the 2-wavelength inversion scheme proposed in this work, i.e., using an $AOD_{est}(808)$ and the forward integration Klett method. This set of profiles, follow the descent of the layer centered at 4.8 km asl detected in T2, now placed between 4 and 5 km asl with higher aerosol concentration at 532 nm (extinction: 74 Mm^{-1} at 532 nm and ~40 Mm^{-1} at 808 nm). Similarly to T2, the layer presents PLDR values of 0.03. Moreover, a layer below 3.5 km asl is also detected with higher values of extinction (100 Mm^{-1} at 532 nm and ~50 Mm^{-1} at 808 nm) and PLDR below 0.05. Both layers show high values of EAE (~1.8), BAE (~2.6) and identical lower values of ACR, CR (~0.33). Thus, an increasing presence of non-ash particles is evidenced, in accordance with the increase of EAE_{ph} (1.8) respect T2 and T1 (1.4 and 1.6 respectively).

(d) ***T4 (2021-09-24 15:00 to 2021-09-24 17:00 UT, Fig. 5.26d):*** the effective LR retrieved at both wavelengths are $47 \pm 4\ sr$ at 532 nm and $56 \pm 6\ sr$ at 808 nm. This set of profiles is characterized by the presence of a layer centered at 4 km asl of 0.5 km width with considerable extinction coefficients (150 Mm^{-1} at 532 nm and ~80 Mm^{-1} at 808 nm). Moreover, PLDR values are around 0.05 and EAE and BAE are around of the EAE_{ph} (1.75). Once again, the predominant presence of non-ash particles is distinguished.

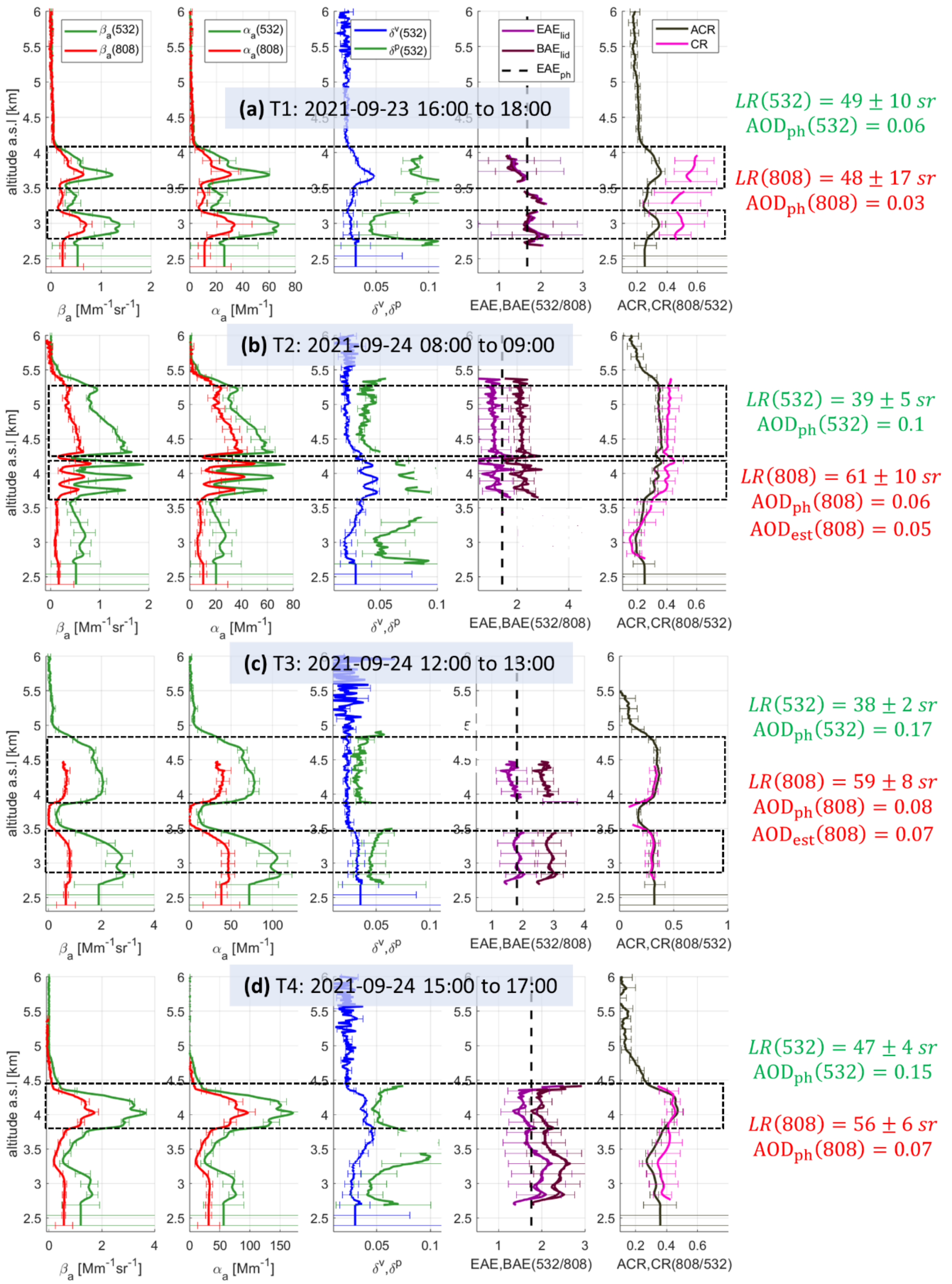

Figure 5.26: Aerosol properties for selected time-threshold during the intrusion of volcanic aerosols from 22 to 24 September 2021 at IZO. The selected time-thresholds are presented by panels of profiles, (a) T1 from 2021-09-23 16:00 to 2021-09-23 18:00 UT, (b) T2 from 2021-09-24 08:00 to 2021-09-24 09:00 UT, (c) T3 from 2021-09-24 12:00 to 2021-09-24 13:00 UT and (d) T4 (2021-09-24 15:00 to 2021-09-24 17:00 UT. The profiles correspond (from left to right) to aerosol backscatter β_a and aerosol extinction α_a at both wavelengths, VLDR and PLDR at 532 nm, EAE and BAE for 532-808 nm and ACR and CR for 808-532nm. The aerosol layers of interest are highlighted by black dashed line boxes.

As a result, we can imply that the multiple aerosols plumes observed at IZO (Fig. 5.24), analyzed through selected time-thresholds (Fig. 5.26), most likely contain non-ash particles (fine and spherical aerosols) rather than ash (coarse non-spherical aerosols). In agreement with the results presented by Sicard et al. (2022) and Córdoba-Jabonero et al. (2023), indications of higher non-ash concentration (lower values of PLDR) is observed while the layer altitude increases. Moreover, Córdoba-Jabonero et al. (2023) reported higher concentration for ash particles within the first two kilometers which also explains the low impact of ash at IZO station.

The following subsection will present the study of the aerosols produced at the Cumbre Vieja eruption, transported to ATOLL (~3000 km far) within an atmospheric river of SO_2.

5.5.2 Long range transport (ATOLL, 19-20 October 2021)

During the nearly 3 months of Cumbre Vieja eruptive episode, gas and particle volcanic emissions impacted mostly at a regional level. Moreover, Milford et al. (2023) evidenced two phases of the volcanic episode. The first phase from 19 September until 7 November 2021 was characterized by the trade wind inversion altitude ranging around 1 km asl (Cumbre Vieja ~1.1 km asl), higher SO_2 emissions and higher PM_{10} concentrations (~100 $\mu g m^{-3}$ per day) with respect to the second phase.

An important decrease of SO2 emissions and higher altitude of the trade wind inversion characterized the second phase, from 7 November until 13 December 2021. In particular during the first phase, a significant reduction of the trade wind inversion altitude (towards below 500 m) was observed, from 15 October to 21 October, accompanied by a 4 km eruptive column. At the same time, a deep low-pressure system descending through North Atlantic Ocean (from high to lower latitudes), pushed the air masses from the sub-tropical region towards North.

Thus, an unprecedented SO_2 atmospheric river formed transporting gas and aerosols from Cumbre Vieja to France (3000 km away) almost following a straight line (Fig. 5.27). Under this particular scenario, ATOLL was impacted by the Cumbre Vieja emissions on 19 and 20 October 2021.

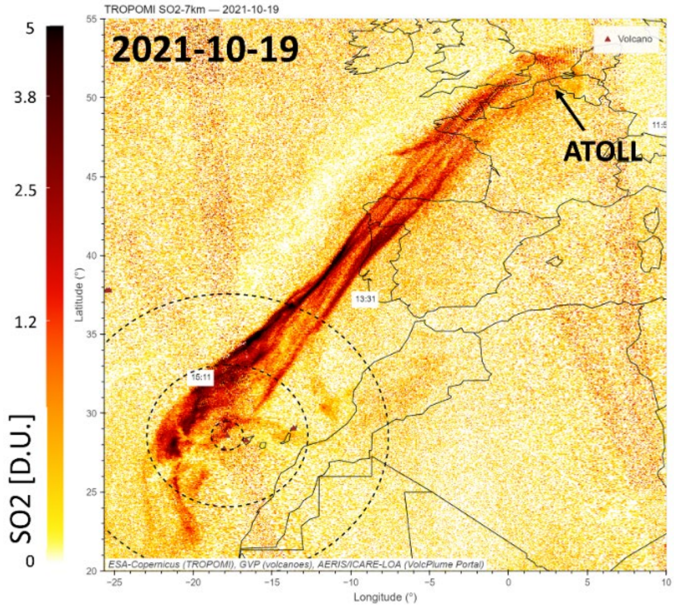

Figure 5.27: TROPOMI SO2 total vertical column density (in DU) image for 19 October 2021. The TROPOMI images are available at VolcPlume portal https://volcplume.aeris-data.fr/, source: Boichu, M. & Mathurin, T. (2022).

In the following lines, a comprehensive analysis of the observations, using CE376 lidar and photometer at ATOLL, during 19 and 20 October is presented.

CE376 lidar-photometer analysis

During this period, METIS (CE376 lidar) was under test at the current configuration (i.e., improved window roof), thus enhanced depolarization measurements were already achieved. At this time, METIS blind zone defined from the overlap function estimations (i.e., r_o where O(r) <0.1) for each channel were: $r_o(532par) = 0.5\ km$, $r_o(532per) = 0.5\ km$ with and $r_o(808tot) = 0.15\ km$. The first 2 km agl of the total signal RCS at 532 nm are influenced by relative errors of 4 % at 2 km going towards 15 % at 500 m. In the case of RCS at 808 nm, the influence of overlap error goes from 4 % at 1 km towards 10 % at 150 m. It is worth to mention that only METIS lidar was performing measurements during this event, LILAS Raman lidar was not operational at this time.

In particular, during 19 October 2021, tests on the lidar position with respect to the window roof were performed, resulting in changes on backscatter light intensity. Nevertheless, changes on the molecular depolarization (used as reference) were not observed regardless the changes on the position of the lidar, in this way corroborating the improvements on the configuration. Moreover, on this day a depolarization calibration was performed at 20:00 UT. Figure 5.28 presents an overview of the synergetic CE376 and photometer observations from 19 October 2021 at 12:00 UT to 20 October 2021 at 05:00 UT. In particular, the changes in lidar position and the depolarization calibration are marked by the gaps on the observations. Two aerosol layers (L1 and L2) likely to be transported from Cumbre Vieja eruption are highlighted by dashed white line boxes.

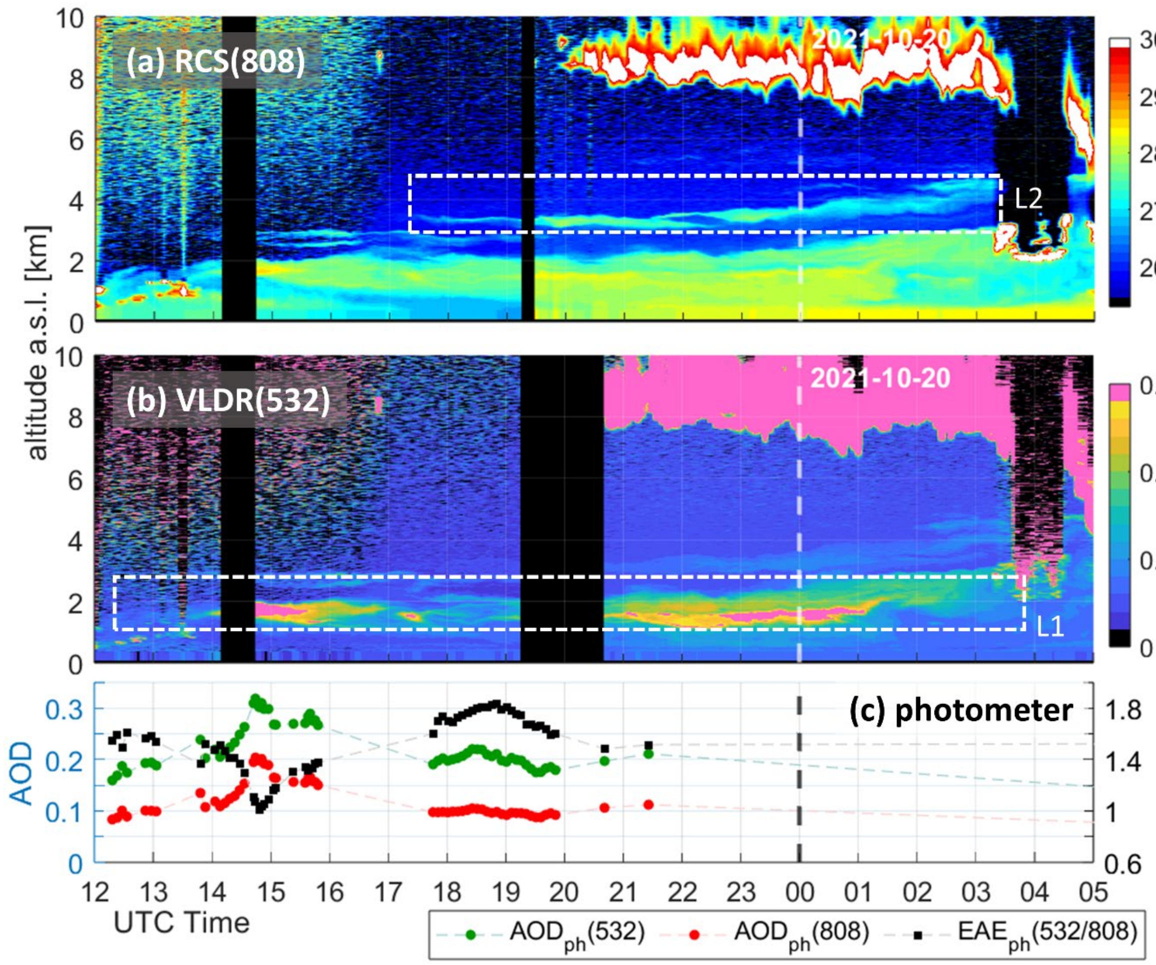

Figure 5.28: Overview of atmospheric optical properties from synergetic measurements of METIS and sun/moon photometer at ATOLL observatory from 2021-10-19 12:00 UT to 2021-10-20 05:00 UT. Heigh-temporal variation of (a) ln(RCS) at 808 nm, (b) VLDR at 532 nm and (c) time series of AOD$_{ph}$ at 532 nm and 808 nm with EAE$_{ph}$ 532/808 derived from the photometer are presented. White dashed line boxes highlight the presence of 2 aerosol layers (L1, L2) arriving to ATOLL.

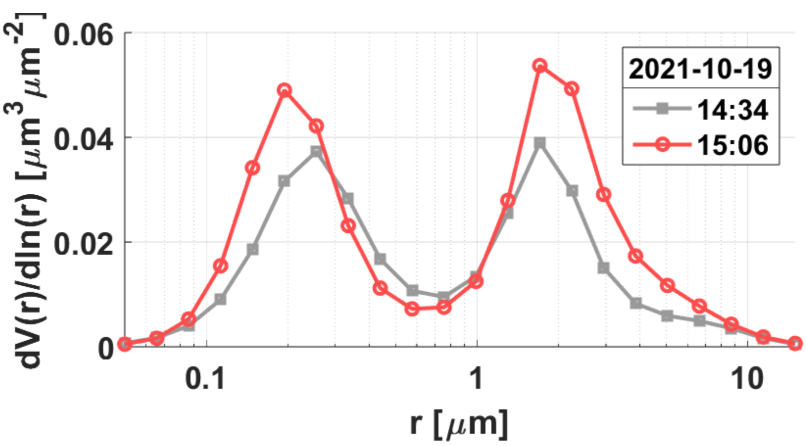

Figure 5.29: VSD derived from photometer sky almucantar and AOD measurements during 2021-10-19 at ATOLL. Data is level 2 from AERONET version 3 algorithms.

In contrast to IZO observations, higher VLDR values (up to 0.15, Fig. 5.28b) are observed within the layers identified (L1 and L2). Similarly to previous studies (Córdoba-Jabonero et al., 2023) of Cumbre Vieja eruption, higher depolarization is evidenced at lower altitudes (L1), indicating as well a major concentration of coarse non-spherical aerosols with respect to non-ash (fine spherical) particles. Moreover, VSD distributions (Fig. 5.29) at 14:34 and 15:06 on 19 October 2021, show comparable volume concentrations of fine and coarse aerosols centered on radius 0.2 μm and 1.7 μm, in agreement with higher AOD and lower EAE (~1.4). However, photometer observations show an increase of EAE values during 19 October 2021, indicating the increasing predominance of fine aerosols (EAE~1.8 at 19:00). Regardless that it was full moon phase, direct moon photometer measurements were not possible due to clouds above 8 km asl.

The radius of the coarse aerosols indicated by the VSD is comparable to the reported values during the transported pure dust events at IZO and ATOLL (Sect. 5.2, Sect. 5.3), moreover depolarization values up to 0.15 can indicate as well dust mixed with fine aerosols. Hence, doubts on the aerosol types arise for layer L1. To corroborate that the coarse aerosols are effectively product of the eruption rather than dust from the Sahara, back-trajectories were analyzed.

Back-trajectories analysis

Back-trajectories ending at 3 altitudes and covering 7 days of transport are considered for 4 different arrival times 12:00 UT (Fig. 5.30a) and 18:00 UT (Fig. 5.30b) on 19 October 2021, 00:00 UT (Fig. 5.30c) and 04:00 UT (Fig. 5.30d) on 20 October 2021. The altitudes considered represent the ABL (500 m in red), the lower layer L1 (1.9 km in blue) and the upper layer L2 (3 km in green). From these back-trajectories, no indication of dust transported from the Sahara is observed. Moreover, the air-masses arriving at 1.9 km and 3 km always pass through the trail of the SO_2 atmospheric river, validated by TROPOMI observations in previous days (not shown). Similarly, air masses influencing the ABL (500 m) follow the same trajectory as the other two layers at 12:00 UT on 19 October 2021 (Fig. 5.30a) and 00:00 UT on 20 October 2021 (Fig. 5.30c). These findings suggest that sulfur compounds and aerosols from Cumbre Vieja eruption impacted ATOLL atmospheric column from ground level to higher altitudes (up to 4-5 km as seen by lidar). Thus, observations at ground level at ATOLL showed, as well, the presence of sulfur compounds. In particular, measurements of SO_4 from the ACSM (Aerosol

Chemical Speciation Monitor) showed a pick of concentration on 19 October 2021 from ~12:00 to 16:00 UT (highlighted by dashed line circle in Fig. 5.31).

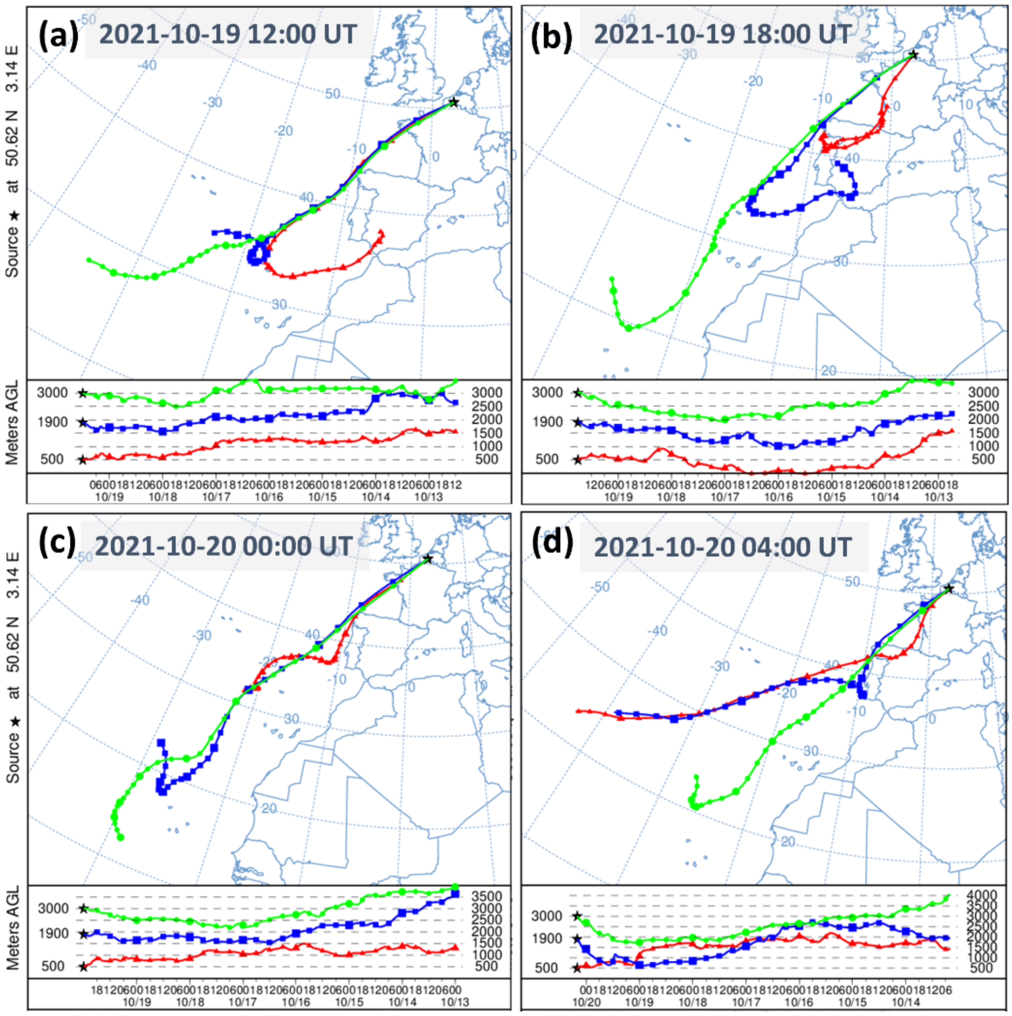

Figure 5.30: NOAA HYSPLIT back-trajectories ending at 0.5 km (in red), 1.9 km (in blue) and 3 km (in green) above ATOLL (Lille, France). Different arrival times are considered: (a) 12:00 UT on 19 October 2021, (b) 18:00 UT on 19 October 2021, (c) 00:00 UT on 20 October 2021 and (d) 04:00 UT on 20 October. GFSQ meteorological data is used to run the model for 7 days of transport. The web interface was used to obtain these results (https://www.ready.noaa.gov/HYSPLIT_traj.php).

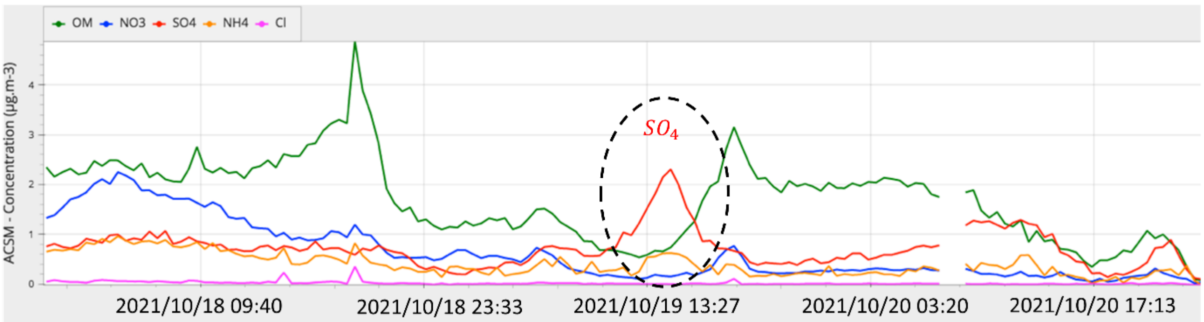

Figure 5.31: Concentration of aerosol chemical components using ACSM at ATOLL on 18 to 20 October 2021. A pick of sulfate aerosols is highlighted by a dashed black line circle.

In contrast, the trajectories arriving at 18:00 UT on 19 October 2021 (Fig. 5.30b) and 04:00 UT on 20 October 2021 (Fig. 5.30d) suggest a possible influence from urban emissions in the ABL.

In addition, DOD images (not shown) from the dust monitoring center do not indicate events of Saharan dust outbreaks affecting the region of interest during this period of time. Thus, we can infer that the aerosol layers detected with the lidar-photometer observations (Fig. 5.28) certainly contain ash and non-ash (sulfate) particles produced by the Cumbre Vieja eruption.

Aerosol retrievals

During this event, the presence of a cloud affects considerably the photometer observations and consequently, the retrieval of an effective LR at both wavelengths. Also, the search of a free aerosol region (needed for Klett BW inversion) under the cloud is not an easy task. However, some retrievals were possible. A time-threshold is therefore selected for further study of the event. At 15:00-16:00 UT on 19 October 2021, the layers have clearly different depolarization ratios (Fig. 5.28b) and the presence of two aerosol sizes are also confirmed by the VSD distributions (Fig. 5.29).

The effective LR retrieved are $78 \pm 4\ sr$ at 532 nm and $67 \pm 3\ sr$ at 808 nm. From the profiles of retrievals (Fig. 5.32), three aerosol layers can be distinguished.

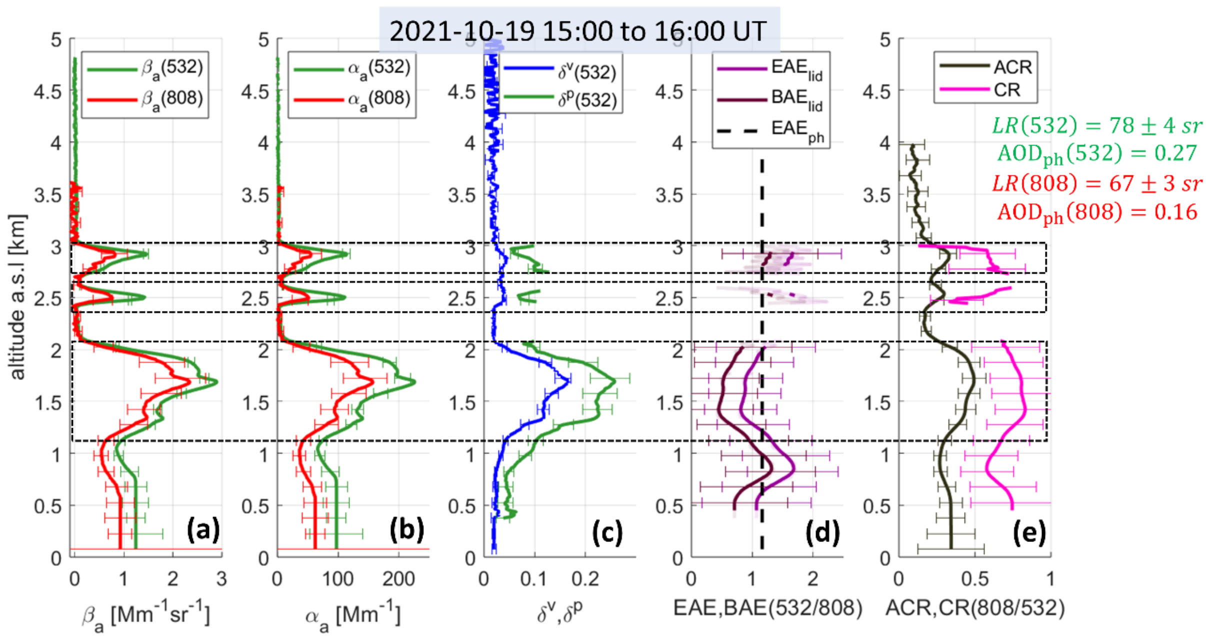

Figure 5.32 : Aerosol properties retrieved during the intrusion of Cumbre Vieja volcanic aerosols at 15:00-16:00 UT on 19 October 2021.The profiles presented correspond (from left to right) to (a) aerosol backscatter β_a and (b) aerosol extinction α_a at both wavelengths, (c) VLDR and PLDR at 532 nm, (d) EAE and BAE for 532-808 nm and (e) ACR and CR for 808-532nm. The aerosol layers of interest are highlighted by black dashed line boxes.

The lower layer of ~1 km width presents high PLDR values around 0.22 (Fig. 5.32c), suggesting presence of non-spherical particles. Furthermore, maximum extinction values were observed at 1.7 km asl, $215 \pm 12\ Mm^{-1}$ at 532 nm and $144 \pm 35\ Mm^{-1}$ at 808 nm. At higher altitudes, two thin layers at 2.5 km asl and 3 km asl (0.1 km and 0.3 km width) are detected, with considerably lower PLDR values (0.09 and 0.08), related to the presence of spherical particles and comparable to the values observed at IZO (Sect. 5.5.1).

Moreover, lower extinction was detected, both layers with $100 \pm 7\ Mm^{-1}$ at 532 nm and 54 $\pm$ 18 Mm^{-1} at 808 nm. Both derived properties, EAE and BAE (Fig. 5.32d), show lower values than the EAE_{ph} (1.2) for the wider and highly depolarizing layer and higher EAE values for the thin aerosol layers. Thus, EAE and BAE indicate higher presence of coarse aerosols in the lower layer (L1) than on the thin aerosol layers (L2). Similarly, ACR and CR values (Fig. 5.32e) are lower for the 2 thin layers (L2) than for the wider layer (L1), indicating higher concentration of fine aerosols within the thin layers.

Through the ensemble of results, aerosols emitted during the eruption of Cumbre Vieja volcano were detected 3000 km away from source at ATOLL, Lille, France. Both ash (non-spherical coarse particles) and fine non-ash (spherical fine particles, mostly associated to sulfates) particles were identified. In contrast to the observations at IZO, higher predominance of ash particles is observed at ATOLL, in relation with the altitude of the layers. Likewise, the results at ATOLL are comparable to previous studies of transported ash and fine particles during the *Eyjafjallajökull* eruption (Iceland) in spring 2010 (Table 5.8).

Table 5.8: Aerosol properties obtained in previous studies for volcanic aerosols, ash (a) and fine non-ash (na) particles. In parenthesis the standard deviations are presented. *CALIPSO algorithms consider the classification of ash and sulfates only in the stratosphere.

	Location	**LR [sr]**		**PLDR**	**BAE (532/1064)**	**EAE (532/1064)**
		532	**1064 or 808**	**532**		
This work	France	78 (4)	67 (3)	a: 0.22 (0.03) na: 0.09 (0.01)	a: 0.6 (0.58) na: 1.25 (0.8)	a: 1 (0.6) na: 1.6 (0.8)
CALIPSO V4 (Kim et al., 2018)	Stratosphere*	a: 44 (9) na: 50 (18)	a: 44 (13) na:30 (14)	-	-	-
(Navas-Guzmán et al., 2013)	Spain	75	-	<0.07	1.5 (0.1)	-
(Groß et al., 2013)	Central Europe	50 (5)	-	0.35	-	-

5.5.3 Conclusions

In this section, the volcanic eruption of Cumbre Vieja was studied at two different locations, one near the volcanic eruption (IZO, Tenerife Canary Islands) and at a long-range distance from the source (ATOLL, Lille, France). Despite observations at ATOLL were limited by the presence of clouds (i.e, no photometer measurements), the analysis of the volcanic plumes was possible. Likewise, at both sites, atmospheric properties derived directly from lidar measurements (β_{att}, $VLDR$ and ACR) and aerosol properties (β_{aer}, α_{aer}, $PLDR$, CR, EAE) were retrieved through the inversion scheme. Temporal series of AOD, EAE from direct sun photometer measurements and VSD derived from almucantar and AOD photometer measurements were also presented.

This study provides comprehensive observations and analysis, emphasizing the transport of volcanic particles at regional level to long distances. Both ash and non-ash particles (presumably sulfate aerosols) were identified, with variations in their concentration depending on the altitude. Higher concentrations of ash particles were found at lower altitudes. Thus, despite the closeness of IZO (140 km away) to the eruption, predominant presence of non-ash (fine spherical) particles is observed, related to the site altitude (~2.4 km asl). In contrast, VSD distributions shown comparable concentration of non-ash and ash (coarse non-spherical) particles arriving to ATOLL (3000 km away, 60 m asl). The depolarization ratios, along with the two-wavelengths of the CE376 lidar, once again provided enhanced capabilities to identify aerosol types, in particular to differentiate the presence of fine spherical and coarse non-spherical aerosols contributions.

5.6 Chapter summary

This chapter presented case studies of aerosol observations using CE376 lidar and photometer at fixed location laboratories. ATOLL platform at Lille University (Lille, France) and IZO observatory operated by IARC-AEMET (Tenerife-Spain) are both considered. The site description and a general overview of the aerosol contributions at both sites are presented. Thus, it was emphasized that the complex mixture of aerosols within and above the ABL than can be observed at the peri-urban ATOLL station. As well, the singular atmospheric conditions at IZO station were described, highlighting the importance of the site for aerosol studies in the free troposphere. Besides, early versions of the CE376 lidar are installed and co-located with CE318-T sun/sky/moon photometers at both sites. Additionally at ATOLL, a Raman lidar is also available and used for comparisons and evaluation. Thus, four case studies were presented:

(a) A Saharan dust outbreak at the IZO station (near source), during the summer of 2021 was evaluated. This case illustrates the dust-laden conditions at IZO, usually encountered during July and August. The study showed a dust layer (coarse non-spherical particles) extending up to 6 km above sea level and identified changes in internal structure with quite consistent depolarization ratios. The results were compared with previous works on Saharan dust characterization using high-power lidar systems.

(b) A Saharan dust outbreak transport to ATOLL platform (far range from source), during early spring of 2021 was presented. The findings shown that pure dust air masses, extended from 1.5 km asl up to 7 km asl, were transported with not significant interaction with other components. The study showed that high aerosol loadings during daytime can limit the observations of the CE376. However, a relative bias of 10 % in depolarization measurements between CE376 lidar and Raman high power lidar under same operational conditions highlighted the reliability on CE376 lidar depolarization ratios.

(c) An event of Saharan dust mixed with smoke aerosols during a heat wave (in July 2022) at ATOLL is also presented. Two distinct periods of the event were identified based on vertical aerosol variations. A dominant layer containing homogeneously distributed mix of dust and smoke on 17 July 2022 was detected, while from 18 to 19 July 2022, three compacted layers were exhibited varying proportions of dust-smoke content. The study emphasized the capabilities and limitations of CE376 lidar for aerosol characterization using intensive derived properties (such as EAE, BAE, CR) and highlighted the reliability of depolarization measurements in complex scenarios. Operational improvements, such as the roof window for continuous observations of CE376 lidar, were noted to enhance the depolarization measurements.

(d) The Cumbre Vieja volcanic eruption (September-December 2021) was studied at two locations: IZO (near the source, 140 km) and ATOLL (at a long-range distance, 3000 km). The findings reveal regional to long-distance transport of both ash (coarse non-spherical) and non-ash (fine spherical) particles, with varying concentrations based on altitude. IZO shows a prevalence of non-ash particles, while ATOLL displays comparable concentrations of both types. For this case study, all the parameters are capable to identify different aerosol types between layers.

Over all, the main limitation of the CE376 lidar to be able to identify aerosol types within different layers is the assumption of a constant LR. In particular in scenarios with really different aerosol types and complex vertical variations, like for the case of dust-smoke at ATOLL, the derived intensive properties (dependent of the LR) such as EAE, BAE, CR cannot be used for aerosol typing. In contrast, the depolarization ratios show to be reliable even in complex cases.

Moreover, the ACR property showed to be an interesting tool to identify the stratification in the atmosphere, separating into aerosol and molecular layers, rather than to imply aerosol sizes, especially in cases with really different aerosol types. This is due to the dependence on the aerosol attenuation (integrative parameter). Nevertheless, in particular at IZO station, where molecular contributions are dominant (FT), ACR showed to be able to imply the aerosol size mode dominating each layer (fine mode for ACR<0.5 and coarse mode for ACR>0.5).

In conclusion, this chapter presented the capabilities and limitations of the CE376 lidar coupled with photometer for aerosol monitoring. The reliability of CE376 lidar to characterize aerosols even in complex scenarios was demonstrated. Thus, the instrument show to be of interest for further applications, such as mobile measurements, which is the purpose of this work. This raises several questions: Can the CE376 lidar adequately monitor aerosol properties while in movement? Is it possible to couple the CE318-T photometer and CE376 lidar aboard mobile vectors? What are the operational limits? These questions will be addressed in the next chapter.

Chapter 6

Mobile aerosol monitoring

"El desarrollo tiene que ir de la mano con el cuidado de la naturaleza"
-Maisa Rojas-

This chapter presents case studies of aerosol observations using lidar and photometer aboard mobile vectors. FIREX-AQ campaign, organized during the summer 2019, focused on studies of smoke aerosols emitted by wildfires on Northwestern US. During the campaign, two mobile remote sensing platforms (DRAGON mobile units 1 and 2) were deployed using dual-wavelength CE376 lidar and CE318-T photometer, and single-wavelength CE370 lidar and PLASMA photometer. Thus, the first part of this chapter is dedicated to smoke aerosol characterization using on-road observations of both mobile platforms (Sanchez Barrero et al., 2024). The capabilities and limitations of the CE376 lidar to perform on-road measurements in extreme environmental conditions (high temperatures, thick smoke plumes, difficult roads) were evaluated. In the second part of the chapter, we switch scenarios and continents with the campaign TRANSAMA. The campaign, organized during April-May 2023, was a valorization project of the oceanographic mission AMARILLYS-AMAGAS. During this campaign, the single-wavelength CE370 lidar, two CE318-T photometers and a lab-built prototype of the Advanced-PLASMA were installed aboard the Marion Dufresne research vessel, which navigated from La Reunion Island to Barbados. The conditions for performing lidar measurements on open sea were evaluated, with future installation of the CE376 lidar aboard ships in mind. Moreover, the tools developed and presented in Chapter 4 facilitated the analysis of the mobile aerosol observations.

6.1 FIREX-AQ Campaign 2019

Every year, agricultural burnings and wildfires are observed around the world according to regional dry seasons. Mid to high latitudes are mostly impacted by dry-warm summers and wet-colder winters. Thus, high temperatures and vegetation dryness are major factors to enhance fire ignition (e.g., boreal forest fires). In contrast, the tropical regions are dominated by humid-warmer season (spring-summer) and dry-colder season (fall-winter). Natural ignitions during dry season are mostly observed in savanna forests (e.g., African savanna); however, there is a significant human influence on both wet and savanna forest is accounted (e.g., Amazon rain-forest) (Kelley et al., 2021). Moreover, due to agriculture and urbanization, human induced forest fires have considerable increased along with the growing population.

Wildfire emissions consist of various gases (carbon monoxide, methane, nitrous dioxide) and carbonaceous aerosols, such as organic carbon (OC) and black carbon (BC). The microphysical and therefore optical properties of aerosols emitted from fires are highly variable due to their complex aging processes (Ansmann, Ohneiser, Mamouri, et al., 2021; Q. Hu et al., 2022; June et al., 2022; Kleinman et al., 2020). Fresh smoke aerosols emitted from wildfires consist of aggregates of BC usually coated by OC (China et al., 2013), whose composition can vary according to diverse factors such as available fuel, meteorological conditions, and burning phase. For example, during the smoldering phase (i.e., less efficient fire, more smoke), characterized by lower temperatures, the fire is likely to produce less light absorbing OC aerosols. Conversely, emissions in the flaming phase have a higher ratio of BC to OC and produce smaller smoke particles (Reid et al., 2005).

Even though natural fires are important in many ecosystems (Mutch, 1994), they represent a costly risk to human health (fine aerosols) and property due to the constant growth of population at the wildland-urban interface. Besides, wildfires generate large volumes of smoke that can be transported from source and affect local and regional air quality for extended periods of time. In the last decades, extreme wildfire seasons have hit North America. Since 1960, the burned area has exceeded 3.6 Mha in a single year in 4 occasions, all of which have occurred in the last 15 years. The study of McClure & Jaffe (2018) shows that the air quality has improved in a large region of US, but in wildfire-prone states in the Northwest is instead getting worse. Moreover, larger, more frequent and intense wildfires are expected in the next years, owed to warmer and drier climate (Flannigan et al., 2000). To address this problematic, the multi-disciplinary campaign FIREX-AQ was deployed.

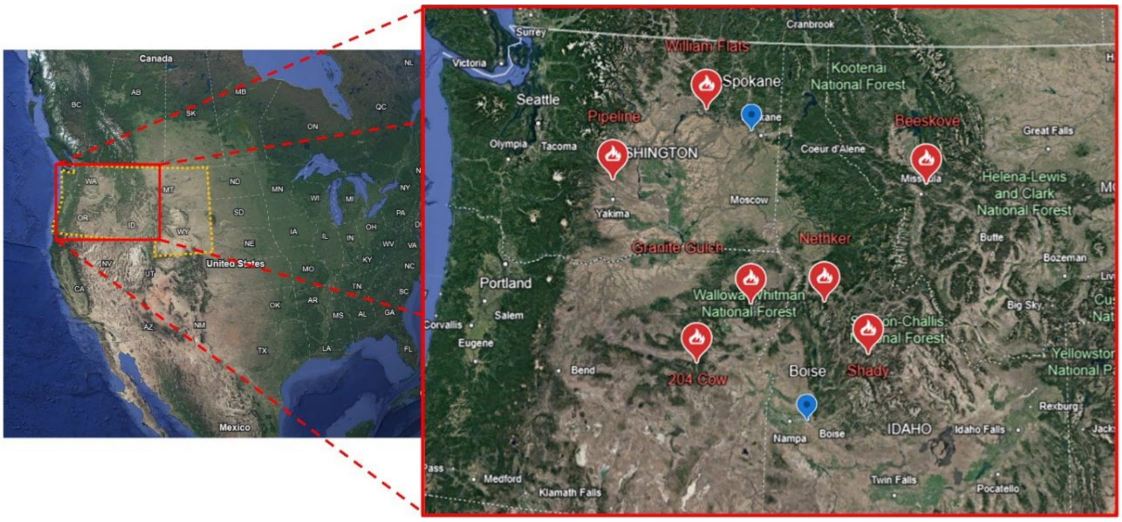

Figure 6.1: Location of the fires (red pins) studied during the FIREX-AQ campaign deployed in the North Western US in summer 2019. The radiosonde sites in the region are indicated in light blue, data of both Boise (ID) and Spokane (WA) sites are available at Wyoming University database. © Google Earth.

The extensive field campaign FIREX-AQ, led by NOAA and NASA, was created with broad science targets (Warneke et al., 2023), mainly focusing on investigating the chemistry and transport of smoke from wildfires and agricultural burning with the aim of improving weather, air quality and climate forecasts. FIREX-AQ has been organized during summer 2019 over the Northwest states of US (Fig. 6.1), where intense wildfires and agricultural fires take place. During the campaign, seven main fire sources were identified, thus their locations are indicated on the map in Fig. 6.1. The two radiosonde sites in the region studied, Boise and Spokane, are showed as well.

Remote sensing platforms

In order to evaluate and study smoke properties at the source and its transport on a local and regional scale, remote sensing instruments were installed in both stationary and mobile DRAGON payloads, in addition to the permanent AERONET sites (Holben et al., 2018). In total, three DRAGON networks (not presented in this work) were installed in Missoula, Taylor Ranch, and McCall and two mobile units with photometer-lidar were deployed.

The two Dragon Mobile Units called DMU-1 and DMU-2 (Fig. 6.2), both equipped with photometer and lidar, performed on-road mobile measurements around major fires sources. The installation of the remote sensing instruments in the DMUs followed the design of MAMS

(Mobile Aerosol Monitoring System) platform, which is described in detail by Popovici et al. (2018).

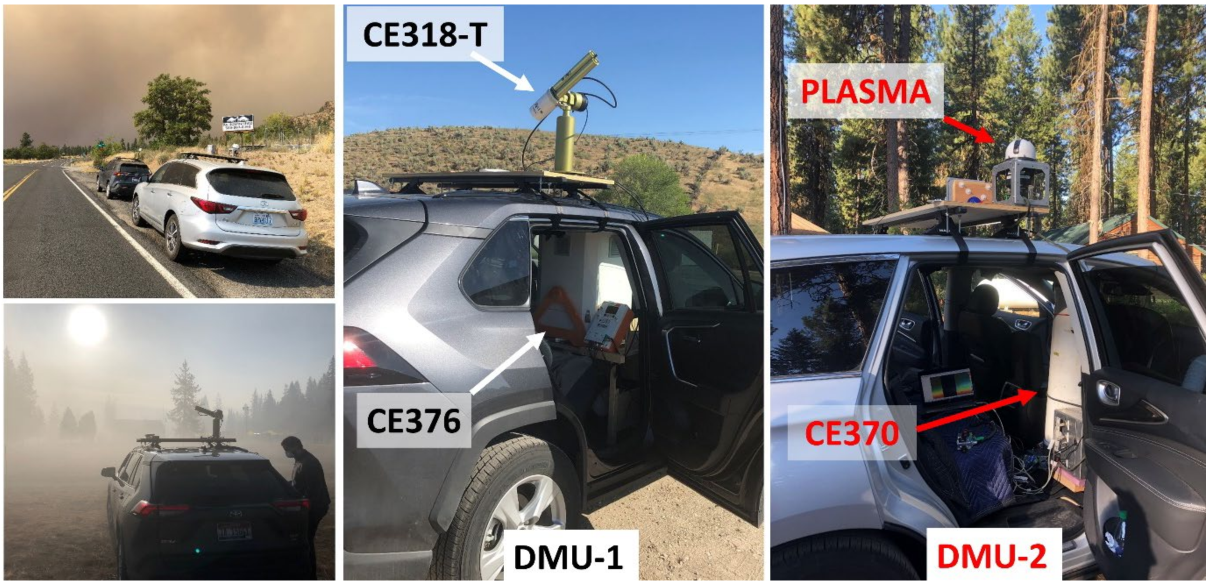

Figure 6.2: Mobile platforms deployed during the FIREX-AQ campaign, DMU-1 and DMU-2. Photographs taken by the DRAGON mobile team.

- **DMU-1** was equipped with an early version of CE376, two-wavelength polarization lidar, and with the CE318-T sun-sky-lunar photometer (ship-borne CE318-T). In this case the lidar system had higher laser energy for the 532 nm emission. Depolarization measurements at 532 nm followed a configuration with φ=0°, measuring the parallel component on the PBS transmitted branch (Chapter 3 Sect. 3.3.1). The measurements were taken through an open hatch in the rooftop of the vehicles, so no influence of a window on the depolarization measurements.
- **DMU-2** was equipped with CE370 single-wavelength lidar and PLASMA sun photometer, both tested and used in prior mobile campaigns (Popovici et al., 2018; Hu et al., 2019; Popovici et al., 2022).

The temperature control inside both mobile units was not possible during mobile measurements (only using the car's air conditioning), so stationary and in movement measurements were alternated with pauses to preserve the instruments performance, especially during daytime when extremely high temperatures and dry conditions were met. Both lidars systems were impacted by high internal temperatures (Fig. 6.3), affecting their performance. Particularly for the 532 nm channels of the CE376 lidar the overlaps were affected by the daily evolution of temperatures varying some days from 15 °C during nighttime to 40 °C during daytime. We remind that in Chapter 3 Sect. 3.5.2, it has been discussed temperature effects on the overlap function for 532 nm channels. Therefore, only quality-assured data are considered for the inversion scheme. Likewise, the temperature effect was accounted on the overlap correction, from where relative errors of 10 % at 2 km going to 30 % at 400 m are estimated and propagated on the derived aerosol optical properties.

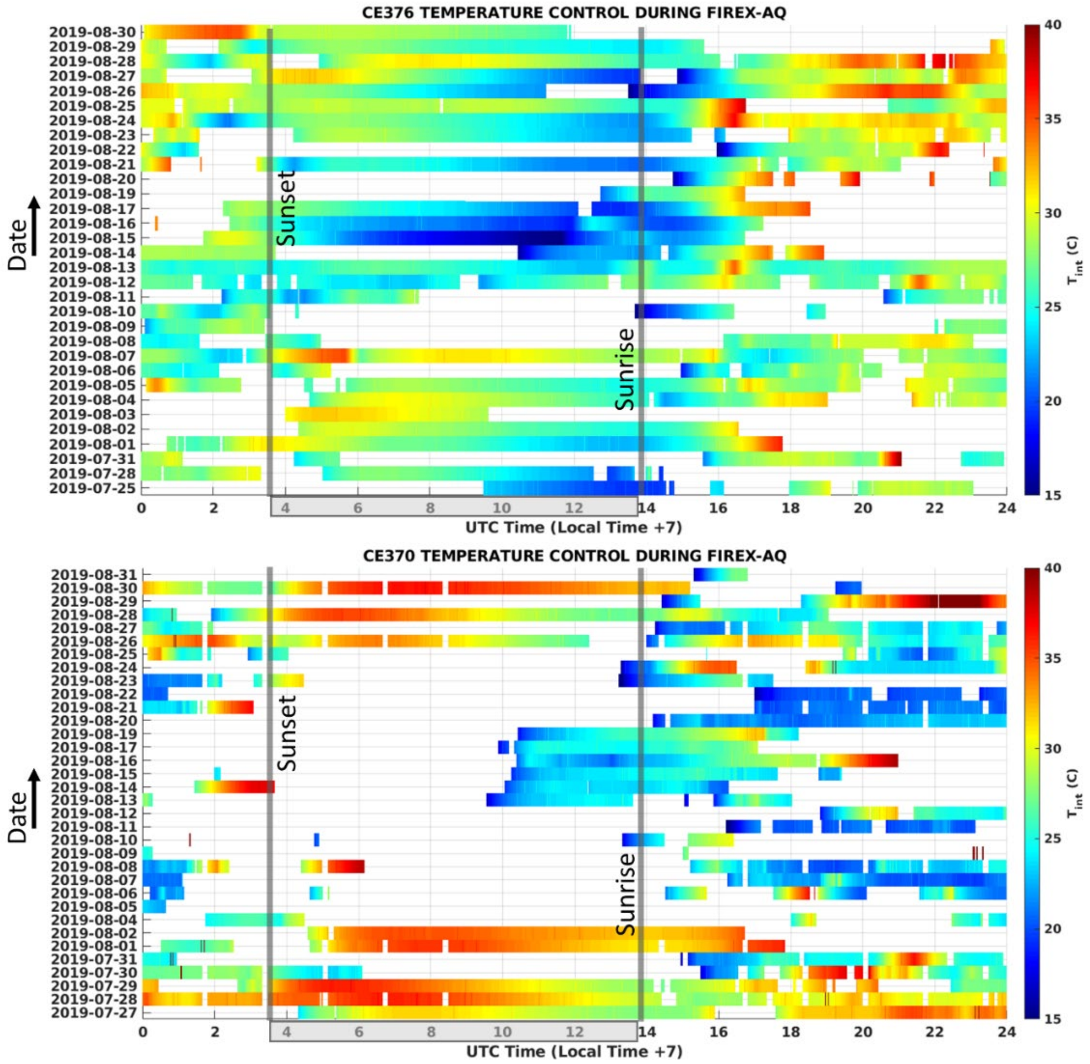

Figure 6.3: Temporal variations of the lidar internal temperature during the FIREX-AQ campaign. On the top, the CE376 lidar internal temperature is presented and, on the bottom, the CE370 lidar internal temperature. The aproximative time of sunset and sunrise are indicated by lines on top the graphs.

Moreover, the CE318-T photometer aboard DMU-1 was adapted and used for ship-borne type of mobile measurements, i.e., for slow motion, before the campaign. Therefore, some difficulties were faced when using a car, especially due to the velocity and the complexity of the terrain and roads. The sun-tracking and geo-location communication were not fast enough for these particular conditions. As a solution, stationary measurements of 5 to 15 minutes were performed along the DMU-1 trajectories to increase the density of observations with CE318-T photometer. On the other hand, PLASMA sun-photometer was able to successfully perform on-road observations, with difficulties mainly due to the presence of mountains when sun elevations are low and in presence of dense smoke plumes.

Both DMUs performed measurements along the roads around the major fire sources. Although the extreme conditions, such as high temperatures, topography and the presence of thick smoke plumes limited the performance of the instruments, we were able to investigate smoke optical properties close to the source.

6.1.1 Aerosol properties: general overview

A general overview of the mobile observations around seven fires sources is provided in this section. Figure 6.4 presents spatial variability of AOD at 440 nm and EAE at 440/870 nm acquired with both photometers, CE318-T aboard DMU-1 and PLASMA aboard DMU-2. Moreover, the average values around each fire are presented in Table 6.1.

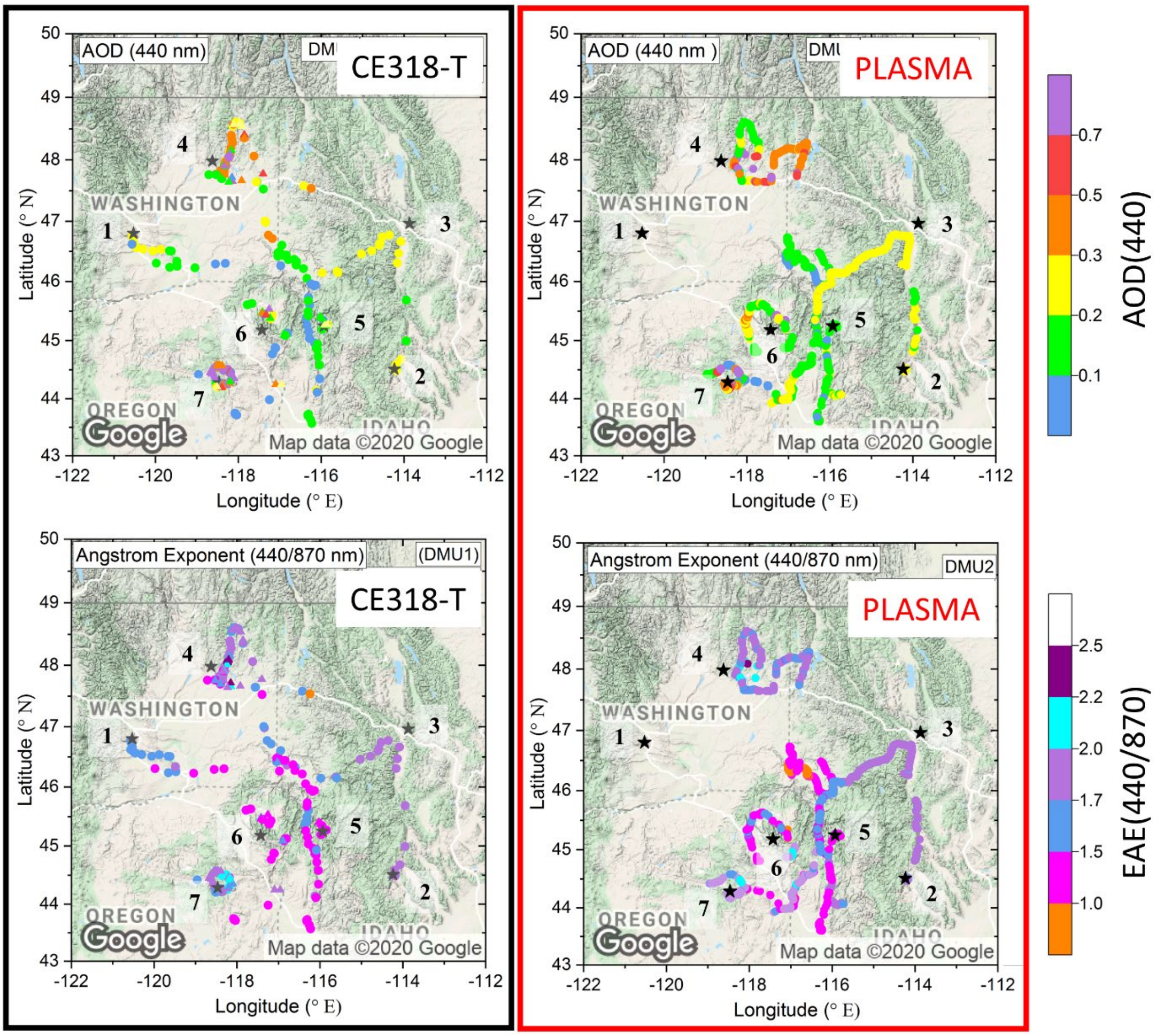

Figure 6.4: Spatial variations of AOD(440) and EAE(440/870) around 7 fires during FIREX-AQ. The aerosol properties are derived from direct sun photometer measurements, CE318-T aboard DMU-1 (left) and PLASMA aboard DMU-2 (right). The fires are indicated by numbers on the maps: (1) Pipeline, (2) Shady, (3) Beeskove, (4) William Flats, (5) Nethker, (6) Granite Gulch and (7) 204 Cow. Credits: I. Popovici.

Measurements in and out of smoke plumes within ~150 km from the fires are taken into account for the average values presented in Table 6.1. Higher AODs were found around 204 Cow fire (7), followed by William Flats fire (4). Conversely, the lowest AOD were found around the first fire, Pipeline (1), and around Nethker fire (5). Moreover, at Nethker fire the reported EAE, 1.32, is the lowest with respect to the other fires.

Table 6.1. Overview of photometer measurements embarked on-board DMU-1 (CE318-T) and DMU-2 (PLASMA). Averaged measurements around 7 fires sources during the FIREX-AQ campaign.

Fire Name	Location (State)	Dates	AOD_{ph} (440)	EAE_{ph} (440-870)
Pipeline (1)	46.83° N, 120.52° W (WA)	25-28 July, 2019	0.17±0.06	1.55±0.08
Shady (2)	44.52° N, 115.02° W (ID)	29-31 July, 2019	0.21±0.01	1.90±0.04
Beeskove (3)	46.96° N, 113.87° W (MT)	31 July, 2019	0.25±0.01	1.84±0.03
William Flats (4)	47.94° N, 118.62° W (WA)	05-09 August, 2019	0.45±0.34	1.83±0.13
Nethker (5)	45.25° N, 115.93° W (ID)	13-20 August, 2019	0.20±0.10	1.32±0.10
Granite Gulch (6)	45.18° N, 117.43° W (OR)	20-22 August, 2019	0.26±0.11	1.44±0.08
204 Cow (7)	44.29° N, 118.46° W (OR)	23-29 August, 2019	0.70±0.48	1.84±0.21

The high concentration of fine mode aerosols (expected for fresh smoke) is detected at a regional level, with EAE_{ph}(440/870) always higher than 1.3, and varying 5% from the averages at each fire. On the other hand, measured AOD_{ph}(440) are varying up to 40 % from the averages at each fire, showing a non-homogeneous distribution of aerosols around the source. In particular, the William Flats fire was one of the major fires detected during the campaign and therefore one of the most studied. Thus, the next section is dedicated to the description of the mobile remote sensing observations around the William Flats fire.

6.1.2 William Flats Fire

The western US was affected by a persistent deep trough of low pressure in the months prior to FIREX-AQ resulting in elevated soil/vegetation moisture when the fire season began, which controlled the regional fires spread. However, during the first days of the campaign (22 July-5 August 2019), high pressure (anticyclone) weather conditions controlled the moisture transport in the mid-troposphere with wide spread of cloud cover and thunderstorms (Fig. 6.5a). Combined with dry conditions in the lower troposphere, precipitation normally evaporated before reaching the ground, allowing the ignition of various fires due to lightning strikes. A low-pressure trough approaching from the West (W) on 6-9 August 2019 broke the high-pressure ridge, increasing gradually surface wind speed (Fig. 6.5b). William Flats fire, hereafter denominated simply as **WFF**, in the North-East (NE) of Washington state was in particular controlled by the unique synoptic weather conditions, with fire spread and smoke release progressively increasing as the low-pressure approached. A more detailed description of the synoptic meteorological conditions dominating the campaign can be found in Warneke et al. (2023). Moreover, a camping base has been installed at Fort Spokane (47.905° N, 118.308° W, 430 m a.sl.), which is located on the East (E) side of WFF at ~15 km from the source and separated by the Columbia River.

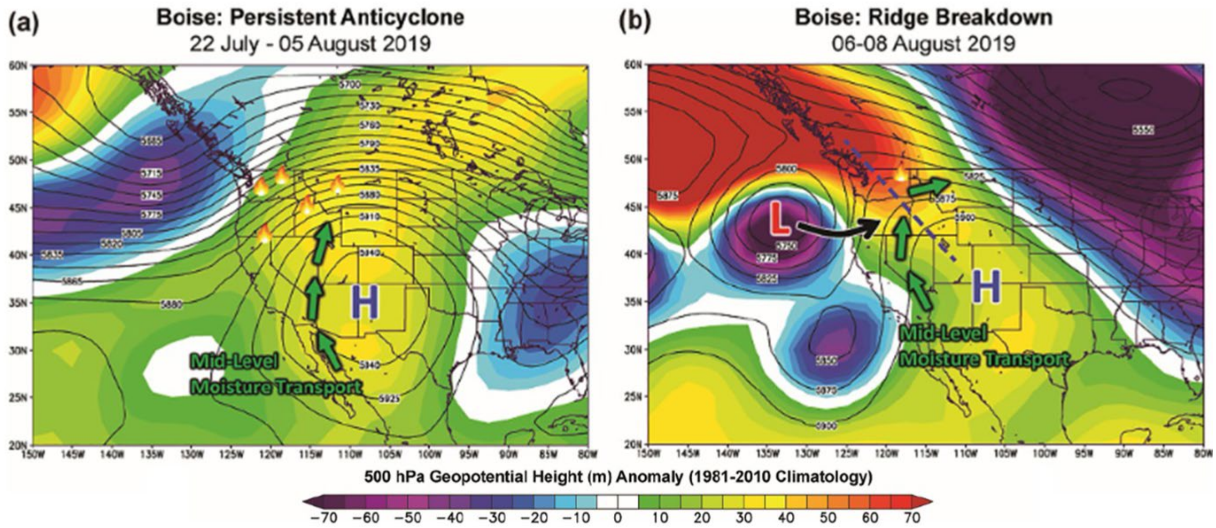

Figure 6.5: Large scale weather conditions impacting William Flats fire. Adapted from Warneke et al. (2023).

Mobile observations from selected on-road trajectories completed during 6-7 August 2019 are taken into account to reveal the distribution of aerosols properties around the active WFF. Thus, the GPS track of lidar measurements and the photometer observations from both DMU-1 and DMU-2 are displayed in Fig. 6.6. The selected trajectories (T) for DMU-1 (T1 to T4), in the top panel, and for DMU-2 (T1 to T5), in the bottom panel, are represented by different symbols. The time used to cover each of them is indicated on the legend and also on top of the maps, all times are in UT (Local time + 7h). In addition, the AOD_{ph} values at 440 nm from both photometers are given by the symbol size, and EAE_{ph} values at 440-870 nm are color-coded. The fire ignition point is indicated on the maps with a red star symbol and Fort Spokane is pointed with a blue arrow. The extension of the active fire for each day is represented by the thermal anomalies, or hot spots, from the satellite-based sensor MODIS. The MODIS Thermal anomalies product is derived from the Terra and Aqua satellites and is available to the public through NASA Worldview (https://wvs.earthdata.nasa.gov).

Differences on both photometer performances are clear in Fig. 6.6. PLASMA sun-photometer was capable to perform more measurements in contrast to the CE318-T. In general, both DMU-

1 and DMU-2 observations during 6-7 August 2019, show the predominance of fine aerosols with EAE_{ph} values always higher than 1.4, as well as high variability of aerosols distribution with AOD_{ph} ranging from 0.1 to 1.1.

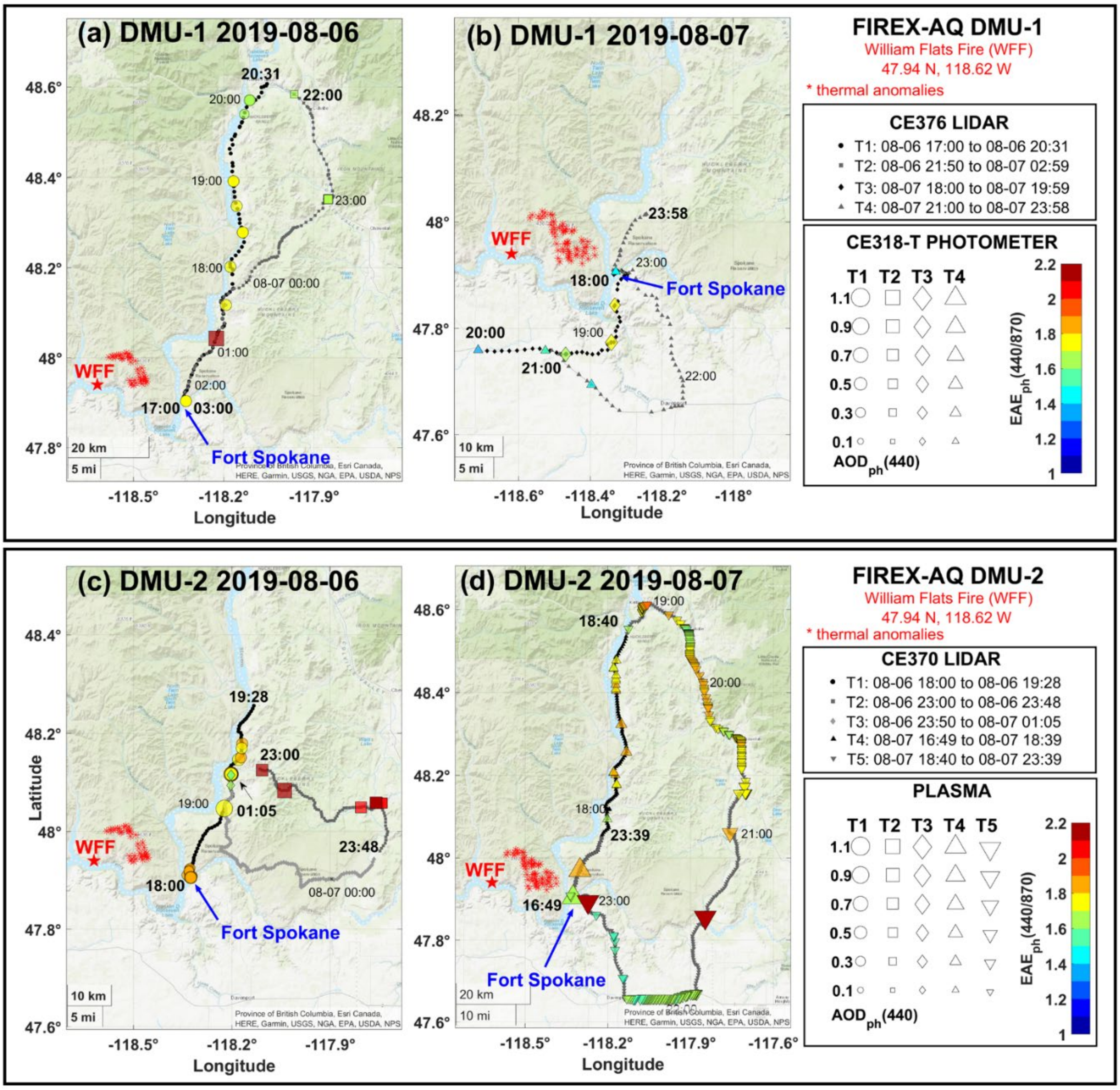

Figure 6.6: Mobile observations around WFF during 2019-08-06 and 2019-08-07 in UTC time. GPS tracks of DMU-1 and DMU-2 are presented in the top and bottom panel respectively. For each trajectory (T) a different symbol is used. Photometers measurements are presented with color coded symbols, EAE(440/870) represented by the color and AOD(440) by the symbol size. The ignition point of WFF is represented by a red star. The extension of the fire is represented by thermal anomalies from MODIS AQUA/TERRA detected during each day.

For further interpretation of the photometer mobile observations, it is convenient to mention the solar azimuth angle during the WFF. Hence, at sunrise (~13:40 UT) the azimuth is 68^{o} (NEE), at solar noon (~21:00 UT) it is 180.4^{o} (S) with elevation of 58.7^{o} and at sunset (~04:40^{+1day} UT) the azimuth is 292^{o} (WNW). In the following sub-sections, the analysis of mobile observations from DMU-1 and DMU-2 for each day are presented.

6.1.2.1 Case study: 6 August 2019

On 6 August 2019, WFF was spread to the NE from its ignition point, with hot spots elevations ranging around 0.7-1.2 km asl (Fig. 6.6 panels a and c). Plumes of emitted smoke were mostly moving to E direction with respect to the source, as one can see from MODIS images (Fig. 6.7). During day-time on 6 August 2019, the smoke plumes are slightly moving towards SE at 19:07 UT (image from Terra), and towards NE with diffused smoke northwards at 20:51 UT (image from Aqua).

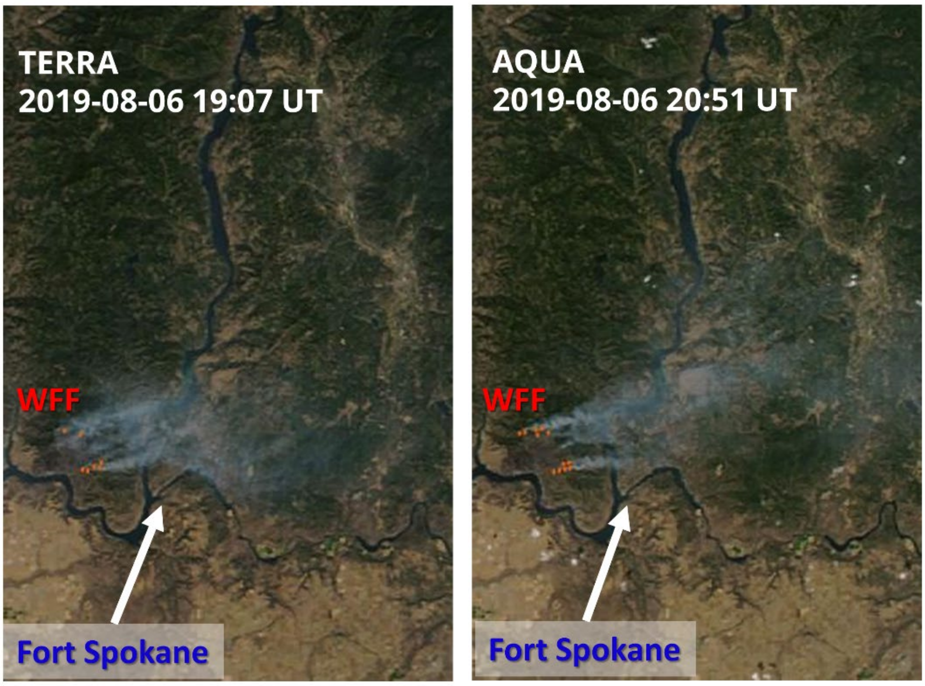

Figure 6.7: True Color Corrected Reflectance and Thermal anomalies obtained from MODIS aboard TERRA (left) and AQUA (right) during 6 August 2019. The limits of the images are top right: 48.7 N, 117.6 W and bottom left: 47.6 N, 118.7 W. Source: NASA Worldview Snapshots (https://wvs.earthdata.nasa.gov).

The height-temporal variations of properties derived directly from DMU-1 lidar observations during 06 August 2019 are presented in Fig. 6.8. The RCS at 532 nm and 808 nm and VLDR at 532 nm are presented, along with the photometer temporal series of AOD_{ph} at 532 nm and 808 nm and $EAE_{ph}(532/808)$.The two trajectories DMU-1 T1 and DMU-1 T2 (presented in Fig. 6.6a) are highlighted, showing the evolution of the fire during the day, especially when DMU-1 is near Fort Spokane (beginning of T1 and end of T2). Approaching to sunset (~04:40^{+1day} UT), smoke release progressively increased with the temperature rising, thus the smoke plume was denser and at higher altitude. Over all, the VLDR values are always below 0.08, which is expected for smoke aerosols (coated fine aerosols).

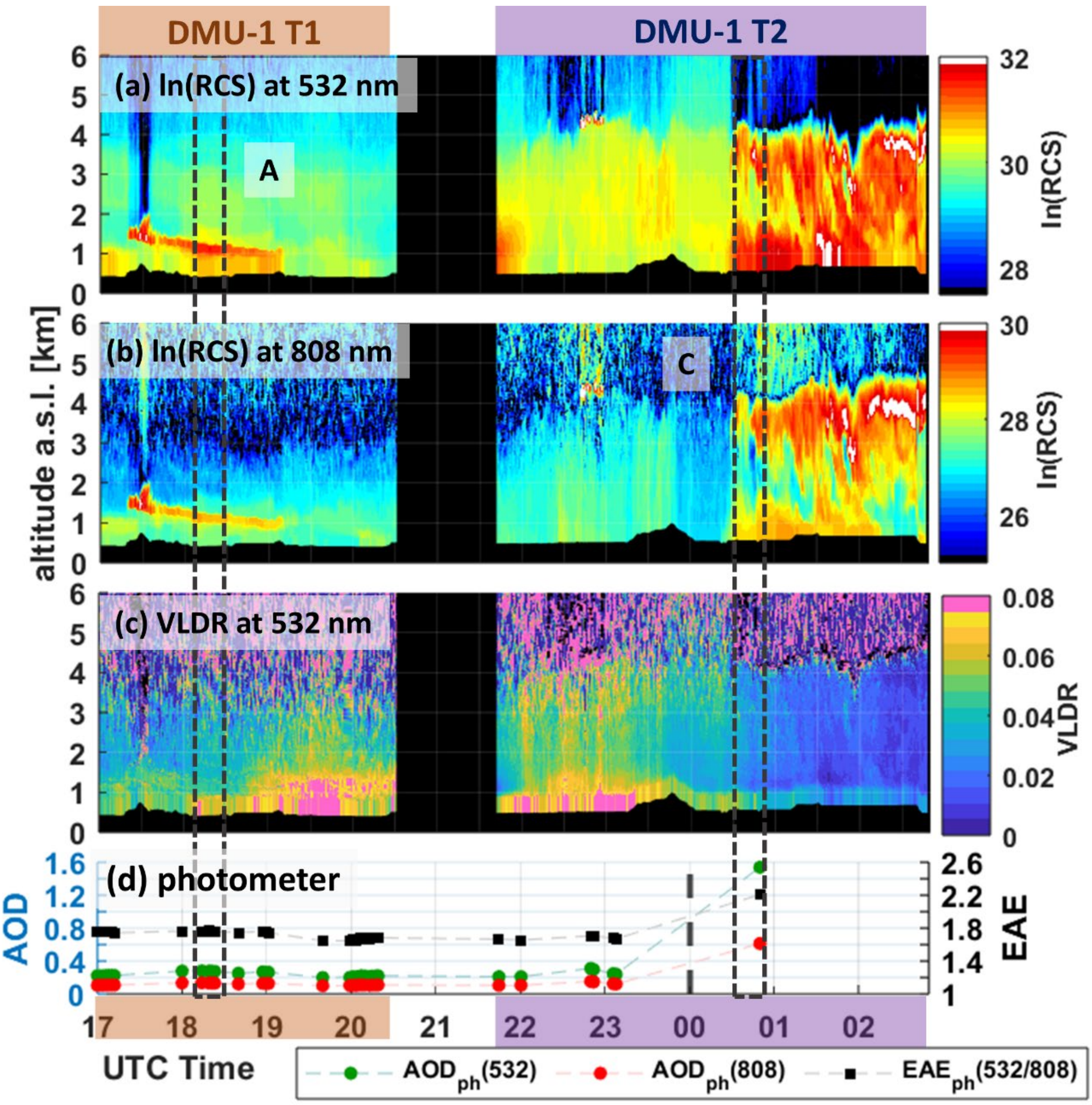

Figure 6.8: DMU-1 height-temporal variation of (a) ln(RCS) at 532 nm, (b) ln(RCS) at 808 nm and (c) VLDR at 532 nm, and the photometer temporal series, AOD at 532 nm and 808 nm and EAE during 06 August 2019. The two trajectories T1 (orange) and T2 (purple) correspond to the present trajectories in Fig. 6.7a. Two thresholds of time A and B are highlighted by dashed black line boxes and will be used in further analysis.

The height-temporal variations in Fig. 6.8 are useful to clearly see the parameters temporal evolution, however by their own, do not clearly represent the spatial variations seen by the mobile observations. Hence, the spatio-temporal variation of aerosols along the trajectories for both DMU-1 (top panel) and DMU-2 (bottom panel) are presented in Fig. 6.9. For each trajectory, the 3D spatio-temporal distribution of β_{att} at 532 nm is plotted on top of the 3D Digital Elevation Model (DEM) map of the region. The DEM used in Fig. 6.9 is the product 1 arc-second global coverage (~30 m resolution) from Shuttle Radar Topography Mission (SRTM), available through Earth Explorer interface of United States Geological Survey (https://earthexplorer.usgs.gov/). Moreover, both β_{att} and DEM maps are color coded, each one with its own color bar scale. In the same way as in Fig. 6.6 panels (a) and (c), red points represent the thermal anomalies showing the extension of the active WFF detected on 6 August 2019.

During 6 August 2019, residual smoke in all the trajectories was detected up to 4 km asl and higher AOD_{ph} and EAE_{ph} values were identified under the presence of dense smoke plumes. The Columbia River acted like an air canal with the prevailing valley winds in the morning (De Wekker & Kossmann, 2015; Whiteman, 2000), directing a diffused smoke plume northward, as well observed on the Aqua MODIS image (Fig. 6.7).

The trajectory DMU-1 T1 (Fig. 6.9a, also in Fig. 6.6a and Fig. 6.8) covered ~80 km between 17:00 to 20:31 UT along the Columbia riverside going from Fort Spokane to Kettle Falls (48.60° N, 118.06° W). $AOD_{ph}(440)$ ranged around 0.3 and $EAE_{ph}(440/870)$ was higher than 1.6.

DMU-2 T1 (Fig. 6.9c, also Fig. 6.6c) covered 40 km of the same route between 18:00 to 19:28 UT, starting with 30 min of stationary measurements at Fort Spokane. $AOD_{ph}(440)$ values within 0.3-0.7 and $EAE_{ph}(440/870)$ above 1.7 were observed (Fig. 6.6c). During both trajectories DMU-1 T1 and DMU-2 T1, azimuthal solar angles vary from 101° to 153° (E to S), meaning that both photometers, CE318 and PLASMA, were taking measurements towards the E side of WFF against the movement of the vehicles and limited by the mountain slopes. Hence, both DMUs followed and measured the diffused smoke plume with one hour time difference. In particular, DMU-2 T1 lidar-photometer measurements indicate an increase of smoke release and accumulation northward, with higher AOD_{ph} and β_{att} (below 2 km asl) values.

The trajectory DMU-1 T2 (Fig. 6.9b, also in Fig. 6.6a and Fig. 6.8) was completed from 21:50 to 02:59 UT, i.e., in the afternoon, and covered ~100 km on the way back to Fort Spokane from Kettle Falls, passing through Colville River basin. Hence, the residual smoke well mixed up to 4 km asl is contained along the valley (Fig. 6.8) showing $AOD_{ph}(440)$ varying between 0.3-0.5 and $EAE_{ph}(440/870)$ of 1.6 (solar azimuth 206° to 292°, i.e., photometer pointing to E side of WFF, towards WFF). Approaching Fort Spokane, the development of a convective smoke plume was observed (Fig. 6.10b). One exceptional sampling of the dense smoke plume was possible, at ~01:00 UT and 20 km E away from the fire, with an AOD_{ph} of 1.1 and EAE_{ph} of 2.2 (Fig. 9a).

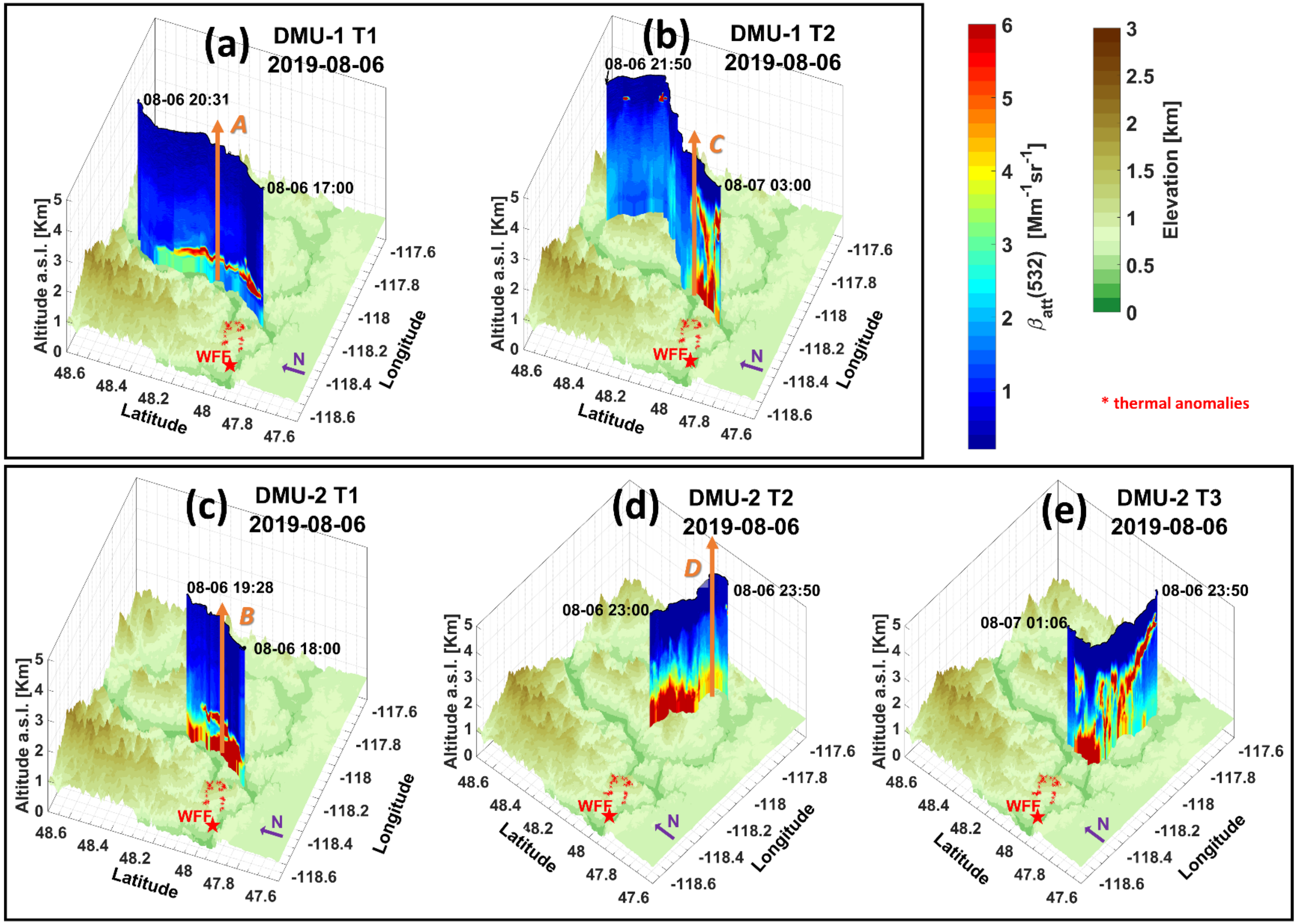

Figure 6.9: Spatial-temporal distribution of total attenuated backscatter at 532 nm for the trajectories on 2019-08-06 from Fig. 6.6 (a) and (c). Trajectories of DMU-1 (CE376 lidar) are presented in the top panel and DMU-2 (CE370 lidar) in the bottom panel. The lidar trajectories are plotted on top DEM from SRTM at 1 Arc-Second resolution (~30 m). The ignition point of WFF is represented by a red star and the extension of the active fire by MODIS thermal anomalies. Orange arrows represent the selected profiles for further analysis in Fig. 6.11.

DMU-2 T2 (Fig. 6.9d, also Fig. 6.6c) performed measurements in the afternoon from 23:00 to 23:48 UT, going downwind WFF and covering ~60 km horizontally to E (solar azimuth 228° to 245°, i.e., towards WFF). This trajectory in particular shows how smoke accumulated and settled across the valleys. High $AOD_{ph}(440)$ values above 0.7 and $EAE_{ph}(440/870)$ values above 2 (Fig. 6.6c) were observed.

DMU-2 T3 (Fig. 6.9e, also Fig. 6.6c) also completed during the afternoon (23:50 - 01:05 UT), is covering the return route to Fort Spokane. While it got closer to the source, higher values of β_{att} (> 6 $Mm^{-1}sr^{-1}$) were detected from 4 km asl towards ground level. Although no photometer data is available due to presence of the thick smoke plume and lower zenithal solar angle, lidar provides a glimpse of the convective smoke plume transect. The smoke plume raised up to 4.2 km asl at 50 km away (horizontally to E) from its source, ~3 km higher than the active fire and above the mountain ridges.

Aerosol optical properties: selected profiles

From the DMU-1 and DMU-2 trajectories on 6 August 2019, selected coincident lidar and photometer data are averaged over 5 to 15 minutes and are used to enhance the aerosols characterization presented so far. The selected times are displayed in Fig. 6.8 by black dashed boxes and in Fig. 6.9 by orange arrows in the 3D β_{att} quicklook. The profiles' location with respect to the fire is shown on a polar plot in Fig. 6.10.

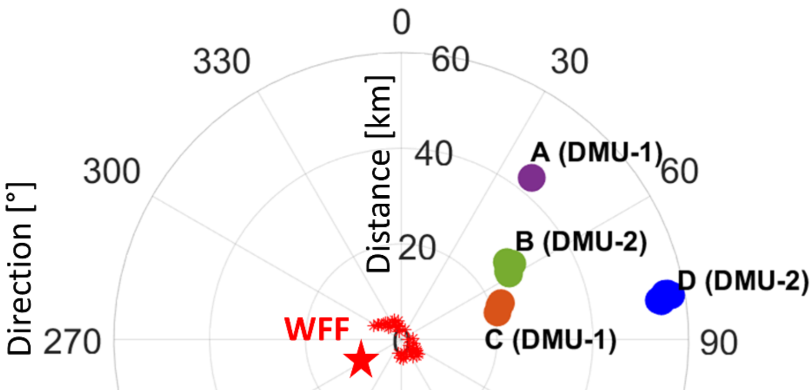

Figure 6.10: Location of the selected profiles with respect to the WFF in polar coordinates during 6 August 2019. The angle represents the direction (considering North as 0°) and the radius represents the distance, both with respect to the center of the active WFF. The ignition point is marked with a red star.

In Fig. 6.11, the profiles of aerosol properties for each selected dataset differentiated by color are presented. Hence, profiles of backscatter, extinction at 532 nm and 808 nm, and profiles of PLDR, EAE and ACR are shown. For the lidar inversion, data below 400 m is considered constant due to high uncertainties (>30%) on RCS at 532 nm. Molecular coefficients are calculated using radiosonde measurements at Spokane station (47.68º N, 117.63º W) from Wyoming University database (https://weather.uwyo.edu/upperair/sounding.html). Moreover, the detection limit is defined at SNR=1 for all channels to extract more information, in particular from 808 nm. Detection limits for 808 nm and 532 nm cross polarized channels from CE376 are below 2 km and 3-4 km, respectively, due to high solar background. Nevertheless, we were able to study the diffuse smoke plume transported along the Columbia River with retrievals profiles from selected data.

The dataset A, attained during DMU-1 T1, is showed in Fig. 11 top panel along with dataset B, from DMU-2 T1. The dataset A corresponds to the averaged CE376 lidar data from 18:10 to 18:25 UT on 6 August 2019, located ~40 km away to the NNE of WFF (Fig. 6.10). AOD_{ph} from CE318-T photometer was 0.28 and 0.13 at 532 nm and 808 nm respectively, EAE_{ph}(532/808) was 1.76 and the AOD_{est} at 808 nm is 0.1 (needed for retrieval). The smoke plume is identified at 1-1.3 km asl, with maximum values of extinction at 1.14 km asl. Thus, extinction values of 370 ± 70 Mm^{-1} (with LR=35 ± 1 sr) at 532 nm, and 207 ± 20 Mm^{-1} (with LR= 57 ± 4 sr) at 808 nm were observed. Other aerosol properties inside the smoke plume were 0.06 ± 0.04 for PLDR, 1.2 ± 2.5 for EAE and 0.5 ± 0.3 for ACR. On the other hand, dataset B corresponds to averaged CE370 lidar data from 19:05 to 19:15 UT on 6 August 2019, ~1 h after the dataset A was obtained. Dataset B is located 25 km to the NNE away from WFF (Fig. 6.10), with values of 0.35 for AOD_{ph} at 532 nm and 1.7 for EAE_{ph} (440/870). The smoke plume is identified at 1.6-1.9 km asl with maximum values of extinction at 1.7 km asl. Thus, values of 380 ± 20 Mm^{-1} (with LR=39 ± 1 sr) for extinction at 532 nm were retrieved.

The identified smoke plumes for both datasets, A and B, are almost the same, except for the altitude. The higher extinction below 1 km asl for dataset B is related to the increase of smoke released through the day. Moreover, a layer of residual smoke at 2-3 km asl is detected for both cases, with less intensity for dataset B but still noticeable. PLDR in the residual layer (0.08 ± 0.02) is in agreement with reported values of fresh smoke transported one day from source (Alados-Arboledas et al., 2011; Ansmann et al., 2021; Balis, 2003; Tesche et al., 2009b). Aside the high uncertainties that are attached to the profiles in the first hundreds of meters (due to overlap uncertainties), ACR values suggest the presence of bigger aerosols in the smoke plume at 1 km asl than in the residual layer at 2-3 km asl, in the same way as EAE. The observed bigger aerosols could be related to the release of fine-ash particles (sizes below 2 µm) within the smoke plume (Adachi et al., 2022).

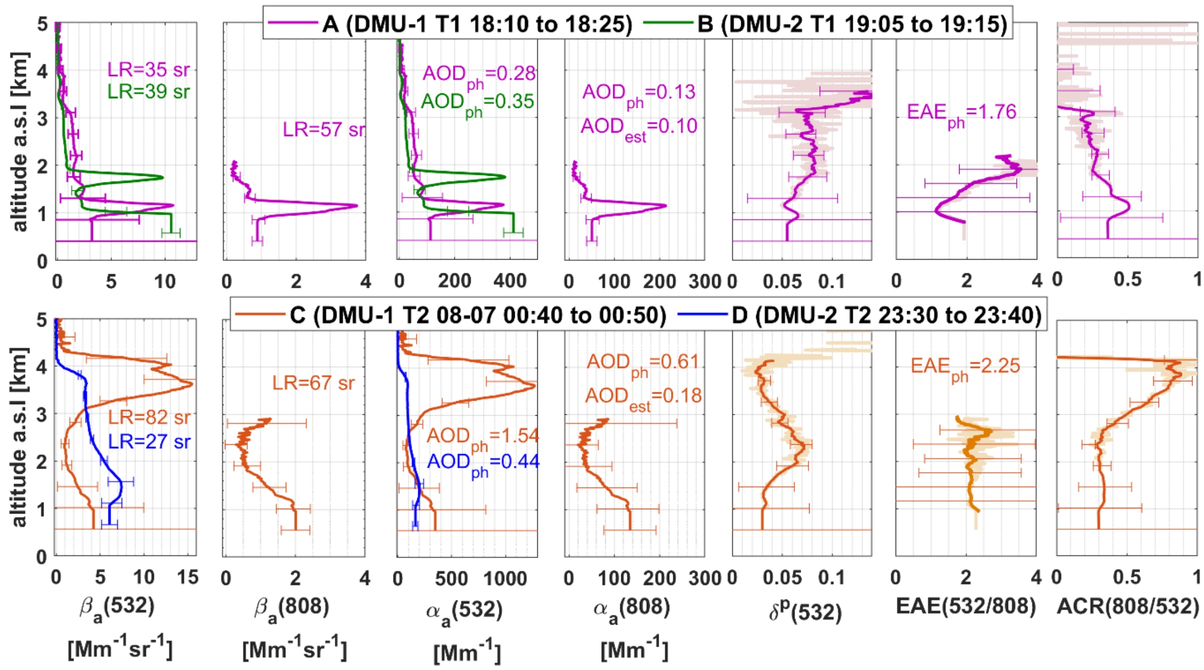

Figure 6.11: Profiles of aerosol optical properties from averaged selected datasets of both DMU-1 and DMU-2 mobile observations during 6 August 2019. Each dataset is differentiated by color. From left to right: Profiles of backscatter at 532 nm and 808 nm, extinction at 532 nm and 808 nm, PLDR, EAE and ACR.

The dataset C showed in Fig. 6.11 bottom panel, obtained during DMU-1 T2 (Fig. 6.9b), corresponds to averaged CE376 lidar data from 00:40 to 00:50 UT, toward sunset on 6 August 2019. This dataset, located 20 km E of WFF (Fig. 6.10), is particularly interesting because it provides information on the convective smoke plume. Values of 1.54 and 0.61 for AOD_{ph} at 532 nm and 808 nm, respectively, were detected by the photometer, as well an EAE_{ph}(532/808) of 2.25, and AOD_{est} at 808 nm of 0.18 (below the smoke plume). The convective plume is identified at 3-4.3 km asl, with maximum values of extinction at 3.57 km asl. Thus, 1270 ± 330 Mm^{-1} (with LR= 82 ± 2 sr) for extinction at 532 nm was observed. Inside the plume, a decrease of PLDR from 0.05 ± 0.01 to 0.03 ± 0.01 is detected, in addition to values progressively increasing from 0.4 ± 0.1 to 0.9 ± 0.1 for ACR. Both parameters suggest the predominance of big spherical particles towards the smoke layer top, which could be related to the fast increase in the coating mass of soot particles within minutes from emission (China et al., 2013; Kleinman et al., 2020). Moreover, the high LR estimated can also indicate a higher presence of light absorbing aerosols, which can be related to active emissions of OC and BC.

The dataset D showed in Fig. 6.11 bottom panel was obtained during DMU-2 T2 (Fig. 6.9d) and corresponds to averaged CE370 lidar data from 23:30 and 23:40 UT. This dataset, located ~60 km E of WFF (Fig. 6.10), captures the presence of diffused smoke within a valley downwind of the fire. The smoke is extended up to 4 km asl with an important loading, AOD_{ph} of 0.4 at 532 nm, 30% higher than the reported diffused smoke northwards to the fire.

6.1.2.2 Case study: 7 August 2019

During 7 August 2019, the WFF extended towards E getting closer to the Columbia River ridge, and more hot spots were detected than the day before (Fig. 6.6b and Fig. 6.6d). Through the day, smoke convective plumes moved, mostly influenced by the strong winds, towards E direction and slightly to SE, as seen from MODIS images (Fig. 6.12). Similar to the day before, the smoke plumes are moving towards SE at 19:50 UT (image from Terra) and towards E with diffused smoke moving northwards along the Columbia River at 21:33 UT (image from Aqua). Moreover, in the afternoon, black and white ash depositions were reported, in addition to pyrocumulus clouds formation observed close to sunset (~04:40^{+1day} UT). At that point, the presence of heavy smoke plumes saturated the lidar signals and restricted photometers measurements close to the source. Therefore, trajectories were performed mostly outside the smoke plumes.

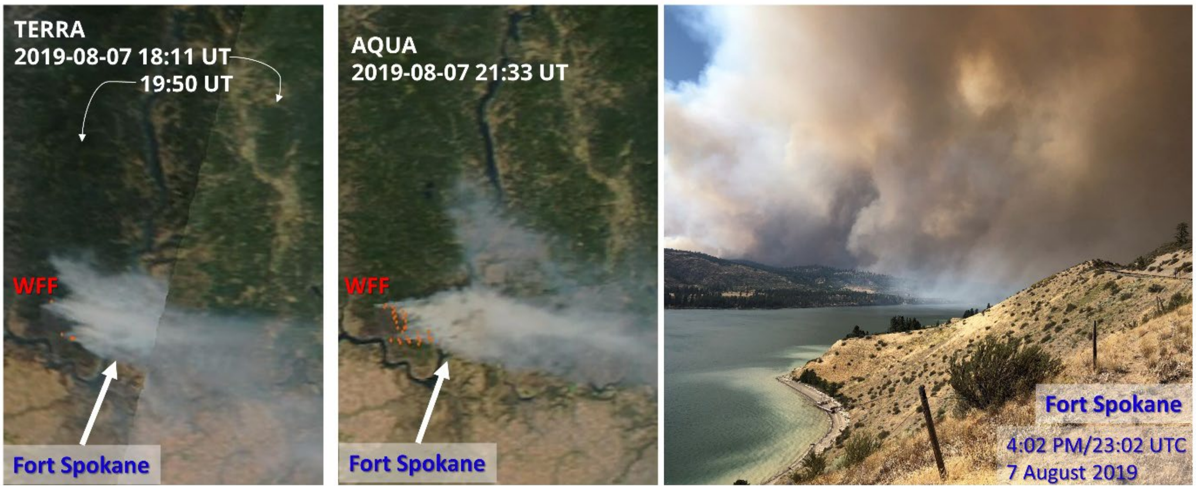

Figure 6.12: Photograph of the heavy smoke plume (right), and the true color corrected reflectance and thermal anomalies obtained from MODIS aboard TERRA (left) and AQUA (center) during 7 August 2019. The limits of the satellite images are top right: 48.7 N, 117.6 W and bottom left: 47.6° N, 118.7° W. Source: NASA Worldview Snapshots (https://wvs.earthdata.nasa.gov). The photograph was taken by the DRAGON mobile team.

Same as for the day before, the height-temporal variations of properties derived directly from DMU-1 lidar observations during 07 August 2019 are presented in Fig. 6.13. This time, the two trajectories DMU-1 T3 and DMU-1 T4 (presented in Fig. 6.6b) are highlighted and showing the southern region of WFF. The influence of smoke plumes, saturating the lidar signals, are observed when DMU-1 is near Fort Spokane (beginning of T3 and end of T4). Over all, the

VLDR values are below 0.08, like on 6 August. Artifacts on the VLDR profiles are observed which are related to the influence of temperature on the overlap functions at 532 nm.

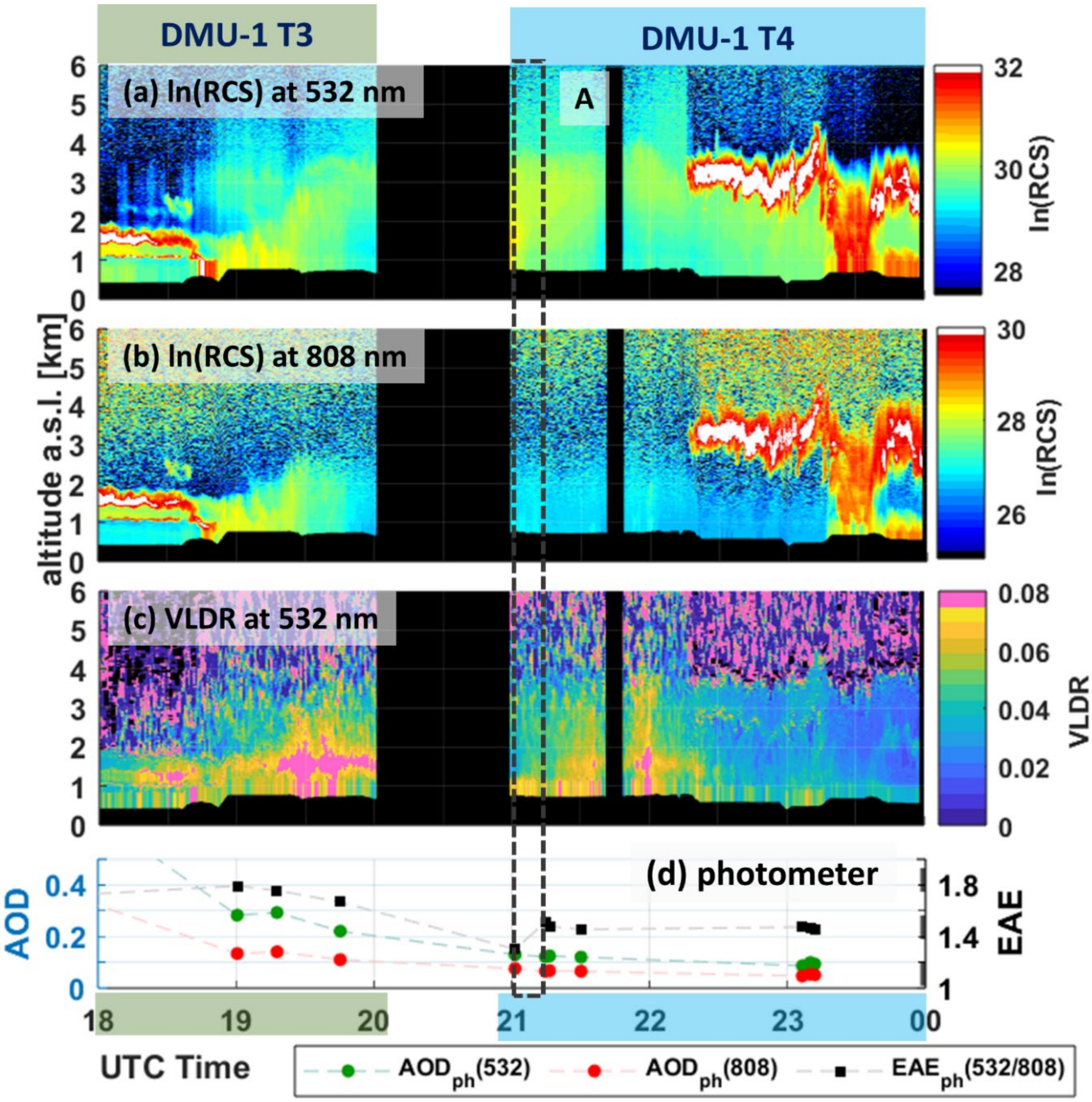

Figure 6.13: DMU-1 height-temporal variation of (a) ln(RCS) at 532 nm, (b) ln(RCS) at 808 nm and (c) VLDR at 532 nm, and the photometer temporal series, AOD at 532 nm and 808 nm and EAE during 07 August 2019. The two trajectories T3 (green) and T4 (blue) correspond to the presented trajectories in Fig. 6.7b. One threshold of time A is highlighted by a dashed black line box and will be used in further analysis.

Same as for lidar observations presented in the previous case study, 3D spatio-temporal distributions of β_{att} at 532 nm for all the trajectories during 7 August 2019 are presented in Fig. 6.13. Thus, trajectories of both DMUs are presented and evaluated in the following lines.

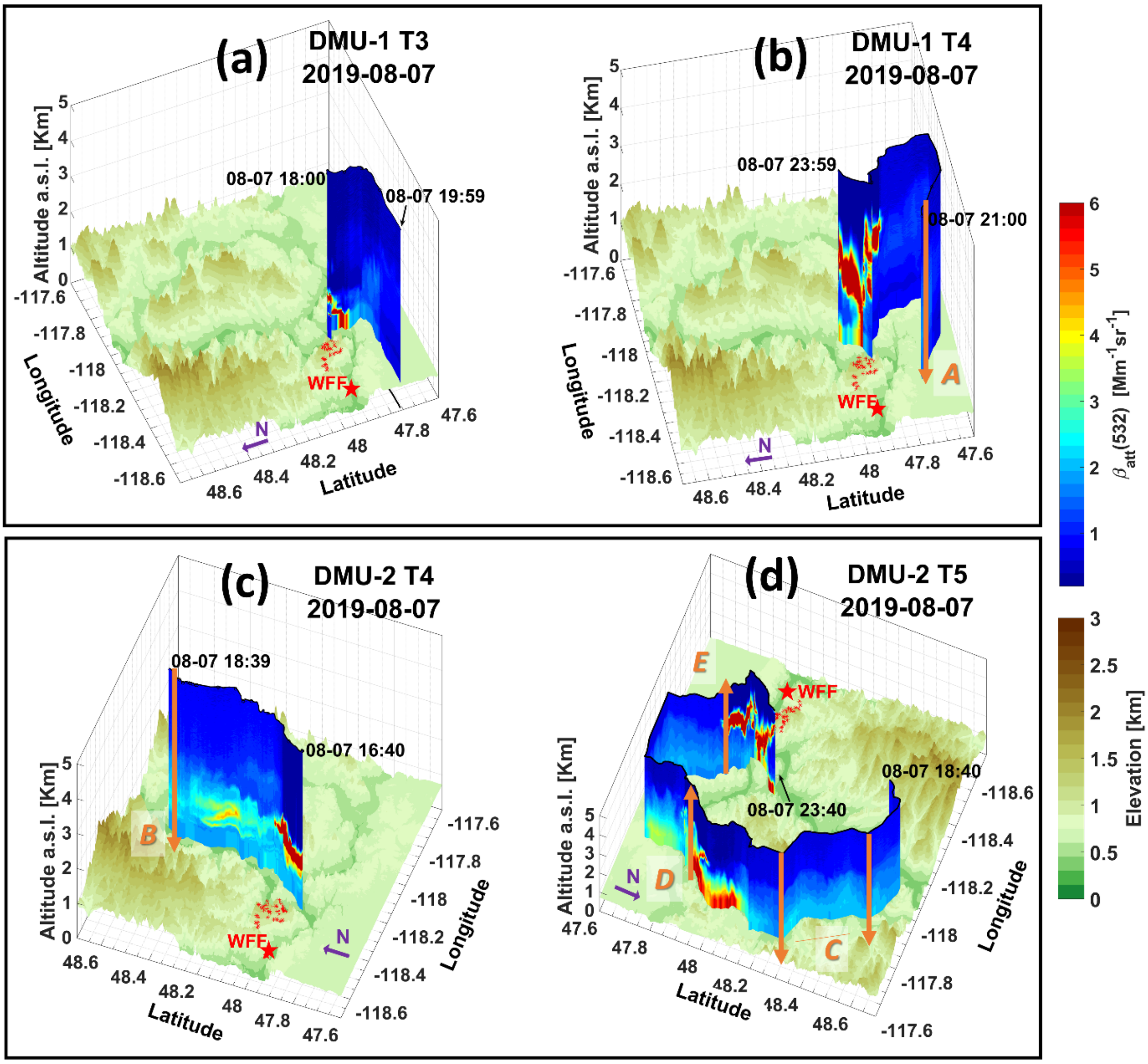

Figure 6.14: Spatial-temporal distribution of total attenuated backscatter at 532 nm, same as Fig. 6.9 but for the trajectories during 7 August 2019.

The trajectory DMU-1 T3 (Fig. 6.14a, also in Fig. 6.6b and Fig. 6.13) covered ~40 km from Fort Spokane to the S of WFF between 18:00 to 19:58 UT. DMU-1 T4 (Fig. 6.14b) covered ~70 km of route from S to E side of WFF, between 21:00 to 23:59 UT. For both trajectories, few data points from photometer were collected and might not represent the same conditions for the zenithal lidar measurements. Photometer is looking towards SE to SW from the WFF, against the winds flow. $AOD_{ph}(440)$ ranging between 0.1-0.2 and $EAE_{ph}(440/870)$ above 1.6 were observed, which are indication of lower loading of residual smoke on the S region of WFF. Both trajectories seen by the lidar show no direct influence of the smoke plumes on the S SW of WFF and present considerably lower values of β_{att}. Nevertheless, similarly to observations on 6 August 2019, a convective smoke plume reaching up to 4 km asl is observed in the afternoon towards sunset (Fig. 6.14b).

On the other hand, the trajectory DMU-2 -T4 (Fig. 6.14c, also in Fig. 6.6d) is covering the NNE of WFF along the Columbia riverside and following a branch of the smoke plume. DMU-2 T4 covered ~80 km from Fort Spokane to Kettle Falls, from 16:49 to 18:39 UT and with $AOD_{ph}(440)$ ranging within 0.1-0.3 and $EAE_{ph}(440/870)$ values of 1.6-1.8, higher AOD values being measured closer to the fire. This time, the vertical extent of the smoke plume is ~200 m higher and it is denser than the day before. But in the same way as the day before, the Columbia River is the main driver of the channeling effect of the smoke towards the N in the morning.

The trajectory DMU-2 T5 (Fig. 6.14d and also Fig. 6.6d) covered ~200 km between 18:40 to 23:40 UT from Kettle Falls (80 km NNE from WFF) towards Davenport (47.65° N, 118.15° W, ~40 km SE of WFF) going through valleys and returning to Fort Spokane. Along the way, DMU-2 measured residual smoke accumulated in the NE valley basins, with $AOD_{ph}(440)$ around 0.3 and $EAE_{ph}(440/870)$ of 1.6-1.8. In addition, residual smoke, SE of WFF, was measured with lower values of $AOD_{ph}(440)$ around 0.1-0.3 and $EAE_{ph}(440/870)$ values around 1.5-1.6. During this transect the DMU-2 crossed 2 times the smoke plume, one at 21:20-21:23 UT 40 km downwind WFF, and the second time at 23:00 UT 15 km away from the WFF. From the DMU-2 T5 3D aerosol distribution (Fig. 6.14d) and photometer (Fig. 6.6d), one can see the effect of the diffuse smoke from WFF on the NE region, characterized by its mountains and valleys.

The complex topography combined with the prevailing synoptic conditions (low pressure trough approaching from the W) have important effects on the development of the fire and its surroundings (Whiteman, 2000). While in the morning the river basin acted almost independently, channeling smoke northward, one can notice how the evolving ABL is coupled to the mountain winds systems. The diffused smoke is mixed and subsided along the valleys, with higher aerosols loading closer to the fire downwind.

Moreover, fire emissions get stronger while temperatures rise up, permitting the convective loft of the smoke above the mountain ridges, impacting an extended region downwind the fire (Fig. 6.15). During 7 August 2019, Missoula city, which is located 360 km away from WFF, was impacted by the smoke released.

Figure 6.15: Impacted region by the smoke plume emitted at WFF during 7 August 2019. True color corrected reflectance and thermal anomalies obtained from MODIS aboard AQUA.

Aerosol optical properties: selected profiles

From the DMU-1 and DMU-2 trajectories on 7 August 2019, selected coincident lidar and photometer data are averaged over 5 to 30 minutes. The selected times are displayed in Fig. 6.14 by orange arrows in the 3D β_{att} quicklook. Hence, the aerosol properties derived for each selected dataset, differentiated by color, are presented in Fig. 6.16. From left to right, profiles of backscatter at 532 nm and 808 nm, extinction at 532 nm and 808 nm, PLDR at 532 nm, EAE(532/808) and ACR(808/532) are shown. In this case, only one profile is considered from DMU-1 (top panel) and then four datasets are considered from DMU-2 (middle and bottom panel). Likewise, the profiles' location with respect to the fire is shown on a polar plot (within the dashed line box) in Fig. 6.16.

Dataset A showed in the top panel of Fig. 6.16, located 25-30 km S of WFF (DMU-1 T4 21:00 to 21:09 UT on 7 August 2019), and dataset C showed in the middle panel of Fig 6.16, located ~60 km NE of WFF (DMU-2 T5 20:00 to 20:30 UT on 7 August 2019), present residual smoke. Both datasets have values of 0.13 for AOD_{ph} at 532 nm. The dataset A shows a residual layer extending up to 4 km asl, with average values of 44 ± 17 Mm^{-1} (with LR= 37 ± 3 sr) for extinction at 532 nm, and 28 ± 15 Mm^{-1} (with LR=87 ± 15 sr) at 808 nm. In particular, the LR at 808 nm is considerable higher than the LR at 532 nm, probably influenced by the lower part of the profile which shows lower values of extinction with respect to the values presented above 2 km asl. Recall that the LR is derived from the convergence of calculated AODs to the value from photometer (in this case, the AOD_{est}). Moreover, PLDR is 0.09 ± 0.03, EAE is 1.5 ± 1.5 and ACR is 0.3 ± 0.1. One has noticed, that ACR values are constant within the residual layer, suggesting that smoke is well mixed. Dataset C shows the residual smoke in the NE side of the WFF going up to 3 km asl with a LR of 73 ± 7 sr, higher than for dataset A.

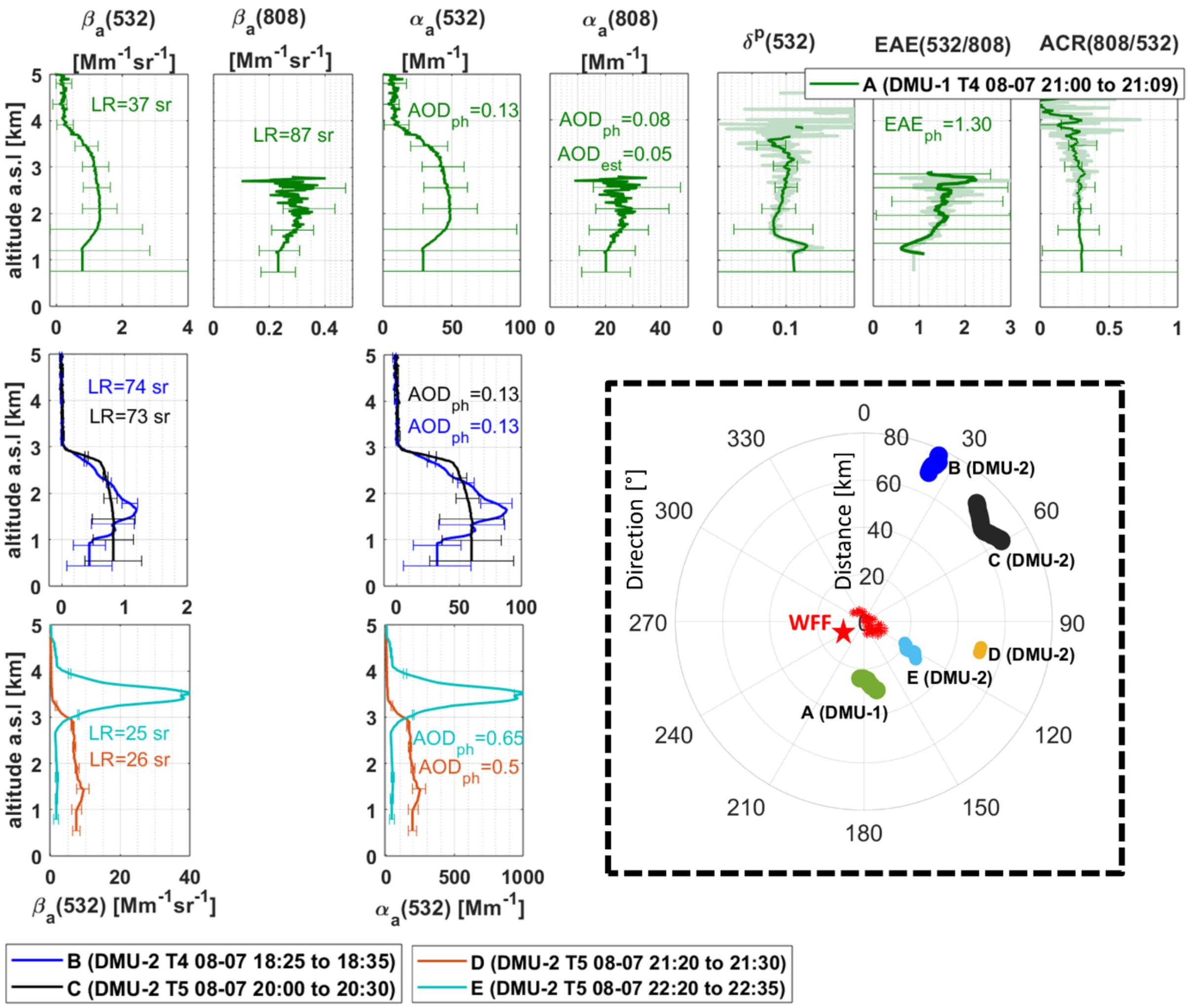

Figure 6.16. Profiles of aerosol optical properties from averaged selected datasets of both DMU-1 and DMU-2 mobile observations during 7 August 2019. Each dataset is differentiated by color. From left to right: Profiles of backscatter at 532 nm and 808 nm, extinction at 532 nm and 808 nm, PLDR, EAE and ACR. Likewise, the location of the selected profiles with respect to the WFF in polar coordinates during 7 August 2019 is presented within the dash black line box.

Dataset B (middle panel Fig. 6.16), located 80 km NE of WFF (DMU-2 T4 18:25 to 18:35 UT), presents similar LR (74 ± 8 sr) as the dataset C and the same $AOD_{ph}(532)$ of 0.13. Both datasets B and C are located NE of WFF and separated ~20 km from each other. The difference is given by the shape of the profiles, dataset B is directly influenced by the diffused smoke transported northwards by the Columbia River while dataset C is situated in the adjacent valley.

Dataset D (bottom panel Fig. 6.16) is located 50 km E of WFF (DMU-2 T5 21:20 to 21:30 UT), downwind the fire. Dataset E (bottom panel Fig. 6.16) is located ~25 km E of WFF (DMU-2 T5 22:20 to 22:35 UT) and captures the smoke plume downwind closer to the fire. For both datasets, the LR at 532 nm (26 ± 1 sr for D and 25 ± 1 sr for E) is lower than the one estimated in presence of residual or diffused smoke, which can be related to an important presence of light scattering aerosols (i.e., higher values of aerosol backscatter). This can also be observed on the

MODIS images (Fig. 6.12) obtained during 7 August, where the smoke plume scatter more the sunlight (the surface is not visible) in contrast with the day before (Fig. 6.7). Moreover the AOD_{ph} at 532 nm (0.5 for D and 0.6 for E) is lower than the day before (1.54 for dataset C on Fig. 6.11) in presence of the smoke plume. During this day, a transition to smoldering phase is presumed, given by the observations of ash deposition, less effective combustion which is related to the production of less light absorbing OC aerosols. The main results obtained in this section are summarized in Table 6.2.

Table 6.2: Overview of the aerosol properties retrieved from CE376 lidar and CE318-T photometer for the WFF case studies. The estimated uncertainties are in parenthesis. The position with respect to WFF is included and for the case of convective smoke, f make reference to flaming fire and s to smoldering fire. *Aerosol properties retrieved from CE370 lidar and PLASMA photometer.

Aerosol type		**Diffuse smoke**	**Convective smoke**	**Residual Smoke**
Altitude asl [km]		1-1.3 (40 km NNE)	f: 3-4.3 (20 km E) s: 3-4 (60 km NE) *	1.2-4 (25 km S) 0.9-3 (60 km NE) *
LR [sr]	**532 nm**	35 (1)	f: 82 (2) s: 25 (1) *	37 (3) 73 (7) *
	808 nm	57 (4)	-	87 (15)
α_a [Mm^{-1}]	**532 nm**	370 (73)	f:1270 (330) s: 960 (80)*	45 (17) 54 (9) *
	808 nm	207 (20)	-	28 (15)
δ^v	**532 nm**	0.04 (0.02)	f: 0.03 (0.01)	0.05 (0.01)
δ^p	**532 nm**	0.06 (0.04)	f: 0.04 (0.01)	0.09 (0.03)
EAE (532/808)	**LID**	1.2 (2.5)	-	1.5 (1.5)
	PH	1.76	f: 2.25 s: 2.25*	1.3 1.7*
ACR (808/532)		0.5 (0.3)	0.6 (0.1)	0.3 (0.1)
CR (808/532)		0.4 (0.3)	-	0.2 (0.1)

6.1.3 Conclusions

This section presented ground-based lidar and photometer mobile observations, mapping smoke aerosol properties near the source during the FIREX-AQ campaign in 2019. The smoky background air was identified by the photometer measurements, with EAE values always higher than 1.3. The study focuses on the William Flats Fire (WFF) in Washington state, which presented unique and challenging environmental conditions for the exploratory platforms.

The 3D mapping of lidar and photometer observations enabled the identification of aerosol properties in diffuse, convective, and residual smoke layers near the WFF. The fire's evolution passing from flaming phase to the smoldering phase was evidenced by the aerosol properties. Moreover, detailed spatio-temporal analyses of aerosol distribution during August 6 and 7, 2019, were provided, showing the impact of terrain on smoke plume diffusion. The results showed that complex topography and synoptic conditions played crucial roles in the WFF development and smoke transport to regions beyond the fire site (e.g., Missoula 370 km away from the fire).

The study presented in this work provides insights into the complex dynamic involved in fire evolution, showcasing the necessity of mobile platforms to access valuable information near aerosol sources. *The study revealed the capabilities of CE376 aboard mobile platforms to characterize smoke aerosols' optical properties. At the same time, the limitations of the CE376 lidar (early version used in 2019) and the photometer in harsh environmental conditions (complex topography, high temperatures, thick smoke plumes) were acknowledged.*

The main operational challenge to overcome for enhanced mobile observations with the early CE376 lidar is related to the opto-mechanical stability, particularly for the 532 nm detection channels. The extreme temperatures (up to 40° C) during the campaign influenced the incomplete overlap of the 532 nm channels and, therefore, added uncertainty to the lower region of the profiles. This specific challenge is being addressed by the CIMEL company. Thus, in 2024, upgraded versions of the CE376 lidar are intend to overcome this operational constraint and provide more robust instrument. Moreover, improvements in the aerosol properties derived from CE376 lidar measurements can be achieved by averaging properties within aerosol layers, thereby reducing noise impacts. Looking ahead, both algorithmic and operational assessments have the potential to advance, enhancing the lidar system's capabilities for mobile observations and bridging observational gaps within ground-based networks.

6.2 TRANSAMA Campaign 2023

It is well known that forests act as sinks of atmospheric CO_2 by transforming the carbon compounds into biomass. Thus, the Amazon Forest, one of the largest ecosystems on Earth, plays an important role in the global climate system. However, the Amazon's role as a carbon sink depends on various processes, such as the intensity and distribution of continental precipitation and soil fertilization by Saharan dust, among others. In particular, the Amazon Cone, a geological feature along the South American continental shelf, is characterized by the accumulation of sediments carried by the Amazon River to the ocean. This deposit of sediments is of great interest for studying past climate variations, including changes on the seasonal transatlantic transport of mineral dust. Concerns have aroused in the last decades regarding the effects of climate change on the transport of Saharan dust to the Amazon basin, which can influence the global carbon cycle (Prospero et al., 2020). Thus, both paleoclimatic reconstruction and the study of the current climate are important to improve our understanding of the Earth's system.

Remote sensing and in-situ observations are therefore needed to address the current atmospheric composition over oceans. Studying aerosols in the North Atlantic helps understand mineral dust transport from Africa to the Amazon, while investigating marine aerosols in pristine environments (i.e., no anthropogenic influence) provides insights into pre-industrial meteorological conditions (Mascaut, 2023). Hence, pristine oceanic regions, identified in the South Atlantic, South Indian, and Pacific oceans, are characterized by AOD lower than 0.1 (Koren et al., 2014). Small changes in aerosol loading can significantly impact clouds in such low-concentration regions, as suggested by Koren et al. (2014). Moreover, Mallet et al. (2018) identified a bias between satellite-derived AOD and ground-based photometer measurements in the pristine region of South Indian Ocean, linked to errors in quantifying marine aerosols from satellite. Thus, ground-based aerosol observations in both scenarios, pure and "polluted" marine conditions remain crucial.

The oceanographic mission AMARYLLIS-AMAGAS, titled "From Amazon sediments to natural climate variability and slope instability processes", was conducted from May 16 to July 3, 2023 (https://www.insu.cnrs.fr/). The campaign took place aboard the Marion Dufresne research vessel, the largest oceanographic ship of the French fleet operated by Ifremer (Institut Français de Recherche pour l'Exploitation de la Mer, https://www.ifremer.fr/). The Franco-

Brazilian campaign aimed to collect sediment cores from and near the Amazon cone to study the role of the Amazon Forest in past climates. Specifically, the collected sediment can provide insights into past atmospheric composition, offering the opportunity to study environmental responses to extreme and/or rapid climate changes.

As part of the oceanographic mission AMARYLLIS-AMAGAS, the Marion Dufresne vessel departed from La Réunion Island in mid-April 2023, navigated around the South African continent, crossed the Atlantic Ocean, and reached Barbados by mid-May 2023. Thus, the TRANSAMA valorization project was deployed to study aerosols along the route covered by the Marion Dufresne. The project aimed to (i) employ remote sensing instruments for aerosol observations in pristine and dusty marine conditions, (ii) collect mineral dust using filter-based techniques, and (iii) perform operational assessments on the instrumentation embarked on the ship.

TRANSAMA remote sensing instrumentation

MAP-IO (Marion Dufresne Atmospheric Program – Indian Ocean, http://www.mapio.re/) is an observatory aboard the Marion Dufresne, that aims to study ocean-atmosphere processes in a long-term basis to assess climate studies. The observatory accounts with a radiometer (measuring solar flux), in-situ instruments for gas and aerosol monitoring and a CE318-T photometer, all of them measuring since 2021. It is worth mentioning that the Marion Dufresne covers mostly the South Indian Ocean (pristine environment) during two annual missions in the Austral French territory (TAAF, Terres Australes et Antarctiques Françaises).

The observations of the photometer, functional since 2021, revealed operational challenges, such as wrong sun/moon tracking due to strong waves hitting the ship or given by slow communication between the control/acquisition software and GPS modules. To address these challenges, during TRANSAMA, a second CE318-T photometer was installed aboard the Marion Dufresne and was monitored continuously. The first photometer, hereafter called photometer A, was installed, from the beginning, on the ship's main mast (Fig. 6.17) to minimize potential obstacles for tracking sun/moon. Nevertheless, photometer A can be impacted by strong winds and abrupt movements of the boat. The second photometer, photometer B, was installed on deck I (Fig. 6.17), so it was accessible for the continuous assessments during the campaign. Moreover, photometer B accounted an updated software for improving the communication between the control and GPS modules. Both photometers were adapted for the marine conditions, using a pump to inject air on the collimators, so the deposition of sea salt can be avoided. The data acquired by the photometers was directly transmitted to the data centers at LOA and AERONET, and was analyzed in NRT.

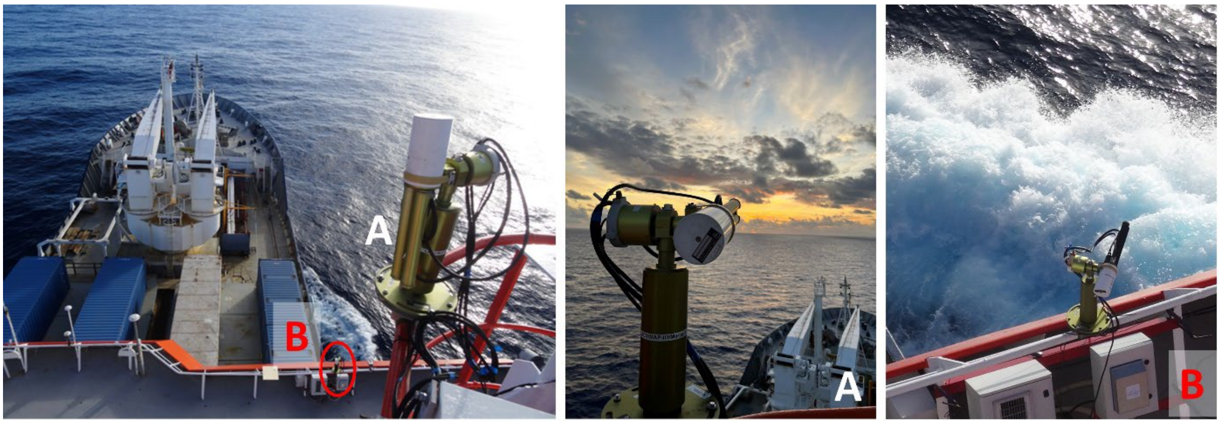

Figure 6.17: CE318-T photometers (A and B) installed aboard Marion Dufresne research vessel. Photographs taken during the TRANSAMA campaign. Credits: TRANSAMA team (Luc Blarel, Philippe Goloub and me).

Likewise, during the campaign, we installed the CE370 single-wavelength lidar. The laser source of this lidar is connected to the emission/reception telescope by a 10 m optical fiber, which provided the possibility to install the laser source inside the ship and the telescope on deck. The laser source was arranged in MAP-IO laboratory which is temperature-controlled. Moreover, the system was placed on the adapted structure designed for the MAP-IO instruments, which isolates the vibrations of the ship motor and dissipate movement (Fig. 6.18a). After realignment of the laser injection into the optical fiber, the fiber passed through the adapted holes for the air inlets (of in-situ MAP-IO instruments) and got connected to the telescope installed on deck I.

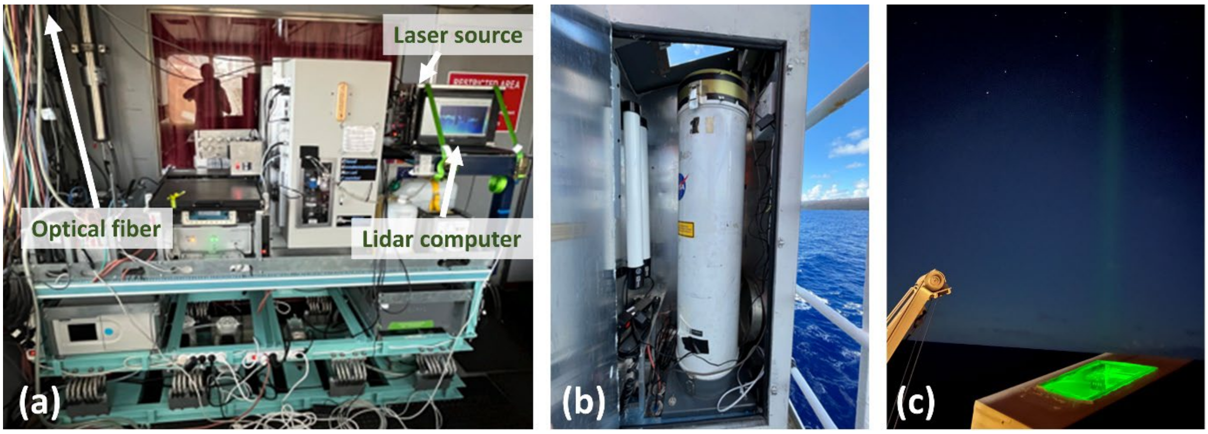

Figure 6.18: CE370 single-wavelength lidar installation aboard the Marion Dufresne research vessel during TRANSAMA campaign. Credits: TRANSAMA team (Luc Blarel, Philippe Goloub and me).

The lidar emission/reception telescope was placed inside an enclosure adapted for the instrument at LOA (Fig. 6.18b). To avoid the direct sunlight on the lidar system, an automatic blind system was added on the enclosure. The control for closing or opening the blind system was connected to a GPS. Thus, the solar zenithal angle was continuously re-calculated and when the sun approached too close to the zenith, the closing system was activated, protecting in this way the optics of the lidar.

In the same way as the photometers, the lidar data was intended to be transmitted continuously to LOA data center. Nevertheless, due to the volume of the data (300 kB every 10 minutes) and the poor internet connection in the middle of the ocean, the data transmission was not always possible. However, with the tools developed in this work, we were able to analyze the data aboard the ship. Moreover, the operational challenges that need to be addressed for future installations of ship-borne lidars is related to the deposition of sea spray on the enclosure window. During the campaign, we had to clean this window with fresh water 1 to 2 times a day. Thus, several strategies to face this challenge are possible and need to be evaluated. In the context of this thesis, the deployment of ship-borne remote sensing instruments during TRANSAMA provided an opportunity to evaluate a future installation of the CE376 lidar aboard the Marion Dufresne. The operational challenges described here are therefore considered for further developments.

In the following subsections, the aerosol properties derived from both lidar and photometer during the campaign are presented.

6.2.1 Aerosol properties: general overview

Before presenting the general overview of the campaign observations, it is worth mentioning how the sea spray deposition on the lidar enclosure window affected the signal. A change in light transmission was evidenced, resulting in a reduced lidar signal (Fig. 6.19a), and sometimes, when the salt accumulated enough, no measurements were possible. For this lidar, measuring total backscattered light (i.e., no polarization components), the change on the lidar signals can be corrected by normalization (Fig. 6.19b). Normalizing the profiles, one can notice the structure that was hidden before. Nevertheless, looking ahead for a ship-borne CE376 lidar, which accounts for depolarization measurements, this operational challenge needs to be carefully addressed. The sea spray deposition on a window, will not only change the transmission of light but also might induce changes on light polarization state, and therefore induce biases on signal which are difficult to quantify.

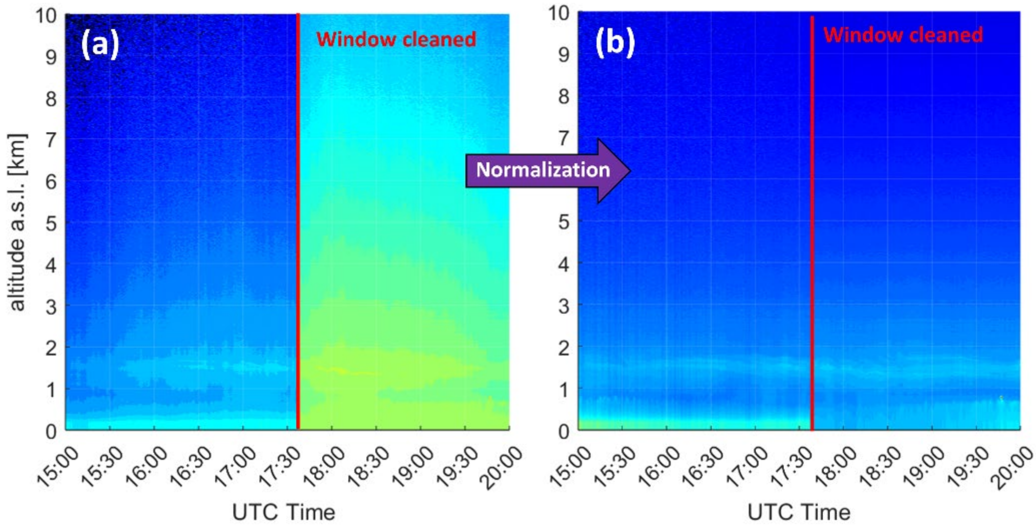

Figure 6.19: (a) Lidar signal affected by Sea spray deposition on the enclosure window, red line marks when the window got cleaned. (b) Normalization applied to all profiles in (a), showing atmospheric structure that was hidden due to the differences in signal amplitude.

During TRANSAMA, the instruments started to perform measurements the 20 April 2023, while the ship was at the port at La Reunion Island (20.93° S, 55.29° E). On 21 April 2023 an alert of volcanic activity was activated on the Island, hence a signature of volcanic aerosols was likely detected (in between clouds) just before the departure later that day. Figure 6.20 presents an overview of spatio-temporal variabilities of measurements collected, using lidar and photometer B, since 21 April 2023 to 15 May 2023. The 3D spatial variation (height, latitude and longitude) of normalized RCS (Fig. 6.20a) shows aerosols confined to the lower marine boundary layer (MBL) for almost all the transect, below 700 m. Sporadic clouds formed at the top of the MBL were detected all the way and on some occasions at ~2 km where the limit of a residual layer was observed. During the campaign, we detected pristine conditions with rather low AOD values at 440 nm, below 0.05, (Fig. 6.20b) and EAE values at 440/870 nm below 0.4 (Fig. 6.20c). The photometer observations correspond to direct sun/moon measurements, averaged to 3 hours.

Along the transect, lidar measurements were stopped due to absence of permission for active sensing measurements in territories of Madagascar, South Africa and Brazil. Nevertheless, photometer measurements (passive) were allowed (except on Brazilian territory). Hence, in vicinity to coastal cities, the AOD at 440 nm showed to increase above 0.1. The EAE at 440/870 nm showed to increase above 0.8 in vicinity of La Reunion Island and Madagascar, indicating a major presence of fine aerosols, either related to anthropogenic influence or volcanic degassing, i.e., formation of secondary aerosols such as sulfates.

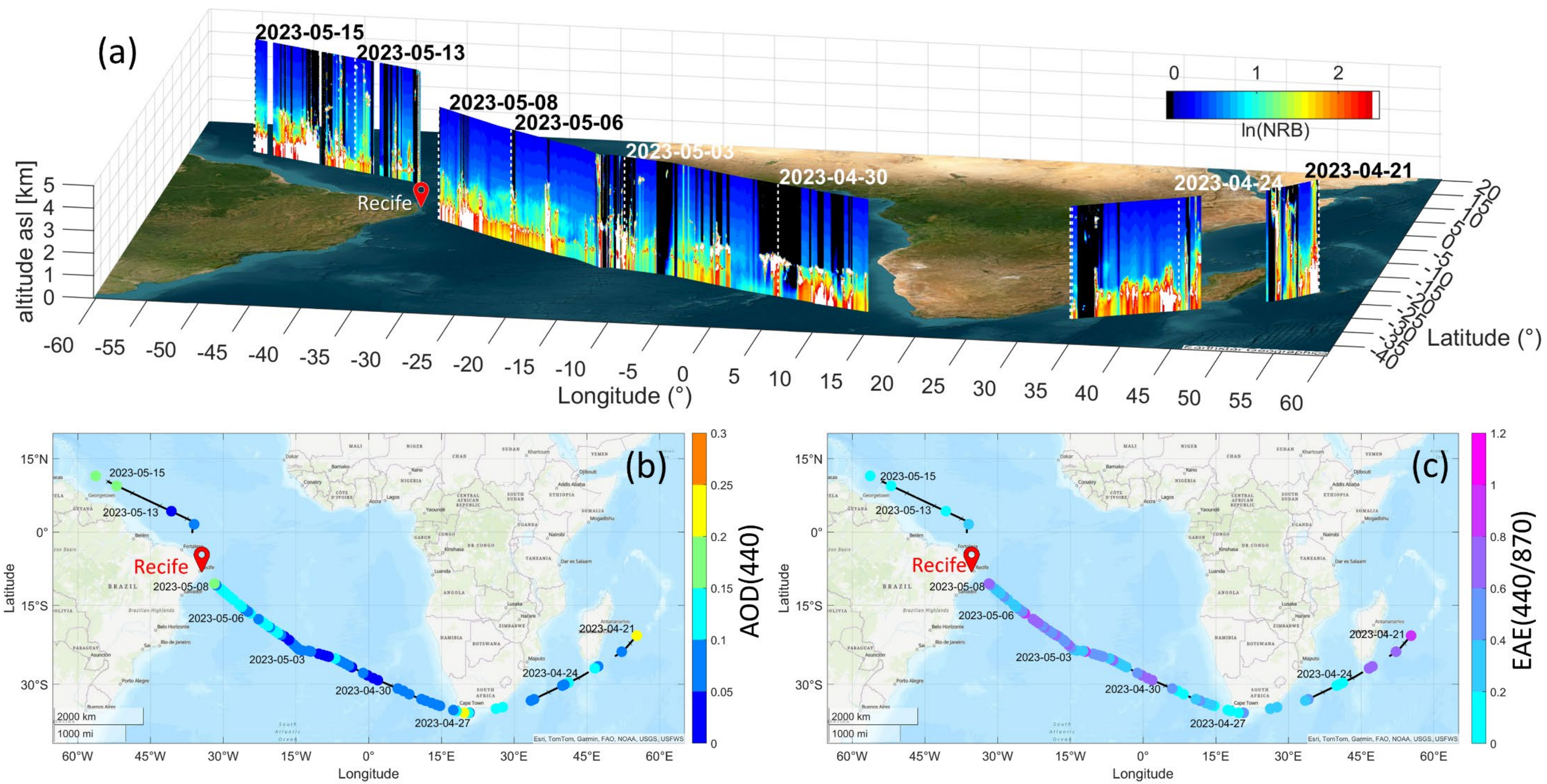

Figure 6.20: Spatio-temporal variabilities of lidar and photometer aerosol measured properties aboard the Marion Dufresne research vessel, during the TRANSAMA campaign (20 April to 15 May 2023), from La Reunion Island to Barbados. (a) 3D variation of Normalized RCS at 532 nm from lidar on top true color image of the regions covered, (b) AOD at 440 nm and (c) EAE at 440/870 nm from sun/moon photometer (B) observations on top of topographic maps. The photometer observations correspond to averages of 3 hours. The port in Recife, Brazil is indicated by a red pin.

Unexpectedly, while crossing the pristine region on the South Atlantic Ocean, an event of transported aerosols at 2 km, was detected with the lidar. Values of AOD slightly increased but maintained below 0.1, and EAE increased up to 0.8, indicating a presence of fine aerosols. In particular, this event will be further studied in Section 6.2.2.

On 9 May 2023, the ship stopped at port Recife, Brazil (8.05° S, 34.87° W) to embark the Brazilian scientific team for AMARYLLIS-AMAGAS campaign. From Recife to Barbados, towards the end of TRANSAMA campaign, observations of aerosol layers in between clouds (seen by lidar) suggested presence of mineral dust transported from the Sahara (dust outbreak observed in previous days).

Photometer comparisons

During the campaign, both photometers performed measurements continuously. Thus, Figure 6.21 presents linear regressions of the observations acquired from photometers A and B, considering photometer B (installed during the campaign and closely monitored) as reference. Average values of 1 hour were considered for coincident observations (109 hours in total), and there is no distinction between night or day measurements. In general the slopes on the 3 linear regressions, for AOD(440) (Fig. 6.21a), AOD(870) (Fig. 6.21b) and EAE(440/870) (Fig. 6.21c), are close to 1 with R-squared higher than 0.7. These regressions show good correlation between both photometer observations, nevertheless we can expect a better agreement.

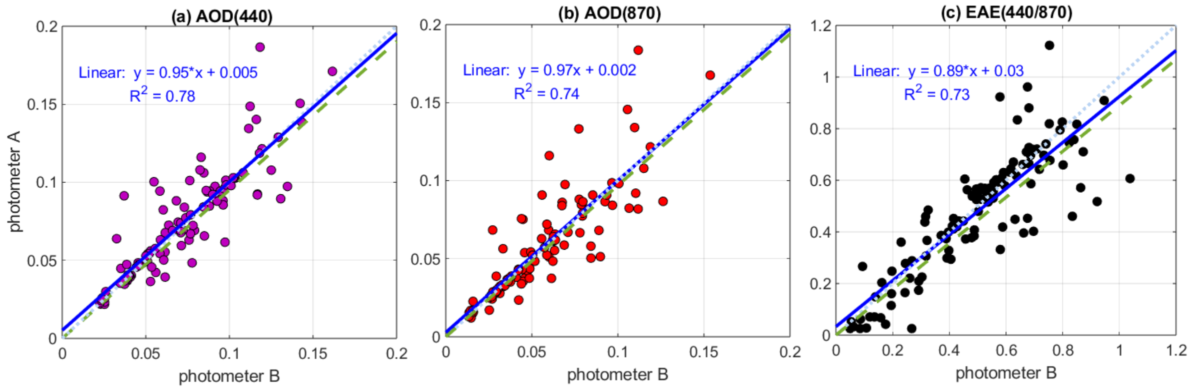

Figure 6.21: Linear regressions of (a) AOD(440), (b)AOD(870) and (c)EAE(440/870) observations obtained with photometers A and B during the TRANSAMA campaign. In blue line is the linear regression, in dashed light blue line is considering a slope of 1, and in dashed green line is considering the intercept at 0.

This analysis is performed using level 1.5 data with no filtering of outlier points. The R-squared obtained can be explained by several factors, such as the impact of the photometer uncertainty at low aerosol loading, the appearance of sporadic low clouds (less than 15 min presence, seen by lidar) not filtered and not detected at the same time with the instruments. Moreover, the photometer B, installed during the campaign, accounted with an updated and faster acquisition software and therefore more data points, at least until the update of photometer A (updated during the campaign). However, from this first assessment, it is not observed any bias between instrument observations nor any influence of the installation spot aboard the ship. A further study to corroborate these outcomes, can include filtering of data in presence of clouds, the differentiation between day and nighttime measurements, differentiation of before and after the photometer A software is updated.

6.2.2 Aerosols in maritime environment

As mentioned in the prior subsection, pristine conditions were identified with AOD values below 0.05 and EAE below 0.4, related to coarse aerosols. Contrary to what it was expected in the South Atlantic Ocean, aerosols were detected above the MBL (at ~2 km) with a not evident increase on aerosol loading (AOD still below 0.1), that could pass like pristine conditions if lidar measurements were not available. From 30 April to 07 May 2023, a persistent thin aerosol layer is detected across the ocean. The influence of the aerosol layer is better observed during 4 to 6 May 2023, where minor incidence of low clouds is detected. Thus, we focus the attention on these peculiar days. Figure 6.22 presents the height-temporal variations of normalized RCS at 532 nm, from the CE370 single-wavelength lidar, and temporal variations of the sun/moon photometer observations during the 5 to 7 may 2023. During these days, sunrise is expected at 07:00 UT and sunrise at 20:00 UT.

Clouds are formed at the top of the MBL all day and they are sporadically observed on the lidar signal, so short thresholds of time are identified without cloud influence. Thus, it was possible to acquire sun/moon direct measurements with photometer within clouds. However, sometimes the included filtering in level 1.5 was not enough to eliminate the data contaminated by clouds. Regardless the intermittent saturation of lidar signal (due to clouds), persistent thin aerosol layers above the marked MBL are observed. These layers are hardly product of the sea, because both sea spray primary (sea salt) and secondary (sulfate, ammonium, and organic species) products are contained within the MBL (Rinaldi et al., 2010; Mayer et al., 2020). Thus, the aerosols detected above the MBL are likely transported.

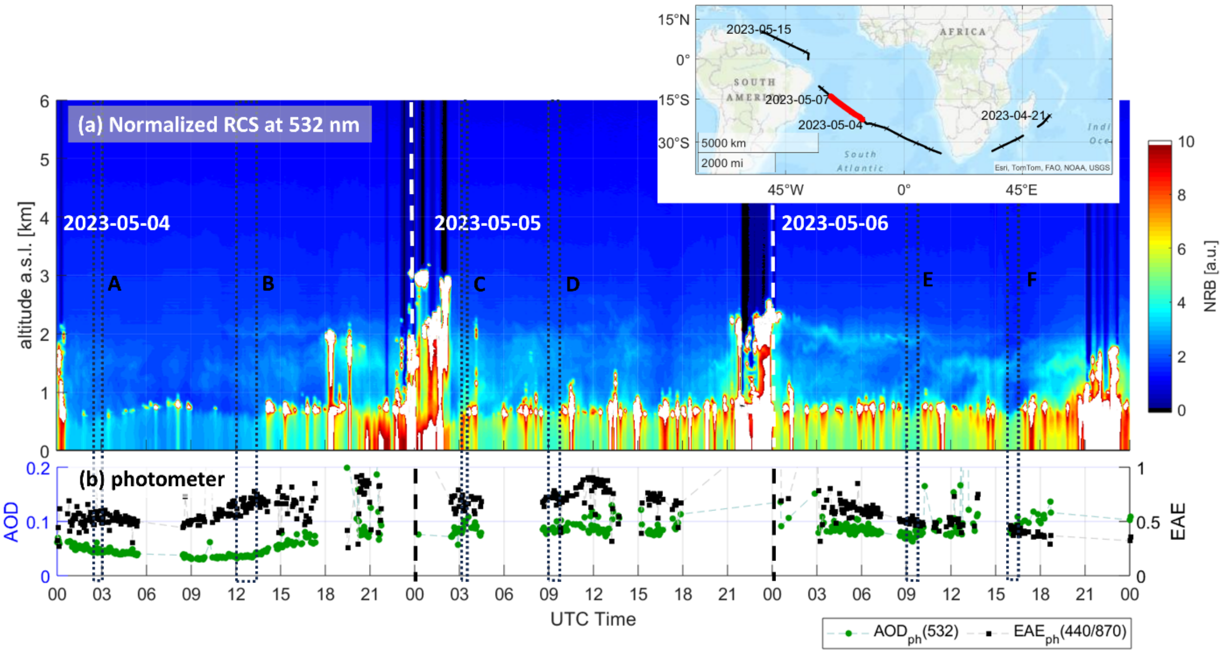

Figure 6.22: Height-temporal variation of (a) normalized RCS (NRB) at 532 nm, and (b) photometer temporal series, AOD at 532 nm and EAE at 440/870 nm during 04 May to 06 May 2023. The transect of the route covered is indicated in red line on the map (top right). Selected datasets for further studies are highlighted by pointed black line boxes (A to F).

Figure 6.23 shows aerosol properties of averaged profiles during selected time-threshold (A to F in Fig. 6.22). In this case, the molecular contributions are estimated with the tropical standard atmosphere. The aerosol layers above the MBL are highlighted by dotted black line boxes. Moreover, each dataset is distinguished by a color and its corresponding back-trajectory (ending at 2 km) is presented in Fig. 6.24.

In general, all profiles presented in Fig. 6.23 show a marked difference between the MBL and the aerosol layers above. The MBL is characterized by higher extinction coefficients than the layers above, indicating a stronger contribution to the measured AOD. For the cases where the extinction within the aerosol layers is less than 0.5 times the extinction in the MBL (dataset C and E), the LR is lower (23 sr and 30 sr), which is related to the major contribution of marine aerosols in the MBL with respect to the layers above. On the other hand, following the back-trajectories of the aerosols detected above the MBL (ending at 2 km asl), the origin of the transported aerosols seems to be the active fires in forests located on SE Angola, SW Zambia and N Botswana. The wildfire source is clear for the datasets C, D and E (purple, black and light blue respectively), with back-trajectories passing (1 to 2 km) above the fires and transported across Angola, Namibia and over the South Atlantic Ocean for ~10 days (~4 500 km). The back-trajectories for datasets A, B and F do not relate to the fires directly, though they show that air masses circulated over a small region of the ocean for more than 4 days, suggesting a possible influence of the aerosols from wildfires.

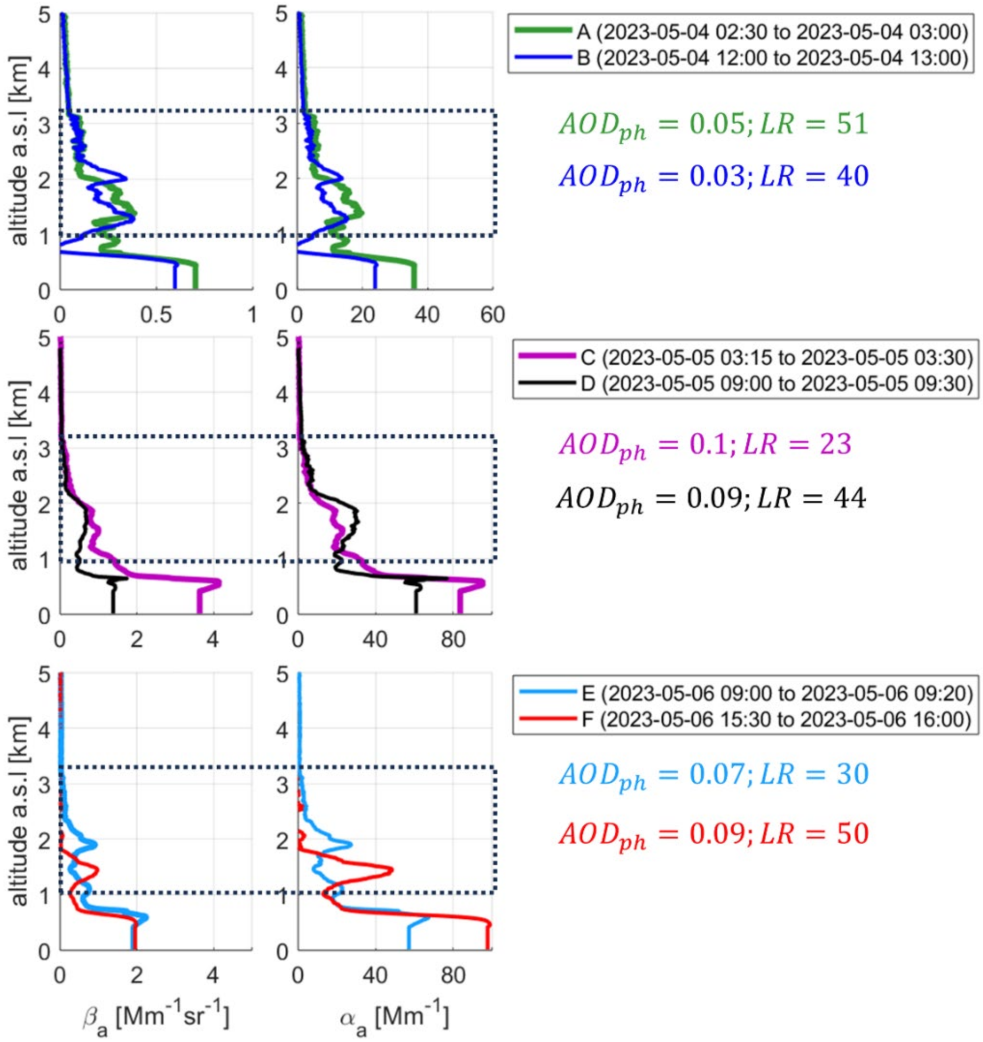

Figure 6.23: Profiles of aerosol optical properties from averaged selected datasets of mobile observations during 4 May to 6 May 2023. Each dataset is differentiated by color. From left to right: Profiles of backscatter and extinction at 532 nm. Likewise, a pointed black line box highlights the aerosol layers detected above the MBL for each dataset.

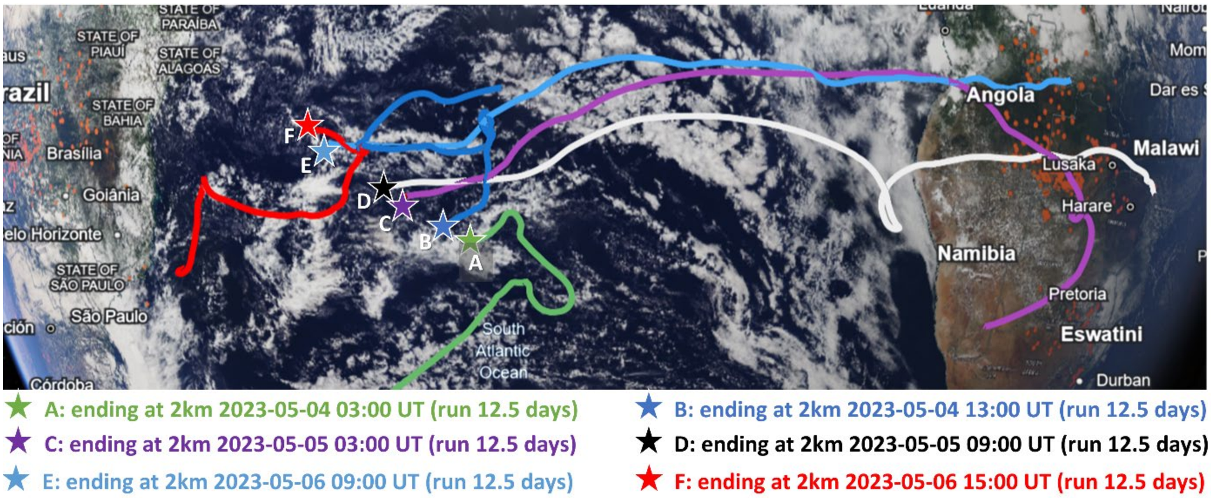

Figure 6.24: NOAA HYSPLIT back-trajectories ending at 2 km above Marion Dufresne (marked by stars) for the times selected in Figure 6.23 (each dataset differentiated by color) on top of the true color MODIS image for the 2023-04-26 (including thermal anomalies). The back-trajectories use GDAS meteorological data (1 degree) and run-time of 12.5 days (300 hours). Source MODIS image: NASA Worldview Snapshots (https://wvs.earthdata.nasa.gov). Image composed (back-trajectories and MODIS) on Google Earth.

Though the influence of the smoke, probably mixed with urban aerosols, is low (extinction less than 30 Mm^{-1} averaged by layer), the presence of the thin layers was consistently observed across the entire route over South Atlantic Ocean. Thus, the pristine conditions expected in the middle of the ocean were in reality influenced by continental emissions, regardless the distance from the continent. Moreover, the presence of these aerosols might have also an important role in the cloud formation over the ocean, as suggested by previous studies (Koren et al., 2014; Mascaut, 2023) and observed with lidar measurements showing formation of clouds at 2 km (above the MBL top).

6.2.3 Conclusions

The oceanographic mission AMARYLLIS-AMAGAS was introduced within a general context and its objectives. It was emphasized that the Amazon Forest plays a crucial role in the global climate system by acting as a carbon sink, and can, at the same time, be influenced by Saharan dust. Moreover, the mission highlights the importance of both paleoclimatic and current atmospheric composition for a better understanding of the Earth's climate.

The TRANSAMA campaign, a valorization project part of AMARYLLIS-AMAGAS, aimed to study aerosols along the route covered by the Marion Dufresne research vessel before the oceanographic mission. Instruments installed included photometers and CE370 single-wavelength lidar, which faced operational challenges such as sea spray deposition affecting measurements. Comparisons between CE318-T photometers A and B showed good correlation, though improvements in data acquisition software were noted for photometer B and possible improvements on the comparisons with further cloud filtering.

During the campaign, observations revealed aerosol properties along the route from La Réunion Island to Barbados. Pristine conditions were identified in the South Atlantic Ocean, with low AOD values. Although the initial interest was in dust aerosols, the study case presented in this work corresponds to unexpected aerosol layers detected above the MBL, likely transported from sources such as wildfires in SE Angola, SW Zambia, and N Botswana.

Overall, the campaign provided valuable insights into aerosol dynamics in maritime environments, demonstrating the influence of continental emissions even in remote oceanic regions. These findings can contribute to our understanding of climate processes and the role of aerosols in cloud formation.

6.3 Chapter summary

This chapter provided an overview of two significant mobile observations campaigns using lidar and photometer: one focusing on observations during the FIREX-AQ campaign in 2019, and the other focusing on the TRANSAMA campaign as part of the oceanographic mission AMARYLLIS-AMAGAS in 2023.

In the FIREX-AQ campaign, the study concentrated on mapping smoke aerosol properties near major fire sources in NW US. The photometer measurements allowed the identification of smoky background air, with EAE values consistently higher than 1.3. Moreover, through 3D mapping of lidar and photometer observations, different smoke layers near the William Flats fire were characterized, including diffuse, convective, and residual smoke layers. Detailed spatio-temporal analyses revealed the impact of terrain and synoptic conditions on smoke plume diffusion, emphasizing the complexity of fire evolution and smoke transport.

The study emphasizes the importance of mobile platforms for accessing critical information near sources. It showcases the capabilities of the CE376 lidar aboard mobile platforms in characterizing smoke aerosol optical properties, while acknowledging its limitations in harsh environmental conditions (high temperatures, complex terrain). Operational challenges, particularly related to opto-mechanical stability and overlap functions, were discussed.

On the other hand, the TRANSAMA campaign aimed to study aerosols along the route covered by the Marion Dufresne research vessel, focusing on the transport of Saharan dust to the Amazon basin. Despite initial interest in dust aerosols, unexpected aerosol layers above the marine boundary layer were detected, likely transported from wildfires in Southern Africa. These findings highlight the influence of continental emissions even in remote oceanic regions, which can pass unnoticed only with photometer data, emphasizing the importance of lidar measurements over the oceans.

Moreover, TRANSAMA provided valuable opportunities to evaluate the operational conditions for a future CE376 ship-borne lidar. Future developments in algorithmic and operational assessments are expected to improve the lidar system's capabilities for mobile observations (aboard cars, ships) and to bridge observational gaps within ground-based networks.

Chapter 7

Conclusions and perspectives

"El futuro queda hacia adelante"
-Mafalda, Quino-

7.1 Conclusions

This work aims to assess spatio-temporal variabilities of aerosol properties using a compact dual-wavelength depolarization lidar (CE376 lidar), particularly when it is aboard moving vectors and co-located with a photometer. Both algorithmic and instrumental assessments were conducted to investigate the capabilities and limitations of the CE376 lidar. The instruments used for assessments in this work are early versions of the CE376 lidar, making their evaluation important for the instrument's later evolution. The main achievements of my PhD thesis presented through this manuscript are summarized as follows:

- A technical qualification of the CE376 lidar performance was accounted through studies on its detection limits and stability while operating under difficult conditions (high temperatures). Improvements in the operational conditions at ATOLL enhanced the depolarization measurements. Nevertheless, an unexpected large incomplete overlap function on the 532 nm channels for the early version of the CE376 lidar was highlighted, related to the optical and mechanical design, which impacts observations in the first thousand meters. The technical challenges encountered in fixed and mobile laboratories are currently being addressed by CIMEL company, which has improved the performance of later versions of the CE376 lidar.
- Algorithmic assessments were conducted to develop a prototype processing system for aerosol monitoring. The prototype integrates height-resolved two-wavelength observations from lidar and direct sun/moon photometer measurements (column-integrated). Thus, a modified two-wavelength Klett inversion was proposed to estimate aerosol properties by constraining the solutions with photometer observations.

Moreover, the developed tools accounted for observations in mobile and fixed laboratories, considering developments towards near real-time aerosol monitoring.

- Case studies were selected from continuous observations of CE376 lidars at two sites, ATOLL (Lille, France) and IZO (Izaña, Tenerife Island, Spain). Events involving mineral dust, dust-smoke, and volcanic aerosols were presented, showing the instrument's capabilities to identify different aerosol types. Moreover, comparisons of aerosol properties obtained from METIS (CE376 lidar) and LILAS (Raman lidar) validated the instrumental assessments and methods. Likewise, the limitations in deriving aerosol properties were also evaluated and linked mainly to the assumption of a vertically constant LR, opening the discussion on possible solutions to improve the results. Nevertheless, the reliability of the CE376 lidar to retrieve information even in complex scenarios was demonstrated with the depolarization measurements. Thus, the results pave the way for further developments towards aerosol typing and air quality monitoring.
- Results from the first mobile campaign (FIREX-AQ) using CE376 lidar and CE318-T photometer aboard a car were presented. The study enabled the characterization of smoke aerosols close to active fires, highlighting the feasibility of operating the lidar system aboard mobile vectors even in challenging operational conditions (high temperatures, difficult roads and thick aerosol plumes). Moreover, both capabilities and limitations of the remote sensing instruments to characterize aerosols while in movement were presented, opening the discussion for further developments. Thus, the operational challenges to be faced in future mobile laboratories, accounting for two moving vectors, cars (temperature control, opto-mechanical stability) and ships (sea spray deposition on lidar window), are under evaluation. These results emphasized the possibility of employing mobile platforms for accessing valuable information near aerosol sources.

The advancements presented in this work mark significant steps in enhancing our understanding of aerosol dynamics and environmental monitoring. The demonstrated versatility of the compact CE376 lidar for monitoring aerosol properties offers a solution to fill the observational gaps within ground-based networks. Therefore, upcoming mobile campaigns (aboard ships, trains, and cars) and permanent sites in the southern hemisphere are planned to include the upgraded, more robust version of the CE376 lidar.

7.2 Perspectives

From the studies presented in this work, several perspectives emerge for further developments and applications, and are presented as follows:

Perspectives on technical developments involve the evolution of the CE376 lidar. There is a need for ongoing improvements to enhance data quality, in particular to reduce the incomplete overlap region and provide a more robust stable instrument. The new version of the CE376 lidar addressed these issues, and ongoing tests evaluate its performances. The new version features a modified optical design that facilitates calibrations and re-alignment of the optics. Moreover, an important reduction on the incomplete overlap has been evidenced (< 1 km compared to 3 km), and its stability over time is under evaluation. Additionally, the new versions of the CE376 lidar include a motorized HWP to improve the precision of depolarization calibration.

The upgraded CE376 lidar provides promising capabilities for aerosol monitoring aboard mobile vectors and at fixed sites. The Polar POD (https://www.polarpod.fr/), a floating scientific platform that will circle the Earth around Antarctica, will include a CE376 automatic lidar, along with several other instruments. In the frame of OBS4CLIM (système d'observation intégré de l'atmosphère, https://www.obs4clim.fr/), four CE376 lidars will be installed between 2024-2025, one of them will be placed aboard a moving vector, car or ship. Thus, a possible installation of the CE376 lidar aboard Marion Dufresne research vessel is under evaluation. The other three lidars will be installed at fixed laboratories in La Paz-Bolivia, Amsterdam Island and Ivory Coast (Africa). These three locations will cover different environments and will be influenced by different aerosols sources, enhancing our observation; capability requested for better understanding the climate system.

- The lidar at La Paz, Bolivia will be located above 3 km asl along with other in-situ instruments. The region is surrounded by the Altiplano plateau, a dry and arid territory, and separated from the Amazon by the Andes, though it is impacted by Amazon wildfires during the dry season. Moreover, dust from the Altiplano can be studied, which has not been measured before by a two-wavelength depolarization lidar system.
- The lidar on Amsterdam Island will be located in the pristine environment on the Austral French territory. The effects of a changing climate have been evidenced in this region regardless of its isolation from continental anthropogenic influence. Studies with the

lidar system will enable the detection of aerosols transported and possibly deposited over the Austral Islands.

- Likewise, the lidar on Ivory Coast will be located in proximity to the Sahel African region, characterized as a transition between the Savanna Forest and the Sahara Desert. This location will provide unique opportunities to study continuously mineral dust and smoke transported from the region.

Perspectives on algorithmic developments involve improvements in the tools developed in this work. On one hand, the adaptation of parts of the code developed and its further extension into a robust NRT software will be evaluated in the frame of AGORA-Lab. The future versions of iAAMS and BASIC will host the tools developed in this work. On the other hand, further developments imply exploring new methods for aerosol retrievals. Hence, two approaches can be followed; integrating observations by aerosol layer to derive differentiated LR and the use of advanced retrieval methods like GRASP (Generalized Retrieval of Aerosol and Surface Properties). In the case of the integrated layer approach, we can explore the forward iterative method presented in chapter 4. On the other hand, with GRASP algorithms the spectral AOD and downward sky radiance from CE318-T photometers can be combined with the RCS at two wavelengths from CE376, providing aerosol properties with estimated contributions of fine and coarse aerosols. Nevertheless, GRASP algorithms only use daytime measurements, which complicates the selection of case studies from CE376 lidar (low detection limit by day). But now that the detection limits and performance of the CE376 were defined, we can explore the GRASP products knowing the limits of the instrument. Moreover, microphysical aerosol properties retrieved from sky measurements, particularly those performed by mobile photometers, can also be addressed through GRASP. Likewise, GRASP-AOD, which enables the estimation of VSD distributions from spectral AOD measurements, can be further explored for the mobile CE318-T photometer.

The versatility of the CE376 lidar can also be used for air quality monitoring. In this context, the need is to estimate mass concentration profiles, particularly within the ABL. Thus, the identification of the aerosol type is important to better assess the estimations on particulate matter. Two possible strategies are known; imposing one aerosol type for the entire column of air or identification by aerosol layer contributions. However, as we saw through case studies from ATOLL, assuming one aerosol type in the entire column is far from reality. This work presented different aerosol properties widely used for aerosol typing, such as EAE, BAE and CR, which indicate aerosol size, and PLDR related to aerosol shape. Nevertheless, the reliability of EAE, BAE and CR is low in complex scenarios due to the instrument's limits. Thus, the ACR property, which can be related to aerosol size, was introduced and explored through the case studies. Even though the property is affected by aerosol attenuation, it demonstrated to be capable to assess the aerosol stratification. Moreover, ACR showed the ability to identify aerosol size in presence of a homogeneous aerosol background, like at IZO (molecular background) and during FIREX-AQ (residual smoke background). By estimating the aerosol attenuation at each layer, we will be able to correct the ACR property. Having both ACR and PLDR, aerosol size and shape, we can explore a strategy for aerosol typing and therefore better estimate the mass concentration for air quality assessments.

The demonstrated capacities of the CE376 lidar for aerosol monitoring expands the horizon for further developments not only for mobile laboratories, but also in other fields. We are confident that the improved version of the lidar can be a versatile tool for aerosol research and air quality assessments, and therefore to assess public health concerns.

I would like to express my deepest gratitude for reading this document, which represents the hard work of three years during my PhD program. I hope that the content you found here is useful and generates curiosity about the next steps of the CE376 lidar.

I emphasize that this work wouldn't have been possible without the collaborations of all my colleagues at LOA and CIMEL. The fruitful discussions and conferences were essential to generate new ideas. I am convinced that networking and multi-disciplinary efforts are key to fight against climate inequalities.

As a scientist, my promise is to keep learning and working so we can overcome the challenges that we face as a society.

References

Ackermann, J. (1997). Two-wavelength lidar inversion algorithm for a two-component atmosphere. *Applied Optics*, *36*(21), 5134. https://doi.org/10.1364/AO.36.005134

Ackermann, J. (1998). Two-wavelength lidar inversion algorithm for a two-component atmosphere with variable extinction-to-backscatter ratios. *Applied Optics*, *37*(15), 3164. https://doi.org/10.1364/AO.37.003164

Ackermann, J. (1999). Analytical solution of the two-frequency lidar inversion technique. *Applied Optics*, *38*(36), 7414. https://doi.org/10.1364/AO.38.007414

Adachi, K., Dibb, J. E., Scheuer, E., Katich, J. M., Schwarz, J. P., Perring, A. E., Mediavilla, B., Guo, H., Campuzano-Jost, P., Jimenez, J. L., Crawford, J., Soja, A. J., Oshima, N., Kajino, M., Kinase, T., Kleinman, L., Sedlacek, A. J., Yokelson, R. J., & Buseck, P. R. (2022). Fine Ash-Bearing Particles as a Major Aerosol Component in Biomass Burning Smoke. *Journal of Geophysical Research: Atmospheres*, *127*(2), e2021JD035657. https://doi.org/10.1029/2021JD035657

Adam, M., Nicolae, D., Stachlewska, I. S., Papayannis, A., & Balis, D. (2020). Biomass burning events measured by lidars in EARLINET – Part 1: Data analysis methodology. *Atmospheric Chemistry and Physics*, *20*(22), 13905–13927. https://doi.org/10.5194/acp-20-13905-2020

Adebiyi, A., Kok, J. F., Murray, B. J., Ryder, C. L., Stuut, J.-B. W., Kahn, R. A., Knippertz, P., Formenti, P., Mahowald, N. M., Pérez García-Pando, C., Klose, M., Ansmann, A., Samset, B. H., Ito, A., Balkanski, Y., Di Biagio, C., Romanias, M. N., Huang, Y., & Meng, J. (2023). A review of coarse mineral dust in the Earth system. *Aeolian Research*, *60*, 100849. https://doi.org/10.1016/j.aeolia.2022.100849

Ahrens, D. (2000). *Essentials of Meteorology-An Invitation to the Atmosphere* (Third edition). Brooks Cole.

Alados-Arboledas, L., Müller, D., Guerrero-Rascado, J. L., Navas-Guzmán, F., Pérez-Ramírez, D., & Olmo, F. J. (2011). Optical and microphysical properties of fresh biomass burning aerosol retrieved by Raman lidar, and star-and sun-photometry: REMOTE SENSING OF FRESH BB AEROSOL. *Geophysical Research Letters*, *38*(1), n/a-n/a. https://doi.org/10.1029/2010GL045999

Almansa Rodríguez, A. F. (2021). *Desarrollo y evaluación de técnicas radiométricas de observación de aerosoles y vapor de agua en la atmósfera desde plataformas terrestres* [Universidad de Valladolid]. https://doi.org/10.35376/10324/48614

Ancellet, G. M., Kavaya, M. J., Menzies, R. T., & Brothers, A. M. (1986). Lidar telescope overlap function and effects of misalignment for unstable resonator transmitter and coherent receiver. *Applied Optics*, *25*(17), 2886. https://doi.org/10.1364/AO.25.002886

Anderson, T. L., Masonis, S. J., Covert, D. S., Ahlquist, N. C., Howell, S. G., Clarke, A. D., & McNaughton, C. S. (2003). Variability of aerosol optical properties derived from in situ aircraft measurements during ACE-Asia. *Journal of Geophysical Research: Atmospheres*, *108*(D23), 2002JD003247. https://doi.org/10.1029/2002JD003247

Ansmann, A., Baars, H., Tesche, M., Müller, D., Althausen, D., Engelmann, R., Pauliquevis, T., & Artaxo, P. (2009). Dust and smoke transport from Africa to South America: Lidar profiling over Cape Verde and the Amazon rainforest. *Geophysical Research Letters*, *36*(11), L11802. https://doi.org/10.1029/2009GL037923

Ansmann, A., Bösenberg, J., Chaikovsky, A., Comerón, A., Eckhardt, S., Eixmann, R., Freudenthaler, V., Ginoux, P., Komguem, L., Linné, H., Márquez, M. Á. L., Matthias, V., Mattis, I., Mitev, V., Müller, D., Music, S., Nickovic, S., Pelon, J., Sauvage, L., … Wiegner, M. (2003). Long-range transport of Saharan dust to northern Europe: The 11-16 October 2001 outbreak observed with EARLINET: SAHARAN DUST TRANSPORT OVER EUROPE. *Journal of Geophysical Research: Atmospheres*, *108*(D24), n/a-n/a. https://doi.org/10.1029/2003JD003757

Ansmann, A., Ohneiser, K., Chudnovsky, A., Baars, H., & Engelmann, R. (2021). CALIPSO Aerosol-Typing Scheme Misclassified Stratospheric Fire Smoke: Case Study From the 2019 Siberian

Wildfire Season. *Frontiers in Environmental Science*, *9*, 769852. https://doi.org/10.3389/fenvs.2021.769852

Ansmann, A., Ohneiser, K., Mamouri, R.-E., Knopf, D. A., Veselovskii, I., Baars, H., Engelmann, R., Foth, A., Jimenez, C., Seifert, P., & Barja, B. (2021). Tropospheric and stratospheric wildfire smoke profiling with lidar: Mass, surface area, CCN, and INP retrieval. *Atmospheric Chemistry and Physics*, *21*(12), 9779–9807. https://doi.org/10.5194/acp-21-9779-2021

Ansmann, A., Tesche, M., Seifert, P., Groß, S., Freudenthaler, V., Apituley, A., Wilson, K. M., Serikov, I., Linné, H., Heinold, B., Hiebsch, A., Schnell, F., Schmidt, J., Mattis, I., Wandinger, U., & Wiegner, M. (2011). Ash and fine-mode particle mass profiles from EARLINET-AERONET observations over central Europe after the eruptions of the Eyjafjallajökull volcano in 2010. *Journal of Geophysical Research*, *116*, D00U02. https://doi.org/10.1029/2010JD015567

Baars, H., Seifert, P., Engelmann, R., & Wandinger, U. (2017). Target categorization of aerosol and clouds by continuous multiwavelength-polarization lidar measurements. *Atmospheric Measurement Techniques*, *10*(9), 3175–3201. https://doi.org/10.5194/amt-10-3175-2017

Balis, D. (2003). Raman lidar and sunphotometric measurements of aerosol optical properties over Thessaloniki, Greece during a biomass burning episode. *Atmospheric Environment*, *37*(32), 4529–4538. https://doi.org/10.1016/S1352-2310(03)00581-8

Barreto, Á., Cuevas, E., García, R. D., Carrillo, J., Prospero, J. M., Ilic, L., Basart, S., Berjón, A. J., Marrero, C. L., Hernández, Y., Bustos, J. J., Nicˇkovic, S., & Yela, M. (2022). Long-term characterisation of the vertical structure of the Saharan Air Layer over the Canary Islands using lidar and radiosonde profiles: Implications for radiative and cloud processes over the subtropical Atlantic Ocean. *Atmos. Chem. Phys.*

Barreto, Á., Cuevas, E., Granados-Muñoz, M.-J., Alados-Arboledas, L., Romero, P. M., Gröbner, J., Kouremeti, N., Almansa, A. F., Stone, T., Toledano, C., Román, R., Sorokin, M., Holben, B., Canini, M., & Yela, M. (2016). The new sun-sky-lunar Cimel CE318-T multiband photometer – a comprehensive performance evaluation. *Atmospheric Measurement Techniques*, *9*(2), 631–654. https://doi.org/10.5194/amt-9-631-2016

Barreto, Á., García, R. D., Guirado-Fuentes, C., Cuevas, E., Almansa, A. F., Milford, C., Toledano, C., Expósito, F. J., Díaz, J. P., & León-Luis, S. F. (2022). Aerosol characterisation in the subtropical eastern North Atlantic region using long-term AERONET measurements. *Atmospheric Chemistry and Physics*, *22*(17), 11105–11124. https://doi.org/10.5194/acp-22-11105-2022

Basart, S., Nickovic, S., Terradellas, E., Cuevas, E., Pérez García-Pando, C., García-Castrillo, G., Werner, E., & Benincasa, F. (2019). The WMO SDS-WAS Regional Center for Northern Africa, Middle East and Europe. *E3S Web of Conferences*, *99*, 04008. https://doi.org/10.1051/e3sconf/20199904008

Bedoya-Velásquez, A. E., Hoyos-Restrepo, M., Barreto, A., García, R. D., Romero-Campos, P. M., García, O., Ramos, R., Roininen, R., Toledano, C., Sicard, M., & Ceolato, R. (2022). Estimation of the Mass Concentration of Volcanic Ash Using Ceilometers: Study of Fresh and Transported Plumes from La Palma Volcano. *Remote Sensing*, *14*(22), 5680. https://doi.org/10.3390/rs14225680

Bergamaschi, P., Bräunlich, M., Marik, T., & Brenninkmeijer, C. A. M. (2000). Measurements of the carbon and hydrogen isotopes of atmospheric methane at Izaña, Tenerife: Seasonal cycles and synoptic-scale variations. *Journal of Geophysical Research: Atmospheres*, *105*(D11), 14531–14546. https://doi.org/10.1029/1999JD901176

Bibi, H., Alam, K., Chishtie, F., Bibi, S., Shahid, I., & Blaschke, T. (2015). Intercomparison of MODIS, MISR, OMI, and CALIPSO aerosol optical depth retrievals for four locations on the Indo-Gangetic plains and validation against AERONET data. *Atmospheric Environment*, *111*, 113–126. https://doi.org/10.1016/j.atmosenv.2015.04.013

Birkmann, J., E. Liwenga, R. Pandey, E. Boyd, R. Djalante, F. Gemenne, W. Leal Filho, P.F. Pinho, L. Stringer, and D. Wrathall. (2022). Poverty, Livelihoods and Sustainable Development. In *Climate Change 2022 – Impacts, Adaptation and Vulnerability: Working Group II Contribution to the Sixth Assessment Report of the Intergovernmental Panel on Climate Change [H.-O. Pörtner, D.C. Roberts, M. Tignor, E.S. Poloczanska, K. Mintenbeck, A. Alegría, M. Craig, S. Langsdorf, S. Löschke, V. Möller, A. Okem, B. Rama (eds.)]* (1st ed., pp. 1171–1274).

Cambridge University Press, Cambridge, UK and New York, NY, USA. https://doi.org/10.1017/9781009325844

Bohlmann, S., Baars, H., Radenz, M., Engelmann, R., & Macke, A. (2018). Ship-borne aerosol profiling with lidar over the Atlantic Ocean: From pure marine conditions to complex dust–smoke mixtures. *Atmospheric Chemistry and Physics*, *18*(13), 9661–9679. https://doi.org/10.5194/acp-18-9661-2018

Boichu, M. & Mathurin, T. (2022). VolcPlume Portal. [InteractiveResource]. *AERIS*. https://doi.org/10.25326/362

Boichu, M., Grandin, R., Blarel, L., Torres, B., Derimian, Y., Goloub, P., Brogniez, C., Chiapello, I., Dubovik, O., Mathurin, T., Pascal, N., Patou, M., & Riedi, J. (2023). Growth and Global Persistence of Stratospheric Sulfate Aerosols From the 2022 Hunga Tonga–Hunga Ha'apai Volcanic Eruption. *Journal of Geophysical Research: Atmospheres*, *128*(23), e2023JD039010. https://doi.org/10.1029/2023JD039010

Bond, T. C., & Bergstrom, R. W. (2006). Light Absorption by Carbonaceous Particles: An Investigative Review. *Aerosol Science and Technology*, *40*(1), 27–67. https://doi.org/10.1080/02786820500421521

Boucher, O., D. Randall, P. Artaxo, C. Bretherton, G. Feingold, P. Forster, V.-M. Kerminen, Y. Kondo, H. Liao, U., & Lohmann, P. Rasch, S.K. Satheesh, S. Sherwood, B. Stevens and X.Y. Zhang. (2013). Clouds and Aerosols. In *Climate Change 2013: The Physical Science Basis. Contribution of Working Group I to the Fifth Assessment Report of the Intergovernmental Panel on Climate Change* (Stocker, T.F., D. Qin, G.-K. Plattner, M. Tignor, S.K. Allen, J. Boschung, A. Nauels, Y. Xia, V. Bex and P.M. Midgley (eds.)). Cambridge University Press, Cambridge, United Kingdom and New York, NY, USA. https://www.ipcc.ch/site/assets/uploads/2018/02/WG1AR5_Chapter07_FINAL-1.pdf

Bovchaliuk, V., Goloub, P., Podvin, T., Veselovskii, I., Tanre, D., Chaikovsky, A., Dubovik, O., Mortier, A., Lopatin, A., Korenskiy, M., & Victori, S. (2016). Comparison of aerosol properties retrieved using GARRLiC, LIRIC, and Raman algorithms applied to multi-wavelength lidar and sun/sky-photometer data. *Atmospheric Measurement Techniques*, *9*(7), 3391–3405. https://doi.org/10.5194/amt-9-3391-2016

Burton, S. P., Ferrare, R. A., Vaughan, M. A., Omar, A. H., Rogers, R. R., Hostetler, C. A., & Hair, J. W. (2013). *Aerosol classification from airborne HSRL and comparisons with the CALIPSO vertical feature mask* [Preprint]. Aerosols/Remote Sensing/Validation and Intercomparisons. https://doi.org/10.5194/amtd-6-1815-2013

Burton, S. P., Hair, J. W., Kahnert, M., Ferrare, R. A., Hostetler, C. A., Cook, A. L., Harper, D. B., Berkoff, T. A., Seaman, S. T., Collins, J. E., Fenn, M. A., & Rogers, R. R. (2015). Observations of the spectral dependence of linear particle depolarization ratio of aerosols using NASA Langley airborne High Spectral Resolution Lidar. *Atmospheric Chemistry and Physics*, *15*(23), 13453–13473. https://doi.org/10.5194/acp-15-13453-2015

Chazette, P., & Totems, J. (2023). Lidar Profiling of Aerosol Vertical Distribution in the Urbanized French Alpine Valley of Annecy and Impact of a Saharan Dust Transport Event. *Remote Sensing*, *15*(4), 1070. https://doi.org/10.3390/rs15041070

Chesnoiu, G. (2023). *Environnement solaire et pollutions atmospheriques particulaires en region Hauts-de-France: evolution recente et scenarios futurs* [Lille University].

China, S., Mazzoleni, C., Gorkowski, K., Aiken, A. C., & Dubey, M. K. (2013). Morphology and mixing state of individual freshly emitted wildfire carbonaceous particles. *Nature Communications*, *4*(1), 2122. https://doi.org/10.1038/ncomms3122

Chu, D. A., Kaufman, Y. J., Ichoku, C., Remer, L. A., Tanré, D., & Holben, B. N. (2002). Validation of MODIS aerosol optical depth retrieval over land. *Geophysical Research Letters*, *29*(12). https://doi.org/10.1029/2001GL013205

Córdoba-Jabonero, C., Sicard, M., Barreto, Á., Toledano, C., López-Cayuela, M. Á., Gil-Díaz, C., García, O., Carvajal-Pérez, C. V., Comerón, A., Ramos, R., Muñoz-Porcar, C., & Rodríguez-Gómez, A. (2023). Fresh volcanic aerosols injected in the atmosphere during the volcano eruptive activity at the Cumbre Vieja area (La Palma, Canary Islands): Temporal evolution and vertical impact. *Atmospheric Environment*, *300*, 119667. https://doi.org/10.1016/j.atmosenv.2023.119667

Crumeyrolle, S., Kontkanen, J. S. S., Rose, C., Velazquez Garcia, A., Bourrianne, E., Catalfamo, M., Riffault, V., Tison, E., Ferreira De Brito, J., Visez, N., Ferlay, N., Auriol, F., & Chiapello, I. (2023). Measurement report: Atmospheric new particle formation at a peri-urban site in Lille, northern France. *Atmospheric Chemistry and Physics*, *23*(1), 183–201. https://doi.org/10.5194/acp-23-183-2023

Daskalopoulou, V., Raptis, P. I., Tsekeri, A., Amiridis, V., Kazadzis, S., Ulanowski, Z., Charmandaris, V., Tassis, K., & Martin, W. (2023). Linear polarization signatures of atmospheric dust with the SolPol direct-sun polarimeter. *Atmospheric Measurement Techniques*, *16*(19), 4529–4550. https://doi.org/10.5194/amt-16-4529-2023

De Leeuw, J., Schmidt, A., Witham, C. S., Theys, N., Taylor, I. A., Grainger, R. G., Pope, R. J., Haywood, J., Osborne, M., & Kristiansen, N. I. (2021). The 2019 Raikoke volcanic eruption – Part 1: Dispersion model simulations and satellite retrievals of volcanic sulfur dioxide. *Atmospheric Chemistry and Physics*, *21*(14), 10851–10879. https://doi.org/10.5194/acp-21-10851-2021

De Wekker, S. F. J., & Kossmann, M. (2015). Convective Boundary Layer Heights Over Mountainous Terrain—A Review of Concepts. *Frontiers in Earth Science*, *3*. https://doi.org/10.3389/feart.2015.00077

Dho, S. W., Park, Y. J., & Kong, H. J. (1997a). Application of Geometrical Form Factor in Differential Absorption Lidar Measurement. *Optical Review*, *4*(4), 521–526. https://doi.org/10.1007/s10043-997-0521-3

Dho, S. W., Park, Y. J., & Kong, H. J. (1997b). Experimental determination of a geometric form factor in a lidar equation for an inhomogeneous atmosphere. *Applied Optics*, *36*(24), 6009. https://doi.org/10.1364/AO.36.006009

Dieudonné, E., Chazette, P., Marnas, F., Totems, J., & Shang, X. (2015). Lidar profiling of aerosol optical properties from Paris to Lake Baikal (Siberia). *Atmospheric Chemistry and Physics*, *15*(9), 5007–5026. https://doi.org/10.5194/acp-15-5007-2015

Dubovik, O., Holben, B., Eck, T. F., Smirnov, A., Kaufman, Y. J., King, M. D., Tanré, D., & Slutsker, I. (2002). Variability of Absorption and Optical Properties of Key Aerosol Types Observed in Worldwide Locations. *Journal of the Atmospheric Sciences*, *59*(3), 590–608. https://doi.org/10.1175/1520-0469(2002)059<0590:VOAAOP>2.0.CO;2

Dubovik, O., & King, M. D. (2000). A flexible inversion algorithm for retrieval of aerosol optical properties from Sun and sky radiance measurements. *Journal of Geophysical Research: Atmospheres*, *105*(D16), 20673–20696. https://doi.org/10.1029/2000JD900282

Dubovik, O., Sinyuk, A., Lapyonok, T., Holben, B. N., Mishchenko, M., Yang, P., Eck, T. F., Volten, H., Muñoz, O., Veihelmann, B., Van Der Zande, W. J., Leon, J., Sorokin, M., & Slutsker, I. (2006). Application of spheroid models to account for aerosol particle nonsphericity in remote sensing of desert dust. *Journal of Geophysical Research: Atmospheres*, *111*(D11), 2005JD006619. https://doi.org/10.1029/2005JD006619

Fernald, F. G. (1984). Analysis of atmospheric lidar observations: Some comments. *Applied Optics*, *23*(5), 652. https://doi.org/10.1364/AO.23.000652

Fernald, F. G., Herman, B. M., & Reagan, J. A. (1972). Determination of Aerosol Height Distributions by Lidar. *Journal of Applied Meteorology*, *11*(3), 482–489. https://doi.org/10.1175/1520-0450(1972)011<0482:DOAHDB>2.0.CO;2

Flannigan, M. D., Stocks, B. J., & Wotton, B. M. (2000). Climate change and forest fires. *Science of The Total Environment*, *262*(3), 221–229. https://doi.org/10.1016/S0048-9697(00)00524-6

Floutsi, A. A., Baars, H., Engelmann, R., Althausen, D., Ansmann, A., Bohlmann, S., Heese, B., Hofer, J., Kanitz, T., Haarig, M., Ohneiser, K., Radenz, M., Seifert, P., Skupin, A., Yin, Z., Abdullaev, S. F., Komppula, M., Filioglou, M., Giannakaki, E., … Wandinger, U. (2023). DeLiAn – a growing collection of depolarization ratio, lidar ratio and Ångström exponent for different aerosol types and mixtures from ground-based lidar observations. *Atmospheric Measurement Techniques*, *16*(9), 2353–2379. https://doi.org/10.5194/amt-16-2353-2023

Freudenthaler, V. (2016). About the effects of polarising optics on lidar signals and the Δ90 calibration. *Atmospheric Measurement Techniques*, *9*(9), 4181–4255. https://doi.org/10.5194/amt-9-4181-2016

Freudenthaler, V., Esselborn, M., Wiegner, M., Heese, B., Tesche, M., Ansmann, A., MüLLER, D., Althausen, D., Wirth, M., Fix, A., Ehret, G., Knippertz, P., Toledano, C., Gasteiger, J., Garhammer, M., & Seefeldner, M. (2009). Depolarization ratio profiling at several wavelengths in pure Saharan dust during SAMUM 2006. *Tellus B: Chemical and Physical Meteorology*, *61*(1), 165–179. https://doi.org/10.1111/j.1600-0889.2008.00396.x

Freudenthaler, V., Linné, H., Chaikovski, A., Rabus, D., & Groß, S. (2018). *EARLINET lidar quality assurance tools* [Preprint]. Aerosols/Remote Sensing/Instruments and Platforms. https://doi.org/10.5194/amt-2017-395

García, R. D., García, O. E., Cuevas-Agulló, E., Barreto, Á., Cachorro, V. E., Marrero, C., Almansa, F., Ramos, R., & Pó, M. (2022). Spectral Aerosol Radiative Forcing and Efficiency of the La Palma Volcanic Plume over the Izaña Observatory. *Remote Sensing*, *15*(1), 173. https://doi.org/10.3390/rs15010173

Gimmestad, G. G. (2001). Comment on two-wavelength lidar inversion techniques. *Applied Optics*, *40*(12), 2004. https://doi.org/10.1364/AO.40.002004

Groß, S., Esselborn, M., Weinzierl, B., Wirth, M., Fix, A., & Petzold, A. (2013). Aerosol classification by airborne high spectral resolution lidar observations. *Atmospheric Chemistry and Physics*, *13*(5), 2487–2505. https://doi.org/10.5194/acp-13-2487-2013

Guerrero-Rascado, J. L., Costa, M. J., Bortoli, D., Silva, A. M., Lyamani, H., & Alados-Arboledas, L. (2010). Infrared lidar overlap function: An experimental determination. *Optics Express*, *18*(19), 20350. https://doi.org/10.1364/OE.18.020350

Haarig, M., Ansmann, A., Engelmann, R., Baars, H., Toledano, C., Torres, B., Althausen, D., Radenz, M., & Wandinger, U. (2022). First triple-wavelength lidar observations of depolarization and extinction-to-backscatter ratios of Saharan dust. *Atmospheric Chemistry and Physics*, *22*(1), 355–369. https://doi.org/10.5194/acp-22-355-2022

Hansen, J., Lacis, A., Ruedy, R., & Sato, M. (1992). Potential climate impact of Mount Pinatubo eruption. *Geophysical Research Letters*, *19*(2), 215–218. https://doi.org/10.1029/91GL02788

Heintzenberg, J. (2009). The SAMUM-1 experiment over Southern Morocco: Overview and introduction. *Tellus B: Chemical and Physical Meteorology*, *61*(1), 2. https://doi.org/10.1111/j.1600-0889.2008.00403.x

Hervo, M., Poltera, Y., & Haefele, A. (2016). An empirical method to correct for temperature-dependent variations in the overlap function of CHM15k ceilometers. *Atmospheric Measurement Techniques*, *9*(7), 2947–2959. https://doi.org/10.5194/amt-9-2947-2016

Holben, B. N., Eck, T. F., Slutsker, I., Tanré, D., Buis, J. P., Setzer, A., Vermote, E., Reagan, J. A., Kaufman, Y. J., Nakajima, T., Lavenu, F., Jankowiak, I., & Smirnov, A. (1998). AERONET—A Federated Instrument Network and Data Archive for Aerosol Characterization. *Remote Sensing of Environment*, *66*(1), 1–16. https://doi.org/10.1016/S0034-4257(98)00031-5

Holben, B. N., Kim, J., Sano, I., Mukai, S., Eck, T. F., Giles, D. M., Schafer, J. S., Sinyuk, A., Slutsker, I., Smirnov, A., Sorokin, M., Anderson, B. E., Che, H., Choi, M., Crawford, J. H., Ferrare, R. A., Garay, M. J., Jeong, U., Kim, M., … Xiao, Q. (2018). An overview of mesoscale aerosol processes, comparisons, and validation studies from DRAGON networks. *Atmospheric Chemistry and Physics*, *18*(2), 655–671. https://doi.org/10.5194/acp-18-655-2018

Hu, Q. (2018). *Advanced aerosol characterization using sun/sky photometer and multi-wavelength Mie-Raman lidar measurements*. Universite de Lille 1.

Hu, Q., Goloub, P., Veselovskii, I., Bravo-Aranda, J.-A., Popovici, I. E., Podvin, T., Haeffelin, M., Lopatin, A., Dubovik, O., Pietras, C., Huang, X., Torres, B., & Chen, C. (2019). Long-range-transported Canadian smoke plumes in the lower stratosphere over northern France. *Atmospheric Chemistry and Physics*, *19*(2), 1173–1193. https://doi.org/10.5194/acp-19-1173-2019

Hu, Q., Goloub, P., Veselovskii, I., & Podvin, T. (2022). The characterization of long-range transported North American biomass burning plumes: What can a multi-wavelength Mie–Raman-polarization-fluorescence lidar provide? *Atmospheric Chemistry and Physics*, *22*(8), 5399–5414. https://doi.org/10.5194/acp-22-5399-2022

Hu, S., Wang, X., Wu, Y., Li, C., & Hu, H. (2005). Geometrical form factor determination with Raman backscattering signals. *Optics Letters*, *30*(14), 1879. https://doi.org/10.1364/OL.30.001879

Jaeglé, L., Quinn, P. K., Bates, T. S., Alexander, B., & Lin, J.-T. (2011). Global distribution of sea salt aerosols: New constraints from in situ and remote sensing observations. *Atmospheric Chemistry and Physics*, *11*(7), 3137–3157. https://doi.org/10.5194/acp-11-3137-2011

Jin, Y., Sugimoto, N., Shimizu, A., Nishizawa, T., Kai, K., Kawai, K., Yamazaki, A., Sakurai, M., & Wille, H. (2018). Evaluation of ceilometer attenuated backscattering coefficients for aerosol profile measurement. *Journal of Applied Remote Sensing*, *12*(04), 1. https://doi.org/10.1117/1.JRS.12.042604

June, N. A., Hodshire, A. L., Wiggins, E. B., Winstead, E. L., Robinson, C. E., Thornhill, K. L., Sanchez, K. J., Moore, R. H., Pagonis, D., Guo, H., Campuzano-Jost, P., Jimenez, J. L., Coggon, M. M., Dean-Day, J. M., Bui, T. P., Peischl, J., Yokelson, R. J., Alvarado, M. J., Kreidenweis, S. M., … Pierce, J. R. (2022). Aerosol size distribution changes in FIREX-AQ biomass burning plumes: The impact of plume concentration on coagulation and OA condensation/evaporation. *Atmospheric Chemistry and Physics*, *22*(19), 12803–12825. https://doi.org/10.5194/acp-22-12803-2022

Karol, Y., Tanré, D., Goloub, P., Vervaerde, C., Balois, J. Y., Blarel, L., Podvin, T., Mortier, A., & Chaikovsky, A. (2013). Airborne sun photometer PLASMA: Concept, measurements, comparison of aerosol extinction vertical profile with lidar. *Atmospheric Measurement Techniques*, *6*(9), 2383–2389. https://doi.org/10.5194/amt-6-2383-2013

Kasten, F., & Young, A. T. (1989). Revised optical air mass tables and approximation formula. *Applied Optics*, *28*(22), 4735. https://doi.org/10.1364/AO.28.004735

Kelley, D. I., Burton, C., Huntingford, C., Brown, M. A. J., Whitley, R., & Dong, N. (2021). Technical note: Low meteorological influence found in 2019 Amazonia fires. *Biogeosciences*, *18*(3), 787–804. https://doi.org/10.5194/bg-18-787-2021

Khaykin, S., Legras, B., Bucci, S., Sellitto, P., Isaksen, L., Tencé, F., Bekki, S., Bourassa, A., Rieger, L., Zawada, D., Jumelet, J., & Godin-Beekmann, S. (2020). The 2019/20 Australian wildfires generated a persistent smoke-charged vortex rising up to 35 km altitude. *Communications Earth & Environment*, *1*(1), 22. https://doi.org/10.1038/s43247-020-00022-5

Kim, M.-H., Omar, A. H., Tackett, J. L., Vaughan, M. A., Winker, D. M., Trepte, C. R., Hu, Y., Liu, Z., Poole, L. R., Pitts, M. C., Kar, J., & Magill, B. E. (2018). The CALIPSO version 4 automated aerosol classification and lidar ratio selection algorithm. *Atmospheric Measurement Techniques*, *11*(11), 6107–6135. https://doi.org/10.5194/amt-11-6107-2018

King, M. D., Kaufman, Y. J., Menzel, W. P., & Tanre, D. (1992). Remote sensing of cloud, aerosol, and water vapor properties from the moderate resolution imaging spectrometer (MODIS). *IEEE Transactions on Geoscience and Remote Sensing*, *30*(1), 2–27. https://doi.org/10.1109/36.124212

Kleinman, L. I., Sedlacek Iii, A. J., Adachi, K., Buseck, P. R., Collier, S., Dubey, M. K., Hodshire, A. L., Lewis, E., Onasch, T. B., Pierce, J. R., Shilling, J., Springston, S. R., Wang, J., Zhang, Q., Zhou, S., & Yokelson, R. J. (2020). Rapid evolution of aerosol particles and their optical properties downwind of wildfires in the western US. *Atmospheric Chemistry and Physics*, *20*(21), 13319–13341. https://doi.org/10.5194/acp-20-13319-2020

Klett, J. D. (1981). Stable analytical inversion solution for processing lidar returns. *Applied Optics*, *20*(2), 211. https://doi.org/10.1364/AO.20.000211

Klett, J. D. (1985). Lidar inversion with variable backscatter/extinction ratios. *Applied Optics*, *24*(11), 1638. https://doi.org/10.1364/AO.24.001638

Kloss, C., Berthet, G., Sellitto, P., Ploeger, F., Taha, G., Tidiga, M., Eremenko, M., Bossolasco, A., Jégou, F., Renard, J.-B., & Legras, B. (2021). Stratospheric aerosol layer perturbation caused by the 2019 Raikoke and Ulawun eruptions and their radiative forcing. *Atmospheric Chemistry and Physics*, *21*(1), 535–560. https://doi.org/10.5194/acp-21-535-2021

Kokhanenko, G. P., Balin, Y. S., Klemasheva, M. G., Nasonov, S. V., Novoselov, M. M., Penner, I. E., & Samoilova, S. V. (2020). Scanning polarization lidar LOSA-M3: Opportunity for research of crystalline particle orientation in the ice clouds. *Atmospheric Measurement Techniques*, *13*(3), 1113–1127. https://doi.org/10.5194/amt-13-1113-2020

Kokkalis, P. (2017). Using paraxial approximation to describe the optical setup of a typical EARLINET lidar system. *Atmospheric Measurement Techniques*, *10*(8), 3103–3115. https://doi.org/10.5194/amt-10-3103-2017

Koren, I., Dagan, G., & Altaratz, O. (2014). From aerosol-limited to invigoration of warm convective clouds. *Science*, *344*(6188), 1143–1146. https://doi.org/10.1126/science.1252595

Kovalev, V. A. (1995). Sensitivity of the lidar solution to errors of the aerosol backscatter-to-extinction ratio: Influence of a monotonic change in the aerosol extinction coefficient. *Applied Optics*, *34*(18), 3457. https://doi.org/10.1364/AO.34.003457

Kovalev, V. A. (2004). Distortions of the extinction coefficient profile caused by systematic errors in lidar data. *Applied Optics*, *43*(15), 3191. https://doi.org/10.1364/AO.43.003191

Kumar, A., Pierce, R. B., Ahmadov, R., Pereira, G., Freitas, S., Grell, G., Schmidt, C., Lenzen, A., Schwarz, J. P., Perring, A. E., Katich, J. M., Hair, J., Jimenez, J. L., Campuzano-Jost, P., & Guo, H. (2022). Simulating wildfire emissions and plume rise using geostationary satellite fire radiative power measurements: A case study of the 2019 Williams Flats fire. *Atmospheric Chemistry and Physics*, *22*(15), 10195–10219. https://doi.org/10.5194/acp-22-10195-2022

Kunz, G. J. (1999). Two-wavelength lidar inversion algorithm. *Applied Optics*, *38*(6), 1015. https://doi.org/10.1364/AO.38.001015

Kunz, G. J., & De Leeuw, G. (1993). Inversion of lidar signals with the slope method. *Applied Optics*, *32*(18), 3249. https://doi.org/10.1364/AO.32.003249

Landulfo, E., Vega, A. R., Yoshida, A. C., Bastidas, A., Dos Santos, A. V., Silva, A., Gomes, A. A., Gonzalez, B. B., Melo-Luna, C. A., Hoyos, C. D., De Souza Rae, C. T., Camilo, D., Vivas, D., Gouveia, D. A., Wolfram, E., Collini, E., Lopes, F. J. S., De Arruda Moreira, G., De Melo Jorge Barbosa, H., … Papandrea, S. (2020). Lalinet Network Status. *EPJ Web of Conferences*, *237*, 05008. https://doi.org/10.1051/epjconf/202023705008

Li, D., Wu, Y., Gross, B., & Moshary, F. (2021). Capabilities of an Automatic Lidar Ceilometer to Retrieve Aerosol Characteristics within the Planetary Boundary Layer. *Remote Sensing*, *13*(18), 3626. https://doi.org/10.3390/rs13183626

Liou, K. N. (2002). *An introduction to Atmospheric Radiation*. Academic Press.

López-Cayuela, M. Á., Córdoba-Jabonero, C., Bermejo-Pantaleón, D., Sicard, M., Salgueiro, V., Molero, F., Carvajal-Pérez, C. V., Granados-Muñoz, M. J., Comerón, A., Couto, F. T., Barragán, R., Zorzano, M.-P., Bravo-Aranda, J. A., Muñoz-Porcar, C., Costa, M. J., Artíñano, B., Rodríguez-Gómez, A., Bortoli, D., Pujadas, M., … Guerrero-Rascado, J. L. (2023). Vertical characterization of fine and coarse dust particles during an intense Saharan dust outbreak over the Iberian Peninsula in springtime 2021. *Atmospheric Chemistry and Physics*, *23*(1), 143–161. https://doi.org/10.5194/acp-23-143-2023

Lu, X., Jiang, Y., Zhang, X., Wang, X., & Spinelli, N. (2011). Two-wavelength lidar inversion algorithm for determination of aerosol extinction-to-backscatter ratio and its application to CALIPSO lidar measurements. *Journal of Quantitative Spectroscopy and Radiative Transfer*, *112*(2), 320–328. https://doi.org/10.1016/j.jqsrt.2010.07.013

Mallet, P.-É., Pujol, O., Brioude, J., Evan, S., & Jensen, A. (2018). Marine aerosol distribution and variability over the pristine Southern Indian Ocean. *Atmospheric Environment*, *182*, 17–30. https://doi.org/10.1016/j.atmosenv.2018.03.016

Mamouri, R. E., Amiridis, V., Papayannis, A., Giannakaki, E., Tsaknakis, G., & Balis, D. S. (2009). Validation of CALIPSO space-borne-derived attenuated backscatter coefficient profiles using a ground-based lidar in Athens, Greece. *Atmospheric Measurement Techniques*, *2*(2), 513–522. https://doi.org/10.5194/amt-2-513-2009

Mascaut, F. (2023). *Interactions aérosols-vapeur d'eau-nuages en région océanique pristine* [Lille University]. https://theses.hal.science/tel-04198315

Mascaut, F., Pujol, O., Verreyken, B., Peroni, R., Metzger, J. M., Blarel, L., Podvin, T., Goloub, P., Sellegri, K., Thornberry, T., Duflot, V., Tulet, P., & Brioude, J. (2022). Aerosol characterization in an oceanic context around Reunion Island (AEROMARINE field campaign). *Atmospheric Environment*, *268*, 118770. https://doi.org/10.1016/j.atmosenv.2021.118770

Mayer, K. J., Wang, X., Santander, M. V., Mitts, B. A., Sauer, J. S., Sultana, C. M., Cappa, C. D., & Prather, K. A. (2020). Secondary Marine Aerosol Plays a Dominant Role over Primary Sea Spray Aerosol in Cloud Formation. *ACS Central Science*, *6*(12), 2259–2266. https://doi.org/10.1021/acscentsci.0c00793

McArdle, C. E., Dowling, T. C., Carey, K., DeVies, J., Johns, D., Gates, A. L., Stein, Z., van Santen, K. L., Radhakrishnan, L., Kite-Powell, A., Soetebier, K., Sacks, J. D., Sircar, K., Hartnett, K. P.,

& Mirabelli, M. C. (2023). Asthma-Associated Emergency Department Visits During the Canadian Wildfire Smoke Episodes—United States, April– August 2023. *Missing Data*, *72*(34).

McClure, C. D., & Jaffe, D. A. (2018). US particulate matter air quality improves except in wildfire-prone areas. *Proceedings of the National Academy of Sciences*, *115*(31), 7901–7906. https://doi.org/10.1073/pnas.1804353115

McGill, M. J., Vaughan, M. A., Trepte, C. R., Hart, W. D., Hlavka, D. L., Winker, D. M., & Kuehn, R. (2007). Airborne validation of spatial properties measured by the CALIPSO lidar. *Journal of Geophysical Research: Atmospheres*, *112*(D20), 2007JD008768. https://doi.org/10.1029/2007JD008768

McMurry, P. H. (2000). A review of atmospheric aerosol measurements☆. *Atmospheric Environment*.

Middleton, N. J., & Goudie, A. S. (2001). Saharan dust: Sources and trajectories. *Transactions of the Institute of British Geographers*, *26*(2), 165–181. https://doi.org/10.1111/1475-5661.00013

Milford, C., Torres, C., Vilches, J., Gossman, A.-K., Weis, F., Suárez-Molina, D., García, O. E., Prats, N., Barreto, Á., García, R. D., Bustos, J. J., Marrero, C. L., Ramos, R., Chinea, N., Boulesteix, T., Taquet, N., Rodríguez, S., López-Darias, J., Sicard, M., … Cuevas, E. (2023). Impact of the 2021 La Palma volcanic eruption on air quality: Insights from a multidisciplinary approach. *Science of The Total Environment*, *869*, 161652. https://doi.org/10.1016/j.scitotenv.2023.161652

Mishchenko, M. I., & Travis, L. D. (1994). T-matrix computations of light scattering by large spheroidal particles. *Optics Communications*, *109*(1–2), 16–21. https://doi.org/10.1016/0030-4018(94)90731-5

Mona, L., Amodeo, A., Pandolfi, M., & Pappalardo, G. (2006). Saharan dust intrusions in the Mediterranean area: Three years of Raman lidar measurements. *Journal of Geophysical Research*, *111*(D16), D16203. https://doi.org/10.1029/2005JD006569

Morille, Y., Haeffelin, M., Drobinski, P., & Pelon, J. (2007). STRAT: An Automated Algorithm to Retrieve the Vertical Structure of the Atmosphere from Single-Channel Lidar Data. *Journal of Atmospheric and Oceanic Technology*, *24*(5), 761–775. https://doi.org/10.1175/JTECH2008.1

Mortier, A. (2013a). *Tendances et variabilités de l'aérosol atmosphérique à l'aide du couplage Lidar/Photomètre sur les sites de Lille et Dakar*. Universite de Lille 1.

Mortier, A. (2013b). *Tendances et variabilites de l'aerosol atmospherique a l'aide du couplage Lidar/Photometre sur les sites de Lille et Dakar* (Vol. 0). University of Lille.

Mortier, A., Goloub, P., Podvin, T., Deroo, C., Chaikovsky, A., Ajtai, N., Blarel, L., Tanre, D., & Derimian, Y. (2013). Detection and characterization of volcanic ash plumes over Lille during the Eyjafjallajökull eruption. *Atmospheric Chemistry and Physics*, *13*(7), 3705–3720. https://doi.org/10.5194/acp-13-3705-2013

Mutch, R. W. (1994). Fighting fire with prescribed fire - a return to ecosystem health. Journal of Forestry, 92(11), 31–33

Müller, D., Hostetler, C. A., Ferrare, R. A., Burton, S. P., Chemyakin, E., Kolgotin, A., Hair, J. W., Cook, A. L., Harper, D. B., Rogers, R. R., Hare, R. W., Cleckner, C. S., Obland, M. D., Tomlinson, J., Berg, L. K., & Schmid, B. (2014). Airborne Multiwavelength High Spectral Resolution Lidar (HSRL-2) observations during TCAP 2012: Vertical profiles of optical and microphysical properties of a smoke/urban haze plume over the northeastern coast of the US. *Atmospheric Measurement Techniques*, *7*(10), 3487–3496. https://doi.org/10.5194/amt-7-3487-2014

Müller, D., Veselovskii, I., Kolgotin, A., Tesche, M., Ansmann, A., & Dubovik, O. (2013). Vertical profiles of pure dust and mixed smoke–dust plumes inferred from inversion of multiwavelength Raman/polarization lidar data and comparison to AERONET retrievals and in situ observations. *Applied Optics*, *52*(14), 3178. https://doi.org/10.1364/AO.52.003178

Navas-Guzmán, F., Müller, D., Bravo-Aranda, J. A., Guerrero-Rascado, J. L., Granados-Muñoz, M. J., Pérez-Ramírez, D., Olmo, F. J., & Alados-Arboledas, L. (2013). Eruption of the Eyjafjallajökull Volcano in spring 2010: Multiwavelength Raman lidar measurements of sulphate particles in the lower troposphere. *Journal of Geophysical Research: Atmospheres*, *118*(4), 1804–1813. https://doi.org/10.1002/jgrd.50116

Nicolae, D., Nemuc, A., Müller, D., Talianu, C., Vasilescu, J., Belegante, L., & Kolgotin, A. (2013). Characterization of fresh and aged biomass burning events using multiwavelength Raman lidar and mass spectrometry: BIOMASS BURNING AEROSOLS FROM LIDAR & AMS. *Journal of Geophysical Research: Atmospheres*, *118*(7), 2956–2965. https://doi.org/10.1002/jgrd.50324

O'Connor, E. J., Illingworth, A. J., & Hogan, R. J. (2004). A Technique for Autocalibration of Cloud Lidar. *Journal of Atmospheric and Oceanic Technology*, *21*(5), 777–786. https://doi.org/10.1175/1520-0426(2004)021<0777:ATFAOC>2.0.CO;2

Omar, A. H., Winker, D. M., Vaughan, M. A., Hu, Y., Trepte, C. R., Ferrare, R. A., Lee, K.-P., Hostetler, C. A., Kittaka, C., Rogers, R. R., Kuehn, R. E., & Liu, Z. (2009). The CALIPSO Automated Aerosol Classification and Lidar Ratio Selection Algorithm. *Journal of Atmospheric and Oceanic Technology*, *26*(10), 1994–2014. https://doi.org/10.1175/2009JTECHA1231.1

Osborne, M. J., De Leeuw, J., Witham, C., Schmidt, A., Beckett, F., Kristiansen, N., Buxmann, J., Saint, C., Welton, E. J., Fochesatto, J., Gomes, A. R., Bundke, U., Petzold, A., Marenco, F., & Haywood, J. (2022). The 2019 Raikoke volcanic eruption – Part 2: Particle-phase dispersion and concurrent wildfire smoke emissions. *Atmospheric Chemistry and Physics*, *22*(5), 2975–2997. https://doi.org/10.5194/acp-22-2975-2022

Pal, S., Xueref-Remy, I., Ammoura, L., Chazette, P., Gibert, F., Royer, P., Dieudonné, E., Dupont, J.-C., Haeffelin, M., Lac, C., Lopez, M., Morille, Y., & Ravetta, F. (2012). Spatio-temporal variability of the atmospheric boundary layer depth over the Paris agglomeration: An assessment of the impact of the urban heat island intensity. *Atmospheric Environment*, *63*, 261–275. https://doi.org/10.1016/j.atmosenv.2012.09.046

Pappalardo G., EARLINET: the European Lidar network for aerosol study at continental scale, Feature article in EARSeL Newsletter, N. 82, 13-18, June 2010.

Papayannis, A., Amiridis, V., Mona, L., Tsaknakis, G., Balis, D., Bösenberg, J., Chaikovski, A., De Tomasi, F., Grigorov, I., Mattis, I., Mitev, V., Müller, D., Nickovic, S., Pérez, C., Pietruczuk, A., Pisani, G., Ravetta, F., Rizi, V., Sicard, M., … Pappalardo, G. (2008). Systematic lidar observations of Saharan dust over Europe in the frame of EARLINET (2000–2002). *Journal of Geophysical Research*, *113*(D10), D10204. https://doi.org/10.1029/2007JD009028

Pelon, J., Mallet, M., Mariscal, A., Goloub, P., Tanré, D., Bou Karam, D., Flamant, C., Haywood, J., Pospichal, B., & Victori, S. (2008). Microlidar observations of biomass burning aerosol over Djougou (Benin) during African Monsoon Multidisciplinary Analysis Special Observation Period 0: Dust and Biomass-Burning Experiment. *Journal of Geophysical Research*, *113*, D00C18. https://doi.org/10.1029/2008JD009976

Petty, G. W. (2006). *A first course in atmospheric radiation* (2. ed). Sundog Publ.

Pierce, J. R., & Adams, P. J. (2006). Global evaluation of CCN formation by direct emission of sea salt and growth of ultrafine sea salt. *Journal of Geophysical Research: Atmospheres*, *111*(D6), 2005JD006186. https://doi.org/10.1029/2005JD006186

Platt, C. M. R. (1973). Lidar and Radioinetric Observations of Cirrus Clouds. *Journal of the Atmospheric Sciences*, *30*(6), 1191–1204. https://doi.org/10.1175/1520-0469(1973)030<1191:LAROOC>2.0.CO;2

Popovici, I. (2018). *Aerosol spatial and temporal variability as seen by Mobile Aerosol Monitoring System (MAMS)*. Lille University.

Popovici, I. E., Deng, Z., Goloub, P., Xia, X., Chen, H., Blarel, L., Podvin, T., Hao, Y., Chen, H., Torres, B., Victori, S., & Fan, X. (2022). Mobile On-Road Measurements of Aerosol Optical Properties during MOABAI Campaign in the North China Plain. *Atmosphere*, *13*(1), 21. https://doi.org/10.3390/atmos13010021

Popovici, I. E., Goloub, P., Podvin, T., Blarel, L., Loisil, R., Unga, F., Mortier, A., Deroo, C., Victori, S., Ducos, F., Torres, B., Delegove, C., Choël, M., Pujol-Söhne, N., & Pietras, C. (2018). Description and applications of a mobile system performing on-road aerosol remote sensing and in situ measurements. *Atmospheric Measurement Techniques*, *11*(8), 4671–4691. https://doi.org/10.5194/amt-11-4671-2018

Potter, J. F. (1987). Two-frequency lidar inversion technique. *Applied Optics*, *26*(7), 1250. https://doi.org/10.1364/AO.26.001250

Pratt, K. A., & Prather, K. A. (2010). Aircraft measurements of vertical profiles of aerosol mixing states. *Journal of Geophysical Research: Atmospheres*, *115*(D11), 2009JD013150. https://doi.org/10.1029/2009JD013150

Prospero, J. M., Barkley, A. E., Gaston, C. J., Gatineau, A., Campos Y Sansano, A., & Panechou, K. (2020). Characterizing and Quantifying African Dust Transport and Deposition to South America: Implications for the Phosphorus Budget in the Amazon Basin. *Global Biogeochemical Cycles*, *34*(9), e2020GB006536. https://doi.org/10.1029/2020GB006536

Qi, S., Huang, Z., Ma, X., Huang, J., Zhou, T., Zhang, S., Dong, Q., Bi, J., & Shi, J. (2021). Classification of atmospheric aerosols and clouds by use of dual-polarization lidar measurements. *Optics Express*, *29*(15), 23461. https://doi.org/10.1364/OE.430456

Reid, J. S., Koppmann, R., Eck, T. F., & Eleuterio, D. P. (2005). A review of biomass burning emissions part II: intensive physical properties of biomass burning particles. *Atmos. Chem. Phys.*

Renard, J.-B., Dulac, F., Berthet, G., Lurton, T., Vignelles, D., Jégou, F., Tonnelier, T., Jeannot, M., Couté, B., Akiki, R., Verdier, N., Mallet, M., Gensdarmes, F., Charpentier, P., Mesmin, S., Duverger, V., Dupont, J.-C., Elias, T., Crenn, V., … Daugeron, D. (2016). LOAC: A small aerosol optical counter/sizer for ground-based and balloonmeasurements of the size distribution and nature of atmospheric particles – Part 2: First results from balloon and unmanned aerial vehicleflights. *Atmospheric Measurement Techniques*, *9*(8), 3673–3686. https://doi.org/10.5194/amt-9-3673-2016

Rinaldi, M., Decesari, S., Finessi, E., Giulianelli, L., Carbone, C., Fuzzi, S., O'Dowd, C. D., Ceburnis, D., & Facchini, M. C. (2010). Primary and Secondary Organic Marine Aerosol and Oceanic Biological Activity: Recent Results and New Perspectives for Future Studies. *Advances in Meteorology*, *2010*, 1–10. https://doi.org/10.1155/2010/310682

Rocadenbosch, F., Frasier, S., Kumar, D., Lange Vega, D., Gregorio, E., & Sicard, M. (2012). Backscatter Error Bounds for the Elastic Lidar Two-Component Inversion Algorithm. *IEEE Transactions on Geoscience and Remote Sensing*, *50*(11), 4791–4803. https://doi.org/10.1109/TGRS.2012.2194501

Rodríguez, S., Cuevas, E., Prospero, J. M., Alastuey, A., Querol, X., López-Solano, J., García, M. I., & Alonso-Pérez, S. (2015). Modulation of Saharan dust export by the North African dipole. *Atmospheric Chemistry and Physics*, *15*(13), 7471–7486. https://doi.org/10.5194/acp-15-7471-2015

Royer, P., Chazette, P., Sartelet, K., Zhang, Q. J., Beekmann, M., & Raut, J.-C. (2011). Comparison of lidar-derived PM10 with regional modeling and ground-based observations in the frame of MEGAPOLI experiment. *Atmospheric Chemistry and Physics*, *11*(20), 10705–10726. https://doi.org/10.5194/acp-11-10705-2011

Russell, P. B., Swissler, T. J., & McCormick, M. P. (1979). Methodology for error analysis and simulation of lidar aerosol measurements. *Applied Optics*, *18*(22), 3783. https://doi.org/10.1364/AO.18.003783

Saiz-Jimenez, C. (1993). Deposition of airborne organic pollutants on historic buildings. *Atmospheric Environment. Part B. Urban Atmosphere*, *27*(1), 77–85. https://doi.org/10.1016/0957-1272(93)90047-A

Salby, M. L. (1996). *Fundamentals of atmospheric physics*. Academic Press.

Sanchez Barrero, M. F., Popovici, I. E., Goloub, P., Victori, S., Hu, Q., Torres, B., Podvin, T., Blarel, L., Dubois, G., Ducos, F., Bourrianne, E., Lapionak, A., Proniewski, L., Holben, B., Giles, D. M., & LaRosa, A. (2023). *Enhancing Mobile Aerosol Monitoring with CE376 Dual-Wavelength Depolarization Lidar* [Preprint]. Aerosols/Remote Sensing/Instruments and Platforms. https://doi.org/10.5194/egusphere-2023-2579

Sasano, Y., & Browell, E. V. (1989). Light scattering characteristics of various aerosol types derived from multiple wavelength lidar observations. *Applied Optics*, *28*(9), 1670. https://doi.org/10.1364/AO.28.001670

Sasano, Y., Browell, E. V., & Ismail, S. (1985). Error caused by using a constant extinction/backscattering ratio in the lidar solution. *Applied Optics*, *24*(22), 3929. https://doi.org/10.1364/AO.24.003929

Sasano, Y., Shimizu, H., Takeuchi, N., & Okuda, M. (1979). Geometrical form factor in the laser radar equation: An experimental determination. *Applied Optics*, *18*(23), 3908. https://doi.org/10.1364/AO.18.003908

Sassen, K., & Dodd, G. C. (1982). Lidar crossover function and misalignment effects. *Applied Optics*, *21*(17), 3162. https://doi.org/10.1364/AO.21.003162

Schneider, M., Romero, P. M., Hase, F., Blumenstock, T., Cuevas, E., & Ramos, R. (2010). Continuous quality assessment of atmospheric water vapour measurement techniques: FTIR, Cimel, MFRSR, GPS, and Vaisala RS92. *Atmospheric Measurement Techniques*, *3*(2), 323–338. https://doi.org/10.5194/amt-3-323-2010

Seinfeld, J. H., and Pandis, S. N. (2016). *Atmospheric Chemistry and Physics: from Air Pollution to Climate Change* 3rd Ed., Wiley, Hoboken, N.J.

Seneviratne, S.I., X. Zhang, M. Adnan, W. Badi, C. Dereczynski, A. Di Luca, S. Ghosh, I. Iskandar, J. Kossin, S. Lewis, F. Otto, I. Pinto, M. Satoh, S.M. Vicente-Serrano, M. Wehner, and B. Zhou, 2021: Weather and Climate Extreme Events in a Changing Climate. In Climate Change 2021: The Physical Science Basis. Contribution of Working Group I to the Sixth Assessment Report of the Intergovernmental Panel on Climate Change [Masson-Delmotte, V., P. Zhai, A. Pirani, S.L. Connors, C. Péan, S. Berger, N. Caud, Y. Chen, L. Goldfarb, M.I. Gomis, M. Huang, K. Leitzell, E. Lonnoy, J.B.R. Matthews, T.K. Maycock, T. Waterfield, O. Yelekçi, R. Yu, and B. Zhou (eds.)]. Cambridge University Press, Cambridge, United Kingdom and New York, NY, USA, pp. 1513–1766, doi:10.1017/9781009157896.013.

Shang, X., Chazette, P., & Totems, J. (2018). Analysis of a warehouse fire smoke plume over Paris with an N_2 Raman lidar and an optical thickness matching algorithm. *Atmospheric Measurement Techniques*, *11*(12), 6525–6538. https://doi.org/10.5194/amt-11-6525-2018

Sicard, M., Córdoba-Jabonero, C., Barreto, A., Welton, E. J., Gil-Díaz, C., Carvajal-Pérez, C. V., Comerón, A., García, O., García, R., López-Cayuela, M.-Á., Muñoz-Porcar, C., Prats, N., Ramos, R., Rodríguez-Gómez, A., Toledano, C., & Torres, C. (2022). Volcanic Eruption of Cumbre Vieja, La Palma, Spain: A First Insight to the Particulate Matter Injected in the Troposphere. *Remote Sensing*, *14*(10), 2470. https://doi.org/10.3390/rs14102470

Sicard, M., Rodríguez-Gómez, A., Comerón, A., & Muñoz-Porcar, C. (2020). Calculation of the Overlap Function and Associated Error of an Elastic Lidar or a Ceilometer: Cross-Comparison with a Cooperative Overlap-Corrected System. *Sensors*, *20*(21), 6312. https://doi.org/10.3390/s20216312

Sinyuk, A., Holben, B. N., Eck, T. F., Giles, D. M., Slutsker, I., Korkin, S., Schafer, J. S., Smirnov, A., Sorokin, M., & Lyapustin, A. (2020). The AERONET Version 3 aerosol retrieval algorithm, associated uncertainties and comparisons to Version 2. *Atmospheric Measurement Techniques*, *13*(6), 3375–3411. https://doi.org/10.5194/amt-13-3375-2020

Skiles, S. M., Flanner, M., Cook, J. M., Dumont, M., & Painter, T. H. (2018). Radiative forcing by light-absorbing particles in snow. *Nature Climate Change*, *8*(11), 964–971. https://doi.org/10.1038/s41558-018-0296-5

Smirnov, A., Holben, B. N., Eck, T. F., Dubovik, O., & Slutsker, I. (2000). Cloud-Screening and Quality Control Algorithms for the AERONET Database. *Remote Sensing of Environment*, *73*(3), 337–349. https://doi.org/10.1016/S0034-4257(00)00109-7

Smirnov, A., Holben, B. N., Slutsker, I., Giles, D. M., McClain, C. R., Eck, T. F., Sakerin, S. M., Macke, A., Croot, P., Zibordi, G., Quinn, P. K., Sciare, J., Kinne, S., Harvey, M., Smyth, T. J., Piketh, S., Zielinski, T., Proshutinsky, A., Goes, J. I., … Jourdin, F. (2009). Maritime Aerosol Network as a component of Aerosol Robotic Network. *Journal of Geophysical Research*, *114*(D6), D06204. https://doi.org/10.1029/2008JD011257

Speidel, J., & Vogelmann, H. (2023). Correct(ed) Klett–Fernald algorithm for elastic aerosol backscatter retrievals: A sensitivity analysis. *Applied Optics*, *62*(4), 861. https://doi.org/10.1364/AO.465944

Stefanis, N.-A., Theoulakis, P., & Pilinis, C. (2009). Dry deposition effect of marine aerosol to the building stone of the medieval city of Rhodes, Greece. *Building and Environment*, *44*(2), 260–270. https://doi.org/10.1016/j.buildenv.2008.03.001

Stein, A. F., Draxler, R. R., Rolph, G. D., Stunder, B. J. B., Cohen, M. D., & Ngan, F. (2015). NOAA's HYSPLIT Atmospheric Transport and Dispersion Modeling System. *Bulletin of the American Meteorological Society*, *96*(12), 2059–2077. https://doi.org/10.1175/BAMS-D-14-00110.1

Stull, R. (1988). *An introduction to Boundary Layer Meteorology*. Kluwer Academic Publishers.

Szopa, S., V. Naik, B. Adhikary, P. Artaxo, T. Berntsen, W.D. Collins, S. Fuzzi, L. Gallardo, A. Kiendler-Scharr, Z. Klimont, H. Liao, N. Unger, and P. Zanis. (2021). Short-lived Climate Forcers. In *Climate Change 2021 – The Physical Science Basis: Working Group I Contribution* to the Sixth Assessment Report of the Intergovernmental Panel on Climate Change (1st ed.). Cambridge University Press. https://doi.org/10.1017/9781009157896

Tackett, J. L., Kar, J., Vaughan, M. A., Getzewich, B. J., Kim, M.-H., Vernier, J.-P., Omar, A. H., Magill, B. E., Pitts, M. C., & Winker, D. M. (2023). The CALIPSO version 4.5 stratospheric aerosol subtyping algorithm. *Atmospheric Measurement Techniques*, *16*(3), 745–768. https://doi.org/10.5194/amt-16-745-2023

Tesche, M., Ansmann, A., Müller, D., Althausen, D., Engelmann, R., Freudenthaler, V., & Groß, S. (2009). Vertically resolved separation of dust and smoke over Cape Verde using multiwavelength Raman and polarization lidars during Saharan Mineral Dust Experiment 2008. *Journal of Geophysical Research*, *114*(D13), D13202. https://doi.org/10.1029/2009JD011862

Tesche, M., Ansmann, A., MüLLER, D., Althausen, D., Mattis, I., Heese, B., Freudenthaler, V., Wiegner, M., Esselborn, M., Pisani, G., & Knippertz, P. (2009). Vertical profiling of Saharan dust with Raman lidars and airborne HSRL in southern Morocco during SAMUM. *Tellus B: Chemical and Physical Meteorology*, *61*(1), 144–164. https://doi.org/10.1111/j.1600-0889.2008.00390.x

Tesche, M., Gross, S., Ansmann, A., Müller, D., Althausen, D., Freudenthaler, V., & Esselborn, M. (2011). Profiling of Saharan dust and biomass-burning smoke with multiwavelength polarization Raman lidar at Cape Verde. *Tellus B: Chemical and Physical Meteorology*, *63*(4), 649–676. https://doi.org/10.1111/j.1600-0889.2011.00548.x

Thompson, D. W. J., Wallace, J. M., Jones, P. D., & Kennedy, J. J. (2009). Identifying Signatures of Natural Climate Variability in Time Series of Global-Mean Surface Temperature: Methodology and Insights. *Journal of Climate*, *22*(22), 6120–6141. https://doi.org/10.1175/2009JCLI3089.1

Torres, B. (2012). *Study on the influence of different error sources on sky radiance measurements and inversion-derived aerosol products in the frame of AERONET*. Universidad de Valladolid.

Torres, B., Dubovik, O., Fuertes, D., Schuster, G., Cachorro, V. E., Lapyonok, T., Goloub, P., Blarel, L., Barreto, A., Mallet, M., Toledano, C., & Tanré, D. (2017). Advanced characterisation of aerosol size properties from measurements of spectral optical depth using the GRASP algorithm. *Atmospheric Measurement Techniques*, *10*(10), 3743–3781. https://doi.org/10.5194/amt-10-3743-2017

Torres, B., Dubovik, O., Toledano, C., Berjon, A., Cachorro, V. E., Lapyonok, T., Litvinov, P., & Goloub, P. (2014). Sensitivity of aerosol retrieval to geometrical configuration of ground-based sun/sky radiometer observations. *Atmospheric Chemistry and Physics*, *14*(2), 847–875. https://doi.org/10.5194/acp-14-847-2014

Vasilakopoulou, C. N., Matrali, A., Skyllakou, K., Georgopoulou, M., Aktypis, A., Florou, K., Kaltsonoudis, C., Siouti, E., Kostenidou, E., Błaziak, A., Nenes, A., Papagiannis, S., Eleftheriadis, K., Patoulias, D., Kioutsioukis, I., & Pandis, S. N. (2023). Rapid transformation of wildfire emissions to harmful background aerosol. *Npj Climate and Atmospheric Science*, *6*(1), 218. https://doi.org/10.1038/s41612-023-00544-7

Vaughan, G., Wareing, D., & Ricketts, H. (2021). Measurement Report: Lidar measurements of stratospheric aerosol following the 2019 Raikoke and Ulawun volcanic eruptions. *Atmospheric Chemistry and Physics*, *21*(7), 5597–5604. https://doi.org/10.5194/acp-21-5597-2021

Vaughan, M. (2004). *Algorithm for retrieving lidar ratios at 1064 nm from space-based lidar backscatter data* (C. Werner, Ed.; p. 104). https://doi.org/10.1117/12.510770

Vaughan, M. A., Young, S. A., Winker, D. M., Powell, K. A., Omar, A. H., Liu, Z., Hu, Y., & Hostetler, C. A. (2004). *Fully automated analysis of space-based lidar data: An overview of the CALIPSO retrieval algorithms and data products* (U. N. Singh, Ed.; p. 16). https://doi.org/10.1117/12.572024

Velazquez Garcia, A. (2023). *Chemical and optical properties of particulate pollution in the Lille area, Northern France based on ATOLL observations* [Lille University]. https://theses.hal.science/tel-04107963

Velazquez-Garcia, A., Crumeyrolle, S., De Brito, J. F., Tison, E., Bourrianne, E., Chiapello, I., & Riffault, V. (2023). Deriving composition-dependent aerosol absorption, scattering and extinction mass efficiencies from multi-annual high time resolution observations in Northern France. *Atmospheric Environment*, *298*, 119613. https://doi.org/10.1016/j.atmosenv.2023.119613

Velotta, R., Bartoli, B., Capobianco, R., Fiorani, L., & Spinelli, N. (1998). Analysis of the receiver response in lidar measurements. *Applied Optics*, *37*(30), 6999. https://doi.org/10.1364/AO.37.006999

Veselovskii, I., Goloub, P., Podvin, T., Bovchaliuk, V., Derimian, Y., Augustin, P., Fourmentin, M., Tanre, D., Korenskiy, M., Whiteman, D. N., Diallo, A., Ndiaye, T., Kolgotin, A., & Dubovik, O. (2016). Retrieval of optical and physical properties of African dust from multiwavelength Raman lidar measurements during the SHADOW campaign in Senegal. *Atmospheric Chemistry and Physics*, *16*(11), 7013–7028. https://doi.org/10.5194/acp-16-7013-2016

Veselovskii, I., Hu, Q., Goloub, P., Podvin, T., Barchunov, B., & Korenskii, M. (2022). Combining Mie–Raman and fluorescence observations: A step forward in aerosol classification with lidar technology. *Atmospheric Measurement Techniques*, *15*(16), 4881–4900. https://doi.org/10.5194/amt-15-4881-2022

Veselovskii, I., Hu, Q., Goloub, P., Podvin, T., Choël, M., Visez, N., & Korenskiy, M. (2021). Mie–Raman–fluorescence lidar observations of aerosols during pollen season in the north of France. *Atmospheric Measurement Techniques*, *14*(7), 4773–4786. https://doi.org/10.5194/amt-14-4773-2021

Veselovskii, I., Hu, Q., Goloub, P., Podvin, T., Korenskiy, M., Derimian, Y., Legrand, M., & Castellanos, P. (2020). Variability in lidar-derived particle properties over West Africa due to changes in absorption: Towards an understanding. *Atmospheric Chemistry and Physics*, *20*(11), 6563–6581. https://doi.org/10.5194/acp-20-6563-2020

Vladimir A. Kovalev & William E. Eichinger. (2004). *Elastic Lidar: Theory, Practice and Analysis methods*. John Wiley & Sons.

Wallace, J. M., & Hobbs, P. V. (2006). *Atmospheric science: An introductory survey* (2nd ed). Elsevier Academic Press.

Wandinger, U., & Ansmann, A. (2002). Experimental determination of the lidar overlap profile with Raman lidar. *Applied Optics*, *41*(3), 511. https://doi.org/10.1364/AO.41.000511

Wang, D., Stachlewska, I. S., Delanoë, J., Ene, D., Song, X., & Schüttemeyer, D. (2020). Spatio-temporal discrimination of molecular, aerosol and cloud scattering and polarization using a combination of a Raman lidar, Doppler cloud radar and microwave radiometer. *Optics Express*, *28*(14), 20117. https://doi.org/10.1364/OE.393625

Warneke, C., Schwarz, J. P., Dibb, J., Kalashnikova, O., Frost, G., Al-Saad, J., Brown, S. S., Brewer, Wm. A., Soja, A., Seidel, F. C., Washenfelder, R. A., Wiggins, E. B., Moore, R. H., Anderson, B. E., Jordan, C., Yacovitch, T. I., Herndon, S. C., Liu, S., Kuwayama, T., … The FIREX-AQ Science Team. (2023). Fire Influence on Regional to Global Environments and Air Quality (FIREX-AQ). *Journal of Geophysical Research: Atmospheres*, *128*(2). https://doi.org/10.1029/2022JD037758

Wei, J., Li, Z., Peng, Y., & Sun, L. (2019). MODIS Collection 6.1 aerosol optical depth products over land and ocean: Validation and comparison. *Atmospheric Environment*, *201*, 428–440. https://doi.org/10.1016/j.atmosenv.2018.12.004

Weitkamp, C. (Ed.). (2005). *Lidar: Range-resolved optical remote sensing of the atmosphere*. Springer.

Welton, E. J., & Campbell, J. R. (2002). Micropulse Lidar Signals: Uncertainty Analysis. *Journal of Atmospheric and Oceanic Technology*, *19*(12), 2089–2094. https://doi.org/10.1175/1520-0426(2002)019<2089:MLSUA>2.0.CO;2

Welton, E. J., Campbell, J. R., Spinhirne, J. D., & Scott Iii, V. S. (2001). *Global monitoring of clouds and aerosols using a network of micropulse lidar systems* (U. N. Singh, T. Itabe, & N. Sugimoto, Eds.; p. 151). https://doi.org/10.1117/12.417040

Whiteman, C. D. (2000). *Mountain meteorology: Fundamentals and applications*. Oxford Univ. Press.

Winker, D. M., Vaughan, M. A., Omar, A., Hu, Y., Powell, K. A., Liu, Z., Hunt, W. H., & Young, S. A. (2009). Overview of the CALIPSO Mission and CALIOP Data Processing Algorithms. *Journal of Atmospheric and Oceanic Technology*, *26*(11), 2310–2323. https://doi.org/10.1175/2009JTECHA1281.1

Winker, D., Vaughan, M., & Hunt, B. (2006). *The CALIPSO mission and initial results from CALIOP* (U. N. Singh, T. Itabe, & D. N. Rao, Eds.; p. 640902). https://doi.org/10.1117/12.698003

Yang, P., & Liou, K. N. (1996). Geometric-optics–integral-equation method for light scattering by nonspherical ice crystals. *Applied Optics*, *35*(33), 6568. https://doi.org/10.1364/AO.35.006568

Yin, Z., Ansmann, A., Baars, H., Seifert, P., Engelmann, R., Radenz, M., Jimenez, C., Herzog, A., Ohneiser, K., Hanbuch, K., Blarel, L., Goloub, P., Dubois, G., Victori, S., & Maupin, F. (2019). Aerosol measurements with a shipborne Sun–sky–lunar photometer and collocated multiwavelength Raman polarization lidar over the Atlantic Ocean. *Atmospheric Measurement Techniques*, *12*(10), 5685–5698. https://doi.org/10.5194/amt-12-5685-2019

Young, A. T. (1994). Air mass and refraction. *Applied optics*, *33*(6), 1108-1110.

Young, S. A. (1995). Analysis of lidar backscatter profiles in optically thin clouds. *Applied Optics*, *34*(30), 7019. https://doi.org/10.1364/AO.34.007019

Zhang, J., Reid, J. S., & Holben, B. N. (2005). An analysis of potential cloud artifacts in MODIS over ocean aerosol optical thickness products. *Geophysical Research Letters*, *32*(15), 2005GL023254. https://doi.org/10.1029/2005GL023254

Zhang, Q., Ma, X., Tie, X., Huang, M., & Zhao, C. (2009). Vertical distributions of aerosols under different weather conditions: Analysis of in-situ aircraft measurements in Beijing, China. *Atmospheric Environment*, *43*(34), 5526–5535. https://doi.org/10.1016/j.atmosenv.2009.05.037

List of Tables

List of Figures

Abbreviations and Glossary

AR	Assessment Report
ABL	Atmospheric Boundary Layer
ACR	Attenuated Color Ratio
ACTRIS	Aerosol, Clouds and Trace gases Research InfraStructure
AEMET	Agencia Estatal de METeorologia
AERIS	Data Center, Atmosphere data and services hub
AERONET	AErosol Robotic NETwork
AGORA-Lab	LOA-CIMEL joint laboratory
AMARYLLIS-AMAGAS	oceanographic mission “From Amazon sediments to natural climate variability and slope instability processes”
AOD	Aerosol Optical Depth
APD	Avalanche PhotoDiode
ATOLL	ATmospheric Observatory of liLLe
BAE	Backscatter Angstrom Exponent
BASIC	LOA software for lidar retrievals in NRT
BC	Black Carbon
BW	Backward
CALIOP	Cloud-Aerosol Lidar with Orthogonal Polarization
CALIPSO	Cloud-Aerosol Lidar and Infrared Pathfinder Satellite Observations
CAL/VAL	Calibration Validation
CARS	Center for Aerosol Remote Sensing
ch532par	channel of 532 nm signal with parallel polarization
ch532per	channel of 532nm signal with perpendicular polarization

ch532tot	532 nm total signal
ch808par	channel of 808 nm signal with parallel polarization
ch808per	channel of 808 nm signal with perpendicular polarization
ch808tot	808 nm total signal
CR	Color Ratio
DEM	Digital Elevation Model
DMU	Dragon Mobile Unit
DOD	Dust Optical Depth
DRAGON	Distributed Regional Aerosol Gridded Observations Networks
EAE	Extinction Angstrom Exponent
EARLINET	European Aerosol Research LIdar Network
E-PROFILE	Automatic low power lidar European network
ERIC	European Research Infrastructure Consortium
FIREX-AQ	Fire Influence on Regional to Global Environments and Air Quality
FT	Free Troposphere
FW	Forward
GAW	Global Atmospheric Watch
GFSQ	Global Forecast System 0.25 degrees
GRASP	Generalized Retrieval of Atmosphere and Surface Properties
HSRL	High Spectral Resolution Lidar
HWP	Half Wave-Plate
HYSPLIT	Hybrid Single Particle Lagrangian Integrated Trajectory
IARC	Izaña Atmospheric Research Center
IPCC	Inter-Governmental Panel on Climate Change
IR	Infrared

IZO	Izaña Observatory
Lidar	Light Detection And Ranging
LILAS	LIlle Lidar AtmosphereS, operative at ATOLL
LOA	Laboratoire d'Optique Atmospherique
LR	Lidar Ratio, extinction to backscatter ratio
MAN	Maritime Aerosol Network
MAP-IO	Marion Dufresne Atmospheric Program – Indian Ocean
MBL	Marine Boundary Layer
METIS	CIMEL CE376 lidar operative at ATOLL
MODIS	Moderate Resolution Imaging Spectrometer
MPLNET	Micro-Pulse Lidar Network
NIR	Near infrared
NRT	Near Ral Time
OC	Organic Carbon
PBS	Polarizer BeamSplitter cube
PHOTONS	PHOtométrie pour le Traitement Opérationnel de Normalisation Satellitaire
PLASMA	Photomètre Léger Aéroporté pour la Surveillance des Masses d´Air
PLDR	Particle Linear Depolarization Ratio
PM	Particulate Matter
POLIPHON	POlarisation LIdar PHOtometer Networking
QC	Quality Control
RCS	Range Corrected Signal
SAMUM	Saharan Mineral dUst ExperiMent
SD	Standard Deviation

SDS-WAS	Sand and Dust Storm Warning Advisory and Assessment System
SE	Standard Error
SHADOW	SaHAran Dust Over West Africa
SNR	Signal to Noise Ratio
SRTM	Shuttle Radar Topography Mission
SSA	Single Scattering Albedo
TOA	Top Of Atmosphere
TRANSAMA	TRANSit to AMAGAS-AMARYLLIS campaign
TROPOMI	TROPOspheric Monitoring Instrument
VLDR	Volume Linear Depolarization Ratio
VolcPlum	interactive portal for volcano monitoring
VSD	Volume Size Distribution
WFF	William Flats Fire
WHO	World Health Organization
WMO	World Meteorological Organization

Appendix A

The following pages contain the research article published in the Atmospheric Measurements Techniques (AMT) journal.

Sanchez Barrero, M. F., Popovici, I. E., Goloub, P., Victori, S., Hu, Q., Torres, B., Podvin, T., Blarel, L., Dubois, G., Ducos, F., Bourrianne, E., Lapionak, A., Proniewski, L., Holben, B., Giles, D. M., and LaRosa, A.: Enhancing mobile aerosol monitoring with CE376 dual-wavelength depolarization lidar, Atmos. Meas. Tech., 17, 3121–3146, https://doi.org/10.5194/amt-17-3121-2024, 2024.

Atmos. Meas. Tech., 17, 3121–3146, 2024
https://doi.org/10.5194/amt-17-3121-2024
© Author(s) 2024. This work is distributed under
the Creative Commons Attribution 4.0 License.

Atmospheric Measurement Techniques
Open Access

Enhancing mobile aerosol monitoring with CE376 dual-wavelength depolarization lidar

Maria Fernanda Sanchez Barrero[1,2], Ioana Elisabeta Popovici[1,2], Philippe Goloub[1], Stephane Victori[2], Qiaoyun Hu[1], Benjamin Torres[1], Thierry Podvin[1], Luc Blarel[1], Gaël Dubois[1], Fabrice Ducos[1], Eric Bourrianne[1], Aliaksandr Lapionak[1], Lelia Proniewski[2], Brent Holben[3], David Matthew Giles[3,4], and Anthony LaRosa[3,4]

[1]UMR8518 – LOA – Laboratoire d'Optique Atmosphérique, Centre National de la Recherche Scientifique (CNRS), University of Lille, 59000 Lille, France
[2]R&D Department, Cimel Electronique, 75011 Paris, France
[3]Goddard Space Flight Center-NASA, Greenbelt, MD 20771, USA
[4]Science Systems and Applications, Inc., Lanham, MD 20706, USA

Correspondence: Maria Fernanda Sanchez Barrero (mariafernanda.sanchezbarrero@univ-lille.fr)

Received: 2 November 2023 – Discussion started: 21 November 2023
Revised: 13 March 2024 – Accepted: 28 March 2024 – Published: 24 May 2024

Abstract. We present the capabilities of a compact dual-wavelength depolarization lidar to assess the spatiotemporal variations in aerosol properties aboard moving vectors. Our approach involves coupling the lightweight Cimel CE376 lidar, which provides measurements at 532 and 808 nm and depolarization at 532 nm, with a photometer to monitor aerosol properties. The assessments, both algorithmic and instrumental, were conducted at ATOLL (ATmospheric Observatory of LiLle) platform operated by the Laboratoire d'Optique Atmosphérique (LOA), in Lille, France. An early version of the CE376 lidar co-located with the CE318-T photometer and with a multi-wavelength Raman lidar were considered for comparisons and validation. We developed a modified Klett inversion method for simultaneous two-wavelength elastic lidar and photometer measurements. Using this setup, we characterized aerosols during two distinct events of Saharan dust and dust smoke aerosols transported over Lille in spring 2021 and summer 2022. For validation purposes, comparisons against the Raman lidar were performed, demonstrating good agreement in aerosol properties with relative differences of up to 12 % in the depolarization measurements. Moreover, a first dataset of CE376 lidar and photometer performing on-road measurements was obtained during the FIREX-AQ (Fire Influence on Regional to Global Environments and Air Quality) field campaign deployed in summer 2019 over the northwestern USA. By lidar and photometer mapping in 3D, we investigated the transport of released smoke from active fire spots at William Flats (northeast WA, USA). Despite extreme environmental conditions, our study enabled the investigation of aerosol optical properties near the fire source, distinguishing the influence of diffuse, convective, and residual smoke. Backscatter, extinction profiles, and column-integrated lidar ratios at 532 and 808 nm were derived for a quality-assured dataset. Additionally, the extinction Ångström exponent (EAE), color ratio (CR), attenuated color ratio (ACR), and particle linear depolarization ratio (PLDR) were derived. In this study, we discuss the capabilities (and limitations) of the CE376 lidar in bridging observational gaps in aerosol monitoring, providing valuable insights for future research in this field.

1 Introduction

Improving knowledge of the spatiotemporal distribution of aerosols and their local, regional, and global impact, as well as reducing the uncertainties in the aerosol properties, is fundamental to quantify their radiative impacts (Boucher et al., 2013). Thus, following aerosol transport from the emission sources and evaluating of their complex horizontal and vertical distribution are therefore needed. Negative effects on human health and the economy are attributed to aerosols as well, increasing the demand for continuous air quality control to develop early-warning systems as more frequent and

Published by Copernicus Publications on behalf of the European Geosciences Union.

extreme environmental events are detected (Papagiannopoulos et al., 2020; Seneviratne et al., 2021). Photometer and lidar instruments are convenient tools to assess aerosol properties and their impact on climate. To this end, the development of networks plays a key role in aerosol monitoring. Some examples are the AERONET network (AErosol RObotic NETwork; Holben et al., 1998) for photometers; EARLINET (European Aerosol Research Lidar Network; Pappalardo et al., 2014; Sicard et al., 2015), now part of ACTRIS ERIC (Aerosol, Clouds and Trace gases Research Infrastructure; European Research Infrastructure Consortium), for Raman lidars; and MPLNet (Micro-Pulse Lidar Network; Welton et al., 2001) for micro-pulse lidars. Studies conducted with multiple network sites allowed the assessment of the variability in the aerosol properties at a regional level, like dust outbreaks (Ansmann et al., 2003; Papayannis et al., 2008; López-Cayuela et al., 2023) or long-range transport of biomass burning smoke episodes (Nicolae et al., 2013; Adam et al., 2020). However, instruments at fixed sites are restricted by their local conditions and position with respect to the aerosol sources. Furthermore, some regions that are difficult to access, such as oceans or mountains, remain unexplored. Thus, the deployment of mobile laboratories (aboard ship cruises and airplanes or in cars) provided a solution to fill these observational gaps in networks (Smirnov et al., 2009; Tesche et al., 2009; Müller et al., 2014; Bohlmann et al., 2018; Popovici et al., 2018; Yin et al., 2019).

In recent years, the multispectral Sun–sky–lunar Cimel CE318-T photometer (Barreto et al., 2016), widely used in AERONET sites and designed by the Cimel company, has been fully adapted for automatic Sun or lunar tracking during movement aboard ships (Yin et al., 2019). The ship-borne CE318-T photometer is operational and has continuously provided aerosol optical depth (AOD) data since January 2021 aboard the *Marion Dufresne* research vessel in the framework of the MAP-IO (*Marion Dufresne* Atmospheric Program Indian Ocean). Likewise, the PLASMA (Photomètre Léger Aéroporté pour la Surveillance des Masses d'Air; Karol et al., 2013) photometer was developed exclusively to track the Sun in movement and has been deployed aboard aircraft and vehicles during field campaigns (Popovici, 2018; Popovici et al., 2018, 2022; Hu et al., 2019; Mascaut et al., 2022). The ship-borne CE318-T and PLASMA photometers have been adapted and developed, respectively, in the framework of AGORA-LAB, a common Laboratoire d'Optique Atmosphérique (LOA)/Cimel laboratory (https://www.agora-lab.fr/, last access: 24 October 2023).

Lidar systems are mostly large and complex and require considerable space, regular maintenance, and controlled operational conditions. Upgrades for mobile applications are frequently linked to instrumental modifications and/or the creation of adapted laboratory platforms or transportable containers. Examples are the multiwavelength Polly^{XT} lidars, within the network PollyNET (Althausen et al., 2013; Engelmann et al., 2016), set up in temperature-controlled containers for 24/7 operation, and the micro-pulse lidars from MPLNet, which are automatic and compact systems that can be easily transported. Studies conducted with lidars aboard mobile vectors showed the possibilities of supporting satellite-based observations (Burton et al., 2013; Warneke et al., 2023) and air quality assessment in urban–rural transitions and complex topographies (Royer et al., 2011; Pal et al., 2012; Dieudonné et al., 2015; Shang et al., 2018; Popovici, 2018; Popovici et al., 2022; Chazette and Totems, 2023). Hence, a description of a compact and light mobile system, which integrated a lidar and a Sun photometer was first presented by Popovici et al. (2018). This unique system, deployed by LOA, included the Cimel CE370 mono-wavelength elastic lidar and the PLASMA Sun photometer. For several field campaigns, the integrated system performed on-road mobile measurements (Popovici et al., 2018, 2022), showing the versatility of such a system for aerosol characterization. For that reason, we propose the newest model of Cimel lightweight lidar, the CE376 dual-wavelength lidar, for the enhancement of aerosol properties.

The CE376 lidar measures attenuated backscatter profiles at 532 and 808 nm and depolarization at 532 nm. Algorithmic and instrumental assessment took place at the ATOLL (ATmospheric Observatory of LiLle) platform. METIS, an early version of the CE376 lidar, has been continuously performing observations since 2019. In addition, METIS is co-located with a CE318-T photometer and with a high-power multi-wavelength Raman lidar, LILAS (LIlle Lidar AtmosphereS), part of ACTRIS ERIC, which are also considered for comparison and validation. Multiple studies performed on simultaneous two-wavelength lidar measurements proposed inversion schemes by establishing a constant ratio between wavelengths, and/or requiring the aerosol extinction-to-backscatter ratios, i.e., the lidar ratio (LR), to be known a priori and constant (Potter, 1987; Ackermann, 1997, 1999; Kunz, 1999; Vaughan, 2004; Lu et al., 2011). Therefore, we propose an inversion scheme with a two-wavelength modified Klett inversion, using AOD and the extinction Ångström exponent (EAE) from the photometer to constrain the retrievals. Both forms of the Klett solution, backward and forward integration (Weitkamp, 2005), are used according to detection limits at each wavelength. Profiles of the EAE, color ratio (CR), and particle linear depolarization ratio (PLDR) are derived later. In addition, the attenuated total backscatter and attenuated color ratio (ACR) are derived directly from the measurements. Moreover, the aerosol retrievals are validated through comparison with LILAS Raman lidar, and we establish the reliability of our results. Our study not only outlines the findings but also discusses the limitations and future implications of our approach.

A first dataset of co-located CE376 lidar and photometer mobile observations has been obtained during the FIREX-AQ (Fire Influence on Regional to Global Environments and Air Quality) field campaign organized over the northwestern US in summer 2019 (Warneke et al., 2018). This campaign, led by NASA and NOAA, focused on investigating the chemistry and transport of smoke from wildfires and agricultural burning, in addition to the multiple in situ instruments deployed in fixed platforms around the region and aboard aircraft (Warneke et al., 2023). Remote sensing instruments were installed in both stationary and mobile DRAGON payloads (Distributed Regional Aerosol Gridded Observations Networks; Holben et al., 2018). Thus, two mobile platforms (two sport utility vehicles, SUVs) called DMU-1 and DMU-2 (Dragon Mobile Unit) were equipped with lidars and photometers. The dual-wavelength CE376 lidar and ship-borne CE318-T photometer were installed aboard DMU-1, and the mono-wavelength CE370 lidar and PLASMA photometer were installed on board DMU-2. Both DMUs performed on-road mobile observations around major fire sources and were able to follow the smoke plumes. Height-resolved optical properties of fresh smoke aerosols close to active fire sources were derived despite extreme environmental conditions (e.g., hot and dry ambient temperatures), which limited the performance of the instruments. Hence, in this work, we present aerosol properties mapped for selected case studies during the William Flats fire in northeastern Washington State. Both DMU-1 and DMU-2 are considered for the analysis. Notably, our study provides 3D mapping and the temporal evolution of aerosol properties, showcasing the relevance of coupling the CE376 lidar and CE318-T photometer during this measurement campaign.

The main objective of this work is to show the capabilities of a compact dual-wavelength depolarization lidar to assess the spatiotemporal distribution of aerosol properties, particularly when it is aboard moving vectors and co-located with a photometer. Thus, we explore both capabilities and limitations of CE376 in detail, demonstrating how our study contributes to filling observational gaps within aerosol monitoring networks. This paper is organized as follows. The description of the instruments used is presented in Sect. 2. An extensive description of the methodology applied to derive aerosol properties, using the two-wavelength depolarization lidar and photometer, is presented in Sect. 3. The result section is divided in two parts; Sect. 4 provides the outcomes of the algorithmic and instrumental assessments that occurred at Lille, France. We present two case studies for events of dust and dust–smoke transported over Lille and the validation of aerosol retrievals with comparisons against a Raman lidar. Section 5 shows 3D mapping and the temporal evolution of aerosol properties using the dual-wavelength CE376 lidar and the CE318-T photometer mobile observations for the first time. Case studies from the FIREX-AQ campaign present the optical properties of fresh smoke aerosols close to the source. Finally, Sect. 6 summarizes the results and presents the conclusions and perspectives of this work. The instrumental algorithmic limitations and the uncertainties are discussed throughout the different sections.

2 Remote sensing instrumentation

This section is dedicated to the description of the mobile remote sensing instruments used in this study. Section 2.1 presents the new Cimel CE376 lidar with up to two wavelengths and depolarization channels. Section 2.2 describes the two photometers that were integrated to mobile systems to derive aerosols optical properties.

2.1 Lidars

The CE370 lidar is an eye-safe micro-pulse lidar (Pelon et al., 2008; Mortier et al., 2013; Popovici et al., 2018) operating at 532 nm with 20 µJ pulse energy at 4.7 kHz repetition rate (Table 1). The CE370 is designed with a shared transmitter–receiver telescope connected through a 10 m optical fiber to the control and acquisition system. The backscattered signal is detected by photon counting with an avalanche photodiode (APD). The CE370 lidar was designed by Cimel Electronique to monitor aerosol and cloud properties up to 15–20 km, with a vertical resolution of 15 m. For several field campaigns, the CE370 lidar that embarked on mobile platforms has demonstrated the viability to characterize vertical aerosol properties in movement (Popovici et al., 2018, 2022). Therefore, the latest lidar model, CE376, operable up to two wavelengths, is proposed to replace the CE370 lidar and continue the developments towards mobile aerosol monitoring (https://www.cimel.fr/solutions/ce376/, last access: 24 October 2023). In comparison to the CE370, the CE376 lidar is designed to support up to two wavelengths and depolarization measurements within different model configurations (G is for green; GP is for green polarized; GPN is for green polarized near-infrared; N is for near-infrared). In this study, we use the CE376 GPN (green polarized near-infrared) model that is described as follows.

The CE376 GPN lidar is an autonomous, lightweight, and compact micro-pulse lidar. The lidar operates at two wavelengths, 532 and 808 nm, with 5–10 and 3–5 µJ pulse energy, respectively, at a repetition rate of 4.7 kHz (Table 1). Measurements of elastic backscattered light at both wavelengths and depolarization at 532 nm are acquired. For both systems used in this work (METIS and FIREX-AQ), the laser source at 532 nm has been replaced with one of a higher pulse energy (not eye-safe) to increase the signal-to-noise ratio (SNR). The emission–reception design consists of two Galilean telescopes in a biaxial configuration. The simplified 2D layout of the lidar system is presented in Fig. 1. Light pulses at 532 nm from a frequency-doubled Nd:YAG laser source are transmitted through an arrangement of dichroic mirrors and collimation lenses on the green emission system. Similarly, a simplified optical system including a pulsed narrow bandpass laser diode source (manufactured by DILAS laser diodes; now coherent), optical fiber, and collimation lenses emits light pulses in the near-infrared (NIR) at 808 nm (linewidth 0.4 nm). The elastic backscattered light

Table 1. System specifications for the mobile lidars.

	Cimel CE370[a]	Cimel CE376 GPN	
Wavelength	532 nm	532 nm	808 nm
Laser source	Frequency doubled Nd : YAG	Frequency doubled Nd : YAG	Pulsed laser diode
Pulse energy	20 uJ	5–10 uJ (15–20 µJ)[b]	3–5 uJ
Repetition rate (pulse width)	4.7 kHz (20 ns)	4.7 kHz (20 ns)	4.7 kHz (186 ns)
Emission/reception (E/R)	Coaxial	Biaxial	Biaxial
Telescope (E/R)	Galilean	Galilean	Galilean
Diameter (E/R)	200 mm	100 mm/100 mm	100 mm/100 mm
Half field of view (E/R)	55 µrad	100 µrad/120 µrad	240 µrad/330 µrad
Depolarization	No	Yes	No

[a] Cimel CE370 is no longer commercially available. [b] Systems used in this work had higher pulse energy.

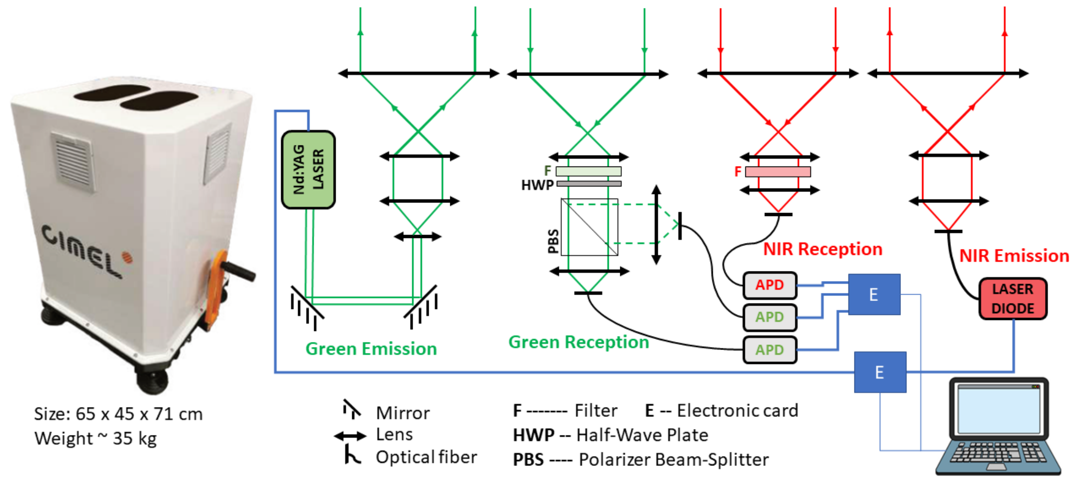

Figure 1. CE376 GPN lidar and its 2D design. The optical design of the biaxial systems at 532 nm (green emission/reception) and 808 nm (NIR emission/reception) and layout of the control/acquisition system through electronic cards are shown in a simplified plan. Source: https://www.cimel.fr/solutions/ce376/ (last access: 21 November 2023).

is collected, collimated, and filtered in the reception at each emitted wavelength and detected with APDs in photon counting mode. Electronic cards developed by Cimel communicate with the control and acquisition software.

Linear depolarization measurements at 532 nm are also acquired by separation in the parallel (co-polarized) and perpendicular (cross-polarized) components of the backscattered light using a polarizing beam-splitter cube (PBS) in the reception. The PBS is a Thorlabs CCM1-PBS25-532 device with reflectivities R_p and R_s and transmittances T_p and T_s (subscripts p and s for parallel and perpendicular polarized light with respect to the PBS incident plane). A manually rotating mount with half-wave plate (HWP) in front of the PBS controls the polarization angle of the incident light with a precision of 2°. Measured signals behind the PBS on the reflected and transmitted branches are named parallel (//) or perpendicular (⊥), according to the reception configuration. More details on the depolarization measurements can be found in Sect. 3.1.1.

For mobile applications, the CE376 lidar is coupled with a GPS module to derive the exact position during measurements. The integration of the geolocation and lidar observations is accounted for in the data pre-processing, as described in Sect. 3.1.2.

2.2 Photometers

The Cimel CE318-T photometer has been adapted for mobile applications. The PLASMA photometer has been developed exclusively for mobile observations. Both instruments follow and meet the AERONET standards and are included in automatic data processing chains. Therefore, automatic near-real time (NRT) aerosol properties are retrieved (https://aeronet.gsfc.nasa.gov/, last access: 23 October 2023) without cloud screening as data level 1.0 and with cloud screening as data level 1.5. It is important to note that AERONET cloud screening was formulated for stationary instruments, and some additional uncertainty in the cloud screening technique may either identify thin clouds as aerosols, or vice versa, especially in the presence of smoke or dust plumes. Furthermore, cirrus cloud screening employed by AERONET Version 3 may be further limited (Giles et al., 2019). After calibration, quality-assured data at level 2.0 are also acquired (Smirnov et al., 2000; Giles et al., 2019). In this work, data level 2.0 is used for stationary measurements (Sect. 4), and data level 1.5 is used for mobile measurements (Sect. 5). Both photometers are used in this work and are briefly described below.

The Sun–sky–lunar Cimel CE318-T photometer developed by Cimel Electronique (Barreto et al., 2016) performs both daytime and nighttime observations. Direct solar/lunar measurements are collected automatically through nine channels (340, 380, 440, 500, 670, 870, 936, 1020, and 1640 nm), deriving spectral AOD with an accuracy of 0.01. EAE is determined by pairs of AOD values at different wavelengths, providing information on the size distribution of aerosols (Kusmierczyk-Michulec, 2002). Moreover, multi-angular sky radiance measurements are acquired in the almucantar plane during daytime. Aerosol microphysical properties, such as the volume size distribution (VSD), complex refractive index, and single-scattering albedo can be also derived through inversion procedures (Dubovik and King, 2000). In the last few years, the photometer has been adapted for mobile measurements aboard cruise ships to cover oceans. The ship-borne CE318-T described by Yin et al. (2019) and developed at LOA, in the framework of AGORA-Lab, enables AOD acquisition during movement. The system is coupled with a compass and GPS modules, obtaining information on the date, time, geolocation, heading, pitch, and roll to target the Sun/Moon continuously. With the help of an accelerated tracking feedback loop, the system switches to its regular tracking mode to improve measurement quality. Downward sky radiances are also measured with additional information (from GPS and a compass) for each almucantar angle to have accurate knowledge of the observation geometry. The ship-borne CE318-T has been operational and continuously measuring since January 2021 on board the *Marion Dufresne* research vessel, as part of MAP-IO (*Marion Dufresne* Atmospheric Program – Indian Ocean) project (http://www.mapio.re, last access: 9 October 2023). Likewise, a second instrument with upgraded software has been installed, and it has been performing measurements since April 2023 aboard *Marion Dufresne*. In this paper, we will show the integration of the CE318-T photometer and CE376 lidar with measurements at a fixed location (Sect. 4) and for the first time on board a car during FIREX-AQ campaign (Sect. 5).

The sun-tracking photometer, PLASMA, developed by LOA and SNO/PHOTONS, has the capability of performing direct solar radiation measurements during movement. The instrument is easy to set up and transport due to its light and compact design ($\sim$5 kg and 23 cm height). PLASMA has nine spectral channels at 339, 379, 440, 500, 674, 870, 1019, and 1643 nm and 937 nm for water vapor measurements. Spectral AOD with an accuracy of 0.01 and EAE are derived from the direct solar radiation measurements (Karol et al., 2013). A more detailed description of the instrument and its application to airborne measurements are presented by Karol et al. (2013). PLASMA, on board an aircraft during AEROMARINE field campaign at Réunion island (Mascaut et al., 2022), shows the alternative use of the instrument to obtain AOD and EAE vertical profiles during the aircraft's ascendent/descendent trajectories. The integration of PLASMA and CE370 lidar performing on-road mobile measurements (Popovici et al., 2018, 2022; Hu et al., 2019) has been carried out during several campaigns. Likewise, PLASMA and CE370 lidar were coupled to perform mobile measurements during the FIREX-AQ campaign (Sect. 5).

3 Methodology

In this article, we describe extensively the methodology applied to derive aerosol optical properties from measurements of the CE376 GPN lidar, simply named CE376 hereafter. Detailed descriptions of the methods and corrections applied to the mono-wavelength CE370 lidar can be found in previous works (Pelon et al., 2008; Mortier et al., 2013; Popovici et al., 2018). For this study, two early versions of CE376 are used, with one performing continuous observations at Lille, France, and the other installed on board a mobile platform during the FIREX-AQ field campaign. Data treatment and quality assurance for both types of measurements, a fixed location, and an on-board mobile platform follow the same steps, with exceptions mainly for the determination of molecular contributions.

In this section, details from pre-processing to aerosol optical property retrievals are presented. Section 3.1 describes the atmospheric parameters derived directly from the observations. The volume linear depolarization ratio (VLDR) is described in Sect. 3.1.1. The total attenuated backscatter is described in Sect. 3.1.2, and the ACR definition is presented in Sect. 3.1.3. Section 3.2 presents the inversion methods applied to obtain aerosol optical properties. The methodology described below is summarized with a block diagram in Fig. 2, showing the atmospheric optical properties derived from the CE376 and CE318-T measurements.

3.1 Lidar data processing

The light backscattered by molecules and aerosols at a distance$r$ from the lidar is collected by a telescope and detected by photon counting with an APD. Considering the lidar equation (Kovalev and Eichinger, 2004; Weitkamp, 2005), the detected elastic backscattered signal can be described as Eq. (1).

$$\mathrm{RCS}(\lambda,r) = C_{\mathrm{L},\lambda}[\beta_{\mathrm{m}}(\lambda,r)+\beta_{\mathrm{a}}(\lambda,r)] \times T^2_{\mathrm{m}}(\lambda,r)T^2_{\mathrm{a}}(\lambda,r) \quad (1)$$

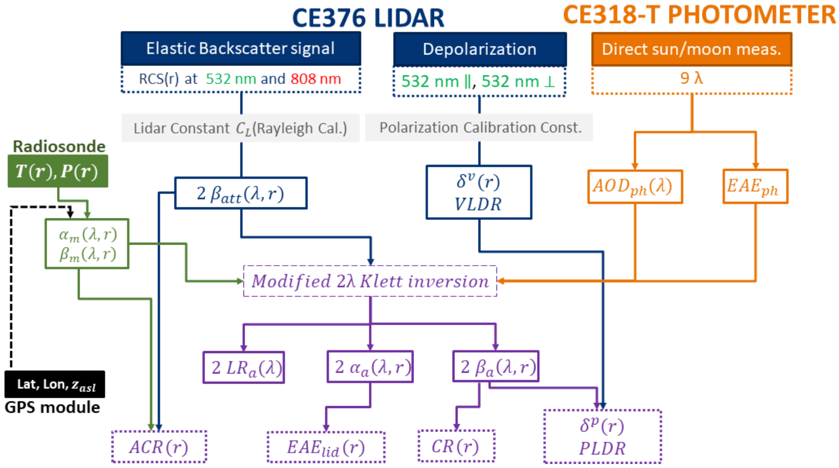

Figure 2. Block diagram of the methodology combining measurements from the CE376 lidar and CE318-T photometer.

$$T_{\mathrm{m}}^2(\lambda,r)T_{\mathrm{a}}^2(\lambda,r) = \exp\left(-2\int_0^r \alpha_{\mathrm{m}}(\lambda,r')\mathrm{d}r'\right) \times \exp\left(-2\int_0^r \alpha_{\mathrm{a}}(\lambda,r')\mathrm{d}r'\right) \quad (2)$$

The range-corrected signal (RCS) ($\mathrm{Ph\,s^{-1}\,m^2}$) is the detected signal after background, range dependence (r^2), and overlap $O(r)$ corrections. RCS profiles are obtained for each detection channel of the CE376, i.e., for co- (parallel) and cross-polarized (perpendicular) signals at 532 nm, $\mathrm{RCS}(532//,r)$ and $\mathrm{RCS}(532\perp,r)$, respectively, and total signal at 808 nm, $\mathrm{RCS}(808,r)$. The right-hand side of Eq. (1) is therefore described only in terms of atmospheric optical properties correlated to the measured signal RCS through a calibration constant $C_{\mathrm{L},\lambda}$ (in $\mathrm{Ph\,s^{-1}\,m^3\,sr}$). The term $\beta(r)$ is the backscatter coefficient ($\mathrm{m^{-1}\,sr^{-1}}$). $T^2(\lambda,r)$ is the non-dimensional two-way atmospheric transmittance defined in Eq. (2), where $\alpha(r)$ is the extinction coefficient ($\mathrm{m^{-1}}$). Subscripts m and a represent contributions of molecules and aerosols, respectively. Background noise and overlap corrections at each detection channel are applied in the same way as for CE370 lidar and are described in previous works (Pelon et al., 2008; Mortier et al., 2013; Popovici et al., 2018).

The integral $\int_0^r \alpha_{\mathrm{a}}(\lambda,r')\mathrm{d}r'$ in Eq. (2) is also known as AOD, and it is directly measured by photometer for the total atmospheric column. Therefore, hereafter subscripts ph and lid will be used to differentiate optical properties from photometer and lidar, respectively. The $\mathrm{AOD_{ph}}$ for the lidar wavelengths, 532 and 808 nm, are interpolated by following the Ångström law using $\mathrm{AOD_{ph}}$ at 440 nm and $\mathrm{EAE_{ph}}$ (440/870 nm).

The main sources of uncertainties in the RCS profiles come from the overlap correction in the lower troposphere and from the background irradiance in the higher atmosphere (Sassen and Dodd, 1982; Welton and Campbell, 2002; Guerrero-Rascado et al., 2010; Popovici et al., 2018; Sicard et al., 2020; Córdoba-Jabonero et al., 2021). For RCS at 532 nm from both CE376 systems used in this work, considerable underestimations in the incomplete overlap region (< 2.5 km) are observed for temperatures below 17 °C and above 35 °C, adding an error into the lower range of the profiles. The profiles $\mathrm{RCS}(532\perp,r)$ and $\mathrm{RCS}(808,r)$ are the most affected by the solar background, reducing the detection limits by day. The relative error induced by the APD in photon counting mode is less than 5 %.

For mobile observations, a GPS module is coupled to the CE376 lidar. The geolocation is measured with high temporal resolution (1 s). For each RCS profile, we determine its latitude, longitude, and altitude above sea level (a.s.l.) by comparing recorded times for both GPS and lidar. We derive the velocity of the mobile platform from the geolocation and time to flag the stationary and mobile measurements for further analysis. In Sect. 5, case studies of mobile observations within a complex topography are presented. Thus, we paid special attention to pairing the geolocation and RCS profiles to properly assess the complexity of the terrain.

3.1.1 Volume linear depolarization ratio

The total RCS and VLDR, $\delta^{\mathrm{v}}(r)$, at 532 nm are derived following the methods described by Freudenthaler et al. (2009). Rotating the HWP, the angle φ between the plane of polarization of the laser and the incident plane of the PBS can be changed for two arrangements ($\varphi = 0$ or 90°). For commercial PBS cubes ($R_{\mathrm{s}} > R_{\mathrm{p}}$ and $T_{\mathrm{p}} > T_{\mathrm{s}}$), the system configuration at $\varphi = 0°$ is defined when the parallel polarized signal is measured in the transmitted branch of the PBS. Moreover, to reduce noise and errors from cross-talk effects, the configuration $\varphi = 90°$ can be also considered. The relative amplification factor V^* is calculated using the $\pm 45°$ calibration

(Freudenthaler et al., 2009) under cloud-free and stable atmospheric conditions.

The HWP rotates the angle of the incident polarization plane φ by means of 2θ with a θ precision of 2°. The error induced by the uncertainty in φ represents less than 5 % of the error in V^* for VLDR values up to 0.3 (Fig. 2; Freudenthaler et al., 2009). Moreover, to improve depolarization measurements, wire grid polarizers can be added to the PBS to reduce the cross-talk. However, additional errors during the calibration and in regular measurements can come from polarizing optical components that need detailed characterization (Freudenthaler, 2016) and which are not considered in this work. For current versions of the CE376, a motorized PBS mount is integrated.

3.1.2 Total attenuated backscatter

For quality assurance of lidar profiles, we follow the standard Rayleigh fit procedure (Freudenthaler et al., 2018), meaning that we normalize $\mathrm{RCS}(\lambda, r)$ to the molecular profile $\beta_\mathrm{m}(\lambda, r)T_\mathrm{m}^2(\lambda, r)$ at a distance r_ref, where we assume a free-aerosol zone, i.e., $\beta_\mathrm{a}(\lambda, r_\mathrm{ref}) = 0$. The molecular backscatter coefficients $\beta_\mathrm{m}(\lambda, r)$ and the two-way molecular transmittance $T_\mathrm{m}^2(\lambda, r)$ are calculated using the pressure and temperature profiles from standard atmosphere models or from available radiosonde data. This method is recurrently applied to signals from each channel of the CE376, especially during night time when SNR is higher. Moreover, we use the same considerations to determine the calibration constant $C_{\mathrm{L},\lambda}$ for total signals $\mathrm{RCS}(532, r)$ and $\mathrm{RCS}(808, r)$. Hence, Eq. (3) can be derived from Eq. (1).

$$C_{\mathrm{L},\lambda} = \mathrm{RCS}(\lambda, r_\mathrm{ref}) \Big/ \left[\beta_\mathrm{m}(\lambda, r_\mathrm{ref})T_\mathrm{m}^2(\lambda, r_\mathrm{ref})T_\mathrm{a}^2(\lambda, r_\mathrm{ref})\right] \quad (3)$$

The aerosol transmittance term $T_\mathrm{a}^2(\lambda, r_\mathrm{ref})$ can be calculated if $\mathrm{AOD_{ph}}$ is available. Assuming that no aerosols are present above r_ref, we have $T_\mathrm{a}^2(\lambda, r_\mathrm{ref}) = \exp(-2\mathrm{AOD_{ph}}(\lambda))$. If there are no changes in the lidar system configuration, the $C_{\mathrm{L},\lambda}$ stability over time is mainly controlled by the laser energy and the opto-mechanical stability. Then the total attenuated backscatter $\beta_\mathrm{att}(\lambda, r)$ is defined by Eq. (4).

$$\beta_\mathrm{att}(\lambda, r) = \mathrm{RCS}(\lambda, r)/C_{\mathrm{L},\lambda} \quad (4)$$

3.1.3 Attenuated color ratio

The CR, defined as the ratio of aerosol backscatter at two different wavelengths, has been used to discriminate clouds from aerosol layers and eventually for aerosol-typing (Omar et al., 2009; Burton et al., 2013; Wang et al., 2020; Qi et al., 2021). In particular, CALIPSO (Cloud–Aerosol Lidar and Infrared Pathfinder Satellite Observation) algorithms use the layer mean total attenuated backscatter as a first approximation of the aerosol backscatter $\overline{\beta}_\mathrm{att} = [1/(r_\mathrm{top} - r_\mathrm{base})]\int_\mathrm{base}^\mathrm{top}\beta_\mathrm{att}(r')\mathrm{d}r'$ and define the layer-integrated attenuated color ratio as $\chi' = \overline{\beta}_\mathrm{att}(1064)/\overline{\beta}_\mathrm{att}(532)$. Then both layer-integrated features are used for the classification of stratospheric aerosols (Vaughan et al., 2004; Omar et al., 2009; Kim et al., 2018). Similarly, the attenuated total backscatter corrected by the two-way molecular transmittance term is considered a first approximation of the aerosol backscatter. Therefore, the ACR for all the ranges is defined by Eq. (5).

$$\begin{aligned}\mathrm{ACR}(r) &= \frac{\beta_\mathrm{att}(808, r)T_\mathrm{m}^{-2}(808, r)}{\beta_\mathrm{att}(532, r)T_\mathrm{m}^{-2}(532, r)} \\ &= \frac{[\beta_\mathrm{m}(808, r) + \beta_\mathrm{a}(808, r)]}{[\beta_\mathrm{m}(532, r) + \beta_\mathrm{a}(532, r)]} \\ &\quad \times \exp\left(-2\int_0^r [\alpha_\mathrm{a}(808, r') - \alpha_\mathrm{a}(532, r')]\mathrm{d}r'\right) \quad (5)\end{aligned}$$

The ACR contains information of molecules and aerosols and mostly provides insights into the aerosol size. For a purely molecular atmosphere, the ACR is reduced to the ratio of molecular backscatter coefficients and ACR ~ 0.19. Clouds are generally composed of large particles, compared to the lidar wavelengths, so the backscatter and extinction coefficients are not expected to show spectral variation. Therefore, ACR values for clouds are likely to be close to 1. Assuming that only one type of aerosol is present and homogeneously distributed in the atmospheric column, the exponential term goes nearly constant, and the ACR is controlled by the ratio $\beta_\mathrm{a}(808, r)/\beta_\mathrm{a}(532, r)$. Under this rough assumption, ACR values for aerosols are between 0 and 1, with low values for fine aerosols and close to 1 for large particles.

3.2 Aerosol optical properties

By solving the Eq. (1) and assuming a constant LR, we derive $\beta_\mathrm{a}(\lambda, r)$, as in Eq. (6) (Weitkamp, 2005), which is well-known as Klett solution (Klett, 1985). A constant extinction-to-backscatter ratio of $8\pi/3\,\mathrm{sr}$ for molecules at all wavelengths is considered. For mobile measurements, we also consider surface altitude (a.s.l.) for each RCS profile to model correctly the molecular profiles, $\beta_\mathrm{m}(\lambda, r)$ and $\alpha_\mathrm{m}(\lambda r)$.

$$\beta_\mathrm{a}(\lambda, r) = \frac{\mathrm{RCS}(\lambda, r) \times \exp\left[-2(\mathrm{LR}(\lambda) - 8\pi/3) \times \int_{r_\mathrm{b}}^{r} \beta_\mathrm{m}(\lambda, r')\mathrm{d}r'\right]}{\frac{\mathrm{RCS}(\lambda, r_\mathrm{b})}{\beta_\mathrm{a}(\lambda, r_\mathrm{b}) + \beta_\mathrm{m}(\lambda, r_\mathrm{b})} - 2\mathrm{LR}(\lambda)\int_{r_\mathrm{b}}^{r} \mathrm{RCS}(\lambda, r') \times \exp\left[-2(\mathrm{LR}(\lambda) - 8\pi/3) \times \int_{r_\mathrm{b}}^{r'} \beta_\mathrm{m}(\lambda, r'')\mathrm{d}r''\right]\mathrm{d}r'} - \beta_\mathrm{m}(\lambda, r) \quad (6)$$

The boundary conditions are given by the position of r_b, and therefore, two forms of the Klett solution are specified. The far end with backward integration given by $r_\mathrm{b} = r_\mathrm{ref}$ is well known as the backward (BW) solution and takes the same considerations as for the Rayleigh fit (Sect. 3.1.2). It is the most used form of the Klett solution, but it has an obvious difficulty when defining r_ref. The near-end solution with a forward integration or forward (FW) solution is given by $r_\mathrm{b} = r_\mathrm{o}$, where r_o is close to the ground. Thus, the total backscatter is $\beta_\mathrm{a}(\lambda, r_\mathrm{o}) + \beta_\mathrm{m}(\lambda, r_\mathrm{o}) = \beta_\mathrm{att}(\lambda, r_\mathrm{o})/T^2_\mathrm{m}(\lambda, r_\mathrm{o})T^2_\mathrm{a}(\lambda, r_\mathrm{o})$, assuming that aerosol transmittance close to the ground is roughly 1. Due to the incomplete overlap and the lidar's instability, especially for high power and complex systems, the FW solution is usually not considered. However, it can be applied to measurements from ceilometer-type systems like the 808 nm channel of CE376, which has available measurements close to the ground and a stable configuration. On the other hand, the effective LR can be derived, for both BW and FW, based on iterative calculation of the solution and constraint by available $\mathrm{AOD_{ph}}$ (Mortier et al., 2013).

During nighttime measurements, the detection limits (using SNR = 1.5 on 30 min averaged profiles) for all CE376 channels is higher than 10 km, so we can usually meet an aerosol-free zone (r_ref) for both 532 and 808 nm wavelengths. Therefore, the BW Klett solution can be applied for both wavelengths. Nevertheless, during daytime, the strong solar background light limits the detection to ∼ 10 km and below 4 km for 532 and 808 nm, respectively. Thus, the BW Klett solution for 532 nm can still be applied but not for 808 nm. However, the blind zone and complete overlap are below 150 m and ∼ 1 km, respectively, for 808 nm, which is in contrast with 400 m and ∼ 2.5 km, respectively for 532 nm. Therefore, we consider the FW Klett solution to be suitable for RCS profiles at 808 nm during daytime. Taking all these considerations into account, we propose a modified two-wavelength inversion scheme as follows:

a. A BW Klett solution is applied to RCS total signals and constrained by $\mathrm{AOD_{ph}}$ at both wavelengths 532 and 808 nm. The r_ref for each wavelength is searched automatically within a threshold a priori defined (e.g., 6 to 10 km) and determined by minimizing the root mean square error with respect to the molecular signal. We derive $\mathrm{LR}(\lambda)$, $\beta_\mathrm{a}(\lambda r)$, and $\alpha_\mathrm{a}(\lambda r)$ at both wavelengths.

b. A FW Klett solution (when $r_\mathrm{ref}(532) > r_\mathrm{lim}(808)$) is applied to RCS at 808 nm if the r_ref determined for 532 nm is higher than the detection limit (r_lim) for 808 nm. We constrain the solution by an estimated AOD at 808 nm ($\mathrm{AOD_{est}}$). $\mathrm{AOD_{est}}$, defined in Eq. (7), is derived from the lidar retrievals at 532 nm and the interpolated $\mathrm{EAE_{ph}}$ for the pair of wavelengths 532 and 808 nm.

$$\mathrm{AOD_{est}}(808) = \left[\int_{r_\mathrm{o}}^{r_\mathrm{lim}} \alpha_\mathrm{a}(532, r)\mathrm{d}r\right]\left(\frac{808}{532}\right)^{-\mathrm{EAE_{ph}}} \quad (7)$$

c. An extinction Ångström exponent profile (EAE_lid) is derived from $2\alpha_\mathrm{a}(\lambda r)$ and defined as $\mathrm{EAE_{lid}}(r) = (-\ln[\alpha_\mathrm{a}(532, r)/\alpha_\mathrm{a}(808, r)])/\ln[532/808]$. This parameter gives insights into the vertical distribution of the aerosol size; EAE values close to 0 indicate the dominant presence of coarse-mode aerosols, and values higher than 1 are related to the fine-mode aerosols.

d. The color ratio (CR) is defined as the ratio between the aerosol backscatter at 808 and 532 nm $\mathrm{CR}(r) = \beta_\mathrm{a}(808, r)/\beta_\mathrm{a}(532, r)$, and it is described in Sect. 3.1.3, along with the ACR.

e. The particle linear depolarization ratio (PLDR) is defined by Eq. (11), where the molecular depolarization ratio δ^m is the theoretical value according to the bandwidth of the filter in front the half-wave plate in a CE376 system ($\delta^\mathrm{m} \sim 0.004$). $R = (\beta_\mathrm{a}(r) + \beta_\mathrm{m}(r))/\beta_\mathrm{m}(r)$ is known as the backscatter ratio, and $\delta^\mathrm{v}(r)$ is the VLDR profile derived directly from depolarization measurements (Sect. 3.1.1). Furthermore, PLDR gives insights into the vertical distribution of the aerosol shape; low values (close to 0) indicate the predominant presence of spherical aerosols. Values above 0.20 correspond to the predominant presence of non-spherical aerosols like dust or ice crystals in cirrus clouds.

$$\delta^\mathrm{p}(r) = \frac{[1+\delta^\mathrm{m}]\delta^\mathrm{v}(r)R(r) - [1+\delta^\mathrm{v}(r)]\delta^\mathrm{m}}{[1+\delta^\mathrm{m}]R(r) - [1+\delta^\mathrm{v}(r)]} \quad (8)$$

A first evaluation of uncertainties at each step in the data processing is approached using first-order derivatives. Thus, error propagation guidelines presented in the literature were followed (Russell et al., 1979; Sasano et al., 1985; Kovalev, 1995, 2004; Welton and Campbell, 2002; Morille et al., 2007; Rocadenbosch et al., 2012; Sicard et al., 2020). The main error sources are related to the overlap function estimation, background noise, lidar constant, and depolarization calibrations. Therefore, standard deviations from the overlap function and calibrations are considered and propagated from the RCS and VLDR to the aerosol retrievals. The uncertainty into the LR is roughly estimated by the convergence within the AOD uncertainties (0.01) in the iterative Klett solution. Errors in the molecular optical properties are negligible. Furthermore, relative errors greater than 15 % in the extinction coefficients at both wavelengths result in absolute uncertainties above 0.5 in EAE (Hu et al., 2019).

The data processing and inversion scheme presented in this section are the first steps towards near-real-time observations integrating the CE376 lidar and CE318-T photometer. Therefore, the capabilities for continuous monitoring of aerosol properties in fixed and mobile observatories are enhanced and presented through case studies in the following sections.

4 Atmospheric observations at Lille, France

In this section, we present the analysis and validation of data from an early version of the CE376 lidar, which is operational at a fixed location in the metropolitan area of Lille, France. In Sect. 4.1, a description of the site and instruments used for this study are presented. Selected case studies and validation of optical properties derived from the CE376 measurements presented through comparisons with a reference lidar are presented in Sect. 4.2.

4.1 ATOLL observatory

METIS is an early version of CE376 that is continuously performing at ATOLL at the University of Lille (50.61° N, 3.14° E; 60 m a.s.l.). The platform is also equipped with online in situ and other remote sensing instruments providing valuable information on aerosol properties and cloud–aerosol interactions. The ATOLL platform is one of the AERONET calibration centers, and it is an ACTRIS ERIC facility. The location is mainly influenced by urban–industrial emissions, marine aerosols (∼ 80 km from the nearest coast), and seasonal pollen outbreaks (Veselovskii et al., 2021). Likewise, events of long-range transport impact the region with aerosols from Saharan mineral dust storms (Veselovskii et al., 2022), North American wildfires (Hu et al., 2019, 2022), and volcanic eruptions (Mortier et al., 2013).

METIS has been operational at the ATOLL platform since 2019 in the framework of AGORA-Lab. METIS depolarization measurements setup currently follows a configuration with $\varphi = 90°$, measuring the parallel component on the PBS reflected branch. Wire grid polarizers behind the PBS branches are used to reduce the cross-talk in the signals ($T_\mathrm{p} \sim 1$, $T_\mathrm{s} \sim 0$ and $R_\mathrm{p} \sim 0$, $R_\mathrm{s} \sim 1$). The continuous measurements are ensured by setting the lidar in a temperature-controlled room and using a high-transmittance glass on the roof. Moreover, METIS is collocated with a CE318-T photometer and with LILAS ACTRIS lidar, which are both considered for this study.

LILAS is a high-powered Mie–Raman depolarization–fluorescence lidar that has been developed and upgraded by LOA and Cimel since 2013. From its simultaneous multiple wavelength measurements, the following independent height-resolved optical properties are derived: three backscatter (355, 532, and 1064 nm), two extinction (355 and 532 nm), three particle depolarization ratio (355, 532, and 1064 nm), and one fluorescence backscatter (at 466 nm) profiles. A detailed description of the LILAS system, retrievals, and uncertainties can be found in previous works (Bovchaliuk et al., 2016; Hu et al., 2019, 2022; Veselovskii et al., 2022). The aerosol optical properties derived with METIS at 532 nm are validated by intercomparisons with LILAS.

Molecular coefficients are modeled using radiosonde measurements from three stations near Lille, depending on availability. Beauvechain (50.78° N, 4.76° E; Belgium) and Herstmonceux (50.90° N, 0.32° E; England) from the Wyoming University database (https://weather.uwyo.edu/upperair/sounding.html, last access: 23 October 2023) and Trappes (48.77° N, 1.99° E; France) from the Météo-France database (https://donneespubliques.meteofrance.fr/, last access: 23 October 2023). Beauvechain is the closest site, about 120 km away from Lille, Herstmonceux is 200 km away, and Trappes is 240 km away from Lille.

4.2 Continuous observations and comparisons with reference lidar

Since the installation of METIS at ATOLL, several studies and instrumental assessments have taken place in order to improve mainly the depolarization measurements. From the first comparisons of METIS and LILAS, an important bias between depolarization measurements was detected (> 20 %). The roof glass window was tempered, had an anti-reflective coating, and suffered from deformations due to its size and weight. All of these aspects created biases in the depolarization measurements. Currently, a frame designed to contain four windows has been installed instead and avoids deformations due to the glass weight. The glass material was also changed to an extra-clear glass, and the windows are attached to the frame using silicone in order to avoid adding stress to the glass.

In the following case studies, continuous observations of METIS and comparisons with LILAS are presented with METIS under two different conditions of measurement. The first case is METIS without a roof window during an event of Saharan dust transported over Lille in spring 2021. The second case is METIS in the current configuration for continuous measurements during a recent event of dust and smoke transported over Lille in summer 2022.

4.2.1 Saharan dust transport over Lille (31 March to 2 April 2021)

Saharan dust layers transported over Lille are frequently observed and monitored with both METIS and LILAS. One of these events took place from 31 March to 2 April 2021. An overview of the METIS and photometer measurements is presented in Fig. 3. During this event, the roof window of METIS was open on 1 April beginning at 07:00 UTC and represented by the dotted black line in Fig. 3a and b. The impact of the roof window on the depolarization measurements can be observed, as VLDR values are higher by 0.02 when METIS is used with the roof window. For this case,

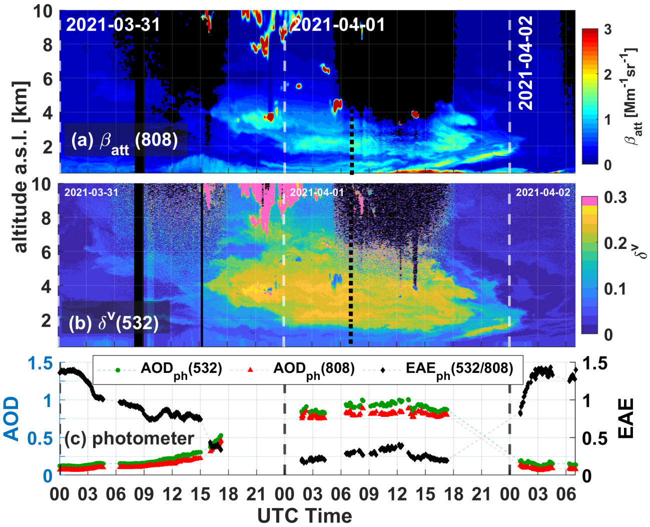

Figure 3. Overview of synergetic measurements of METIS lidar and CE318-T photometer during an event of Saharan dust transport from 31 March 2021 to 2 April 2021. Height–temporal variation in panel **(a)** is β_{att} at 808 nm, **(b)** VLDR is at 532 nm, and **(c)** the time series of AOD_{ph} at 532 and 808 nm with EAE_{ph} (532/808 nm) as derived from the photometer. The dashed black line in panels **(a)** and **(b)** indicates the change in the measurements conditions for METIS lidar.

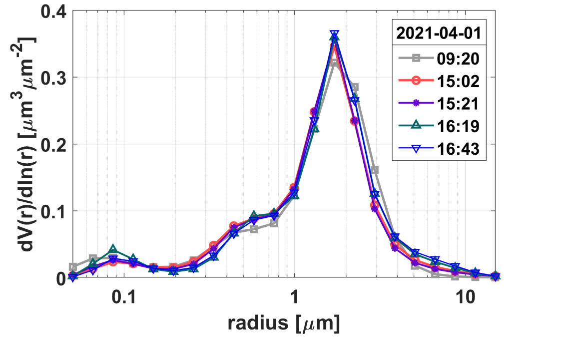

Figure 4. VSD derived from CE318-T photometer sky almucantar measurements during 1 April 2021 at ATOLL. Data are level 2 from AERONET version 3 algorithms (Sinyuk et al., 2020).

only VLDR values without window are considered for analysis.

The dust event had a period of strong aerosol loading during the night of 31 March 2021 to the afternoon of 1 April 2021. Intrusions of aerosol layers between 1.5 and 8 km a.s.l. were observed, with high VLDR values, on average 0.20 ± 0.04 (1 April 2021 at 07:00–19:00 UTC), indicating the presence of non-spherical aerosols. AOD_{ph} values at 532 and 808 nm increase up to 1 and 0.9, respectively. EAE_{ph} (532/808 nm) decreases from 1.4 to 0.2 and is associated with the increase in the coarse-mode particles concentration. Additionally, the VSD derived from photometer observations during 1 April 2021 (Fig. 4) shows the strong predominance of aerosols in the coarse mode with an effective radius of 1.7 µm. Thus, with the identified non-spherical coarse particles, the presence of dust is suggested and corroborated by ancillary analysis using back-trajectories (not shown here). Towards the night of 1–2 April 2021, the dust layers slowly vanish, while a peak of pollution develops close to the surface. A shallow boundary layer (< 500 m) with a strong inversion at the top constrains the mixing of dust within the boundary layer. During the day of 2 April, the EAE_{ph} (532/808 nm) increases up to 1.5, and the VLDR decreases below 0.1.

For comparisons of METIS and LILAS, averaged profiles on 1 April between 20:00 and 22:00 UTC were used when Raman measurements from LILAS were available. Aerosol optical properties were derived with the modified two-wavelength method for METIS CE376 lidar, and Raman inversion is used for LILAS. Molecular coefficients were calculated using the radiosonde data taken at 00:00 UTC on 2 April 2021 from the station Herstmonceux. Lunar measurements were not acquired until later that night, so the two closest pairs of AOD_{ph} were considered to constrain the inversion for METIS on 1 April 2021 at 17:50 and on 2 April 2021 at 00:45 UTC. Hence, backscatter and extinction profiles at 532 and 808 nm for METIS and at 532 nm for LILAS were retrieved and are presented in Fig. 5a and b. VLDR and PLDR at 532 nm for both lidars are also compared (Fig. 5c), as well as LR (Fig. 5f). The ACR and CR of 808–532 nm from METIS are presented (Fig. 5e), as well as EAE (532/808) nm from METIS and the photometer (Fig. 5d). The first 2 km of the RCS at 532 nm are influenced by relative errors of 5 % at 2 km going towards 20 % at 500 m due to the overlap estimations. In the case of RCS at 808 nm, the influence of the overlap error goes from 5 % at 1 km towards 10 % at 150 m. Therefore, to avoid artifacts in the retrievals, RCS values below 500 m are considered constant for both wavelengths. Likewise, PLDR, EAE, and CR values are not shown when the aerosol backscatter at 532 nm is less than 0.3 $Mm^{-1}\,sr^{-1}$ and below 500 m.

Backscatter and extinction profiles comparisons show good agreement between the Cimel CE376 elastic lidar and LILAS Raman lidar. The differences in the extinction observed are related to the constant LR of 54 ± 3 sr for METIS retrievals at 532 nm. From the profile of LR at 532 nm for LILAS (Fig. 5f), we can see that the first layer between 1.5–3 km a.s.l. is 48 sr on average, which is in contrast with 72 sr for the second layer between 3.3–4.7 km a.s.l. Thus, a better agreement in the lower layer than within the second layer, especially for extinction coefficients, is observed. From METIS retrievals, the first layer extinction values are on average 61 ± 14 and 52 ± 10 Mm^{-1} at 532 and 808 nm, respectively. Extinction values in the second layer are in contrast slightly lower, with 43 ± 3 and 35 ± 6 Mm^{-1} at 532 and 808 nm, respectively. The LR at 808 nm that resulted from the retrievals is 69 ± 4 sr. Absolute differences up to 0.03 for the METIS

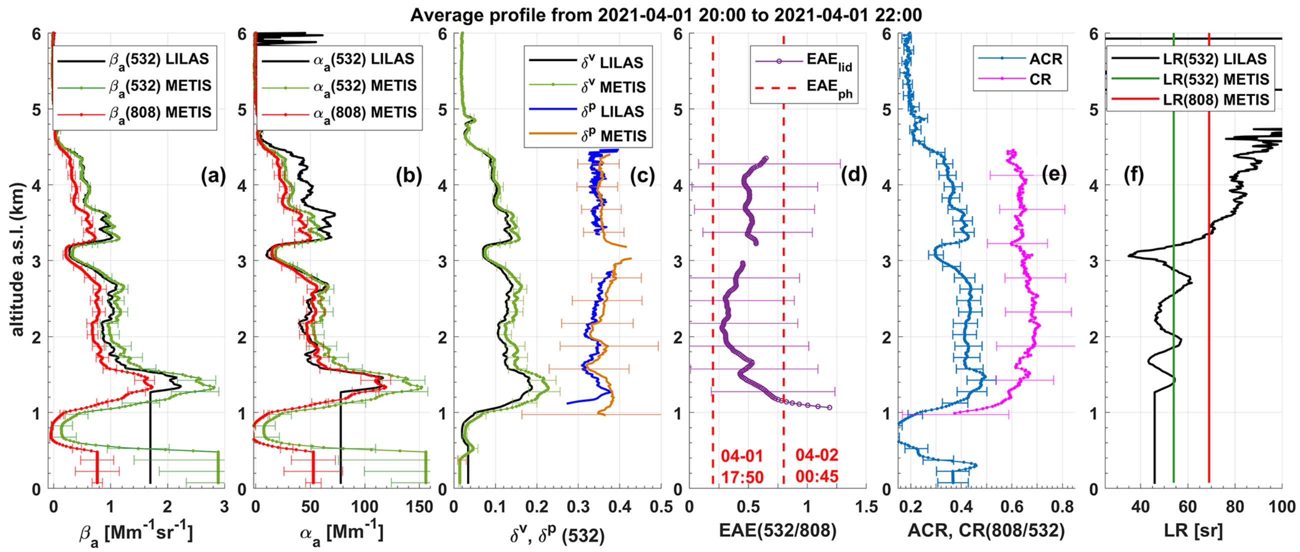

Figure 5. Aerosol optical properties derived from METIS CE376 lidar and intercomparison with LILAS Raman lidar retrievals for the averaged measurements between 20:00 and 22:00 UTC on 1 April 2021. Vertical profiles of **(a)** backscatter, **(b)** extinction, and **(f)** LR at 532 and 808 nm for METIS and at 532 nm for LILAS; **(c)** VLDR and PLDR at 532 nm for METIS and LILAS; **(d)** EAE (532/808 nm) from METIS and the two closest values from photometer given in dashed red lines; and **(e)** ACR and CR (808/532 nm) for METIS.

PLDR profile with respect to LILAS are observed. METIS shows VLDR and PLDR values within the two layers of 0.14 ± 0.02 and 0.36 ± 0.05, respectively, which is comparable to values reported in previous works for Saharan dust transport (Ansmann et al., 2003; Haarig et al., 2022; Floutsi et al., 2023). Lower EAE values (0.4) were observed for the first layer compared to 0.5 for the second layer. The ACR (808/532 nm) and CR (808/532 nm) profiles show values of 0.42 ± 0.05 and 0.69 ± 0.14, respectively, for the lower layer and 0.38 ± 0.04 and 0.65 ± 0.12 at the second layer. These results suggest the presence of two different air masses with larger dust aerosols in the lower layer, which is also shown in the LR profile from LILAS lidar.

METIS showed PLDR values 10 % higher than LILAS under the same operational conditions. This bias comes from differences in the optical design proper to the instruments and that METIS uses a manual half-wave plate for the polarization calibration, while LILAS uses a motorized PBS mount with an obvious higher precision.

4.2.2 Saharan dust and smoke transport over Lille (17 to 20 July 2022)

Several heat waves crossed Europe during spring–summer 2022, meaning that air masses from the equatorial region (North Africa) moved northwards, pushing temperatures up in several areas, especially in western Europe. The unusual long periods of heat during spring intensified the dry conditions for the summer. Moreover, due to the dry vegetation, extreme high temperatures, and high winds, multiple fires were ignited in southwestern Europe in July–August 2022. Unprecedented wildfires started on 12 July 2022 in the Gironde department, southwestern France, and intensified during a heat wave passing and strong winds over $\sim 270\,km^2$ of burned surface which accounted for the highest forest losses in France. During this event, biomass burning smoke injected to the atmosphere by the wildfires mixed with the mineral dust transported within the hot air masses originating over northern Africa. Therefore, at the time that the heat wave traversed Lille, we detected both dust and smoke in the atmospheric column. For this case, METIS was performing measurements under the current operational conditions, i.e., adapted roof window and air conditioning. To assess the continuity of the aerosol optical properties, the closest data points from the photometer are used to constrain the inversion when measurements from photometer are not available.

An overview of the derived aerosol properties from METIS and photometer is presented in Fig. 6 for the period of 17 to 20 July 2022 when the dust and smoke particles were detected up to 6 km altitude. From height–temporal variations in Fig. 6a–d, two periods can be distinguished during the event. On 17 July 2022, a predominant layer of ~ 1.5 km width appears that is quite homogeneously distributed and is observed between 2 and 5 km a.s.l., in contrast to the three compacted layers detected from 18 until 19 July 2022 12:00 UTC. Contrary to the complexity observed with the lidar, the temporal series from the photometer are quite stable (Fig. 6e).

For the first period on 17 July 2022, aerosol optical properties are on average 0.10 ± 0.01 for VLDR, $68 \pm 12\,Mm^{-1}$ (76 ± 34 sr) for extinction (LR) at 532 nm, and $44 \pm 9\,Mm^{-1}$ (33 ± 14 sr) for extinction (LR) at 808 nm, respectively,

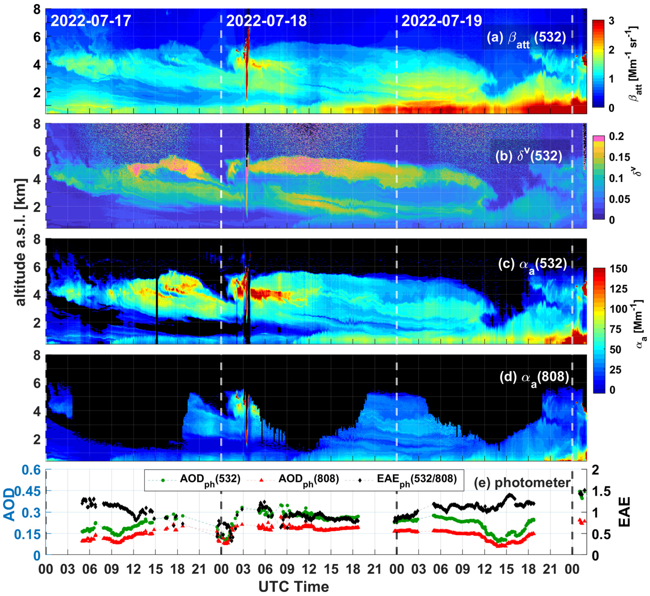

Figure 6. Overview of atmospheric optical properties from synergetic measurements of METIS lidar and CE318-T Sun/lunar photometer at ATOLL platform from 17 to 20 July 2022. Height–temporal variation in the **(a)** β_{att} and **(b)** VLDR at 532 nm, aerosol extinction at **(c)** 532 nm and **(d)** 808 nm, and **(e)** time series of AOD_{ph} at 532 and 808 nm with EAE_{ph} 532/808,nm, southwestern France, derived from the photometer.

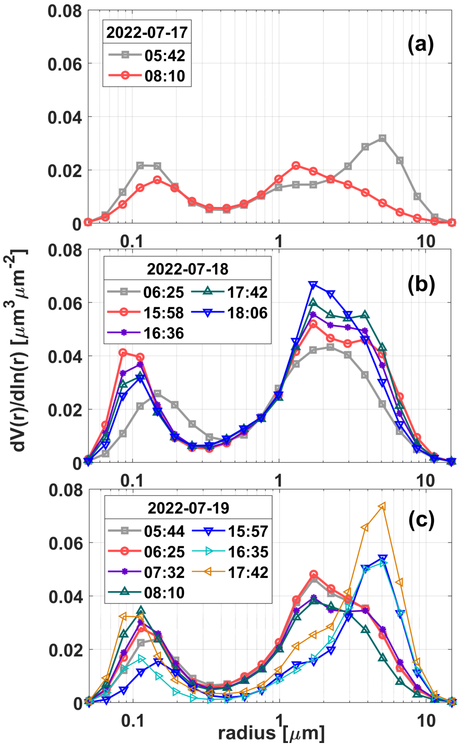

Figure 7. VSD derived from CE318-T photometer sky almucantar measurements during **(a)** 17 July 2022, **(b)** 18 July 2022, and **(c)** 19 July 2022 at ATOLL. Data are level 2 from AERONET version 3 algorithms (Sinyuk et al., 2020).

for the layer at 3–4.5 km a.s.l. Only data from 18:00 to 24:00 UTC are considered for 808 nm. During the second period on 18–19 July 2022, the layer from the day before, now reduced to 0.5 km width, is descending from 3 towards 1 km a.s.l. and accompanied by two separated layers above it. In particular, we focus our attention on the afternoon of 18 July 2022 to the early morning of 19 July 2022, where quite stable AOD_{ph} and EAE_{ph} are observed. LR is on average 47 ± 6 and 35 ± 8 sr at 532 and 808 nm, respectively. The second layer (2.4–3.2 km a.s.l.) shows lower VLDR values of 0.07 ± 0.01 and higher extinction ($50 \pm 3\,Mm^{-1}$ at 532 nm and $36 \pm 2\,Mm^{-1}$ at 808 nm) than the other two layers. The third layer (3.2–4.5 km a.s.l.) is, in comparison, characterized by higher VLDR (0.12 ± 0.02) and lower extinction ($40 \pm 2\,Mm^{-1}$ at 532 nm and $25 \pm 1\,Mm^{-1}$ at 808 nm). VLDR values are similar to those observed towards the end of the pure dust event presented in Sect. 4.2.1. Towards 12:00 UTC on 19 July 2022, the three layers disappear while the boundary layer height increases and probably mixes with the layer closer to the ground.

The VSD distributions during the event (Fig. 7) showed the predominance of three aerosol sizes, namely one in the fine mode centered at 0.11 µm radius, and two in the coarse mode centered at 1.7 µm and 5 µm. On 18 July 2022 (Fig. 7b), five VSDs were retrieved, all having a higher concentration than the day before (Fig. 7a); only one VSD in the morning is offset with higher values (0.15 µm) for the fine-mode peak. On 19 July 2022 (Fig. 7c), seven VSDs were retrieved, with four of them in the morning showing the same shape as the ones from 18 July. The rest of the VSDs show higher contribution at 5 µm size, representing the conditions after 15:00 UTC on 19 July which correspond to a drop in the AOD values and the vanishing of the layers. Therefore, the presence of both smoke (fine-mode) and dust (coarse-mode) aerosols is suggested during the entire event (Fig. 7) and confirmed by the ancillary analysis using back-trajectories (not shown here) with mainly two different stages in the aerosol vertical distributions (Fig. 6).

For comparisons of METIS and LILAS, averaged profiles between 01:00 and 03:00 UTC on 19 July 2022 are used (when Raman measurements from LILAS are available). The lunar measurements available are averaged during the same time period to constrain the inversion for METIS. During this event, LILAS lidar got affected by the extreme environmental conditions, so a higher incomplete overlap is acknowledged, and we will not consider retrieval comparisons below 1.7 km. Also, METIS overlap corrections induce errors in the first 2 km of the RCS at 532 nm from 3 % at 2 km going towards 20 % at 600 m. For RCS at 808 nm, the influence of the overlap error goes from 5 % at 600 m towards 20 % at 100 m. For derived properties using both RCS, values are therefore considered constant below 600 m. Once again, PLDR, EAE, and CR values are not shown when the aerosol backscatter at 532 nm is less than 0.3 $\mathrm{Mm^{-1}\,sr^{-1}}$ and at altitudes below 600 m.

Backscatter coefficient (Fig. 8a) and depolarization ratio (Fig. 8c) comparisons show good agreement between both lidars above 2 km a.s.l., with an obvious influence of the vertically constant LR assumption on METIS for the retrieval of backscatter profiles. The extinction coefficients (Fig. 8b) and consequently the EAE (Fig. 8d) are the most impacted (LR values of 38 ± 2 sr for 532 nm and 40 ± 2 sr for 808 nm), showing the limitation of the inversion method under complex scenarios. However, VLDR and PLDR values calculated from METIS are highly sensitive to the change in the dust–smoke composition within the layers. The first layer between 1.6–2 km a.s.l. and the third layer between 3.5–5 km a.s.l. showed PLDR (VLDR) values on average 0.20 ± 0.02 (0.09 ± 0.01) and 0.27 ± 0.03 (0.12 ± 0.01), respectively, and both layers have a predominant dust presence. In contrast, the second layer (2.4–3.2 km a.s.l.) yields the unique presence of smoke aerosols with PLDR (VLDR) of 0.09 ± 0.01 (0.05 ± 0.01), which is in accordance with reported values of fresh smoke transported 1 d from the source (Balis et al., 2003; Ansmann et al., 2009; Tesche et al., 2009b; Alados-Arboledas et al., 2011). Therefore, EAE values (Fig. 8d) are expected to be higher than 1 for the second layer, which is not the case due to the use of vertically constant LR. Moreover, ACR values directly derived from METIS measurements are influenced by the aerosol attenuation but are still sensitive to the different layers, in contrast to the CR profile derived from the inversion. Furthermore, the limitations discussed can be reduced by adding iterative processes to obtain layer-independent LR, as proposed by Lu et al. (2011).

Thanks to the operational improvements for the roof window of METIS, a reduced relative PLDR bias of 12 % with respect to LILAS is achieved. The results shown here are evidence of the relevant upgrades in the CE376 system relative to the previous model CE370 for an enhanced aerosol characterization. Furthermore, the algorithmic assessment presented in the first part of the results provided us with necessary tools to evaluate the data acquired during the FIREX-AQ campaign.

5 Mobile exploratory platform

In this work, we presented the dual-wavelength CE376 lidar that gives access to valuable information on the particles size with the measurements at two wavelengths and on aerosol shape using the depolarization measurements. The capabilities of the instrument regarding the continuous monitoring and characterization of aerosols have been presented in Sect. 4. Furthermore, the CE376 lidar is automatic, lightweight, and compact, which are favorable attributes for its installation in a reduced space. In comparison with bulky high-power lidars, the CE376 does not demand constant maintenance or high-power consumption. Therefore, the CE376 has been proposed to continue the developments on remote sensing mobile exploratory platforms.

In this section, we present a first dataset obtained with the CE376 lidar and photometer on board a mobile platform during the FIREX-AQ campaign in summer 2019. The general description of the campaign's mobile component is presented in Sect. 5.1, with an overview of the spatiotemporal variability in the smoke optical properties observed during the campaign (Sect. 5.1.1). Combined mobile–stationary measurements during the William Flats fire are presented in Sect. 5.2 through case studies.

5.1 FIREX-AQ Dragon Mobile Unit

The extensive field campaign FIREX-AQ, led by NOAA and NASA, was created with broad science targets (Warneke et al., 2023) and mainly focusing on investigating the chemistry and transport of smoke from wildfires and agricultural burning with the aim of improving weather, air quality, and climate forecasts. FIREX-AQ has been organized during summer 2019 over the northwestern US, where intense wildfires and agricultural fires seasonally occur. In order to evaluate and study the smoke properties at the source and its transport on a local and regional scale, remote sensing instruments were installed in both stationary and mobile DRAGON (Distributed Regional Aerosol Gridded Observations Networks) payloads, in addition to the permanent AERONET sites (Holben et al., 2018). In total, three DRAGON networks were installed in Missoula (Montana), Taylor Ranch (Idaho), and McCall (Idaho), and two mobile units with photometer–lidar were deployed.

The two mobile units called DMU-1 and DMU-2 (Dragon Mobile Unit), both equipped with a photometer and lidar, performed on-road mobile measurements around major fires sources. The installation of the remote sensing instruments in the DMUs followed the design of the MAMS (Mobile Aerosol Monitoring System) platform (Popovici et al., 2018). DMU-2 was equipped with CE370 mono-wavelength lidar and PLASMA Sun photometer, both tested and used in prior mobile campaigns (Popovici et al., 2018; Hu et al., 2019; Popovici et al., 2022). DMU-1 was equipped with an early version of CE376, a two-wavelength polarization lidar, and with the CE318-T Sun–sky–lunar photometer (ship-borne CE318-T). Depolarization measurements at 532 nm followed a configuration with $\varphi = 0°$, measuring the parallel component on the PBS transmitted branch ($R_\mathrm{s} > R_\mathrm{p}$ with $R_\mathrm{s} \sim 1$, $T_\mathrm{p} > T_\mathrm{s}$ and considering $R_\mathrm{p} = 1 - T_\mathrm{p}$ and $R_\mathrm{s} = 1 - T_\mathrm{s}$). The measurements were taken through an open hatch in the rooftop of the vehicles, so there was no influence of a window on the depolarization measurements. The temperature control inside both mobile units was not possible during mobile measurements (only using the car's air conditioning), so stationary and in-movement measurements were alternated with

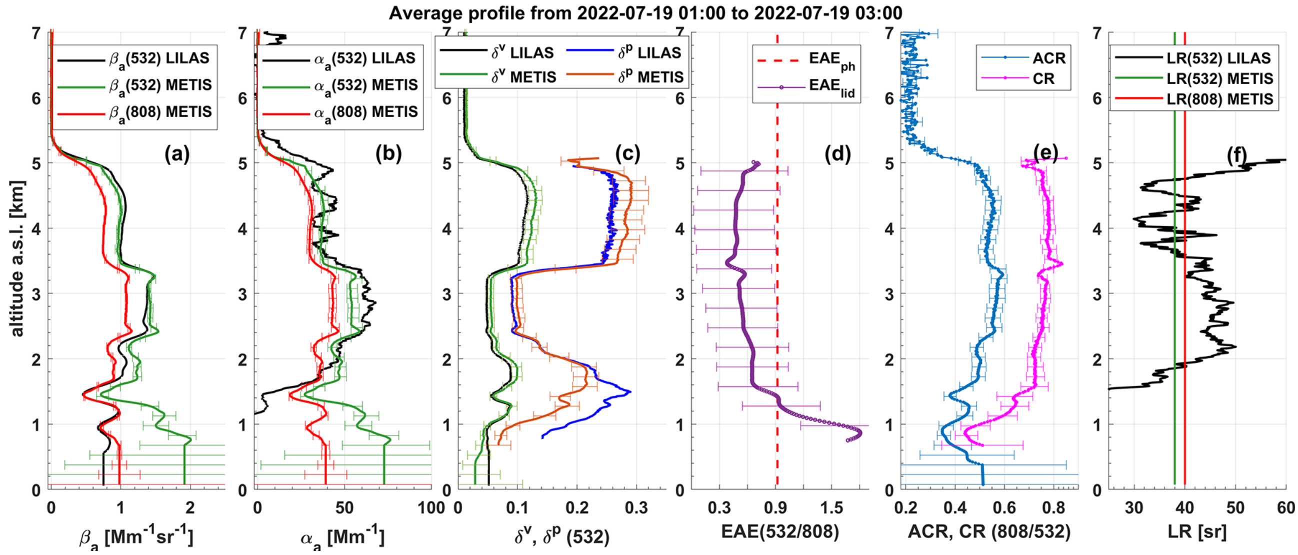

Figure 8. Aerosol optical properties derived from METIS and comparison with LILAS retrievals. Same as Fig. 5 but for the averaged measurements between 01:00 and 03:00 UTC on 19 July 2022.

pauses to preserve the instruments' performance, especially during daytime when extremely high temperatures and dry conditions were met. Particularly for the 532 nm channels of the CE376 lidar, the overlaps were affected by the daily evolution of temperatures that varied some days from 15 °C during nighttime to 40 °C during daytime. Therefore, only quality-assured data are considered for the inversion scheme in this work. Moreover, the temperature effect was accounted for in the overlap correction from where relative errors of 10 % at 2 km that increased to 30 % at 400 m are estimated and propagated on the derived aerosol properties.

5.1.1 Overview of smoke optical property distribution

Both DMUs performed measurements along the roads around the major fire sources. Although the extreme conditions, such as high temperatures, topography, and the presence of thick smoke plumes, limited the performance of the instruments, we were able to investigate smoke optical properties close to the source and downwind. A general overview of the column-integrated optical properties during the campaign is provided by photometer mobile observations around seven fire sources (Table 2). Measurements in and out of smoke plumes within ~ 150 km from the fires are presented as average values of AOD_{ph} (440 nm) and EAE_{ph} (440–870 nm). The high concentration of fine-mode aerosols (expected for fresh smoke) is detected at a regional level, with EAE_{ph} (440/870 nm) always higher than 1.3 and varying 5 % from the averages at each fire. On the other hand, measured AOD_{ph} (440 nm) values are varying up to 40 % from the averages at each fire, showing a non-homogeneous distribution of aerosols around the source.

Adding measurements from the lidar system, a more elaborated study of the spatiotemporal distribution of aerosol properties can be addressed. Therefore, optical properties derived from lidar and photometer measurements are presented in Sect. 5.2 through case studies during William Flats fire.

5.2 William Flats fire at WA, USA (6 to 7 August 2019)

The western US was affected by a persistent deep trough of low pressure in the months prior to FIREX-AQ, resulting in elevated soil/vegetation moisture when the fire season began, which controlled the regional fire spread. However, during the first days of the campaign (22 July–5 August 2019), high-pressure (anticyclone) weather conditions controlled the moisture transport in the mid-troposphere with a wide spread of cloud cover and thunderstorms. Combined with dry conditions in the lower troposphere, precipitation normally evaporated before reaching the ground, allowing the ignition of various fires due to lightning strikes. A low-pressure trough approaching from the west (W) on 6–9 August 2019 broke the high-pressure ridge and increased the surface wind speed gradually. William Flats fire, hereafter abbreviated as WFF, in the northeast (NE) of Washington state was in particular controlled by the unique synoptic weather conditions, with fire spread and smoke release progressively increasing as the low pressure approached. A more detailed description of the synoptic meteorological conditions dominating the campaign can be found in Warneke et al. (2023). Moreover, a camping base has been installed at Fort Spokane (47.905° N, 118.308° W; 430 m a.s.l.), which is located on the east (E) side of the WFF at ~ 15 km from the source and separated by the Columbia River.

Table 2. Overview of photometer measurements embarked upon on board DMU-1 (CE318-T) and DMU-2 (PLASMA). Averaged measurements around seven fires sources during the FIREX-AQ campaign.

Fire name	Location (state)	Dates	AOD_{ph} (440 nm)	EAE_{ph} (440–870 nm)
Pipeline	46.83° N, 120.52° W (WA)	25–28 Jul 2019	0.17 ± 0.06	1.55 ± 0.08
Shady	44.52° N, 115.02° W (ID)	29–31 Jul 2019	0.21 ± 0.01	1.90 ± 0.04
Beeskove	46.96° N, 113.87° W (MT)	31 Jul 2019	0.25 ± 0.01	1.84 ± 0.03
William Flats	47.94° N, 118.62° W (WA)	5–9 Aug 2019	0.45 ± 0.34	1.83 ± 0.13
Nethker	45.25° N, 115.93° W (ID)	13–20 Aug 2019	0.20 ± 0.10	1.32 ± 0.10
Granite Gulch	45.18° N, 117.43° W (OR)	20–22 Aug 2019	0.26 ± 0.11	1.44 ± 0.08
204 Cow	44.29° N, 118.46° W (OR)	23–29 Aug 2019	0.70 ± 0.48	1.84 ± 0.21

Mobile observations from selected on-road trajectories completed during 6–7 August 2019 are examined to reveal the distribution of aerosol properties around the active WFF. Thus, the GPS track of lidar measurements and the photometer observations from both DMU-1 and DMU-2 are displayed in Fig. 9. The selected trajectories (T) for DMU-1 (T1 to T4), in the top panel, and for DMU-2 (T1 to T5), in the bottom panel, are represented by different symbols. The time used to cover each of them is indicated in the legend and also at the top of the maps, and all times are in UTC (local time + 7 h). In addition, the AOD_{ph} values at 440 nm from both photometers are given by the symbol size, and EAE_{ph} values at 440–870 nm are color-coded. To simplify the reading of this section, AOD_{ph} values refer to AOD_{ph} values at 440 nm, and EAE_{ph} values refer to EAE_{ph} values at 440–870 nm when wavelengths are not specified. The fire ignition point is indicated in the maps with a red star symbol, and Fort Spokane is shown with a blue arrow. The extension of the active fire for each day are represented with the thermal anomalies, or hot spots, from the satellite-based sensor MODIS (Moderate Resolution Imaging Spectroradiometer). The MODIS Thermal anomalies product is derived from the Terra and Aqua satellites, and it is available to the public through NASA Worldview (https://wvs.earthdata.nasa.gov, last access: 23 October 2023).

The CE318-T photometer aboard DMU-1 was adapted and used for the ship-borne type of mobile measurements, i.e., for slow motion, before the campaign. Therefore, some difficulties were faced when using a car, especially due to the velocity and the complexity of the terrain and roads. The sun-tracking and geolocation communication were not fast enough for these particular conditions. As a solution, stationary measurements of 5 to 15 min were performed along the DMU-1 trajectories to increase the density of observations with CE318-T photometer. On the other hand, PLASMA Sun photometer was able to successfully perform on-road observations, with difficulties mainly due to the presence of mountains when Sun elevations are low and in presence of dense smoke plumes. Differences in both photometer performances are clear in Fig. 9. In general, both DMU-1 and DMU-2 observations during 6–7 August 2019 show the predominance of fine aerosols with EAE_{ph} values always higher than 1.4, as well as high variability in the aerosol distribution with AOD_{ph} ranging from 0.1 to 1.1. For a further interpretation of the photometer mobile observations, it is convenient to mention the solar azimuth during the WFF. Hence, at sunrise (~ 13:40 UTC), the azimuth is 68° (NEE); at solar noon (~ 21:00 UTC), it is 180.4° (S) with an elevation of 58.7°; and at sunset (~ $04:40^{+1\,d}$ UTC), the azimuth is 292° (WNW). In the following sub-sections, the analysis of mobile observations from DMU-1 and DMU-2 for each day are presented.

5.2.1 Three-dimensional spatiotemporal variation in the smoke properties

On 6 August 2019, the WFF was spread to the NE from its ignition point, with hot spot land elevations ranging around 0.7–1.2 km a.s.l. (Fig. 9a and c). Plumes of emitted smoke were mostly moving to easterly direction with respect to the source. When approaching sunset (~ $04:40^{+1\,d}$ UTC), the smoke release progressively increased with the temperature rising. Hence, the spatiotemporal distribution of aerosols along the trajectories for both DMU-1 (top panel) and DMU-2 (bottom panel) is presented in Fig. 10. For each trajectory, the 3D spatiotemporal distribution of β_{att} at 532 nm is plotted on top of the 3D digital elevation model (DEM) map of the region. The DEM used is the product with 1 arcsec global coverage (~ 30 m resolution) from Shuttle Radar Topography Mission (SRTM) that is available through Earth Explorer interface of United States Geological Survey (USGS, https://earthexplorer.usgs.gov/, last access: 23 October 2023). Moreover, both β_{att} and DEM maps are color-coded, and each one has its own color bar scale. In the same way as in Fig. 9a and c, red points represent the thermal anomalies and show the extension of the active WFF detected on 6 August 2019.

During 6 August 2019, residual smoke in all the trajectories was detected up to 4 km a.s.l., and higher AOD_{ph} and EAE_{ph} values were identified under the presence of dense smoke plumes. The Columbia River acted like an air canal with the prevailing valley winds in the morning (De Wekker and Kossmann, 2015; Whiteman, 2000), directing a dif-

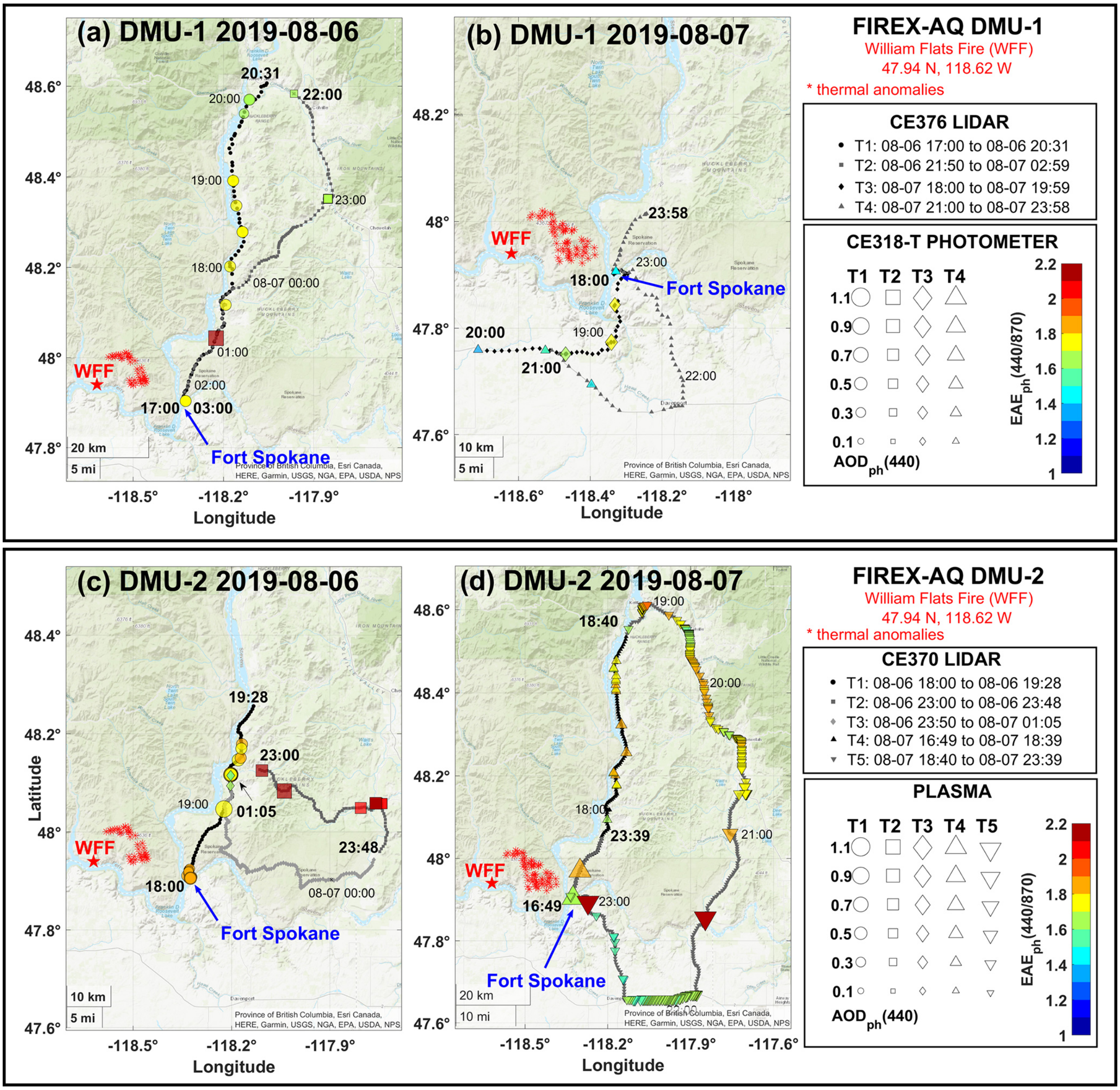

Figure 9. Mobile observations around the WFF during 6 and 7 August 2019 (in UTC). GPS tracks of DMU-1 and DMU-2 are presented in the top and bottom panels, respectively. For each trajectory (T), a different symbol is used. Photometer measurements are presented with color-coded symbols, EAE_{ph} (440/870) represented by the color and AOD_{ph} (440) by the symbol size. The ignition point of the WFF is represented by a red star. The extension of the fire is represented by thermal anomalies from MODIS AQUA/TERRA detected during each day.

fused smoke plume northward. The trajectory of DMU-1 T1 (Fig. 10a) covered ~80 km between 17:00 and 20:31 UTC along the Columbia riverside going from Fort Spokane to Kettle Falls (48.60° N, 118.06° W). AOD_{ph} ranged within 0.2–0.3, and EAE_{ph} was higher than 1.6 (Fig. 9a). DMU-2 T1 (Fig. 10c) covered 40 km of the same route between 18:00 and 19:28 UTC, starting with 30 min of stationary measurements at Fort Spokane. AOD_{ph} values within 0.3–0.7 and EAE_{ph} above 1.7 were observed (Fig. 9c). During both trajectories, azimuthal solar angles vary from 101 to 153° (E to S), meaning that both photometers were taking measurements towards the east side of the WFF against the movement of the vehicles and limited by the mountain slopes. Hence, both DMUs followed and measured the diffuse smoke plume with 1 h time difference. DMU-2 T1 lidar–photometer measurements indicate an increase in smoke release and accumulation northward, with higher AOD_{ph} and β_{att} (below 2 km a.s.l.) values.

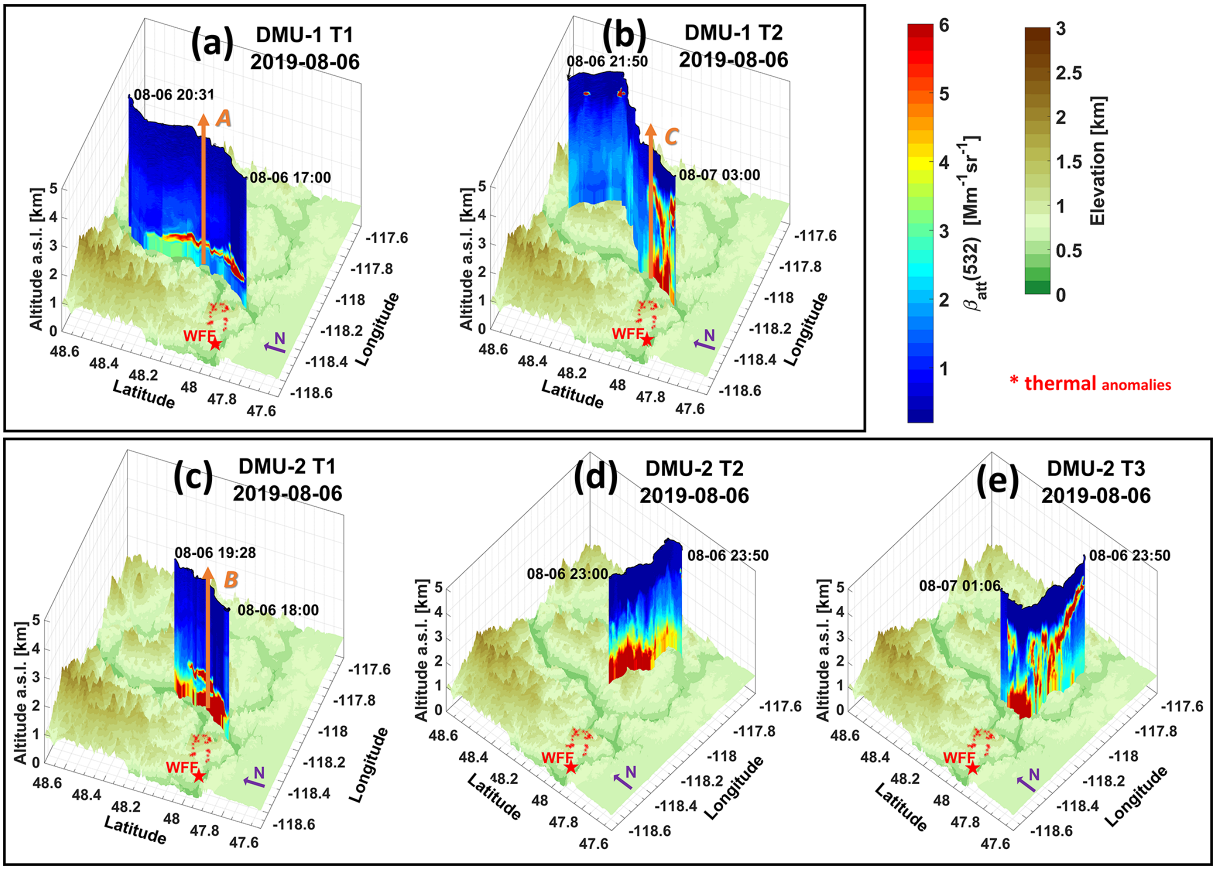

Figure 10. Spatiotemporal distribution of total attenuated backscatter at 532 nm for the trajectories during 6 August 2019 from Fig. 9. Trajectories of DMU-1 (CE376 lidar) are presented in the top panel and DMU-2 (CE370 lidar) in the bottom panel. The lidar trajectories are plotted in the top DEM from SRTM at 1 arcsec resolution (∼ 30 m). The ignition point of the WFF is represented by a red star and the extension of the active fire by MODIS thermal anomalies. Orange arrows represent the selected profiles for further analysis in Fig. 12.

The trajectory DMU-1 T2 (Fig. 10b and also Fig. 9a) was completed from 21:50 to 02:59 UTC, i.e., in the afternoon, and covered ∼ 100 km on the way back to Fort Spokane from Kettle Falls, passing through the Colville River basin. Hence, the residual smoke that is well mixed up to 4 km a.s.l. is contained along the valley, showing AOD_{ph} varying between 0.3–0.5 and EAE_{ph} of 1.6 (solar azimuth 206 to 292°, i.e., photometer pointing to the east side of the WFF towards the WFF). Approaching Fort Spokane, the development of a convective smoke plume was observed (Fig. 10b). One exceptional sampling of the dense smoke plume was possible at ∼ 01:00 UTC and 20 km east, away from the fire, with an AOD_{ph} of 1.1 and EAE_{ph} of 2.2 (Fig. 9a). DMU-2 T2 (Fig. 10d and also Fig. 9c) performed measurements in the afternoon from 23:00 to 23:48 UTC, going downwind of the WFF and covering ∼ 50 km horizontally to the east (solar azimuth 228 to 245°, i.e., towards the WFF). This trajectory in particular shows how smoke accumulated and settled across the valleys. High AOD_{ph} values above 0.7 and EAE_{ph} values above 2 (Fig. 9c) were observed. DMU-2 T3 (Fig. 10e) also completed during the afternoon (23:50–01:05 UTC), covering the return route to Fort Spokane. While it got closer to the source, higher values of β_{att} ($> 6\,\mathrm{Mm^{-1}\,sr^{-1}}$) were detected from 4 km a.s.l. towards the ground level. Although no photometer data are available due to presence of the thick smoke plume, the lidar provides a glimpse of the convective smoke plume transect. The smoke plume raised up to 4.2 km a.s.l. at 50 km away (horizontally to the east) from its source and ∼ 3 km higher than the active fire and above the mountain ridges.

During 7 August 2019, the WFF extended towards the east, getting closer to the Columbia River ridge, and more hot spots were detected than the day before (Fig. 9b and d). Through the day, smoke convective plumes moved, mostly influenced by the strong winds, towards the easterly direction and slightly to the SE. In the afternoon, black and white ash depositions were reported, in addition to cloud formation observed close to sunset (∼ 04:40$^{+1\,\mathrm{d}}$ UTC). At that point, the presence of heavy smoke plumes saturated the lidar signals and restricted photometer measurements close to the source. Therefore, trajectories were performed mostly outside of the smoke plumes. Similar to the lidar observations presented

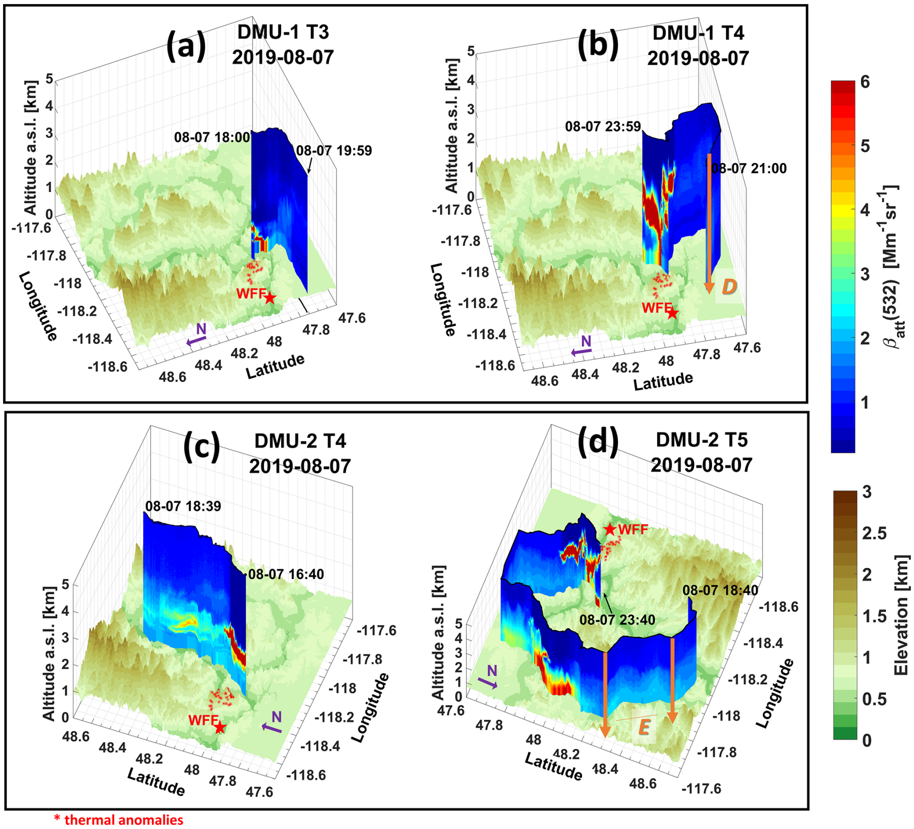

Figure 11. Spatiotemporal distribution of total attenuated backscatter at 532 nm. Same as Fig. 10 but for the trajectories during 7 August 2019.

in Fig. 10, 3D spatiotemporal distributions of β_{att} at 532 nm for all the trajectories during 7 August 2019 are presented in Fig. 11.

The trajectory DMU-1 T3 (Fig. 11a) covered ∼ 40 km from Fort Spokane to the south of the WFF between 18:00 to 19:58 UTC. DMU-1 T4 (Fig. 11b) covered ∼ 70 km of the route (from S to E side of the WFF) between 21:00 and 23:59 UTC. For both trajectories, few data points from photometer were collected and might not represent the same conditions for the zenithal lidar measurements. The photometer is looking towards the SE to the SW from the WFF, against the wind's flow. AOD_{ph} ranging between 0.1–0.2 and EAE_{ph} above 1.6 were observed (Fig. 9b), which are indicative of the low loading of residual smoke in the southern region of the WFF. Both trajectories seen by the lidar show no direct influence of the smoke release on the S–SE of the WFF and present considerably lower values of β_{att}. Nevertheless, similar to observations on 6 August 2019, a convective smoke plume reaching up to 4 km a.s.l. is observed in the afternoon (Fig. 11b).

On the other hand, the trajectory DMU-2 T4 (Fig. 11c) is covering the NNE of the WFF along the Columbia riverside and following the smoke plume. DMU-2 T4 covered ∼ 80 km from Fort Spokane to Kettle Falls, from 16:49 to 18:39 UTC, and with AOD_{ph} ranging within 0.1–0.3 and EAE_{ph} 1.6–1.8, with higher AOD values being measured closer to the fire. This time, the vertical extent of the smoke plume is ∼ 200 m higher, and it is denser than the day before. But in the same way as the day before, the Columbia River is the main driver of the channeling effect of the smoke towards the north in the morning. The trajectory DMU-2 T5 (Fig. 11d and also Fig. 9d) covered ∼ 200 km between 18:40 to 23:40 UTC from Kettle Falls (80 km NNE from the WFF) towards Davenport (47.65° N, 118.15° W; ∼ 40 km SE of the WFF) going through valleys and returning to Fort Spokane. Along the way, DMU-2 measured residual smoke accumulated in the NE valley basins, with AOD_{ph} around 0.3 and EAE_{ph} of 1.6–1.8. In addition, residual smoke, SE of the WFF, was measured with lower values of AOD_{ph} around 0.1–0.3 and EAE_{ph} 1.5–1.6. During this transect, the DMU-2 crossed the smoke plume twice, once at 21:20–21:23 UTC 40 km downwind of the WFF, and the second time at 23:00 UTC about 15 km away from the WFF. From the DMU-2 T5 3D aerosol distribution (Fig. 11d) and photometer (Fig. 9d), one can see the effect of the diffuse smoke from the WFF on the NE region that is characterized by its mountains and valleys.

The complex topography, combined with the prevailing synoptic conditions (low-pressure trough approaching from the west), has important effects on the development of fire (Whiteman, 2000). While the river basin acted almost independently in the morning, channeling smoke northward, we noticed how the evolving boundary layer is coupled to the mountain wind systems. The diffused smoke is mixed and subsided along the valleys, with higher aerosol loading closer to the fire downwind. Moreover, fire emissions get stronger while temperatures rise up, permitting the convective loft of the smoke above the mountain ridges. On 7 August 2019, the convective smoke evolved into the formation of pyrocumulus clouds. For further analysis, in the following section we present aerosol properties of selected datasets from the trajectories presented here.

5.2.2 Aerosol properties for selected profiles

From the DMU-1 and DMU-2 trajectories on 6–7 August 2019, selected coincident lidar and photometer data are averaged over 5 to 15 min and are used to enhance the aerosol characterization presented so far. The selected times are displayed in Figs. 10 and 11 by orange arrows in the 3D β_{att} quick-look. In Fig. 12, we present the profiles of aerosol properties for each selected dataset differentiated by color. Hence, we show profiles of backscatter, extinction at 532 and 808 nm, and profiles of PLDR, EAE, and ACR. For the lidar retrievals, data below 400 m are considered constant due to high uncertainties ($> 30\,\%$) in RCS at 532 nm. Molecular coefficients are calculated using radiosonde measurements at Spokane station (47.68° N, 117.63° W) from the Wyoming University database (https://weather.uwyo.edu/upperair/sounding.html). The detection limit is defined at SNR $= 1$ for all channels to extract more information, in particular from 808 nm.

Detection limits for 808 and 532 nm cross-polarized channels from CE376 are below 2 and 3–4 km, respectively, due to the high solar background. Nevertheless, we were able to study the diffuse smoke plume transported along the Columbia River with retrieval profiles from selected data. The dataset A, attained during DMU-1 T1, is shown in Fig. 12a–g, and dataset B, from DMU-2 T1, is shown in Fig. 12a and c. The dataset A corresponds to the averaged CE376 lidar data from 18:10 to 18:25 UTC on 6 August 2019 that is located 40 km away and to the NNE of the WFF. AOD_{ph} from the CE318-T photometer were 0.28 and 0.13 at 532 and 808 nm, respectively; EAE_{ph}(532/808) was 1.76; and the calculated AOD_{est} at 808 nm is 0.1. The smoke plume is identified at 1–1.3 km a.s.l. with maximum values of extinction at 1.14 km a.s.l. Thus, extinction values of $370 \pm 70\,\mathrm{Mm^{-1}}$ (with LR $= 35 \pm 1$ sr) at 532 nm (Fig. 12c), and $207 \pm 20\,\mathrm{Mm^{-1}}$ (with LR $= 57 \pm 4$ sr) at 808 nm (Fig. 12d) were observed. Other aerosol properties inside the smoke plume were 0.06 ± 0.04 for PLDR (Fig. 12e), 1.2 for EAE (Fig. 12f), and 0.5 ± 0.3 for ACR (Fig. 12g). On the other hand, dataset B corresponds to averaged CE370 lidar data from 19:05 to 19:15 UTC on 6 August 2019, ~ 1 h after dataset A was obtained. Dataset B is located 25 km to the NNE and away from the WFF, with values of 0.35 for AOD_{ph} at 532 nm and 1.7 for EAE_{ph} (440/870). The smoke plume is identified at 1.6–1.9 km a.s.l. with maximum values of extinction at 1.71 km a.s.l. Values of $380 \pm 20\,\mathrm{Mm^{-1}}$ (with LR $= 39 \pm 1$ sr) for extinction at 532 nm were derived. The identified smoke plumes for both datasets are almost the same, except for the altitude. The higher extinction below 1 km a.s.l. for dataset B is related to the increase in the smoke released through the day. Moreover, a layer of residual smoke at 2–3 km a.s.l. is detected for both cases with less, but still noticeable, intensity for dataset B. PLDR in the residual layer (0.08 ± 0.02) is in agreement with reported values of fresh smoke transported 1 d from source (Balis et al., 2003; Ansmann et al., 2009; Tesche et al., 2009b; Alados-Arboledas et al., 2011). Despite the high uncertainties that are attached to the profiles in the few first hundreds of meters, ACR values (Fig. 12g) suggest the presence of bigger aerosols in the smoke plume at 1 km a.s.l. than in the residual layer at 2–3 km a.s.l., similar to EAE. The observed bigger aerosols could be related to the release of fine-ash particles (sizes of 1–2 µm) within the smoke plume (Adachi et al., 2022).

The dataset C shown in Fig. 12h–n, obtained during DMU-1 T2, corresponds to averaged CE376 lidar data from 00:40 to 00:50 UTC toward sunset on 6 August 2019. This dataset, located 20 km east of the WFF, is particularly interesting because it provides information on the convective smoke plume. Values of 1.54 and 0.61 for AOD_{ph} at 532 and 808 nm, respectively, were detected by the photometer, as well as an EAE_{ph}(532/808) of 2.25 and calculated AOD_{est} at 808 nm of 0.18 (below the smoke plume). The convective plume is identified at 3–4.3 km a.s.l., with maximum values of extinction at 3.57 km a.s.l. (Fig. 12j). Thus, $1270 \pm 330\,\mathrm{Mm^{-1}}$ (with LR $= 82 \pm 2$ sr) for extinction at 532 nm was observed. Inside the plume, a decrease in the PLDR (Fig. 12l) from 0.05 ± 0.01 to 0.03 ± 0.01 is detected, in addition to values progressively increasing from 0.4 ± 0.1 to 0.9 ± 0.1 for ACR (Fig. 12n). Both parameters suggest the predominance of big spherical particles towards the smoke layer top, which could be related to the fast increase in the coating mass of soot particles within minutes from emission. In contrast, dataset D shown in Fig. 12o–u, located 25 km south of the WFF (21:00 to 21:09 UTC on 7 August 2019), and dataset E shown in Fig. 12o and q, located 60 km NE of the WFF (20:00 to 20:30 UTC on 7 August 2019), present residual smoke. Both datasets have values of 0.13 for AOD_{ph} at 532 nm. Dataset D shows a residual layer extending up to 4 km a.s.l., with average values of $44 \pm 17\,\mathrm{Mm^{-1}}$ (with LR $= 37 \pm 3$ sr) for extinction at 532 nm (Fig. 12q) and $28 \pm 15\,\mathrm{Mm^{-1}}$ (with LR $= 87 \pm 15$ sr) at 808 nm (Fig. 12r). Moreover, PLDR is 0.09 ± 0.03 (Fig. 12s), EAE is 1.5 (Fig. 12t), and ACR is 0.3 ± 0.1 (Fig. 12u). One notices that

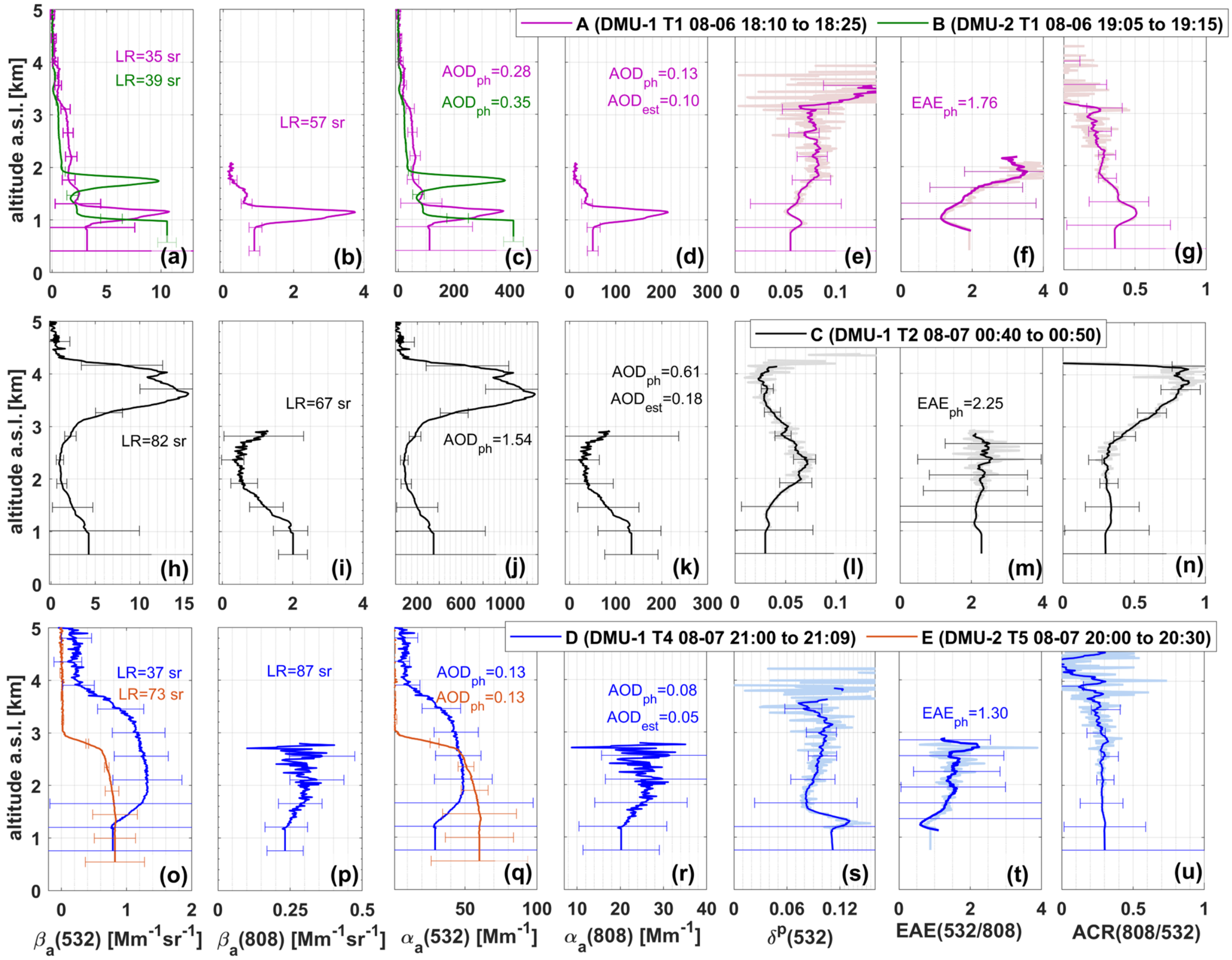

Figure 12. Profiles of aerosol optical properties from averaged selected datasets of both DMU-1 and DMU-2 mobile observations during 6 and 7 August 2019. The selected data are displayed in Figs. 10 and 11 by orange arrows in the 3D β_{att} distributions. Each dataset is differentiated by color. Profiles of backscatter at 532 nm (**a**, **h**, and **o**) and 808 nm (**b**, **i**, and **p**), extinction at 532 nm (**c**, **j**, and **q**) and 808 nm (**d**, **k**, and **r**), PLDR (**e**, **l**, and **s**), EAE (**f**, **m**, and **t**), and ACR (**g**, **n**, and **u**).

ACR values are constant within the residual layer, suggesting that smoke is well mixed. Dataset E shows that the residual smoke in the NE side of the WFF is going up to 3 km a.s.l. with a LR of 73 ± 7 sr, which is higher than for dataset D.

6 Summary and conclusions

In this study, we presented the enhanced capabilities of the Cimel CE376 lidar, a compact dual-wavelength depolarization elastic lidar, for the assessment of spatiotemporal variability in the aerosol properties, especially when deployed aboard moving platforms and co-located with a photometer. Our approach involved a modified two-wavelength Klett inversion constrained by photometer measurements, optimizing the use of synergetic observations. Comprehensive algorithmic and instrumental assessments, including improvements in continuous depolarization measurements, were conducted at the ATOLL observatory. Our findings were organized into two primary parts with the aerosol properties resulting from the case studies at the ATOLL observatory in Lille, France (Sect. 4), and around the William Flats fire in northwestern US during the FIREX-AQ campaign (Sect. 5). Aerosol optical properties obtained in both sections are summarized in Table 3.

Both algorithmic and instrumental assessments of CE376 were tested through case studies (Sect. 4), encompassing events involving aged dust and mixed dust and smoke over Lille (Table 3). Despite the operational limitations, we achieved a relative VLDR bias of 12 % compared to LILAS Raman lidar, and we showcased CE376's ability for the continuous monitoring of aerosol properties. The limitations of our retrieval approach were also evaluated, owing mainly to the assumption of a constant LR in the atmospheric column, where EAE and CR are the most affected. The unusual event of stratified dust and smoke transported over Lille highlights the importance of depolarization measurements

Table 3. Overview of the aerosol properties retrieved from the CE376 lidar and CE318-T photometer for the case studies presented in this work. The estimated uncertainties are in parentheses. For observations at the ATOLL platform, aerosol properties are specified for each layer detected in both case studies, namely aged dust (L1 and L2) and dust smoke (L1, L2, and L3). For the FIREX-AQ campaign, the position with respect to the WFF is included.

Site		ATOLL, France			FIREX-AQ, William Flats fire (USA)		
Aerosol type		Aged dust	Mixture dust + smoke	Smoke	Diffuse smoke	Convective smoke	Residual smoke
Altitude a.s.l. (km)		L1: 1.5–3 L2: 3.3–4.7	L1: 1.6–2 L3: 3.5–5	L2: 2.4–3.2	1–1.3 (40 km NNE)	3–4.3 (20 km E)	1.2–4 (25 km S) 0.9–3* (60 km NE)
LR (sr)	532	$^{\mathrm{L1,L2}}$ 54 (3)	$^{\mathrm{L1,L3}}$ 38 (2)	$^{\mathrm{L2}}$ 38 (2)	35 (1)	82 (2)	37 (3) 73* (7)
	808	$^{\mathrm{L1,L2}}$ 69 (4)	$^{\mathrm{L1,L3}}$ 40 (2)	$^{\mathrm{L2}}$ 40 (2)	57 (4)	–	87 (15)
α_a (Mm^{-1})	532	$^{\mathrm{L1}}$ 61 (14) $^{\mathrm{L2}}$ 43 (3)	$^{\mathrm{L1}}$ 47 (3) $^{\mathrm{L3}}$ 34 (2)	$^{\mathrm{L2}}$ 54 (3)	370 (73)	1270 (330)	45 (17) 54* (9)
	808	$^{\mathrm{L1}}$ 52 (9) $^{\mathrm{L2}}$ 35 (6)	$^{\mathrm{L1}}$ 36 (2) $^{\mathrm{L3}}$ 28 (1)	$^{\mathrm{L2}}$ 43 (2)	207 (20)	–	28 (15)
δ^{v}	532	$^{\mathrm{L1}}$ 0.15 (0.02) $^{\mathrm{L2}}$ 0.12 (0.02)	$^{\mathrm{L1}}$ 0.09 (0.01) $^{\mathrm{L3}}$ 0.12 (0.01)	$^{\mathrm{L2}}$0.05 (0.01)	0.04 (0.02)	0.03 (0.01)	0.05 (0.01)
δ^{p}	532	$^{\mathrm{L1}}$ 0.36 (0.05) $^{\mathrm{L2}}$ 0.36 (0.05)	$^{\mathrm{L1}}$ 0.2 (0.02) $^{\mathrm{L3}}$ 0.27 (0.03)	$^{\mathrm{L2}}$ 0.09 (0.01)	0.06 (0.04)	0.04 (0.01)	0.09 (0.03)
EAE (532/808 nm)	LID	$^{\mathrm{L1}}$ 0.4 (0.6) $^{\mathrm{L2}}$ 0.5 (0.5)	$^{\mathrm{L1}}$ 0.6 (0.4) $^{\mathrm{L3}}$ 0.5 (0.4)	$^{\mathrm{L2}}$ 0.55 (0.4)	1.2 (2.9)	–	1.5 (1.2)
	PH	0.23–0.75	0.92	0.92	1.76	2.25	1.3 1.7*
ACR (808/532 nm)		$^{\mathrm{L1}}$ 0.42 (0.05) $^{\mathrm{L2}}$ 0.38 (0.04)	$^{\mathrm{L1}}$ 0.49 (0.03) $^{\mathrm{L3}}$ 0.5 (0.03)	$^{\mathrm{L2}}$ 0.56 (0.03)	0.5 (0.3)	0.6 (0.1)	0.3 (0.1)
CR (808/532 nm)		$^{\mathrm{L1}}$ 0.69 (0.14) $^{\mathrm{L2}}$ 0.65 (0.12)	$^{\mathrm{L1}}$ 0.72 (0.04) $^{\mathrm{L3}}$ 0.76 (0.03)	$^{\mathrm{L2}}$ 0.73 (0.03)	0.4 (0.3)	–	0.2 (0.1)
Eff. radius VSD (µm)		1.7	1.7 and 5	0.1	–	–	–

* Aerosol properties retrieved from the CE370 lidar and PLASMA photometer.

for aerosol typing within the different aerosol layers, demonstrating CE376's reliability – even in challenging scenarios.

We also presented for the first time ground-based lidar and photometer mobile observations, mapping smoke aerosol properties near the source during the FIREX-AQ campaign in 2019 (Sect. 5). Our study focuses on the William Flats fire (WFF) in Washington state, which presented unique and challenging environmental conditions for the exploratory platforms. The 3D mapping of lidar and photometer observations enabled the identification of aerosol properties in diffuse, convective, and residual smoke layers near the WFF (Table 3). The study revealed the capabilities of CE376 aboard mobile platforms to characterize the smoke aerosol optical properties. At the same time, we acknowledged the limitations of the CE376 lidar and photometer in harsh environmental conditions (complex topography, high temperatures, and thick smoke plumes).

With the demonstrated versatility of the CE376 lidar for monitoring aerosol properties, we look ahead at bridging observational gaps within networks. Therefore, upcoming mobile campaigns (aboard ship cruises, trains, and cars) and permanent sites in the Southern Hemisphere are planned to include the upgraded, more robust, version of the CE376 lidar. The installation of a CE376 lidar aboard *Marion Dufresne* research vessel, in the framework of MAP-IO, is planned in 2024. Moreover, the Polar POD (https://www.polarpod.fr/, last access: 24 October 2023), a floating scientific platform that will circle the Earth around Antarctica, will include a CE376 automatic lidar, along with several other installed scientific instruments. Additionally, ongoing research involving advanced retrieval methods like GRASP (Generalized Retrieval of Aerosol and Surface Properties), combining spectral AOD and downward sky radiance from CE318-T photometers and RCS at two wavelengths from CE376, are underway. These advancements mark significant steps in enhancing our understanding of aerosol dynamics and environmental monitoring.

Data availability. Data from the photometer are available at the AERONET website (https://aeronet.gsfc.nasa.gov/, NASA GSFC, 2023). Radiosonde data are accessible via the Wyoming University database (https://weather.uwyo.edu/upperair/sounding.html, University of Wyoming, 2023) and Météo-France database (https://donneespubliques.meteofrance.fr/, Météo-France, 2023.). The data of DEM from SRTM are available from Earth Explorer interface of the USGS (https://doi.org/10.5066/F7PR7TFT, U.S. Geological Survey, 2023). The MODIS thermal anomalies product is available from NASA Worldview (https://wvs.earthdata.nasa.gov/, EOSDIS, 2023). Lidar data used in this paper are available upon request to the corresponding author.

Author contributions. MFSB analyzed the CE370 and CE376 lidar data, prepared the figures, and wrote the article. PG, SV, and IEP supervised the work and contributed to the writing of the article. DMG revised the paper. PG, SV, IEP, LB, BH, and BT designed and conceptualized the project of lidar and photometer mobile applications. PG, IEP, LB, EB, QH, and TP conceived and performed the experiments at ATOLL platform. MFSB developed the CE376 algorithmic assessments initiated by IEP. IEP, TP, LP, MFSB, and EB supported the instrumental assessments of CE376 lidar. QH and TP performed the experiments with LILAS, and QH analyzed the data. FD and QH developed and supported the LILAS algorithms. PG, IEP, LB, TP, GD, LP, BH, AL, ALR, and DMG conducted the experiments and supported the installation of instruments aboard DMU-1 and DMU-2 during FIREX-AQ.

Competing interests. The contact author has declared that none of the authors has any competing interests.

Disclaimer. Publisher's note: Copernicus Publications remains neutral with regard to jurisdictional claims made in the text, published maps, institutional affiliations, or any other geographical representation in this paper. While Copernicus Publications makes every effort to include appropriate place names, the final responsibility lies with the authors.

Acknowledgements. The authors would like to thank ANRT (Association Nationale de la Recherche et de la Technologie) France and Cimel for supporting the research development in the framework of the CIFRE (grant no. 2020/0442) thesis by Maria Fernanda Sanchez Barrero. We also thank the H2020/GRASP-ACE Marie Skłodowska-Curie project for funding. The authors acknowledge the generous support from the NOAA AC4 program from FIREX FireLab and FIREX-AQ. The authors thank AERONET (NASA GSFC) and the Service National d'Observation PHOTONS/AERONET-EARLINET and Cimel, as well as NASA AERONET staff for coordination with the U.S. Forest Service; Fire Chemistry Lab; and the University of Idaho Taylor Ranch Wilderness School staff for setting up, maintaining, and decommissioning the stationary DRAGON networks.

Financial support. This research has been supported by the CaPPA project (Chemical and Physical Properties of the Atmosphere), funded by the ANR (French National Research Agency) through the PIA (Programme d'Investissement d'Avenir), under contract no. ANR-11LABX-0005-01; ANRT (Association Nationale de la Recherche et de la Technologie) France (CIFRE, grant no. 2020/0442); the European Commission (EU Horizon 2020, GRASP-ACE (grant no. 778349)); the Regional Council Hauts-de-France (project CLIMIBIO); and FEDER (European Funds for Regional Economic Development).

Review statement. This paper was edited by Daniel Perez-Ramirez and reviewed by two anonymous referees.

References

Ackermann, J.: Two-wavelength lidar inversion algorithm for a two-component atmosphere, Appl. Optics, 36, 5134, https://doi.org/10.1364/AO.36.005134, 1997.

Ackermann, J.: Analytical solution of the two-frequency lidar inversion technique, Appl. Optics, 38, 7414, https://doi.org/10.1364/AO.38.007414, 1999.

Adachi, K., Dibb, J. E., Scheuer, E., Katich, J. M., Schwarz, J. P., Perring, A. E., Mediavilla, B., Guo, H., Campuzano-Jost, P., Jimenez, J. L., Crawford, J., Soja, A. J., Oshima, N., Kajino, M., Kinase, T., Kleinman, L., Sedlacek, A. J., Yokelson, R. J., and Buseck, P. R.: Fine Ash-Bearing Particles as a Major Aerosol Component in Biomass Burning Smoke, J. Geophys. Res.-Atmos., 127, e2021JD035657, https://doi.org/10.1029/2021JD035657, 2022.

Adam, M., Nicolae, D., Stachlewska, I. S., Papayannis, A., and Balis, D.: Biomass burning events measured by lidars in EARLINET – Part 1: Data analysis methodology, Atmos. Chem. Phys., 20, 13905–13927, https://doi.org/10.5194/acp-20-13905-2020, 2020.

Alados-Arboledas, L., Müller, D., Guerrero-Rascado, J. L., Navas-Guzmán, F., Pérez-Ramírez, D., and Olmo, F. J.: Optical and microphysical properties of fresh biomass burning aerosol retrieved by Raman lidar, and star-and sun-photometry, Geophys. Res. Lett., 38, L01807, https://doi.org/10.1029/2010GL045999, 2011.

Althausen, D., Engelmann, E., Baars, H., Heese, B., Kanitz, T., Komppula, M., Giannakaki, E., Pfüller, A., Silva, A. M., Preißler, J., Wagner, F., Rascado, J. L., Pereira, S., Lim, J. H., Ahn, J. Y., Tesche, M., and Stachlewska, I. S.: PollyNET – a network of multiwavelength polarization Raman lidars, in: Proc. SPIE 8894, Lidar Technologies, Techniques, and Measurements for Atmospheric Remote Sensing IX, 88940I, 22 October 2013, Dresden, Germany, 8894, https://doi.org/10.1117/12.2028921, 2013.

Ansmann, A., Bösenberg, J., Chaikovsky, A., Comerón, A., Eckhardt, S., Eixmann, R., Freudenthaler, V., Ginoux, P., Komguem, L., Linné, H., Márquez, M. Á. L., Matthias, V., Mattis, I., Mitev, V., Müller, D., Music, S., Nickovic, S., Pelon, J., Sauvage, L., Sobolewsky, P., Srivastava, M. K., Stohl, A., Torres, O., Vaughan, G., Wandinger, U., and Wiegner, M.: Long-range transport of Saharan dust to northern Europe: The 11-16 October 2001 outbreak observed with EARLINET: Saharan dust transport over Europe, J. Geophys. Res., 108, 4783, https://doi.org/10.1029/2003JD003757, 2003.

Ansmann, A., Baars, H., Tesche, M., Müller, D., Althausen, D., Engelmann, R., Pauliquevis, T., and Artaxo, P.: Dust and smoke transport from Africa to South America: Lidar profiling over Cape Verde and the Amazon rainforest, Geophys. Res. Lett., 36, L11802, https://doi.org/10.1029/2009GL037923, 2009.

Balis, D. S., Amiridis, V., Zerefos, C., Gerasopoulos, E., Andreae, M., Zanis, P., Kazantzidisa, A., Kazadzis, S., and Papayannis, A: Raman lidar and sunphotometric measurements of aerosol optical properties over Thessaloniki, Greece during a biomass burning episode, Atmos. Environ., 37, 4529–4538, https://doi.org/10.1016/S1352-2310(03)00581-8, 2003.

Barreto, Á., Cuevas, E., Granados-Muñoz, M.-J., Alados-Arboledas, L., Romero, P. M., Gröbner, J., Kouremeti, N., Almansa, A. F., Stone, T., Toledano, C., Román, R., Sorokin, M., Holben, B., Canini, M., and Yela, M.: The new sun-sky-lunar Cimel CE318-T multiband photometer – a comprehensive performance evaluation, Atmos. Meas. Tech., 9, 631–654, https://doi.org/10.5194/amt-9-631-2016, 2016.

Bohlmann, S., Baars, H., Radenz, M., Engelmann, R., and Macke, A.: Ship-borne aerosol profiling with lidar over the Atlantic Ocean: from pure marine conditions to complex dust–smoke mixtures, Atmos. Chem. Phys., 18, 9661–9679, https://doi.org/10.5194/acp-18-9661-2018, 2018.

Boucher, O., Randall, D., Artaxo, P., Bretherton, C., Feingold, G., Forster, P., Kerminen, V.-M., Kondo, Y., H. Liao, Lohmann, U., Rasch, P., Satheesh, S. K., Sherwood, S., Stevens, B., and Zhang, X. Y.: Clouds and Aerosols, in: Climate Change 2013: The Physical Science Basis. Contribution of Working Group I to the Fifth Assessment Report of the Intergovernmental Panel on Climate Change, Cambridge University Press, Cambridge, United Kingdom and New York, NY, USA, 2013.

Bovchaliuk, V., Goloub, P., Podvin, T., Veselovskii, I., Tanre, D., Chaikovsky, A., Dubovik, O., Mortier, A., Lopatin, A., Korenskiy, M., and Victori, S.: Comparison of aerosol properties retrieved using GARRLiC, LIRIC, and Raman algorithms applied to multi-wavelength lidar and sun/sky-photometer data, Atmos. Meas. Tech., 9, 3391–3405, https://doi.org/10.5194/amt-9-3391-2016, 2016.

Burton, S. P., Ferrare, R. A., Vaughan, M. A., Omar, A. H., Rogers, R. R., Hostetler, C. A., and Hair, J. W.: Aerosol classification from airborne HSRL and comparisons with the CALIPSO vertical feature mask, Atmos. Meas. Tech., 6, 1397–1412, https://doi.org/10.5194/amt-6-1397-2013, 2013.

Chazette, P. and Totems, J.: Lidar Profiling of Aerosol Vertical Distribution in the Urbanized French Alpine Valley of Annecy and Impact of a Saharan Dust Transport Event, Remote Sens.-Basel, 15, 1070, https://doi.org/10.3390/rs15041070, 2023.

Córdoba-Jabonero, C., Ansmann, A., Jiménez, C., Baars, H., López-Cayuela, M.-Á., and Engelmann, R.: Experimental assessment of a micro-pulse lidar system in comparison with reference lidar measurements for aerosol optical properties retrieval, Atmos. Meas. Tech., 14, 5225–5239, https://doi.org/10.5194/amt-14-5225-2021, 2021.

De Wekker, S. F. J. and Kossmann, M.: Convective Boundary Layer Heights Over Mountainous Terrain – A Review of Concepts, Front. Earth Sci., 3, 77, https://doi.org/10.3389/feart.2015.00077, 2015.

Dieudonné, E., Chazette, P., Marnas, F., Totems, J., and Shang, X.: Lidar profiling of aerosol optical properties from Paris to Lake Baikal (Siberia), Atmos. Chem. Phys., 15, 5007–5026, https://doi.org/10.5194/acp-15-5007-2015, 2015.

Dubovik, O. and King, M. D.: A flexible inversion algorithm for retrieval of aerosol optical properties from Sun and sky radiance measurements, J. Geophys. Res., 105, 20673–20696, https://doi.org/10.1029/2000JD900282, 2000.

Engelmann, R., Kanitz, T., Baars, H., Heese, B., Althausen, D., Skupin, A., Wandinger, U., Komppula, M., Stachlewska, I. S., Amiridis, V., Marinou, E., Mattis, I., Linné, H., and Ansmann, A.: The automated multiwavelength Raman polarization and water-vapor lidar Polly^{XT}: the neXT generation, Atmos. Meas. Tech., 9, 1767–1784, https://doi.org/10.5194/amt-9-1767-2016, 2016.

EOSDIS: Worlview: Fires and Thermal Anomalies (Day and Night), Earth Observing System Data and Information System [data set], https://wvs.earthdata.nasa.gov/ (last access: 23 October 2023), 2023.

Floutsi, A. A., Baars, H., Engelmann, R., Althausen, D., Ansmann, A., Bohlmann, S., Heese, B., Hofer, J., Kanitz, T., Haarig, M., Ohneiser, K., Radenz, M., Seifert, P., Skupin, A., Yin, Z., Abdullaev, S. F., Komppula, M., Filioglou, M., Giannakaki, E., Stachlewska, I. S., Janicka, L., Bortoli, D., Marinou, E., Amiridis, V., Gialitaki, A., Mamouri, R.-E., Barja, B., and Wandinger, U.: DeLiAn – a growing collection of depolarization ratio, lidar ratio and Ångström exponent for different aerosol types and mixtures from ground-based lidar observations, Atmos. Meas. Tech., 16, 2353–2379, https://doi.org/10.5194/amt-16-2353-2023, 2023.

Freudenthaler, V.: About the effects of polarising optics on lidar signals and the Δ90 calibration, Atmos. Meas. Tech., 9, 4181–4255, https://doi.org/10.5194/amt-9-4181-2016, 2016.

Freudenthaler, V., Esselborn, M., Wiegner, M., Heese, B., Tesche, M., Ansmann, A., Müller, D., Althausen, D., Wirth, M., Fix, A., Ehret, G., Knippertz, P., Toledano, C., Gasteiger, J., Garhammer, M., and Seefeldner, M.: Depolarization ratio profiling at several wavelengths in pure Saharan dust during SAMUM 2006, Tellus B, 61, 165–179, https://doi.org/10.1111/j.1600-0889.2008.00396.x, 2009.

Freudenthaler, V., Linné, H., Chaikovski, A., Rabus, D., and Groß, S.: EARLINET lidar quality assurance tools, Atmos. Meas. Tech. Discuss. [preprint], https://doi.org/10.5194/amt-2017-395, in review, 2018.

Giles, D. M., Sinyuk, A., Sorokin, M. G., Schafer, J. S., Smirnov, A., Slutsker, I., Eck, T. F., Holben, B. N., Lewis, J. R., Campbell, J. R., Welton, E. J., Korkin, S. V., and Lyapustin, A. I.: Advancements in the Aerosol Robotic Network (AERONET) Version 3 database – automated near-real-time quality control algorithm with improved cloud screening for Sun photometer aerosol optical depth (AOD) measurements, Atmos. Meas. Tech., 12, 169–209, https://doi.org/10.5194/amt-12-169-2019, 2019.

Guerrero-Rascado, J. L., Costa, M. J., Bortoli, D., Silva, A. M., Lyamani, H., and Alados-Arboledas, L.: Infrared lidar overlap function: an experimental determination, Opt. Express, 18, 20350, https://doi.org/10.1364/OE.18.020350, 2010.

Haarig, M., Ansmann, A., Engelmann, R., Baars, H., Toledano, C., Torres, B., Althausen, D., Radenz, M., and Wandinger, U.: First triple-wavelength lidar observations of depolarization and extinction-to-backscatter ratios of Saharan dust, Atmos. Chem. Phys., 22, 355–369, https://doi.org/10.5194/acp-22-355-2022, 2022.

Holben, B. N., Eck, T. F., Slutsker, I., Tanré, D., Buis, J. P., Setzer, A., Vermote, E., Reagan, J. A., Kaufman, Y. J., Nakajima, T., Lavenu, F., Jankowiak, I., and Smirnov, A.: AERONET—A Federated Instrument Network and Data Archive for Aerosol Characterization, Remote Sens. Environ., 66, 1–16, https://doi.org/10.1016/S0034-4257(98)00031-5, 1998.

Holben, B. N., Kim, J., Sano, I., Mukai, S., Eck, T. F., Giles, D. M., Schafer, J. S., Sinyuk, A., Slutsker, I., Smirnov, A., Sorokin, M., Anderson, B. E., Che, H., Choi, M., Crawford, J. H., Ferrare, R. A., Garay, M. J., Jeong, U., Kim, M., Kim, W., Knox, N., Li, Z., Lim, H. S., Liu, Y., Maring, H., Nakata, M., Pickering, K. E., Piketh, S., Redemann, J., Reid, J. S., Salinas, S., Seo, S., Tan, F., Tripathi, S. N., Toon, O. B., and Xiao, Q.: An overview of mesoscale aerosol processes, comparisons, and validation studies from DRAGON networks, Atmos. Chem. Phys., 18, 655–671, https://doi.org/10.5194/acp-18-655-2018, 2018.

Hu, Q., Goloub, P., Veselovskii, I., Bravo-Aranda, J.-A., Popovici, I. E., Podvin, T., Haeffelin, M., Lopatin, A., Dubovik, O., Pietras, C., Huang, X., Torres, B., and Chen, C.: Long-range-transported Canadian smoke plumes in the lower stratosphere over northern France, Atmos. Chem. Phys., 19, 1173–1193, https://doi.org/10.5194/acp-19-1173-2019, 2019.

Hu, Q., Goloub, P., Veselovskii, I., and Podvin, T.: The characterization of long-range transported North American biomass burning plumes: what can a multi-wavelength Mie–Raman-polarization-fluorescence lidar provide?, Atmos. Chem. Phys., 22, 5399–5414, https://doi.org/10.5194/acp-22-5399-2022, 2022.

Karol, Y., Tanré, D., Goloub, P., Vervaerde, C., Balois, J. Y., Blarel, L., Podvin, T., Mortier, A., and Chaikovsky, A.: Airborne sun photometer PLASMA: concept, measurements, comparison of aerosol extinction vertical profile with lidar, Atmos. Meas. Tech., 6, 2383–2389, https://doi.org/10.5194/amt-6-2383-2013, 2013.

Kim, M.-H., Omar, A. H., Tackett, J. L., Vaughan, M. A., Winker, D. M., Trepte, C. R., Hu, Y., Liu, Z., Poole, L. R., Pitts, M. C., Kar, J., and Magill, B. E.: The CALIPSO version 4 automated aerosol classification and lidar ratio selection algorithm, Atmos. Meas. Tech., 11, 6107–6135, https://doi.org/10.5194/amt-11-6107-2018, 2018.

Klett, J. D.: Lidar inversion with variable backscatter/extinction ratios, Appl. Optics, 24, 1638, https://doi.org/10.1364/AO.24.001638, 1985.

Kovalev, V. A.: Sensitivity of the lidar solution to errors of the aerosol backscatter-to-extinction ratio: influence of a monotonic change in the aerosol extinction coefficient, Appl. Optics, 34, 3457, https://doi.org/10.1364/AO.34.003457, 1995.

Kovalev, V. A.: Distortions of the extinction coefficient profile caused by systematic errors in lidar data, Appl. Optics, 43, 3191, https://doi.org/10.1364/AO.43.003191, 2004.

Kovalev, V. A. and Eichinger, W. E.: Elastic Lidar: Theory, Practice and Analysis methods, John Wiley & Sons, 2004.

Kunz, G. J.: Two-wavelength lidar inversion algorithm, Appl. Optics, 38, 1015, https://doi.org/10.1364/AO.38.001015, 1999.

Kusmierczyk-Michulec, J.: Empirical relationships between aerosol mass concentrations and Ångström parameter, Geophys. Res. Lett., 29, 1145, https://doi.org/10.1029/2001GL014128, 2002.

López-Cayuela, M. Á., Córdoba-Jabonero, C., Bermejo-Pantaleón, D., Sicard, M., Salgueiro, V., Molero, F., Carvajal-Pérez, C. V., Granados-Muñoz, M. J., Comerón, A., Couto, F. T., Barragán, R., Zorzano, M.-P., Bravo-Aranda, J. A., Muñoz-Porcar, C., Costa, M. J., Artíñano, B., Rodríguez-Gómez, A., Bortoli, D., Pujadas, M., Abril-Gago, J., Alados-Arboledas, L., and Guerrero-Rascado, J. L.: Vertical characterization of fine and coarse dust particles during an intense Saharan dust outbreak over the Iberian Peninsula in springtime 2021, Atmos. Chem. Phys., 23, 143–161, https://doi.org/10.5194/acp-23-143-2023, 2023.

Lu, X., Jiang, Y., Zhang, X., Wang, X., and Spinelli, N.: Two-wavelength lidar inversion algorithm for determination of aerosol extinction-to-backscatter ratio and its application to CALIPSO lidar measurements, Journal of Quantitative Spectroscopy and Radiative Transfer, 112, 320–328, https://doi.org/10.1016/j.jqsrt.2010.07.013, 2011.

Mascaut, F., Pujol, O., Verreyken, B., Peroni, R., Metzger, J. M., Blarel, L., Podvin, T., Goloub, P., Sellegri, K., Thornberry, T., Duflot, V., Tulet, P., and Brioude, J.: Aerosol characterization in an oceanic context around Reunion Island (AEROMARINE field campaign), Atmos. Environ., 268, 118770, https://doi.org/10.1016/j.atmosenv.2021.118770, 2022.

Météo-France: Catalogue: Observations In situ: Altitude: Observations d'altitude (Radio sondages), Météo-France, https://donneespubliques.meteofrance.fr/ (last access: 23 October 2023), 2023.

Morille, Y., Haeffelin, M., Drobinski, P., and Pelon, J.: STRAT: An Automated Algorithm to Retrieve the Vertical Structure of the Atmosphere from Single-Channel Lidar Data, J. Atmos. Ocean. Tech., 24, 761–775, https://doi.org/10.1175/JTECH2008.1, 2007.

Mortier, A., Goloub, P., Podvin, T., Deroo, C., Chaikovsky, A., Ajtai, N., Blarel, L., Tanre, D., and Derimian, Y.: Detection and characterization of volcanic ash plumes over Lille during the Eyjafjallajökull eruption, Atmos. Chem. Phys., 13, 3705–3720, https://doi.org/10.5194/acp-13-3705-2013, 2013.

Müller, D., Hostetler, C. A., Ferrare, R. A., Burton, S. P., Chemyakin, E., Kolgotin, A., Hair, J. W., Cook, A. L., Harper, D. B., Rogers, R. R., Hare, R. W., Cleckner, C. S., Obland, M. D., Tomlinson, J., Berg, L. K., and Schmid, B.: Airborne Multiwavelength High Spectral Resolution Lidar (HSRL-2) observations during TCAP 2012: vertical profiles of optical and microphysical properties of a smoke/urban haze plume over the northeastern coast of the US, Atmos. Meas. Tech., 7, 3487–3496, https://doi.org/10.5194/amt-7-3487-2014, 2014.

NASA GSFC: AERONET (AErosol RObotic NETwork) program, https://aeronet.gsfc.nasa.gov/ (last access: 23 October 2023), 2023.

Nicolae, D., Nemuc, A., Müller, D., Talianu, C., Vasilescu, J., Belegante, L., and Kolgotin, A.: Characterization of fresh and aged biomass burning events using multiwavelength Raman lidar and mass spectrometry: biomass burning aerosols from lidar & AMS, J. Geophys. Res. Atmos., 118, 2956–2965, https://doi.org/10.1002/jgrd.50324, 2013.

Omar, A. H., Winker, D. M., Vaughan, M. A., Hu, Y., Trepte, C. R., Ferrare, R. A., Lee, K.-P., Hostetler, C. A., Kittaka, C., Rogers, R. R., Kuehn, R. E., and Liu, Z.: The CALIPSO Automated Aerosol Classification and Lidar Ratio Selection Algorithm, J. Atmos. Ocean. Tech., 26, 1994–2014, https://doi.org/10.1175/2009JTECHA1231.1, 2009.

Pal, S., Xueref-Remy, I., Ammoura, L., Chazette, P., Gibert, F., Royer, P., Dieudonné, E., Dupont, J.-C., Haeffelin, M., Lac, C., Lopez, M., Morille, Y., and Ravetta, F.: Spatio-temporal variability of the atmospheric boundary layer depth over the Paris agglomeration: An assessment of the impact of the urban heat island intensity, Atmos. Environ., 63, 261–275, https://doi.org/10.1016/j.atmosenv.2012.09.046, 2012.

Papagiannopoulos, N., D'Amico, G., Gialitaki, A., Ajtai, N., Alados-Arboledas, L., Amodeo, A., Amiridis, V., Baars, H., Balis, D., Binietoglou, I., Comerón, A., Dionisi, D., Falconieri, A., Fréville, P., Kampouri, A., Mattis, I., Mijić, Z., Molero, F., Papayannis, A., Pappalardo, G., Rodríguez-Gómez, A., Solomos, S., and Mona, L.: An EARLINET early warning system for atmospheric aerosol aviation hazards, Atmos. Chem. Phys., 20, 10775–10789, https://doi.org/10.5194/acp-20-10775-2020, 2020.

Papayannis, A., Amiridis, V., Mona, L., Tsaknakis, G., Balis, D., Bösenberg, J., Chaikovski, A., De Tomasi, F., Grigorov, I., Mattis, I., Mitev, V., Müller, D., Nickovic, S., Pérez, C., Pietruczuk, A., Pisani, G., Ravetta, F., Rizi, V., Sicard, M., Trickl, T., Wiegner, M., Gerding, M., Mamouri, R. E., D'Amico, G., and Pappalardo, G.: Systematic lidar observations of Saharan dust over Europe in the frame of EARLINET (2000–2002), J. Geophys. Res., 113, D10204, https://doi.org/10.1029/2007JD009028, 2008.

Pappalardo, G., Amodeo, A., Apituley, A., Comeron, A., Freudenthaler, V., Linné, H., Ansmann, A., Bösenberg, J., D'Amico, G., Mattis, I., Mona, L., Wandinger, U., Amiridis, V., Alados-Arboledas, L., Nicolae, D., and Wiegner, M.: EARLINET: towards an advanced sustainable European aerosol lidar network, Atmos. Meas. Tech., 7, 2389–2409, https://doi.org/10.5194/amt-7-2389-2014, 2014.

Pelon, J., Mallet, M., Mariscal, A., Goloub, P., Tanré, D., Bou Karam, D., Flamant, C., Haywood, J., Pospichal, B., and Victori, S.: Microlidar observations of biomass burning aerosol over Djougou (Benin) during African Monsoon Multidisciplinary Analysis Special Observation Period 0: Dust and Biomass-Burning Experiment, J. Geophys. Res., 113, D00C18, https://doi.org/10.1029/2008JD009976, 2008.

Popovici, I.: Aerosol spatial and temporal variability as seen by Mobile Aerosol Monitoring System (MAMS), PhD thesis, Université de Lille, https://theses.fr/2018LILUR070 (last access: 1 October 2021), 2018.

Popovici, I. E., Goloub, P., Podvin, T., Blarel, L., Loisil, R., Unga, F., Mortier, A., Deroo, C., Victori, S., Ducos, F., Torres, B., Delegove, C., Choël, M., Pujol-Söhne, N., and Pietras, C.: Description and applications of a mobile system performing on-road aerosol remote sensing and in situ measurements, Atmos. Meas. Tech., 11, 4671–4691, https://doi.org/10.5194/amt-11-4671-2018, 2018.

Popovici, I. E., Deng, Z., Goloub, P., Xia, X., Chen, H., Blarel, L., Podvin, T., Hao, Y., Chen, H., Torres, B., Victori, S., and Fan, X.: Mobile On-Road Measurements of Aerosol Optical Properties during MOABAI Campaign in the North China Plain, Atmosphere, 13, 21, https://doi.org/10.3390/atmos13010021, 2022.

Potter, J. F.: Two-frequency lidar inversion technique, Appl. Optics, 26, 1250, https://doi.org/10.1364/AO.26.001250, 1987.

Qi, S., Huang, Z., Ma, X., Huang, J., Zhou, T., Zhang, S., Dong, Q., Bi, J., and Shi, J.: Classification of atmospheric aerosols and clouds by use of dual-polarization lidar measurements, Opt. Express, 29, 23461, https://doi.org/10.1364/OE.430456, 2021.

Rocadenbosch, F., Frasier, S., Kumar, D., Lange Vega, D., Gregorio, E., and Sicard, M.: Backscatter Error Bounds for the Elastic Lidar Two-Component Inversion Algorithm, IEEE T. Geosci. Remote, 50, 4791–4803, https://doi.org/10.1109/TGRS.2012.2194501, 2012.

Royer, P., Chazette, P., Sartelet, K., Zhang, Q. J., Beekmann, M., and Raut, J.-C.: Comparison of lidar-derived PM_{10} with regional modeling and ground-based observations in the frame of MEGAPOLI experiment, Atmos. Chem. Phys., 11, 10705–10726, https://doi.org/10.5194/acp-11-10705-2011, 2011.

Russell, P. B., Swissler, T. J., and McCormick, M. P.: Methodology for error analysis and simulation of lidar aerosol measurements, Appl. Optics, 18, 3783, https://doi.org/10.1364/AO.18.003783, 1979.

Sasano, Y., Browell, E. V., and Ismail, S.: Error caused by using a constant extinction/backscattering ratio in the lidar solution, Appl. Optics, 24, 3929, https://doi.org/10.1364/AO.24.003929, 1985.

Sassen, K. and Dodd, G. C.: Lidar crossover function and misalignment effects, Appl. Optics, 21, 3162, https://doi.org/10.1364/AO.21.003162, 1982.

Seneviratne, S. I., Zhang, X., Adnan, M., Badi, W., Dereczynski, C., Di Luca, A., Ghosh, S., Iskandar, I., Kossin, J., Lewis, S., and Otto, F., Pinto, I., Satoh, M., Vicente-Serrano, S. M., Wehner, M., and Zhou, B.: Weather and Climate Extreme Events in a Changing Climate, in: Climate Change 2021 – The Physical Science Basis: Working Group I Contribution to the Sixth Assessment Report of the Intergovernmental Panel on Climate Change, Cambridge University Press, Cambridge, United Kingdom and New York, NY, USA, https://doi.org/10.1017/9781009157896, 2021.

Shang, X., Chazette, P., and Totems, J.: Analysis of a warehouse fire smoke plume over Paris with an N_2 Raman lidar and an optical thickness matching algorithm, Atmos. Meas. Tech., 11, 6525–6538, https://doi.org/10.5194/amt-11-6525-2018, 2018.

Sicard, M., D'Amico, G., Comerón, A., Mona, L., Alados-Arboledas, L., Amodeo, A., Baars, H., Baldasano, J. M., Belegante, L., Binietoglou, I., Bravo-Aranda, J. A., Fernández, A. J., Fréville, P., García-Vizcaíno, D., Giunta, A., Granados-Muñoz, M. J., Guerrero-Rascado, J. L., Hadjimitsis, D., Haefele, A., Hervo, M., Iarlori, M., Kokkalis, P., Lange, D., Mamouri, R. E., Mattis, I., Molero, F., Montoux, N., Muñoz, A., Muñoz Porcar, C., Navas-Guzmán, F., Nicolae, D., Nisantzi, A., Papagiannopoulos, N., Papayannis, A., Pereira, S., Preißler, J., Pujadas, M., Rizi, V., Rocadenbosch, F., Sellegri, K., Simeonov, V., Tsaknakis, G., Wagner, F., and Pappalardo, G.: EARLINET: potential operationality of a research network, Atmos. Meas. Tech., 8, 4587–4613, https://doi.org/10.5194/amt-8-4587-2015, 2015.

Sicard, M., Rodríguez-Gómez, A., Comerón, A., and Muñoz-Porcar, C.: Calculation of the Overlap Function and Associated Error of an Elastic Lidar or a Ceilometer: Cross-Comparison with a Cooperative Overlap-Corrected System, Sensors, 20, 6312, https://doi.org/10.3390/s20216312, 2020.

Smirnov, A., Holben, B. N., Eck, T. F., Dubovik, O., and Slutsker, I.: Cloud-Screening and Quality Control Algorithms for the AERONET Database, Remote Sens. Environ., 73, 337–349, https://doi.org/10.1016/S0034-4257(00)00109-7, 2000.

Smirnov, A., Holben, B. N., Slutsker, I., Giles, D. M., McClain, C. R., Eck, T. F., Sakerin, S. M., Macke, A., Croot, P., Zibordi, G., Quinn, P. K., Sciare, J., Kinne, S., Harvey, M., Smyth, T. J., Piketh, S., Zielinski, T., Proshutinsky, A., Goes, J. I., Nelson, N. B., Larouche, P., Radionov, V. F., Goloub, P., Krishna Moorthy, K., Matarrese, R., Robertson, E. J., and Jourdin, F.: Maritime Aerosol Network as a component of Aerosol Robotic Network, J. Geophys. Res., 114, D06204, https://doi.org/10.1029/2008JD011257, 2009.

Sinyuk, A., Holben, B. N., Eck, T. F., Giles, D. M., Slutsker, I., Korkin, S., Schafer, J. S., Smirnov, A., Sorokin, M., and Lyapustin, A.: The AERONET Version 3 aerosol retrieval algorithm, associated uncertainties and comparisons to Version 2, Atmos. Meas. Tech., 13, 3375–3411, https://doi.org/10.5194/amt-13-3375-2020, 2020.

Tesche, M., Ansmann, A., MüLLER, D., Althausen, D., Mattis, I., Heese, B., Freudenthaler, V., Wiegner, M., Esselborn, M., Pisani, G., and Knippertz, P.: Vertical profiling of Saharan dust with Raman lidars and airborne HSRL in southern Morocco during SAMUM, Tellus B, 61, 144–164, https://doi.org/10.1111/j.1600-0889.2008.00390.x, 2009.

University of Wyoming: Upper air: Sounding, University of Wyoming, Department of Atmospheric Science [data set], https://weather.uwyo.edu/upperair/sounding.html (last access: 23 October 2023), 2023.

U.S. Geological Survey: USGS EROS Archive – Digital Elevation – Shuttle Radar Topography Mission (SRTM) 1 Arc-Second Global, USGS [data set], https://doi.org/10.5066/F7PR7TFT, 2023.

Vaughan, M.: Algorithm for retrieving lidar ratios at 1064 nm from space-based lidar backscatter data, Proceedings, Laser Radar Technology for Remote Sensing, 12 January 2004, Barcelona, Spain, Proc. SPIE 5240, https://doi.org/10.1117/12.510770, 2004.

Vaughan, M. A., Young, S. A., Winker, D. M., Powell, K. A., Omar, A. H., Liu, Z., Hu, Y., and Hostetler, C. A.: Fully automated analysis of space-based lidar data: an overview of the CALIPSO retrieval algorithms and data products, Proceedings, Laser Radar Techniques for Atmospheric Sensing, 4 November 2004, Maspalomas, Canary Islands, Spain, Proc. SPIE 5575, https://doi.org/10.1117/12.572024, 2004.

Veselovskii, I., Hu, Q., Goloub, P., Podvin, T., Choël, M., Visez, N., and Korenskiy, M.: Mie–Raman–fluorescence lidar observations of aerosols during pollen season in the north of France, Atmos. Meas. Tech., 14, 4773–4786, https://doi.org/10.5194/amt-14-4773-2021, 2021.

Veselovskii, I., Hu, Q., Goloub, P., Podvin, T., Barchunov, B., and Korenskii, M.: Combining Mie–Raman and fluorescence observations: a step forward in aerosol classification with lidar technology, Atmos. Meas. Tech., 15, 4881–4900, https://doi.org/10.5194/amt-15-4881-2022, 2022.

Wang, D., Stachlewska, I. S., Delanoë, J., Ene, D., Song, X., and Schüttemeyer, D.: Spatio-temporal discrimination of molecular, aerosol and cloud scattering and polarization using a combination of a Raman lidar, Doppler cloud radar and microwave radiometer, Opt. Express, 28, 20117, https://doi.org/10.1364/OE.393625, 2020.

Warneke, C., Schwarz, J. P., Ryerson, T., Crawford, J., Dibb, J., Lefer, B., Roberts, J., Trainer, M., Murphy, D., Brown, S., Brewer, A., Gao, R.-S., and Fahey, D.: Fire Influence on Regional to Global Environments and Air Quality (FIREX-AQ), NOAA/NASA [White Paper], https://csl.noaa.gov/projects/firex-aq/whitepaper.pdf (last access: 20 November 2023), 2018.

Warneke, C., Schwarz, J. P., Dibb, J., Kalashnikova, O., Frost, G., Al-Saad, J., Brown, S. S., Brewer, Wm. A., Soja, A., Seidel, F. C., Washenfelder, R. A., Wiggins, E. B., Moore, R. H., Anderson, B. E., Jordan, C., Yacovitch, T. I., Herndon, S. C., Liu, S., Kuwayama, T., Jaffe, D., Johnston, N., Selimovic, V., Yokelson, R., Giles, D. M., Holben, B. N., Goloub, P., Popovici, I., Trainer, M., Kumar, A., Pierce, R. B., Fahey, D., Roberts, J., Gargulinski, E. M., Peterson, D. A., Ye, X., Thapa, L. H., Saide, P. E., Fite, C. H., Holmes, C. D., Wang, S., Coggon, M. M., Decker, Z. C. J., Stockwell, C. E., Xu, L., Gkatzelis, G., Aikin, K., Lefer, B., Kaspari, J., Griffin, D., Zeng, L., Weber, R., Hastings, M., Chai, J., Wolfe, G. M., Hanisco, T. F., Liao, J., Campuzano Jost, P., Guo, H., Jimenez, J. L., Crawford, J., and The FIREX-AQ Science Team: Fire Influence on Regional to Global Environments and Air Quality (FIREX-AQ), J. Geophys. Res.-Atmos., 128, https://doi.org/10.1029/2022JD037758, 2023.

Weitkamp, C. (Ed.): Lidar: range-resolved optical remote sensing of the atmosphere, Springer, New York, 455 pp., ISBN 0387400753, 2005.

Welton, E. J. and Campbell, J. R.: Micropulse Lidar Signals: Uncertainty Analysis, J. Atmos. Ocean. Tech., 19, 2089–2094, https://doi.org/10.1175/1520-0426(2002)019<2089:MLSUA>2.0.CO;2, 2002.

Welton, E. J., Campbell, J. R., Spinhirne, J. D., and Scott, V. S.: Global monitoring of clouds and aerosols using a network of micropulse lidar systems, Second International Asia–Pacific Symposium on Remote Sensing of the Atmosphere, Environment, and Space, 13 February 2001, Sendai, Japan, Proc. SPIE 4153, https://doi.org/10.1117/12.417040, 2001.

Whiteman, C. D.: Mountain meteorology: fundamentals and applications, Oxford Univ. Press, New York, NY, 355 pp., ISBN 0195132718, 2000.

Yin, Z., Ansmann, A., Baars, H., Seifert, P., Engelmann, R., Radenz, M., Jimenez, C., Herzog, A., Ohneiser, K., Hanbuch, K., Blarel, L., Goloub, P., Dubois, G., Victori, S., and Maupin, F.: Aerosol measurements with a shipborne Sun–sky–lunar photometer and collocated multiwavelength Raman polarization lidar over the Atlantic Ocean, Atmos. Meas. Tech., 12, 5685–5698, https://doi.org/10.5194/amt-12-5685-2019, 2019.